Accretion and Emission close to supermassive Black Holes in Quasars and AGN: Modeling the UV-X-spectrum

René Goosmann

Accretion and Emission close to supermassive Black Holes in Quasars and AGN:

Modeling the UV-X-spectrum

Dissertation
zur Erlangung des Doktorgrades
des Fachbereichs Physik
der Universität Hamburg

vorgelegt von
René W. Goosmann
aus Oldenburg (Oldb.)

Hamburg
2006

Gutachter/Gutachterin der Dissertation:
Prof. Dr. Dieter Reimers, Universität Hamburg
Dr. Martine Mouchet, Observatoire de Paris

Gutachter der Disputation:
Prof. Dr. Dieter Reimers, Universität Hamburg
Prof. Dr. Peter Hauschildt, Universität Hamburg

Datum der Disputation: 2. Februar 2006

Vorsitzender des Prüfungsausschusses:
Prof. Dr. Günter Wiedemann, Universität Hamburg

Vorsitzender des Promotionsausschusses:
Prof. Dr. Günter Huber

Dekan des Fachbereichs Physik:
Prof. Dr. Günter Huber

«Les étoiles sont belles à cause d'une fleur que l'on ne voit pas.» —

Antoine de Saint-Exupéry, *Le Petit Prince*

Zusammenfassung

Die neuste Generation von Röntgensatelliten, wie XMM-Newton und Chandra, ermöglicht es, wesentliche neue Erkenntnisse über die Röntgeneigenschaften aktiver galaktischer Kerne (AGN) zu gewinnen. Hochauflösende Spektroskopie und Langzeitbeobachtungen über hunderte von Kilosekunden ergeben neue Einblicke in die Entstehung der Röntgenstrahlung, ihre Wechselwirkungen mit umgebender Materie, und ihre Veränderlichkeit.

In dieser Dissertation stelle ich Strahlungstransportsimulationen für AGN im fernen UV- und im Röntgenspektrum vor. Ich behandele verschiedene Aspekte der beobachteten Röntgenspektren: Compton-Reflexion und Reprocessing, Röntgenveränderlichkeit und Röntgenflares sowie den Einfluss von warm absorbern.

Im Zusammenhang mit dem Reprocessing untersuche ich ausführlich das Flaremodell, das, in Analogie zu Sonnenflares, auf magnetischen Rekonnektionen beruht. Dabei sollten kompakte, leuchtkräftige Quellen entstehen, die auf der Oberfläche der Akkretionsscheibe so genannte hot spots erzeugen. Ich untersuche die physikalischen Eigenschaften der Scheibenmaterie an verschiedenen Stellen eines solchen hot spots und berechne Spektren für das Reprocessing in unterschiedlichen Abstrahlungsrichtungen. Ich betrachte hot spots in verschiedenen Entfernungen vom zentralen Schwarzen Loch und für unterschiedliche Phasenlagen auf der Scheibe. Außerdem variiere ich die Masse des Schwarzen Loches, seine Akkretionsrate, und den Spin-Parameter. Ich berechne auch für einen entfernten Beobachter Spektren, wobei relativistische Korrekturen durch die Anwendung eines Ray-Tracing-Programms berücksichtigt werden. Ich erzeuge zeitabhängige Simulationen von einzelnen Röntgenflares und beziehe dabei Zeitverzögerungseffkte durch die Entfernung zwischen der Quelle und verschiedenen Stellen des hot spots mit ein. Die Modellierung eines Flares geschieht unter der Annahme, dass sich die Akkretionsscheibe im hydrostatischen Gleichgewicht befindet. Dabei wird für den Flare eine deutlich kürzere Dauer als die dynamische Zeitskala der Scheibe angenommen, so dass die vertikale Dichtestruktur während des Flares unverändert bleibt.

Beobachtungen der Seyfert-1-Galaxie MCG -6-30-15 mit XMM-Newton liefern eine Lichtkurve mit einem starken Flare von 2000 s Dauer. Für diesen Flare haben Ponti et al. (2004) Zeitverzögerungen in einzelnen Spektralbändern berechnet. Ich stelle ein einfaches Modell vor, das solche Zeitverzögerungen beschreibt, und dabei annimmt, dass ein entfernter Beobachter die Primärstrahlung des Flares und das Reprocssing als zwei aufeinander folgende Pulse wahrnimmt. Das Modell beschreibt die beobachteten Zeitverzögerungen in MCG -6-30-15 qualitativ korrekt und erlaubt eine Abschätzung des Abstandes zwischen der kompakten Quelle des Flares und der Akkretionsscheibe.

Mit Hilfe der Ergebnisse für die Modellierung eines einzelnen Flares führe ich Monte-Carlo-Rechnungen für Flare-Verteilungen über der Akkretionsscheibe durch. Ich berechne das fractional-variability-spectrum eines solchen Systems für verschiedene radiale Häufigkeitsverteilungen der hot spots und unterschiedlichen Spin des Schwarzen Loches. Die Anwendung dieses Modells auf ein beobachtetes fractional-variability-spectrum liefert Eingrenzungen dieser Parameter für den Fall von MCG -6-30-15.

Schließlich betrachte ich Veränderungen des Röntgenspektrums in Regionen, die weiter von der zentralen Quelle entfernt sind, und modelliere den warm absorber. Ich berechne ein Gitter von Modellen für einen warm absorber im Zustand konstanten Druckes. Ein solcher physikalischer Zustand wurde kürzlich durch die Beobachtung der Seyfert-1-Galaxie NGC 3783 nahe gelegt. Ich beschreibe allgemeine Tendenzen für die Struktur des Mediums und für die resultierenden Spektren und variiere dabei das einfallende Spektrum und die Säulendichte des warm absorbers.

Abstract

With the last generation of X-ray satellites, such as *XMM-Newton* and *Chandra*, our knowledge about the X-ray properties of Active Galactic Nuclei (AGN) has greatly improved. Detailed spectroscopy and long-term observations of hundreds of kilo-seconds have provided new insights into the mechanisms of X-ray production, its modification by intervening matter, and X-ray variability.

In this thesis I present radiative transfer modeling of AGN in the Far-UV and X-ray range. The modeling considers several aspects of the observed X-ray properties: the Compton reflection/reprocessed component, X-ray variability and flares, and the effects of the warm absorber.

For the X-ray reprocessing, I investigate in detail the magnetic flare model assuming solar-like magnetic reconnections above the accretion disk. Such events should produce bright, compact sources of hard X-ray radiation creating a hot spot on the disk surface underneath. I evaluate the physical properties of the disk medium across such a spot and compute spectra of the reprocessed radiation as a function of the position in the spot and of the local viewing direction. Spots at several distances of the central black hole and for different orbital phases are considered and I vary the black hole mass, its accretion rate, and its spin-parameter. Spectra are also computed for a distant observer including a full relativistic treatment, which is based on a ray-tracing technique. I provide time-dependent simulations of single flare events taking into account the time-lags induced by the distance between the compact flare source and different positions of the hot spot. The flare modeling is conducted assuming an underlying accretion disk in hydrostatic equilibrium. The duration of the flare is supposed to be significantly smaller than the dynamical time-scale, so that the vertical density structure of the disk remains constant over the whole flare-period.

Recent observations of the Seyfert-1 galaxy MCG -6-30-15 with *XMM-Newton* revealed a light-curve with a bright symmetric flare over 2000 s. For this flare, Ponti et al. (2004) presented a cross-correlation analysis deriving time-lags in several energy bands. I present a simple toy model describing such time-lags by assuming that the observer detects the primary radiation and the reprocessed component as two consecutive pulses. The toy model qualitatively reproduces the observed time-lags of MCG -6-30-15 and allows an estimation of the distance between the flare source and the disk.

Using the results of the single-flare modeling, Monte-Carlo simulations for distributions of orbiting flare-spots across an accretion disk are conducted. The resulting fractional variability spectrum is constructed for different radial luminosity distributions and values of the black hole spin. These parameters are constrained for MCG -6-30-15 by applying the model to its observed fractional variability spectrum.

Finally, the modification of the X-ray radiation in regions farther away from the central object is considered by modeling the warm absorber. A grid of models is computed for a warm absorber in pressure equilibrium as recently suggested by the observation of the Seyfert-1 galaxy NGC 3783. General tendencies for the stratification of the medium and for the resulting absorption spectra are shown by varying the slope of the incident spectrum, the ionization parameter, and the column density of the warm absorber.

Acknowledgments

I am grateful to my advisers Martine Mouchet at the *Observatoire de Paris* and Dieter Reimers at the *Universität Hamburg*. Martine Mouchet has been a great thesis adviser. Over the three years I spent at the Observatoire de Paris, she provided me with direction, having interesting discussions with me and giving me many useful comments and criticism on my research work. I will keep in very good memory the fact that she was always available to help me whenever I had questions or difficulties. I would also like to thank her for pointing out professional options beyond the PhD thesis to me. Dieter Reimers agreed for a second time to advise me from a distance, so I could prepare this thesis at a foreign institute. Again, this was a great professional and personal experience and I want to thank him for having made it possible.

During my time in the AGN research group at the *Laboratoire de l'Univers et de ses Théories* at Meudon I worked with several people who contributed a lot to what I am presenting in this thesis. Special thanks go to Anne-Marie Dumont who spent many hours explaining to me the computer codes *TITAN* and *NOAR*. Suzy Collin gave me a lot of useful hints on X-ray observations and models of Active Galactic Nuclei. I learned many things about radiative transfer from Loïc Chevallier who also enabled me to print some beautiful color-coded plots for time-dependent spectral data. Also, I had many discussions with Anabela Gonçalves about science and other important things in life. Finally, I am grateful to all the members of the AGN group and the *Laboratoire de l'Univers et de ses Théories* for hosting me for three years - and especially for being so patient at the beginning of my stay when my French was even slower than the science I do.

I worked in an international network based in France, Poland, and the Czech Republic. I am grateful to my collaborators Bożena Czerny and Agata Różańska at the Copernicus Astronomical Center in Warsaw, and to Vladimir Karas and Michal Dovčiak at the Astronomical Institute in Prague.

I have an extra big "thank you" to the following people who all proof-read parts of this thesis: Erin Bonning, Loïc Chevallier, Suzy Collin, Bożena Czerny, Michal Dovčiak, Anne-Marie Dumont, Anabela Gonçalves, Vladimir Karas, Franck Le Petit, Thierry Lehner, Martine Mouchet, Micaela Oertel, and Agata Różańska.

During the period of my PhD, I continued to be supported by the *Hans-Böckler-Stiftung* in Germany. This foundation has put me in touch with other scientists coming from a variety of branches, which was a very interesting experience. Especially, I would like to thank the members of the *Referat Promotionsförderung 2* as well as Gustav Obermair for all their help.

I could not have finished this work without the support of my wonderful family back in Germany. I am grateful to my parents, my sister Insa and her husband Jörg, and the little guy Cedric who is with them for more than a year now. Also, my recently found second family in France was a big support to me. Finally, it is because of you, my dear Edwige, that I had the energy to finish this thesis. And I would like to thank you *avec un très gros bisou!*

René Goosmann
Meudon, December 2005

Contents

1 Introduction **5**

2 The current understanding of AGN **7**
2.1 A quick course in quasar zoology . . . 7
2.2 The overall spectrum of AGN . . . 8
2.2.1 Continuum emission . . . 8
2.2.2 Radio power . . . 9
2.2.3 Infrared emission . . . 10
2.2.4 The big blue bump . . . 10
2.2.5 X-ray spectra . . . 11
2.2.6 Emission and absorption features . . . 11
2.3 Spectral variability of radio-quiet AGN . . . 13
2.3.1 Continuum variability . . . 13
2.3.2 Line variability . . . 15
2.4 The unified scheme . . . 15
2.4.1 Accretion as the origin of AGN emission . . . 16
2.4.2 The α-disk model . . . 16
2.4.3 Emission from relativistic jets . . . 17
2.4.4 Emission line regions . . . 17
2.4.5 Absorption by equatorial dust regions . . . 19

3 X-ray properties of AGN **21**
3.1 Observed spectra . . . 21
3.1.1 The power-law component: coronal emission or a hot inner flow? . . . 22
3.1.2 The soft X-ray-excess . . . 25
3.1.3 The soft X-ray absorption and emission lines . . . 26
3.1.4 The iron Kα-line and the Compton hump: X-ray reprocessing . . . 28
3.2 X-ray variability of AGN . . . 31
3.2.1 Timing analysis using power density spectra . . . 32
3.2.2 X-ray flaring and the variability of the iron Kα-line . . . 34

4 Modeling of X-ray reprocessing in AGN **37**
4.1 Production of the primary component . . . 37
4.2 X-ray reprocessing by the accretion disk . . . 38
4.2.1 Constant density models . . . 39
4.2.2 The hydrostatic equilibrium . . . 41

4.3 Spectral modeling of flare spots . . . 43
4.4 Relativistic effects and orbiting flares . . . 46

5 Applied radiative transfer methods 47
5.1 Determining the vertical disk structure . . . 48
5.1.1 Description of the flux . . . 48
5.1.2 Description of the pressure . . . 49
5.1.3 Description of the temperature . . . 50
5.1.4 Determining the structure of the medium . . . 50
5.2 The photoionization code *TITAN* . . . 50
5.2.1 Solving the radiative transfer problem . . . 51
5.2.2 Physical state of the medium . . . 55
5.2.3 Computational scheme of *TITAN* . . . 56
5.3 The Monte-Carlo code *NOAR* . . . 56
5.3.1 The Monte-Carlo method . . . 57
5.3.2 Physical processes and photon transfer . . . 58
5.3.3 Input and output of *NOAR* . . . 60
5.4 Relativistic ray-tracing with *KY* . . . 61
5.4.1 The transfer functions . . . 61
5.4.2 Computational scheme of *KY* . . . 63

6 Spectral modeling of X-ray flares 65
6.1 The vertical profile of the accretion disk . . . 66
6.1.1 Implementation of the relativistic corrections . . . 66
6.1.2 Results for the vertical disk profile . . . 67
6.2 The local properties of the reprocessed spectra . . . 70
6.2.1 Geometrical aspects of magnetic flares . . . 70
6.2.2 Temperature structure of the medium . . . 72
6.2.3 The reprocessed emission across the hot spot . . . 72
6.2.4 Integrated spectra of a whole spot . . . 78
6.3 Computation of the spectra seen by a distant observer . . . 79
6.3.1 Keplerian motion and relativistic effects . . . 80
6.3.2 Spots at different phases of the orbit . . . 82
6.3.3 Short-term spots at different orbital phases . . . 88
6.4 Summary and discussion . . . 90

7 Modeling time-lags of X-ray flares 97
7.1 Description of the model . . . 97
7.2 Modeling results . . . 100
7.2.1 Dependencies on the intrinsic delay and on the relative normalization . . . 101
7.2.2 Influence of the broadening . . . 103
7.2.3 Modeling measured time-lags of MCG -6-30-15 . . . 105
7.3 Summary and discussion . . . 105

8 Modeling variability by X-ray flares **107**
8.1 Description of the model . . . 108
8.1.1 The applied local spot spectra . . . 108
8.1.2 Flare distribution . . . 109
8.1.3 Ray-tracing and time integration . . . 110
8.2 Modeling results . . . 111
8.2.1 Effect of the spot structure and non-isotropic emission . . . 111
8.2.2 Dependencies on the model parameters . . . 113
8.2.3 Intrinsic randomness in the model . . . 114
8.2.4 The rms-spectrum of MCG -6-30-15 . . . 116
8.3 Summary and discussion . . . 117

9 Modeling the warm absorber **119**
9.1 Description of the model . . . 120
9.2 The difficulty of thermal instabilities . . . 121
9.3 The structure of the warm absorber . . . 123
9.4 Spectral imprints of the warm absorber . . . 124
9.5 Implications of a warm absorber in pressure equilibrium . . . 127

10 Conclusions and Perspectives **129**
10.1 Connection of the flare model to the observations . . . 130
10.2 Further improvements of our modeling technique . . . 131

Chapter 1

Introduction

Active Galactic Nuclei (AGN) are the most luminous persistent objects in the universe. An active galaxy is hosting a central black hole having a mass larger than $10^6 M_\odot$ and giving rise to a tremendous energy output within a relatively small volume. Some AGN are known to have luminosities being 10^4 times larger than those of regular galaxies, even though the size of the emitting region does not exceed the dimension of the solar system. The high luminosities are explained by accretion of matter onto the central supermassive black hole. The gravitational energy stored in the deep relativistic potential provides enough fueling for the strong emission observed.

The spectra of AGN are very broad reaching from the radio band to the X-rays and sometimes even γ-rays. It is now widely believed, that a major part of the accretion flow happens through a geometrical thin and optically thick accretion disk located in the equatorial plane of the black hole. The exact mechanism to transform the gravitational energy of the accreted matter into radiation has long been an unknown component of the accretion disk model. It has been described under the phenomenological α-prescription, where α is a constant of proportionality between the turbulence stress-tensor at a given disk radius and the local pressure. Recently, a promising physical explanation has been proposed by assuming magneto-rotational instabilities, causing turbulent friction between adjacent rings of the disk. A typical accretion disk in AGN has a temperature distribution lying roughly between 10^6 K and 10^4 K and therefore gives rise to the production of an optical/UV-continuum.

A significant fraction of the bolometric luminosity of AGN is dissipated in the X-ray range. The high-energy part of the spectrum is produced in the innermost regions of the accretion disk, where effects of general relativity become important. Detailed X-ray observations therefore allow to probe the models describing the inner accretion flow, connected radiative processes, and the effects induced by the curved space-time in the vicinity of the black hole. Such observations reveal that an accretion disk alone cannot provide an explanation for the high energy radiation of AGN. It is necessary to assume an additional medium being optically thin and very hot with temperatures between 10^8 K and 10^9 K. Radiative coupling between the two media then explains the appearance of the X-ray spectra observed: the hard X-rays produced in the hot phase irradiate the disk and are thus reflected as a soft X-ray component via Compton processes and absorption. This reprocessed component gives also rise to the fluorescent iron Kα-line, seen at 6.4 keV, which is an excellent probe for the innermost regions of AGN accretion disks. Details about the production of the hot medium and its geometrical location are still a matter of debate. One can imagine that the medium forms a hot corona above the surface of the accretion disk. This corona can be either continuous or fragmented ("patchy"). The heating mechanism for the corona can be related to

magnetic reconnection events forming compact, and temporary X-ray flares above the disk. The magnetic fields are assumed to be due to the differential rotation of the partly ionized disk, which should cause magnetic flux loops to rise, analogously to what is observed during solar X-ray flares.

The assumption of local magnetic flares distributed over the accretion disk gives a possibility to explain the fast X-ray variability of AGN. Observed X-ray time-lags of minutes between the radiation coming from the hot plasma and the reprocessed radiation from the disk require short light-traveling times between the two media. It is therefore suggested that the production of X-rays in AGN happens within small regions, which corresponds well to the local nature of magnetic flares.

Soft X-ray spectra of many AGN reveal another medium seen mainly in absorption. Various absorption features in the soft X-ray band can be resolved thanks to the last generation of X-ray satellites such as *XMM-Newton* and *Chandra*. The observations suggest that the absorbing medium, the so-called warm-absorber, is moderately ionized and mainly outflowing. Its connection to the accretion processes is still an open question. It was proposed that the warm absorber consists of an outflow originating from the accretion disk. However, the thermodynamical state, the ionization profile, and the dynamics of the absorbing medium still have to be constrained.

In summary, the production of the X-ray spectrum of AGN is complicated to disentangle. The purpose of this thesis work is to give some constraints on the X-ray production adopting the model of magnetic flares above an accretion disk. We model spectra of individual and multiple flares and also consider their time evolution and variability including the effects of general relativity. Furthermore, we present spectral modeling for the warm absorber depending on properties of the irradiating spectrum and the absorbing medium.

We focus our investigation on radio-quiet AGN. The extended radio-jets, having lengths of up to ~ 100 pc, which are seen in radio-loud AGN, emit synchrotron emission, which partly reaches into the X-ray band and further complicates the picture. Here we would like to investigate physical processes connected to the X-rays in the active nucleus and so we leave aside radio-loud objects.

The thesis is organized as follows: chapter 2 gives an introduction to the phenomenology of AGN and connects it to the standard unification model. In chapter 3, we summarize the current picture of the X-ray properties of AGN, before giving a brief summary of conducted X-ray modeling in chapter 4. We present the radiative transfer codes used for our work in chapter 5.

The remaining chapters describe the modeling projects we conducted while this thesis was prepared. They refer to several aspects of the X-ray spectrum of AGN. In chapter 6, we present modeling of X-ray flares, leading to localized X-ray emission above the accretion disk. We model the spectra expected from such flares and describe in particular the reprocessed radiation coming from the accretion disk. Chapter 7 presents a toy model to consider time-evolution effects of a flare event. The reprocessed component coming from the disk is emitted with a certain delay, because the flare appears at a certain height above the disk. The toy model enables some constraints on the observed time-lags between various X-ray bands, and reproduces observational results for the Seyfert-1 galaxy MCG -6-30-15.

Having focused on several aspects of individual X-ray flares, we extend our studies in chapter 8 to modeling of X-ray variability produced by large flares distributions across the accretion disk. We conduct Monte-Carlo simulations of flares appearing and disappearing above the disk, and we compare our results to the observed X-ray variability of MCG -6-30-15.

In chapter 9 we leave behind the modeling of X-ray flares and focus on the properties of the warm absorber modifying the soft X-ray spectrum of AGN. We present spectral modeling and results for the structure of a warm absorber in pressure equilibrium.

Conclusions drawn from our work and further perspectives are presented in the final chapter 10.

Chapter 2

The current understanding of AGN

In this chapter we give a brief summary of the observational appearance of AGN and summarize the main aspects of the currently accepted standard model, the so-called *unified scheme*. In the beginning, the object class of active galaxies as such did not exist - people discovered new types of astronomical objects that we nowadays summarize under the term AGN. These objects can differ remarkably in their observational appearance. The common ground of AGN is that they contain a very compact source putting out large amounts of energy within tiny volumes. Bright AGN are the most luminous steady sources seen in astronomy. They reveal a very broad spectrum reaching from the radio-band to X-rays or even γ-rays. These spectra vary on all observable time scales.

In the following, we first briefly explain the different types of AGN and their terminology (section 2.1). Then, the properties of the broad AGN spectra are summarized (section 2.2), before we have a look at their variability (section 2.3). The chapter closes with an introduction to the unified scheme (section 2.4).

2.1 A quick course in quasar zoology

In the year 1943, Carl Seyfert discovered six spiral galaxies hosting very luminous cores and showing strong, partly widened optical emission lines (Seyfert, 1943). This optically detected new type of astronomical sources was later called *Seyfert galaxies* and represents a large sub-group of AGN. Seyfert galaxies can be further divided according to the profile of major emission lines: the so-called *Seyfert-1* galaxies exhibit broad emission lines with Doppler widths of thousands of km/s while emission lines of *Seyfert-2* galaxies are more narrow having widths of only hundreds of km/s.

With the beginning of radio astronomy in the 1950s, another important subclass of AGN was discovered, the so-called *radio galaxies* (RGs). These objects reveal the typical broad AGN spectrum but emit particularly strongly in the radio band. Using interferometry on long baselines, it is possible to observe in detail the radio emitting structures that often form elongated jets anchored in the center of the host galaxy and evolve outward along its symmetry axis. The radio-jets can reach out to distances of several hundred kpc from the active galaxy. For the optical emission line spectrum of the active nucleus a similar division as for Seyfert galaxies exists dividing radio galaxies into *broad line radio galaxies (BLRGs)* and *narrow line radio galaxies* (NLRGs).

While in Seyfert and radio galaxies the host galaxy is visible, some active galaxies are so luminous and/or far away that the host galaxy is blended. In fact, some distant AGN with strong radio emission were not immediately identified as such, but had been called *quasi-stellar radio sources*

(quasars). They looked like stellar dots on a photo plate while being surrounded by radio structures similar to those of RGs. Maarten Schmidt discovered in 1963 that one of these quasars, 3C 273, had a surprisingly high redshift putting the object far outside our galaxy (Schmidt, 1963). It hence could not be a stellar source at all. It turned out that this point-like quasar has spectral properties similar to those of Seyfert galaxies and RGs. It shows a luminous active nucleus embedded inside a barely visible host galaxy. Soon after, the same nature was confirmed for other quasars. Meanwhile, also quasars were divided into *type-1* and *type-2* objects according to their emission line characteristics, however, type-2 quasars are still rare. Furthermore, some quasars were found to have only weak radio-emission, they are sometimes referred to as *quasi-stellar objects* (QSOs) or *radio-quiet quasars* (RQQs) in contrast to radio-loud quasars (RLQs). We emphasize here, that the "point-like" definition of a quasar depends strongly on the instrumentation used for the observation. The phenomenological distinction between Seyfert galaxies and QSOs or between radio galaxies and quasars therefore is not precise. The term quasar generally is reserved for objects with a high intrinsic luminosity being significantly greater than for Seyfert or radio galaxies.

Some objects represent active galaxies even though they look quite different from those of the subclasses presented so far. The *BL Lac objects*, named after their first discovery in the constellation Lacerta, show extreme variability in various wavebands. They are AGN showing the typical high luminosities and broad spectra, while they have hardly any lines.

The overview presented here is not complete. For further information about AGN terminology we recommend to consult the textbooks of Peterson (1997) or Krolik (1999). However, denotations of AGN object classes continue to evolve as observational and theoretical progress is made.

2.2 The overall spectrum of AGN

In this section we present the main observational results for the overall AGN-spectrum from the radio to the X-ray range. The X-ray properties are discussed in more detail in chapter 3. We separately describe the spectral appearance for the continuum and for the emission and absorption features.

2.2.1 Continuum emission

A broad continuum spectrum is a defining property of AGN. It covers the whole range from the radio band to the far X-ray, sometimes even γ-ray band. In Fig. 2.1 we show composite spectra of AGN for quasars and Seyfert galaxies. The spectra are normalized to their luminosity at a wavelength of 1 μm. The spectral energy distribution in νF_ν over ν has a rather flat shape between the Far-IR and the X-ray energies. Several prominent features can be distinguished: the power in the radio band divides the sample into *radio-loud* and *radio-quiet* objects and is correlated with the (non-)existence of radio jets. A bump appears in the infrared range, another one in the optical and UV bands. The former one is called the *infra-red bump*, the latter the *big blue bump* (BBB). Both of these features correspond to thermal emission, in the case of the infra-red feature the temperature cannot exceed $\sim$ 1000 K, whereas the BBB represents a continuum of temperatures up to 10^5 K or 10^6 K. The spectrum at even higher energies cannot be explained by only thermal black-body emission and therefore requires other mechanisms.

In the X-ray range, a difference between radio-loud and radio-quiet quasars is observed. The soft X-ray slope is flatter for radio-loud objects as was found by Wilkes & Elvis (1987) and Laor et al. (1997). The X-ray luminosity relative to the luminosity in the optical/UV is higher for Seyfert

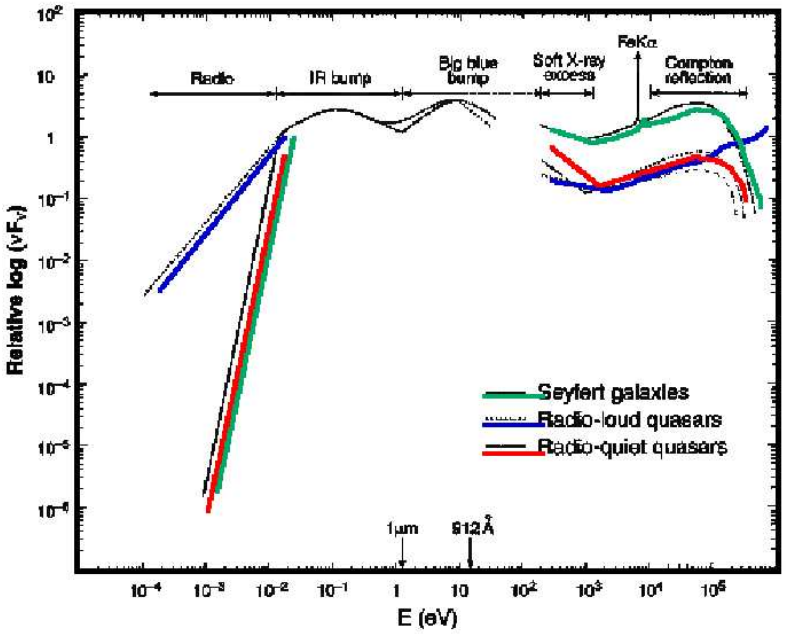

Figure 2.1: Composite spectra for radio-loud and radio-quiet quasars and for Seyfert galaxies from the radio to the hard X-ray range (from Sanders et al., 1989; Collin, 2001).

galaxies than for quasars. The spectra of radio-loud quasars generally reach out very far into the X-rays.

2.2.2 Radio power

The level of radio-power gives a fundamental classification of AGN into radio-loud and radio-quiet objects. Radio-loudness generally is defined by a flux ratio $R \equiv F_{\nu_r}/F_{\nu}(4400\text{Å})$ and declares an object as radio-loud, if this factor is significantly greater than unity. The value of R depends on the reference radio frequency ν_r. If one assumes $\nu_r = 5GHz$ and a threshold of $R = 10$, then $\sim 20\%$ of the Palomar-Green quasar sample are considered as radio-loud (Kellermann et al., 1989). The level R of radio-loudness does not seem to correlate with the luminosity of the objects.

Unlike other wavebands, the morphology of the radio emission regions can be observed in detail with the help of interferometry methods. Radio-loud AGN show bipolar jet structures emerging from the center of the galaxy and extending out to distances of several hundred kpc. The polarization signatures of these radio lobes favor synchrotron emission to be the origin of the radio-spectrum. Therefore, the jets must contain a confined magnetic field and high-energy electrons to explain the strong synchrotron components observed. The synchrotron spectrum partly reaches out into the Far-IR range and merges with the thermal IR-bump. The radio-luminosity along the jets is not uniform but mostly structured in blobs and linear filaments. A further subdivision of radio-loud AGN, introduced by Fanaroff & Riley (1974) distinguishes between *core-dominated* (FR1) and *lobe-dominated* (FR2) radio-luminosity distributions along the jet.

Radio-quiet objects are obviously much weaker in the radio-band. However, in most radio-quiet

AGN a smaller and fainter radio-structure oriented perpendicularly to the host galaxy plane can be seen (see e.g. Kukula et al., 1998).

2.2.3 Infrared emission

The infrared spectrum of AGN is dominated by a bump over the range of 1 μm to 25 μm representing thermal emission from a medium at a temperature of several hundreds of Kelvin. Since for most objects the inner structures of AGN cannot be resolved by infrared imaging, it is a difficult task to distinguish between the infrared spectrum coming from the active nucleus and the one produced by the surrounding inner parts of the host galaxy. The composite infrared spectra of a normal galaxy correspond to thermal emission of ~ 30 K, and might be separable from the AGN spectrum. However, the situation is different in starburst galaxies. Actually, AGN compete observationally with a class of galaxies revealed by the IRAS satellite mission - these *ultra-luminous infrared galaxies* (ULIRGs) emit strongly in the IR. It has to be analyzed individually if starbursts generate the strong IR emission or an AGN does.

Unifying models of AGN, that will be discussed in section 2.4, favor dust to be responsible for the thermal IR emission. Mid-IR spectra of different types of AGN reveal features of silicate and Poly-Aromatic-Hydrocarbon (PAH) dust grains, sometimes seen in emission, sometimes in absorption (Hao et al., 2005; Weedman et al., 2005). Infrared variability has revealed details about the spatial dust distribution in some objects (e.g. Glass, 2004) confirming that the inner radius of the dust distribution can be smaller than 100 light-days. While the IR emission in starburst galaxies seems extended over the whole galaxy it is rather compact in Seyfert galaxies (Siebenmorgen et al., 2004).

In radio-loud objects the spectral shape in the IR can be a superposition of thermal emission creating the IR bump and the tail of the synchrotron component coming from the inner parts of the radio-jets. The analysis of the IR spectrum is hence more complicated than for radio-quiet AGN.

2.2.4 The big blue bump

The BBB is prominent and clearly visible only in bright AGN, mainly quasars. In Seyfert galaxies it is less pronounced. Constraining the spectral shape of the BBB is confronted to substantial observational difficulties because of galactic absorption starting at the Lyman-limit of 912 Å. In addition to this, in many AGN the continuum spectrum is blended by Fe II emission lines, and by the Balmer continuum. Also, intrinsic reddening and host galaxy contamination may play an important role.

If these problems are accounted for in the fitting process one obtains an average optical-UV slope of $\alpha_{opt-UV} \sim 0.32$ (Francis et al., 1991) for a $F_\nu \propto \nu^{-\alpha}$ flux dependence. The UV-slope α_{UV} ranges around $\alpha_{UV} \sim 0.99$ (Zheng et al., 1997). As these slopes have been computed from composite spectra of large AGN samples, one should bear in mind that they can vary significantly from object to object. A composite spectrum from ROSAT observations of a large quasar sample obtained by Laor et al. (1997) shows that the Far-UV to Soft X-ray region is a smooth continuation of the spectral shape in the UV. The BBB spectra generally show a maximum in the range of 900 Å to 1100 Å. This shape of the BBB corresponds to a superposition of thermal black-body spectra for a range of temperatures between 10^5 K and 10^6 K.

The BBB can be further decomposed by subtracting the so-called *small blue bump* between 2300 Å and 4000 Å. This component consists of the Balmer continuum and of FeII emission multiplets (Wills et al., 1985).

2.2.5 X-ray spectra

The continuum shape of AGN X-ray spectra can be represented by a power-law, the so-called *primary component*, plus additional superimposed features. In this section, we only give a basic overview of the observed X-ray properties for radio-quiet AGN. More details will be added in chapter 3.

Below 1 keV the soft X-ray spectrum connects rather smoothly with the extreme-UV spectrum showing a spectral index of $\alpha \sim 1.5$, defined as $F_\nu \propto \nu^{-\alpha}$. Above 1 keV this index switches to ~ 0.7. The change in slope creates the so-called *soft X-ray-excess* observed for the majority of all AGN. About 50% of all Seyfert-1 galaxies reveal soft-X-ray absorption lines and edges. Also some quasars reveal narrow absorption lines in this spectral range.

The spectrum above 1 keV shows a superimposed broad *emission line complex at* ~ 6.4 *keV*. This line is identified with the Kα-line of neutral or weakly ionized iron. In some objects, the line complex has a strongly asymmetric profile (Nandra et al., 1997b).

The hard X-ray continuum is dominated by a smooth and *broad hump* centered around 30 keV and reaching out to several hundreds of keV before declining with an *exponential cut-off* (Gondek et al., 1996). The height of this hump is smaller than for the BBB and can be explained by direct Compton scattering events in a strongly ionized medium.

2.2.6 Emission and absorption features

The overall spectrum of radio-quiet AGN shows various emission and absorption features being particularly strong in the optical, the UV-, and the soft X-ray range. These features are different from those produced by stellar sources and by the interstellar medium. They are related to intervening clouds of atomic and molecular gas and of dust located around the central AGN engine. Detailed analysis of AGN emission lines has permitted the development of a rather well-defined classification between type-1 and type-2 AGN (see section 2.1), because the line properties remain very stereotyped within one category.

The infrared spectrum shows several *dust features* and a few atomic emission lines. Strong absorption features are seen at 9.7 μm and 18 μm due to siliceous dust. Poly-Aromatic-Hydrocarbon (PAH) dust features can be observed at 6.2, 7.7, 8.6, and 11.3 μm, they are weaker in AGN than in starburst galaxies (Weedman et al., 2005) and can thus serve as a criterion to distinguish between these two object types. Some forbidden emission lines in the Mid-IR are detectable in AGN (see e.g. Giannuzzo et al., 1995), while no permitted lines are seen in this spectral range.

The optical and UV spectrum is dominated by strong high- and low-ionization *emission lines*. An important criterion in AGN classification is given by the width of these emission lines, dividing them into type-1 and type-2 objects (see section 2.1). In type-1 objects the emission lines show a broad profile corresponding to Doppler velocities of at least 1000 km/s —2000 km/s. The velocity dispersion can reach 8000 km/s and more. The emitting *broad line region* (BLR) is thus a very dynamical part of the AGN. Broad line spectra of AGN are mostly dominated by the Lyα, Hα, and CIV $\lambda\lambda$1549,1551 emission lines. Also, CIII] λ1909 and MgII λ2800 can be strong broad lines in type-1 spectra. In addition to that, there are broad emission multiplets coming from FeII. They are mostly detected in four clusters between 2200 Å and 5350 Å. None of the emission features listed here represent forbidden lines that are hardly detected in the BLR.

There is a correlation between the emission line width and the degree of ionization, with the most highly-ionized lines representing the largest velocity dispersions. This is observed in NGC 5548

(Krolik et al., 1991) and in NGC 4151 (Antonucci & Cohen, 1983; Ulrich et al., 1984). The low-ionization lines are slightly blue-shifted with respect to the high-ionization lines. Such a dependence of the line width and centroid on the ionization state suggests a stratification of the BLR. Further constraints on the geometry and the dynamics of the BLR can be obtained from reverberation mapping techniques (see section 2.3.2).

Another correlation exists between the equivalent width of CIV λ1549 and the continuum luminosity in high-luminosity quasars. It was first pointed out by Baldwin (1977) that the equivalent width of CIV λ1549 decreases with increasing luminosity. Follow-up studies have then revealed that the *Baldwin effect* exhibits a power-law dependence of the equivalent width of CIV λ1549 and the continuum luminosity (Baldwin et al., 1989). However, this correlation is much weaker for other emission lines or lower luminosities.

All radio-quiet AGN have narrow emission lines, in fact, type-1 objects show a combination of narrow and broad emission lines, with the broad components dominating. In type-2 objects only narrow emission lines are detected, being similar to those known from stellar spectroscopy, and having Doppler widths of several hundreds of km/s. The lines are coming from the *narrow line region* (NLR). The narrow line spectra show forbidden lines like the [OIII] $\lambda\lambda$4959,5007 doublet, and [OII] λ3727 which are particularly prominent, along with the [NII] $\lambda\lambda$6548,6583 doublet, [OI] λ6300, and the [SI] $\lambda\lambda$6716,6731 doublet.

For both, broad and narrow emission lines, the line width is correlated with the underlying continuum. This fact suggests, that the line emission is driven by the continuum source irradiating the line producing regions.

We mention here a special type of Seyfert-1 galaxies exhibiting "broad" emission lines, however, with a limited Doppler width of only 1000 km/s —2000 km/s. The lines are not narrow enough to classify the object as Seyfert-2 galaxies. In addition to that, these *narrow-line Seyfert-1* (NLS1) galaxies, show strong emission from FeII. We will come back to this object class in chapter 3 when we will discuss the particular X-ray properties of NLS1 galaxies.

Besides emission lines, AGN spectra also show atomic absorption features. Analysis of the absorption spectra, however, is confronted to the problem that absorption might happen not only inside the AGN but also in the intergalactic medium. This is particularly the case for high-redshift objects. Restricting our attention to the intrinsic absorption in the active nucleus or the host galaxy, the observations show that most AGN suffer from significant absorption. The individual absorption spectra differ from object to object. Several tens of percent of Seyfert-1 galaxies show narrow absorption lines that are generally offset by a Doppler velocity of 1000 km/s to the blue of the line centroid. These lines appear especially in the UV and Far-UV range.

About 50% of all Seyfert-1 galaxies exhibit atomic absorption features in the soft X-ray range, mostly identified by strong absorption edges of OVII and OVIII. Again the absorbing medium imprints a Doppler shift of several thousands of km/s to the blue, indicating an outflow. This medium is called the "warm absorber" and will be discussed more extensively in section 3.1.3.

Far more spectacular absorption lines are found in radio-quiet quasars. About 10% of them show broad absorption lines being blue-shifted from the laboratory wavelength by up to 60.000 km/s (Weymann et al., 1991). They are called broad absorption line QSOs or BALQSOs. A wide variety of absorption troughs are seen in BALQSOs, partly having a smooth profile, partly being of a bumpy shape. Some of these broad absorption lines are so strong that they saturate completely removing all flux around their spectral position. Broad absorption lines almost never appear in radio-loud objects (Stocke et al., 1992).

In the UV, the astonishing observation is made that the expected discontinuity at the Lyman-

limit of 912 Å is absent in most AGN. It is not obvious how to explain this effect, since at this edge the hydrogen dominated matter in AGN changes strongly in opacity. Another missing absorption feature, well-known from the interstellar medium in our galaxy, is the λ2275 absorption trough due to graphite and PAH dust grains. This feature fails to be reported in the extinction curves of most AGN (Maiolino et al., 2001; Gaskell et al., 2004).

2.3 Spectral variability of radio-quiet AGN

Variability is an important property of AGN. The combination of very high luminosities and short variability time scales indicates that the powerful energy source of AGN cannot rely on stellar processes. The observed time scales require a small volume of the emission region (e.g. Fabian, 1979).

Most active galaxies vary over the whole spectral range and on various time-scales from years down to minutes. The overall picture of AGN variability is complicated and not always consistent for all objects of one type. Especially, correlations between changes in different wavebands differ from object to object. The observed spectral changes, and time delays provide information about the nature and the location of emission and scattering regions inside AGN.

In this section, we briefly describe the observed variability properties of radio-quiet AGN. We leave aside radio-loud objects having much more complicated variability patterns. We separately discuss the continuum and the line variations. An extensive review about this subject can be found in Ulrich et al. (1997). The X-ray variability and its correlations with other wavebands are discussed in more detail in chapter 3.

2.3.1 Continuum variability

Observational data for time scales from years to minutes are available for only a few objects. The best studied object in terms of variability is the Seyfert galaxy NGC 4151 having photometric data available for a time period of almost 100 years. An extensively monitored quasar is 3C 273.

The results obtained so far, reveal that the *continuum varies on all observable time scales.* In Fig. 2.2 we show lightcurves in several spectral bands for the Seyfert galaxy NGC 4151. The amplitude of the spectral variations seems to have a maximum in the extreme UV and soft X-ray range. However, variability time scales and amplitudes may differ significantly from object to object. The characteristic time scale for variations of a factor of 2 in the UV scales with some power of the luminosity. For Seyfert galaxies this time scale is of the order of weeks while in luminous quasars it can be several years.

There are correlations between various wavebands marking a delay between the optical, the UV, and the extreme UV range. The *extreme UV drives variations at longer and shorter wavelengths.* The delay between extreme UV and UV is constrained to 0.25 days in NGC 5548 (Marshall et al., 1997), the one between the UV and the optical in NGC 4151 is 0.2 days (Crenshaw et al., 1996).

A well-established result from optical/UV monitoring of AGN is the fact that the *spectrum hardens as the object brightens.* For a number of objects, such spectral hardening can be explained by a decomposition in several spectral components with different variability properties. The small blue bump component that can be subtracted from the BBB (see section 2.2.4) varies with a smaller amplitude causing the observed changes of the BBB shape.

The level of variability is much weaker in the IR, sometimes not detected at all. The time scales are longer than for the UV and optical (Neugebauer et al., 1989; Hunt et al., 1994). At the

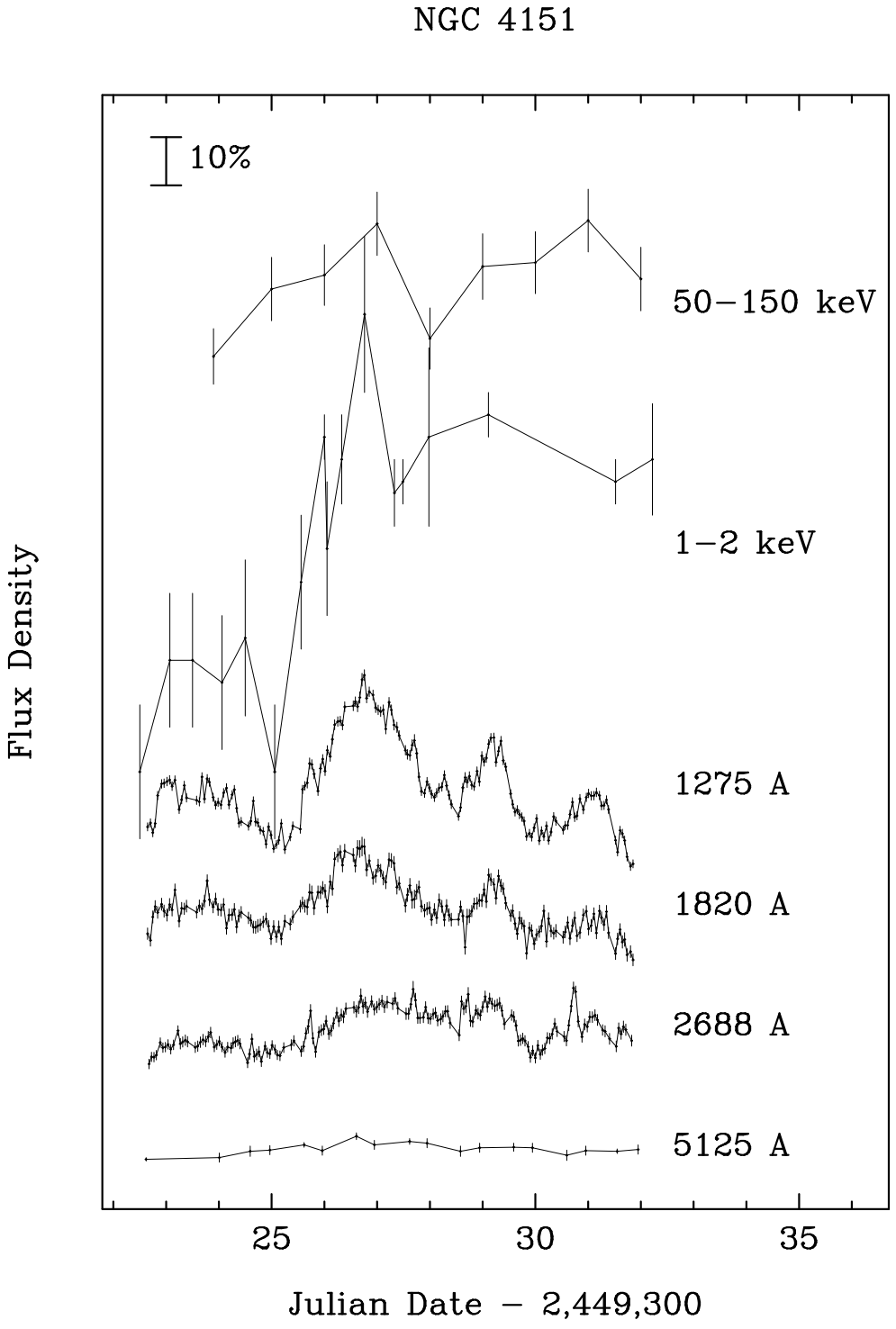

Figure 2.2: Light-curves showing a 10-day multi-wavelength monitoring period of NGC 4151 from the optical to the hard X-ray range. The curves are shifted vertically for convenience. A 10% change is indicated by the bar. The figure is published in Edelson et al. (1996)

same time the IR-variations occur with a delay compared to corresponding UV emission and are therefore consistent with being the re-emission coming from UV-heated dust clouds situated around the source of the optical/UV continuum.

2.3.2 Line variability

The emission line strength in AGN is correlated with the continuum flux, thus, the lines respond in the same sense to the changes of the continuum source. However, there is a delay between the leading continuum and the following line variations. This delay rises with luminosity of the object, suggesting that for a higher luminosity the line producing regions are farther out.

The discrepancy in line width between broad high- and low-ionization emission lines implies that the BLR is stratified. A more profound analysis of this stratification can be obtained from the method of reverberation mapping (Peterson, 1998), in which the time delay between a change in the continuum flux and the corresponding change of the emission lines is measured. Assuming that the continuum is produced by a compact central source illuminating the surrounding BLR, the measured time delay corresponds to the distance between continuum source and BLR. It turns out, that the high-ionization lines such as HeII $\lambda\lambda$1640,4686 NV λ1240 have the shortest time delays, followed by CIV $\lambda\lambda$1548,1551 and the Lyα line. The line wings generally vary faster than the core (Ulrich & Horne, 1996, e.g. for NGC 4151). The low-ionization lines Hα and Hβ have longer time-responses and vary with lower amplitudes than the CIV line. They are therefore assumed to be produced farther away from the continuum source.

Absorption lines in the optical and UV normally vary on longer time scales than the emission lines. The variations may or may not occur in the same sense as the changes of the continuum. Broad absorption lines are observed to change in flux while the line profile keeps the same velocity structure.

2.4 The unified scheme

It is a major challenge to find a satisfying model explaining all the different aspects observed in the context of AGN. In the following, we show that starting from the high luminosities it is necessary to assume accretion onto a supermassive compact object as the origin of the tremendous energy output. The geometry of the accretion flow has been a matter of debate, but recently disk models are favored. The main function of the so-called *standard α-disk* is to transport matter toward the central black hole and angular momentum out. This model was introduced by Shakura & Sunyaev (1973) and computes the radial and vertical structure of an accretion disk. It reveals that the temperature profile rises toward the disk center. The observed optical and UV radiation, the big blue bump, is then interpreted as thermal radiation coming from different radii of the disk.

Apart from the enormous energy output, the various spectral features and variability properties of AGN have to be explained. Therefore, the black hole/accretion disk paradigm has to be further developed by subsequently adding specific emission, absorption and scattering regions. From the radio observations it is obvious that in radio-loud objects large jets have to be present. The IR emission seems to be due to optically thick dust accumulations around the central engine. These dust regions also serve to shield the BLR from the observers view at certain inclinations of the object. The type-1/type-2 dichotomy could therefore be explained as an orientation effect. In the following, we give a brief description of this *unified model*. A more detailed description can be found in Antonucci (1993) and in the textbooks of Krolik (1999) and Peterson (1997).

In this section we give a brief description of the various elements belonging to the unified scheme. In order to check this model against the observations, it is necessary to perform detailed modeling of the various physical processes included.

2.4.1 Accretion as the origin of AGN emission

Explaining the energy balance of AGN presents a major challenge. It is not immediately obvious how the broad spectra, big luminosities and strong variability of quasars can be explained with the additional constraint that the emitting region has a very small angular size. For stars, nuclear fusion is the origin of the emitted radiation. But, apart from the fact that stars cannot explain AGN variability, a compact stellar cluster needed to fuel an average AGN would have a gravitational binding energy being significantly higher than its radiative energy output (Lynden-Bell, 1969). Furthermore, due to outward-transport of angular momentum the center of an AGN collapses to form a black hole. The radiation emitted by AGN can then be explained by accretion of matter onto the black hole, a possibility that had been pointed out first by Salpeter (1964).

2.4.2 The α-disk model

The accretion flow contains angular momentum and is thus supposed to form a differentially rotating disk (Pringle et al., 1973). This accretion disk has to transport angular momentum outwards and matter inwards. The friction between adjacent disk annuli generates heat that gives rise to the optical and UV part of the observed quasar radiation. The question of what creates the friction remains a matter of debate, as simple molecular viscosity is too weak. Significant progress has been made by studying turbulences induced by magneto-rotational instabilities (MRI) (e.g. Hawley & Villiers, 2004; Turner et al., 2005).

Even before knowing about MRI-turbulences, it has been possible to construct a rather sophisticated model for the accretion disk explaining the shape of the optical and UV continuum spectra. The fundamental paper of Shakura & Sunyaev (1973) carried out a standard accretion disk model for the X-ray binary source Cygnus X-1 assuming that any kind of hydrodynamic stress inside the accretion disk is proportional to the total pressure P (including gas and radiation pressure). The disk viscosity can thus be parametrized by a constant α with $\alpha \sim 0.1$. From the considerations of Shakura & Sunyaev (1973) it then follows, that the flux F emitted at the radius R of an accretion disk around a black hole with mass M and accretion rate $\dot{M}$ reads:

$$F(R) = \frac{3G\dot{M}M}{8\pi R^3}\left[1 - \sqrt{\frac{R_m}{R}}\right], \tag{2.1}$$

where R_m denotes the marginal stable orbit of the black hole and G is the gravitational constant. Assuming that this flux is due to blackbody radiation, the temperature $T(R)$ is obtained directly from $F(R) = \sigma\,[T(R)]^4$, with the Stefan-Boltzmann-constant σ. The disk-temperature therefore rises toward the disk center. In the following we will refer to the disk model presented by Shakura & Sunyaev (1973) as the α-disk model.

Although developed for stellar black holes in X-ray binaries, the α-disk model can easily be applied to AGN by scaling up the black hole mass. Pringle et al. (1973) predicted very high luminosities for accretion disks around massive black holes, which is in agreement with the observations.

Within the frame of this model the BBB in the UV can be explained by the thermal emission coming directly from different radii of the accretion disk as pointed out first by Shields (1978) and

reviewed by Rees (1984). The models show an increasing temperature toward the disk center and hence the UV and optical emission consist of a superposition of black body spectra associated with a continuous temperature distribution. The emitted spectral shape and the overall luminosity are mainly determined by the mass M_{bh} of the black hole and by the accretion rate $\dot{M}$.

An important function of the accretion disk is to transport angular momentum outward. The disk hence exhibits a differential rotation and, since it is strongly ionized, it should create a magnetic field. This happens analogously to the solar dynamo effect that is based on the differential rotation of the sun. Studying the magnetic field in accretion disks is of particular interest (see e.g. Miller & Stone, 2000), as it leads to the MRI mechanism. Apart from that, magnetic reconnection above the disk supposedly creates flaring events, again analogously to what is observed in the sun. These flares heat up the atmosphere above the accretion disk and create a hot corona. We are going to investigate the effects of magnetic flaring above the accretion disk in more detail in chapter 6.

2.4.3 Emission from relativistic jets

The appearance or absence of radio-jets are not entirely understood. In the beginning, the double-lobe structures associated with most radio-loud AGN have been thought to be the remnant of a symmetric explosion that had occurred at an earlier time. This hypothesis was given up when Blandford & Rees (1974) suggested a mechanism to support a continuous output of matter along the polar directions of the active galaxy. A big advantage of this model was that it did not require the release of a huge amount of energy in one sudden event. Later detailed VLA observations of radio jets showed linear filaments at close distances from the galaxy center, further supporting the idea of a *continuous transport of matter*. Collimated jets are also associated with other astrophysical objects, such as young stellar objects or galactic black holes. Even though they differ in size, it is assumed that they share the same physics of acceleration and emission (see e.g. de Gouveia dal Pino, 2005).

A major challenge in modeling of radio galaxies and radio-loud quasars is given by the connection between the radio properties and the spectral behavior in other wavebands. From polarization properties in the radio band it could be concluded that the detected radiation is mainly due to *synchrotron emission* (see e.g. Hughes et al., 1989a,b) produced inside magnetic field structures aligned with the jet-direction. The tail of the synchrotron spectrum often reaches into the IR band. Furthermore, the continuous propulsion of the jet should create shock waves, since the jet drives into the surrounding interstellar medium. The emission created in and around the shock fronts can have complicated spectra contributing to all spectral bands. Especially, the inner parts of the jets partly blend the emission form the active nucleus, which further complicates the overall picture of radio-loud objects. Therefore, for this work we only consider radio-quiet objects.

2.4.4 Emission line regions

From the variability of broad and narrow emission lines one derives that the distance of the NLR from the ionizing continuum source is much larger than for the BLR. The two regions are thus spatially separated.

The narrow line spectra are similar to those reported for planetary nebulae, with the important difference that the range of different ionization states is much larger. In AGN, fairly low ionization states giving rise to forbidden lines like [OI] or [NI] are observed. But also highly ionized species like [NV] or [FeX] are seen. It is a well established result that photo-ionization is producing the

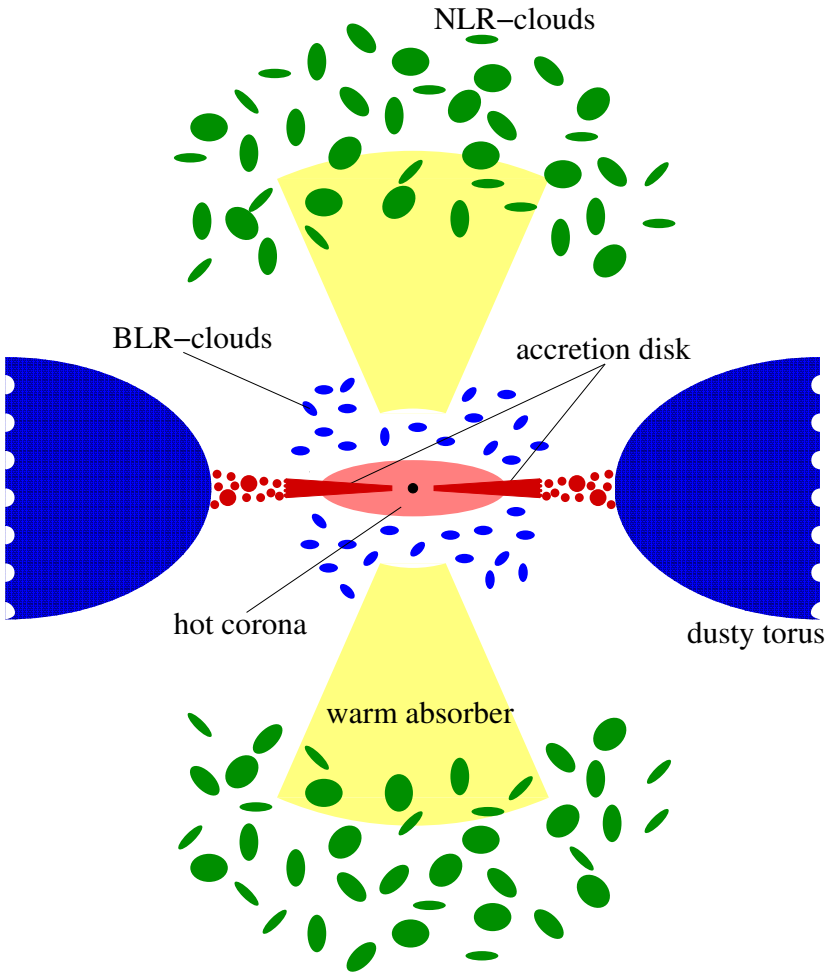

Figure 2.3: Artistic impression for the unified model of radio-quiet AGN. The figure represents a high-luminosity object with a large torus opening angle. For lower luminosities, the funnel of the dusty torus is much narrower forming a smaller half-opening angle.

emission lines. However, a broader ionizing spectrum than for planetary nebulae or HII regions is necessary. Such a continuum source is given by the central engine of the AGN having a spectrum that reaches out far into the UV.

In some nearby Seyfert galaxies, it was possible to map out the geometrical shape of the NLR. It turned out that it is consistent with a double-conical region along the symmetry axis of the host galaxy. These cones extend out to 10^2 pc or 10^3 pc, and are commonly called the *ionization cones*. Since the NLR extends farther out than the central region obscured by the torus, it can be explained that narrow lines are seen in both type-1 and type-2 objects.

The much closer BLR on the other hand is only seen for face on viewing angles. Its extension around the central source is $<\sim 0.2$ lightyears. The broad velocity dispersion measured, might indicate that the BLR is clumpy, made of many clouds moving around the black hole. The velocity field of these BLR clouds must allow, that the projected velocities for a given line of sight reproduce the observed broad line profiles. However, also a continuous medium for the BLR is possible, incorporating the same velocity structure. The actual shape of the BLR still is a matter of debate.

For the low-ionization lines, it can be derived that the clouds have a higher density of $\sim 10^{11}$ cm^{-3} orbit in a disk-like geometry and possibly are emitted by the accretion disk itself (Collin-Souffrin, 1987). The high-ionization lines seem to originate in a more dilute outflow of $\sim 10^9$ cm^{-3} (Collin-Souffrin & Lasota, 1988).

2.4.5 Absorption by equatorial dust regions

In sections 2.1 and 2.2.6 we mentioned the difference between type-1 and type-2 objects with respect to the emission line widths. It is hence observationally confirmed that in some AGN the BLR is visible while in others it is not. It would be possible to conclude that type-2 objects do not have a BLR, but one can also interpret the presence or absence of a BLR as an orientation effect. In this approach it is required to add obscuring elements to the unified model, as for type-2 viewing angles the BLR must be blocked from the observer's view.

Such obscuration can be realized by optically thick distributions of dust, which at the same time can explain the infra-red bump as thermal re-emission of the absorbed UV continuum radiation. Especially, radio-loud objects reveal a preferred direction denoted by the jets - a simple approach for the geometry of the dust absorption region is hence an axisymmetric structure, co-planar with the equatorial plane of the object and with the accretion disk. At low inclinations, when the AGN is seen face-on, its inner parts are visible for the observer. For high inclinations, e.g. for an edge-on view, the center is blocked by the optically thick torus (see Fig. 2.3). In the unified model the BLR is placed within the central parts of the AGN, hence the presence of the torus can explain the dichotomy between type-1 and type-2 objects. The fundamental discovery that Seyfert-2 galaxies are actually *hidden* Seyfert-1 galaxies was made by Antonucci & Miller (1985). They found broad spectral lines in the polarized flux of the Seyfert-2 galaxy NGC 1068. The polarized radiation is scattered off free electrons within the ionization cones and therefore offers a *periscope view* around the torus and toward the central parts of the AGN.

The exact geometrical shape of a dusty torus in AGN still is a matter of debate, but there are strong constraints on its opening angle as it must correspond to the number ratio of type-1 to type-2 AGN. Observations suggest a half-opening angle $\theta \sim 38^\circ - 40^\circ$ (Osterbrock & Shaw, 1988; Tovmassian, 2001, e.g) for Seyfert galaxies. In quasars, larger opening angles are expected, as the central source pushes outward the sublimation radius, beyond which dust particles can survive. This helps to explain, why type-2 quasars are rare.

As both the torus and the accretion disk lie within the equatorial plane of the AGN it is likely that the torus plays a role in the accretion process providing new matter at the outermost parts of the accretion disk.

The equatorial dust regions provide a natural explanation for the thermal emission seen in the IR. The inner surfaces of the torus are directly exposed to the UV continuum source in the center and heated to a temperatures corresponding to the observed IR and Far-IR emission. The observed spectral shapes suggest graphite and silicate to be important components of the dust mixture. However, the exact compositions and grain size distributions of dust in AGN remain a matter of debate and are investigated by the construction of AGN extinction curves. Flat extinction curves (see e.g. Czerny et al., 2004; Gaskell et al., 2004) and dust composition similar to those of the Small Magellanic Cloud (Khare et al., 2004) are seen. The size of the dusty torus is far more difficult to constrain, as it is too small to be resolved for most near-by AGN. An exception is given by the bright and well-studied Seyfert galaxy NGC 1068. This object was recently observed using interferometric methods in the IR, showing a dusty region of 3.4 pc in diameter, and 2.1 pc in height surrounding the active nucleus. The temperature of this torus corresponds to 320 K (Jaffe et al., 2004). Such a torus is unlikely to remain in hydrostatic equilibrium. In order to form a half-opening angle of $\sim 40^\circ$ it would need some support to avoid a self-gravitational collapse. Magnetic and radiative support was proposed (Lovelace et al., 1998; Pier & Krolik, 1992). However, it is possible that the matter forming the torus is not in hydrostatic balance but constantly flowing in or out. Material might stream from the center toward the torus by magnetically expelled winds as described by Konigl & Kartje (1994). Such a *flow model* could also help to explain the broad absorption lines seen in some AGN. Their strong blueshift and velocity dispersion might be due to a line of sight through a turbulent wind in the surface layers of the torus.

Even though the impressive observation of Jaffe et al. (2004) underlines the existence of the dusty torus in NGC 1068, the debate about the geometry of the equatorial dust accumulation in AGN continues. Elvis (2000) provided a synoptical wind model where the obscuration of the central parts in type-2 AGN is realized by an optically thick wind originating from the outer parts of the accretion disk. A distinction between the different models and further constraint on the torus geometry is possible by polarimetric observations and modeling (Goosmann & Gaskell, 2005).

Chapter 3

X-ray properties of AGN

Observations of AGN in the X-ray regime started in the later 1960s using rocket-borne detectors. An X-ray signal was found to be associated with the active galaxy M87 and with the brightest quasar 3C 273 (Friedman & Byram, 1967). Bowyer et al. (1970) confirmed the X-ray radiation from these objects and also found Cen A to be an X-ray emitter. Using satellite-based X-ray astronomy, it became clear that X-ray emission is a common property of AGN and that a significant fraction of their bolometric luminosity is emitted in the X-ray band (Elvis et al., 1978, 1994). The X-ray properties of AGN have been evaluated by various satellite missions with *Chandra* and *XMM-Newton* being the most recent ones. The X-ray radiation reveals information about the innermost parts of the accretion flow, and is therefore subject of relativistic effects in the curved space-time around the black hole. Hence, detailed analysis of X-ray spectra and their time-development should include not only radiative transfer computations in the high-energy range but also relativistic ray-tracing techniques (see chapter 4).

In this chapter we summarize the observational results for X-ray spectra (section 3.1) of AGN and their variability (section 3.2). We connect the observed X-ray properties to the various regimes of the unified scheme. The X-ray spectra of radio-loud and radio-quiet AGN are fundamentally different, because in radio-loud AGN the X-rays are partly produced in the jets. Therefore, we restrict our presentation to radio-quiet objects.

An extensive review about the X-ray spectra and their time variability was given by Mushotzky, Done, & Pounds (1993). More recent reports on a sample of 18 Seyfert-1 galaxies can be found in Nandra et al. (1997b,c) and on the PG quasar sample in George et al. (2000). Another analysis for PG-quasars using *XMM-Newton* is given by the two companion papers Piconcelli et al. (2005) and Jiménez-Bailón et al. (2005). The soft X-ray properties of a sample of Seyfert galaxies are given in Pfefferkorn et al. (2001), and Rush et al. (1996) describe the X-ray properties of AGN taken from the *ROSAT* All-Sky Survey. Laor et al. (1997) present results for soft X-ray observations of a sample of nearby quasars with *ROSAT*.

3.1 Observed spectra

The X-ray radiation, emitted at photon energies $E > 0.1$ keV, is a significant fraction of the bolometric luminosity for all AGN. However, this fraction depends on the AGN type - for Seyfert galaxies it is higher than for quasars (see Fig. 2.1) - and lies between 5% and 40% for AGN with X-ray luminosities $< 10^{44}$ erg/s (Ward et al., 1987). The X-ray spectra show high-amplitude

variability with factors of $\delta I/I \sim 1$ on very short time scales down to hours and even minutes. These extreme variability properties indicate short light-traveling times and therefore imply that the X-ray emitting regions are situated very close to the black hole.

The X-ray spectra of AGN can be decomposed into several characteristic components:

The overall shape of the X-ray spectrum between 2 keV and 50 keV can be roughly fitted by a power-law with an exponential cut-off at the high-energy end.

A strong fluorescent Kα emission line complex of iron in several ionization states is detected between 6.4 keV and 6.9 keV. In the range of 7.1 keV to 9.3 keV K-shell absorption edges of iron are also present.

A prominent and broad bump centered at around 30 keV marks the hard X-ray part of the spectrum.

Many AGN show a soft X-ray-excess just below 1 keV.

Around 50% of all AGN reveal broad absorption features in the soft X-ray range.

In radio-quiet objects, the shape of the X-ray spectrum is quite stereotyped, as shown in Fig. 3.1 where the average spectra of an AGN sample observed with *GINGA* and *OSSE* are plotted (data provided by Zdziarski et al., 1995; Wozniak et al., 1998). The major difference between type-1 and type-2 X-ray spectra occurs in the soft X-ray range. The slope of type-2 objects is remarkably harder. Following the unified scheme and assuming that in type-2 objects the central engine is obscured by the dusty torus, we conclude that the torus is optically thick not only in the optical/UV but also in the soft X-ray range.

In the following, we discuss in more detail the characteristic features of the X-ray spectrum in AGN and we outline current interpretations.

3.1.1 The power-law component: coronal emission or a hot inner flow?

The power-law component of AGN continuum spectra in the X-ray range is observationally well-constrained. While in the optical and UV band the description of the spectral slope is usually made using an index α referring to the flux $F(E) \propto E^{-\alpha}$, X-ray spectra are preferably described by the photon index $\Gamma = \alpha + 1$. The photon index can be constrained most easily in the range between 2 keV and 12 keV. This spectral range can be observed with *XMM-Newton*, and Piconcelli et al. (2005) constrained the average photon index Γ_{2-12} of 35 radio-quiet quasars to ~ 1.89. George et al. (2000) and Reeves & Turner (2000) conducted *ASCA* observations of samples of RQQs and found average values of $\Gamma_{2-10} \sim 1.97$ and $\Gamma_{2-10} \sim 1.89$, respectively.

Seyfert-1 galaxies share the power-law shape of the radio-quiet type-1 quasars (e.g. Nandra et al., 1991). The continuum of type-1 objects can be fitted with a similar power-law together with absorption by cold material in the soft X-ray range. At the high-energy end of the spectra, type-1 and type-2 X-ray spectra are equivalent (Matt, 2004).

The current picture of AGN supposes an underlying, optically thick accretion disk producing the thermal emission in the optical, UV, and partly the soft X-ray range. The temperature of the accretion disk thus lies in the range of 10^4 K —10^5 K. Such a multicolor disk does not explain the power-law shape reaching out into the hard X-ray range, up to several hundreds of keV. Modeling of the X-rays in AGN therefore requires another emission mechanism. It could be provided by a very hot plasma of $\sim 10^8$ K distributed above the disk surface. The hot electrons of such a corona can

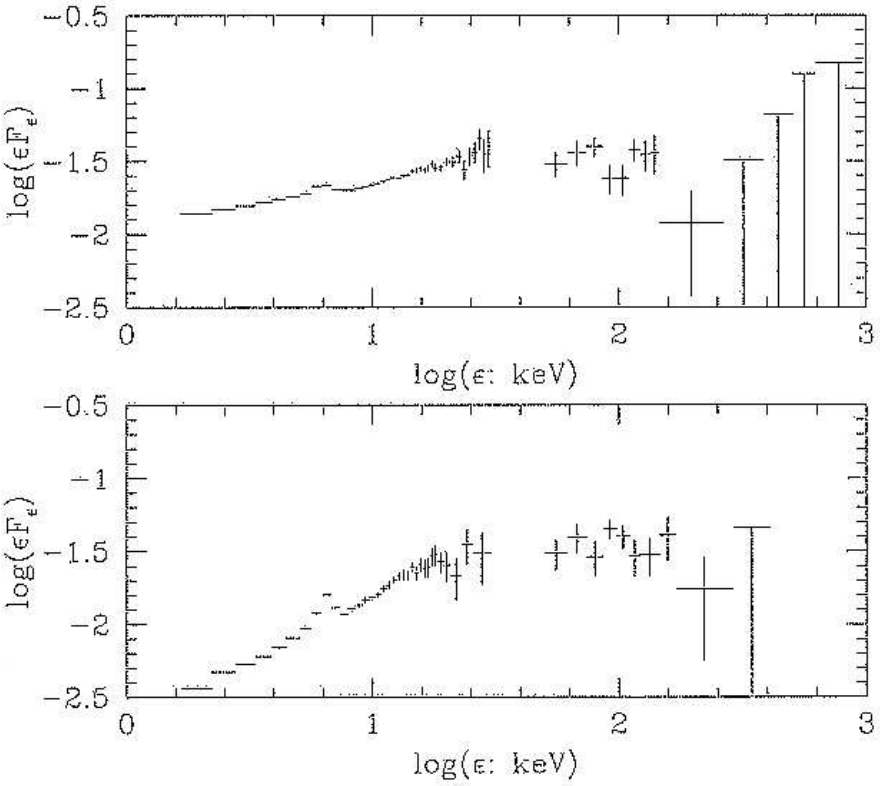

Figure 3.1: The average X-ray spectra of radio-quiet AGN for type-1 (top) and type-2 (bottom) objects (Krolik, 1999)

produce the high-energy photons by inverse Compton scattering of the multi-blackbody radiation coming from the disk (see e.g. Svensson, 1996).

Neither the production of the hot corona, nor its geometrical shape are currently clear. It is possible to associate the primary component to magnetic reconnection events as observed in the solar corona. Since an accretion disk rotates differentially while being highly ionized, dynamo effects create magnetic field structures able to reconnect and release hard X-ray radiation - analogously to what happens during solar flares. If there are continuous reconnection events above the accretion disk atmosphere, the disk continuously supports flaring events. Thus a continuous, while fluctuating hard X-ray component is observed. At the same time, hot plasma can be evaporated at the disk's surface and form the corona due to the heating by the primary radiation (Czerny & Goosmann, 2004).

For low luminosities, the hot plasma might exist in the form of a hot inner flow. This idea is taken from the analogy to galactic black holes, where transitions between so-called *hard states* and *soft states* are seen (see Fig. 3.2). These states correlate with the luminosity of the object, being higher for the soft state. In the modeling of galactic black holes, this is explained by the inner edge of the accretion disk being closer or further away from the innermost stable orbit of the black hole. When the disk is further out, a hot inner flow develops between the inner edge and the innermost stable orbit (see Zdziarski & Gierliński, 2004, for a review). The hot flow gives rise to

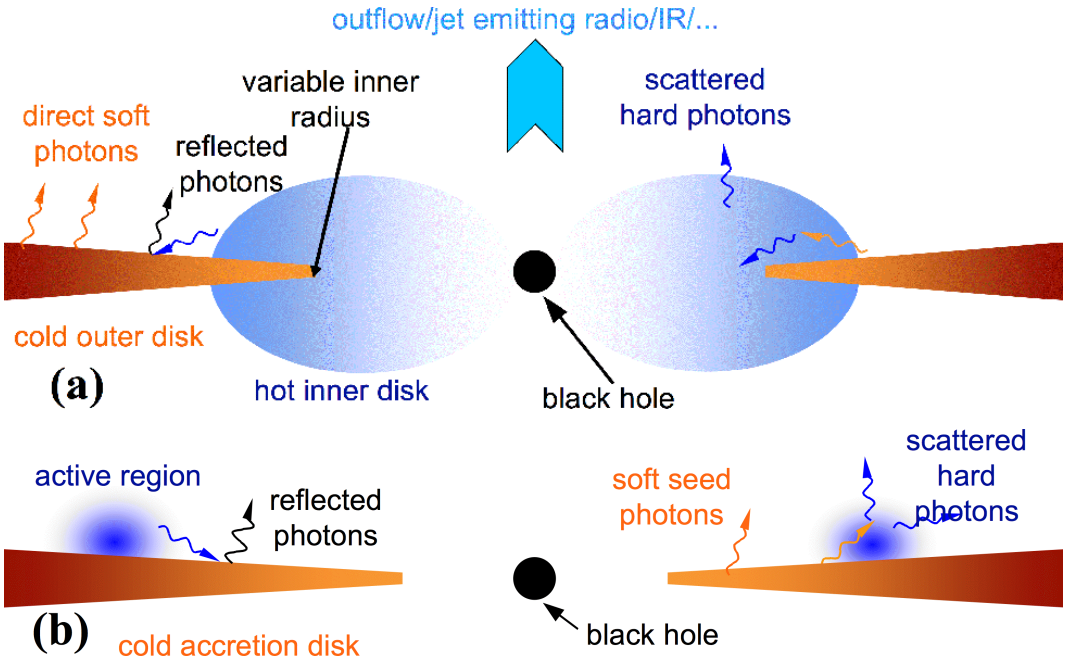

Figure 3.2: Illustration of the hard and soft states of Galactic black holes. In the hard state (a), the inner edge of the accretion disk is truncated and develops a hot flow toward the black hole. This hot flow produces the primary component by inverse Compton scattering of soft photons coming from the disk. For galactic black holes, the inner hot flow gives rise to the propulsion of a jet (the counter jet is omitted in the figure for clarity). In the soft state (b), the inner edge of the disk is much closer to the center, and the hot flow is suppressed. However, Compton reflection and reprocessing can occur from active regions that exist above the disk due to magnetic reconnection events (Zdziarski & Gierliński, 2004).

a hard power-law component as seen in the hard state. In the soft state, the inner flow is much weaker and hence the power-law component is missing. This picture is still simplified, as there are more states to consider for galactic black holes. However, the fundamental difference between hard and soft states in these objects should scale up to black hole masses of AGN (Done & Gierliński, 2004). While in galactic objects state transitions are seen on timescales of days, this is not expected in AGN, because such time-scales are proportional to the mass of the black hole. But it should be possible to observe also AGN in "high" or "low" states being quasi-permanent on human time scales. The states then correspond to AGN-types: if the inner hot flow exists, it produces the primary radiation and the X-rays are strong compared to the thermal radiation from the disk, as is observed for Seyfert galaxies. For AGN with less inner flow, the primary radiation is very weak and the thermal radiation is stronger, as observed for quasars.

Hybrid models of thermal Comptonization by a hot thermal corona and a non-thermal component have also been proposed to explain the continuum shape. In this case the electron population involved might have a Maxwellian (thermal) velocity distribution with a power-law (non-thermal) tail. For an extensive review about hybrid models and their role for AGN and Galactic black holes we refer to Poutanen (1998) and Coppi (1999). The importance of the non-thermal electron

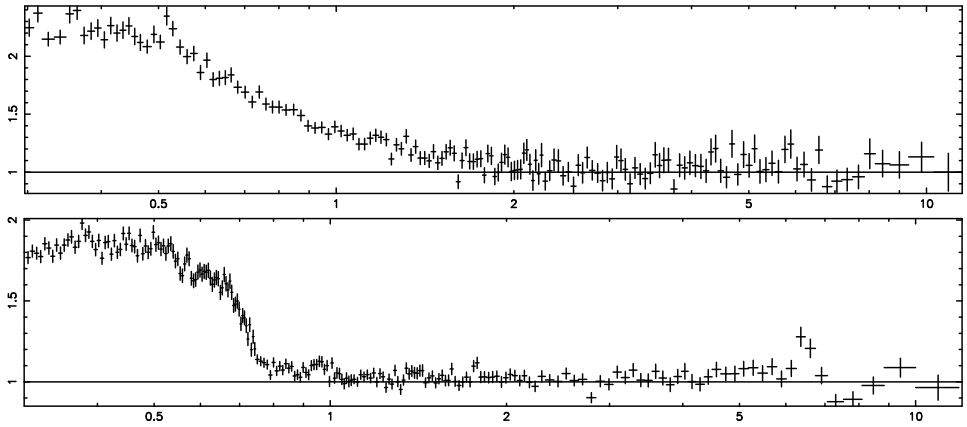

Figure 3.3: XMM-Newton spectra of the Seyfert galaxies Mkn 509 (top) and Mkn 766 (bottom) (Pounds & Reeves, 2002). One can distinguish the different shape of the soft-excess going along with a higher luminosity in Mkn 509 (see text).

populations for the emitted spectra is considered to be minor in AGN (Zdziarski et al., 1997). Eventual synchrotron emission from populations of relativistic electrons should leave imprints in the X-ray region but also in the IR, which is not observed in radio-quiet AGN. However, the injection of relativistic electrons could be important as a short-term effect during magnetic flare events (Torricelli-Ciamponi et al., 2005) creating active regions above the disk (see Fig. 3.2 for the analogy in Galactic black holes). Since the integration time in X-ray observations is mostly longer than such flare events in AGN, the non-thermal emission by the electrons will be blended by the thermal component. We are going to discuss magnetic flares and their spectral results in more detail in the chapters 4 and 6.

3.1.2 The soft X-ray-excess

Around 1 keV the majority of all AGN show a soft-excess, a small bump created by a change of the continuum slope. The exact spectral shape seems to depend on the luminosity of the object (Pounds & Reeves, 2002). For lower luminosities, the soft-excess has a sharp rise at ~ 0.7 keV, while for higher luminosities the spectral rise is smoother starting at ~ 3 keV (see Fig. 3.3). The interpretation of the soft-excess still is a matter of debate (see e.g. Sobolewska & Done, 2005). Often, its presence is coupled with a spectral deficit around 7 keV.

For a sample of PG quasars observed with *XMM-Newton* Piconcelli et al. (2005) modeled the soft-excess using different models. Each model contained a power-law fit and an additional component to represent the soft-excess: a (multi-)blackbody component, a second soft X-ray power-law, emission by bremsstrahlung, and thermal Comptonization. Possible contributions from starburst regions could be excluded, because the quasar emission is much more luminous and blends all radiation from the host galaxies. All models applied to the *XMM-Newton* data, enabled acceptable fits. Therefore, the decision, which combination of models is correct, has to be made on physical grounds.

It turns out that the results for *blackbody* or *multi-blackbody* models require an electron temperature of the Comptonizing medium exceeding the maximum temperature expected from the accretion disk (see also Page et al., 2004; de Rosa et al., 2004). The soft-excess can therefore not be

identified with even the most inner parts of the accretion disk. Another, hotter emitting medium would have to be added to the unified scheme. Besides, this model does not account at all for the deficit observed around 7 keV. Therefore modeling the soft-excess by high-temperature blackbody radiation seems not realistic.

Invoking a *second power-law component* (see Perola et al., 2000; de Rosa et al., 2004, for BeppoSAX observations of Mrk 509), gives a purely phenomenological description of the soft X-ray spectrum and lacks a clear physical interpretation.

Emission by *bremsstrahlung* could come from a transition layer between the accretion disk and the corona as was proposed by Nayakshin et al. (2000). The authors claim that for sources with spectra being dominated by thermal UV disk emission, bremsstrahlung from the transition layer could be important.

Another mechanism to account for the soft-excess is a *second Comptonizing region* with higher optical depth and lower temperature as the one responsible for the Compton bump and the broad iron Kα line. Such a region could be situated at the transition between the accretion disk and a hot inner flow (see Magdziarz et al., 1998, for the Seyfert galaxy NGC 5548), or in a warm skin on the surface of the accretion disk (Janiuk et al., 2001, for the quasar PG 1211+143). If one explains the soft-excess with the help of Comptonization of soft X-rays coming from the disk, a striking property of the Comptonizing medium can be found: the electron temperature from object to object remains practically constant being fixed in the range of 0.1 keV to 0.2 keV.

A problem in modeling the soft-excess by reprocessing was revealed during the monitoring of NGC 3516 with *RXTE* and *ASCA*. The observations show, that no significant variability time-lags exist between the hard X-ray range, representing basically the primary continuum, and the soft X-rays including the excess (Edelson et al., 2000). In a reprocessing model one would expect to measure a time-lag according to the distance between the source of the primary radiation and the Comptonizing mirror.

In this context, we also report the case of the source NGC 5506 hosting a heavily reddened NLS1 core. Its soft-excess was found to originate from an extended region with 350 pc diameter around the nucleus (Bianchi et al., 2003). This region is asymmetric but coincides well with radio structures published before by Schmitt et al. (2001). It turns out that the best model for the soft-excess invokes the *reflection and reprocessing* by the extended ionized region.

Analyzing *XMM-Newton* data of PG quasars, Gierliński & Done (2004) proposed that the *soft-excess appears due to absorption* of a softer continuum than given by $\Gamma = 1.9$. It is necessary to assume an ionized wind in turbulent motion with bulk velocities up to $0.2c$ in order to smear out the absorption lines and form a continuum-like trough over the region below 1 keV. However, such physical conditions do not seem very realistic ad moreover this model requires an additional source of UV emission. Therefore, Chevallier et al. (2005) favor a "hybrid" model where the primary UV-X-source could be produced by a disk-corona system and then be absorbed by a modest relativistic wind.

3.1.3 The soft X-ray absorption and emission lines

Halpern (1984) observed the quasar MR 2251-178 using the *EINSTEIN* satellite and discovered strong absorption in the soft X-ray spectrum below 3 keV. He suggested to model this feature by photo-absorption in a highly ionized medium, the so-called *warm absorber*. In the following, *ASCA* and *ROSAT* observations revealed that about 50% of all Seyfert galaxies and many quasars show similar absorption features due to warm absorbers (see e.g. Reynolds, 1997; George et al., 1998).

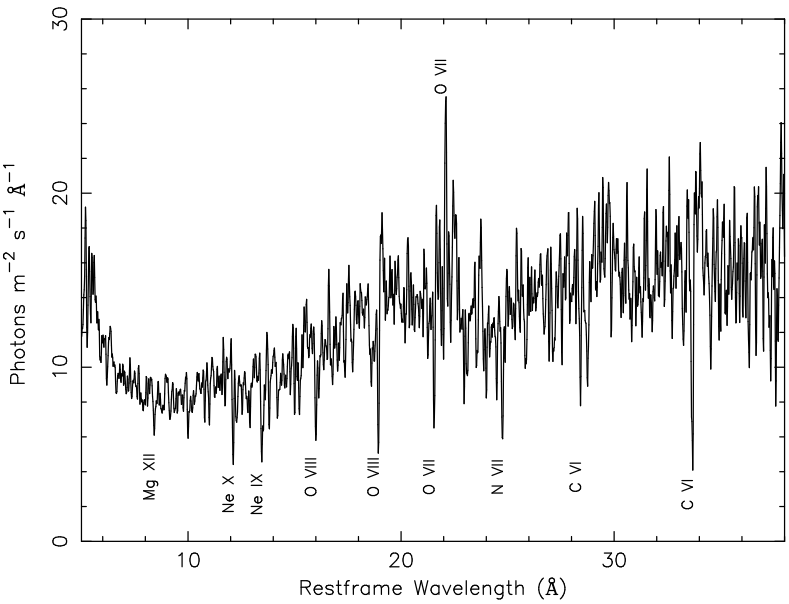

Figure 3.4: Zoom of the soft X-ray spectrum of NGC 5548 reported by Kaastra et al. (2000). Several absorption lines, mostly of hydrogen- and helium-like ions are identified.

At that time, the warm absorber mostly was identified by strong absorption edges of highly ionized metals such as OVII at 720 eV and OVIII at 870 eV. The first detection of these edges was obtained for MCG -6-30-15 by Nandra & Pounds (1992). A review on the *ASCA* and *ROSAT* results is given by Komossa (1999).

The last generation of X-ray satellites like *XMM-Newton* and *Chandra* providing higher resolution spectroscopy has greatly improved our knowledge of the warm absorber and revealed that it exhibits numerous atomic features. Characteristic narrow absorption lines are seen, especially from hydrogen- or helium-like ions of C, N, O, Ne, Na, Mg, Si, and FeXIV —XXI. Fig 3.4 shows a zoom of the soft X-ray spectrum of NGC 5548 obtained with *Chandra* (Kaastra et al., 2000). Several absorption lines are identified.

The composition of the spectral imprints by the warm absorber is complex. For instance, there are numerous M-shell $2p$-$3d$-transitions for different ionization states of iron between wavelengths of 16 Å to 17 Å (equivalent to energies of 730 eV to 775 eV). These absorption lines form a quasi-continuous absorption feature, the so-called unspecified transition array (UTA) (Sako et al., 2001; Behar et al., 2001). In addition to that, some warm absorbers reveal the presence of dust (see e.g. Brandt et al., 1996; Komossa & Bade, 1998). Dust among the absorbing material often goes along with strong optical reddening of the object. The dust can be constrained by an inconsistency of the column densities derived from optical and from X-ray observations. This inconsistency disappears, when both observations are modeled with a mixture of ionized gas and dust (see e.g. Komossa & Fink, 1997, for the case of NGC 3227). The first direct evidence for dust intermixed with a warm absorber was obtained by Lee et al. (2001) detecting an Fe-L absorption complex in the spectra of MCG -6-30-15. This Fe-L feature is attributed to dust extinction.

Generally, the absorption lines in the UV and X-ray range are blueshifted indicating outflow velocities around $\sim$ 1000 km/s (see e.g. Kaspi et al., 2002; Kaastra et al., 2002). The high ionization

states of the absorbing elements suggest, that the medium is part of the AGN irradiated by the central continuum source. Detailed analysis of the absorption spectra shows, that the absorbing material mostly consists of several components covering a certain range of ionization states and group velocities. All in all, the warm absorber seems to represent outflowing material close to the central engine. The wind is assumed to be stretched along the symmetry axis of the common unified AGN scheme. This assumption is supported by observational differences of the warm absorber between Seyfert-1 and Seyfert-2 objects: Seyfert-1 galaxies are dominated by absorption lines while in Seyfert-2 galaxies emission lines are more abundant (Kinkhabwala et al., 2002; Matt et al., 2004), which is consistent with the fact that for a type-1 view the compact and very luminous source appears behind the warm absorber while for type-2 objects it is seen from the side. It was emphasized by Netzer (1993), that reprocessing and the production of emission lines by the warm absorber is important if the optical depth of the medium is high enough. The exact geometry of the warm absorber still is a matter of debate. It could be an outflow originating at the accretion disk surface that is magnetically or radiatively accelerated (Konigl & Kartje, 1994; Murray & Chiang, 1995; Elvis, 2000).

Mathur et al. (1994) confirmed that the warm absorber in the quasar 3C 351 is consistent with the medium causing the UV absorption lines. This was later confirmed for most objects having warm absorbers (see e.g. Mathur et al., 1998; Crenshaw et al., 1999; Monier et al., 2001), although the kinematic features of the UV and soft X-ray range do not always coincide (see e.g. Behar et al., 2003, for the case of NGC 3783).

On the other hand, it was also shown that the UV/X-ray absorber in 3C 351 cannot be identical with the BLR, due to inconsistent physical properties of the photo-ionizing and -absorbing media (Mathur et al., 1994). In the case of the Seyfert galaxy NGC 3227 the warm absorber is intermixed with dust that could not survive in the BLR. Meanwhile, it is found in many AGN that the warm absorber is an independent, eventually dusty medium located farther away from the central engine than the BLR. However, this result is not ubiquitous, in some objects the warm absorber can be modeled as a high-density mass-loss from BLR clouds (Netzer, 1996), or optically thin and highly ionized clouds intermixed with the BLR (Shields et al., 1995).

A thoroughly examined object is the Seyfert galaxy NGC 3783 that was spectroscopically observed for 900 ks with Chandra (Kaspi et al., 2002). We show the obtained spectra in Fig. 3.5. This warm absorber was modeled using photo-ionization simulations by Krongold et al. (2003), who found out that the observed spectrum can be reproduced by a two-phase absorber, irradiated by a power-law continuum. Although both phases of the absorber differ significantly in column density and ionization state, they are consistent with a single outflow in pressure equilibrium. This is a physically probable condition for the absorbing material (Krolik & Kriss, 1995), although not considered in most modeling attempts. We come back to this issue in chapter 9, where we present modeling attempts for the warm absorber.

Note, that absorption in the soft X-ray range also happens in the intergalactic medium, as well as in the interstellar medium of the AGN host galaxy and of our own Galaxy. This "on-the-way-absorption", however, is due to a much colder medium and has a different velocity structure. It can be accounted for in the fitting process.

3.1.4 The iron Kα-line and the Compton hump: X-ray reprocessing

First detections of a strong X-ray emission line at 6.4 keV came from *EINSTEIN* observations of heavily obscured Seyfert galaxies, such as NGC 4151 (Matsuoka et al., 1986). Deep observations

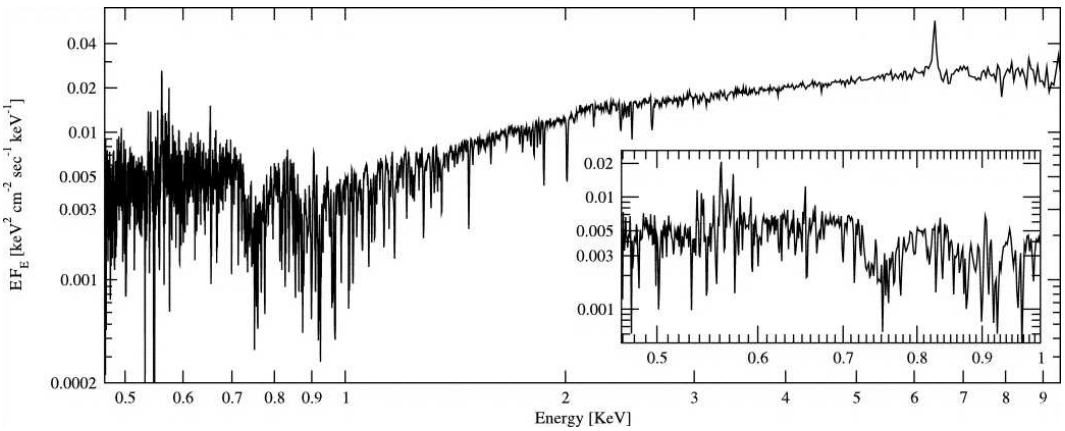

Figure 3.5: Detailed X-ray spectrum of NGC 3783 obtained with Chandra and reported by Kaspi et al. (2002). The inset is a zoom resolving individual lines below 1 keV.

using the *GINGA* satellite revealed that the emission line complex is a common X-ray feature of Seyfert galaxies (see e.g Pounds et al., 1989; Awaki et al., 1991). It is attributed to fluorescent Kα emission. The Kα-line of iron is particularly strong due to a high cosmic abundance and a strong fluorescence yield. The line is often accompanied by a high-energy hump and by an absorption feature at ~ 7 keV, which is due to iron K-shell absorption (Pounds et al., 1990; Nandra & Pounds, 1994).

Contributions to the iron Kα-line complex may come from different ionization states causing line components in a range of 6.4 keV —6.9 keV. However, the ionization states up to FeXVII have line energies close to 6.4 keV and FeXVIII—XXIV Kα-lines reach up to 6.65 keV. Only helium- and hydrogen-like iron produces lines at 6.7 keV and 6.9 keV respectively. The fluorescent lines are actually doublets due to fine structure effects. For neutral iron, the Kα-line at 6.4 keV splits up into a doublet of Kα1 at 6.404 keV and Kα2 at 6.391 keV. However, with current observing technology none of these differences can be resolved.

The *ASCA* satellite mission showed, that the observed line complexes mostly peak around 6.4 keV (Nandra et al., 1997b), indicating nearly neutral iron. The equivalent width of the line complex is in the range of 200 eV —300 eV. From the observations, an anti-correlation between the equivalent widths $EW(K_\alpha)$ and the spectral slope was found. Furthermore, in type-1 AGN the equivalent width of the narrow Kα-line component at 6.4 keV is anti-correlated with the soft X-ray luminosity of the active nucleus. This effect is commonly called the *X-ray Baldwin effect* (Nandra et al., 1997a; Reeves, 2003; Zhou & Wang, 2005). Confirmation of the effect seems less sure in a pure quasar sample, as reported by Jiménez-Bailón et al. (2005).

The absorption edges for K-shell photoionization for various ionization states are regularly distributed between 7.1 keV for neutral iron and 9.3 keV for the hydrogen-like ion. The *GINGA* observations of a sample of Seyfert galaxies conducted by Nandra & Pounds (1994) revealed higher ionization states for the K-shell absorption edges than those necessary to explain the emission lines. They concluded that the line emitting region and the absorbing medium are not identical. The later one should be a hotter, eventually outflowing medium that was identified with the warm absorber (see section 3.1.3).

The launch of the XMM-Newton observatory has greatly improved spectral observations of the

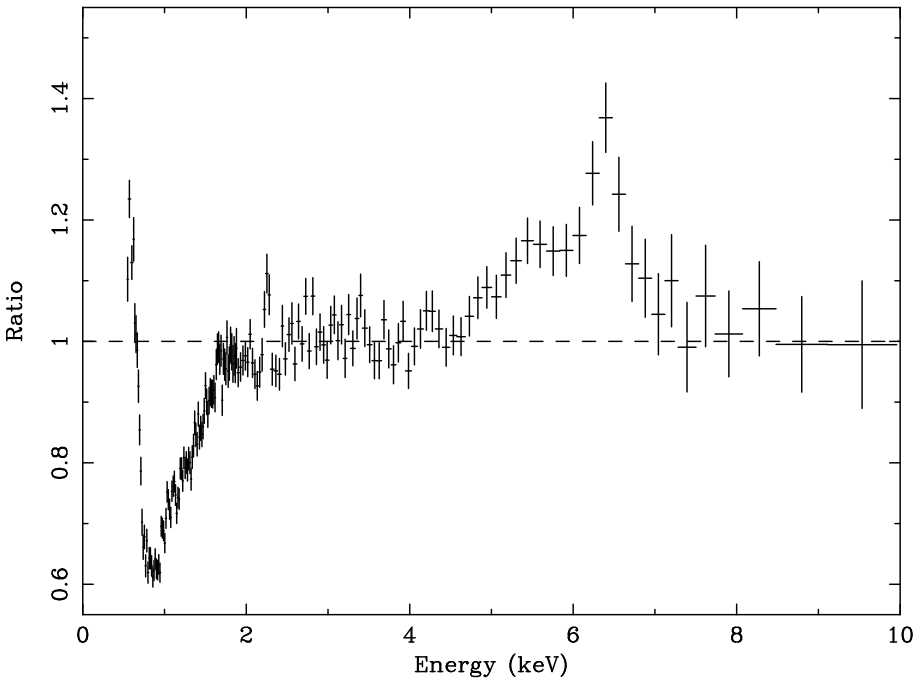

Figure 3.6: The profile of the iron Kα-line complex in MCG -6-30-15 observed with *ASCA* in 1994. The line spectrum is shown as a ratio to a power-law fit. One can clearly distinguish the broad red wing in the asymmetric profile (Iwasawa et al., 1996).

iron Kα-line (see e.g. Reeves, 2003). Even the much weaker Kβ line complex around ~ 7 keV can be detected in some objects, such as the Seyfert-2 galaxy NGC 4388 (Beckmann et al., 2004), or the Seyfert-1 galaxy NGC 3783 (Reeves et al., 2004). It turned out, that all detected Kα-lines from AGN contain a narrow component at 6.4 keV. However, in some objects the line complex shows a very asymmetric and broad profile. As an example, we show *ASCA* observations of the Seyfert galaxy MCG -6-30-15 (Tanaka et al., 1995), plotted as a ratio to a power-law fit, in Fig. 3.6. In this object, the iron Kα line is particularly strong showing a broad red wing. There is increasing evidence that the peculiar line profile is related to relativistic distortions. The line therefore offers a possibility to probe the physical conditions in the close environment of the accreting black hole. The observed line profile depends on many parameters, including the disk inclination, the emissivity distribution across the disk, or intervening matter on the line of sight. Meanwhile, broad iron Kα features are reported for several objects (see e.g. Nandra et al., 1999; Balestra et al., 2004; Porquet et al., 2004; Jiménez-Bailón et al., 2005). Detailed modeling therefore becomes important. We are going to discuss modeling of the iron Kα more extensively in the chapters 4 and 6.

Another peculiar iron Kα-line complex is found in the Seyfert-2 galaxy IRAS 18325-5926 (Iwasawa et al., 1996, 2004). While this line also indicates relativistic broadening, it peaks at a slightly higher energy than 6.4 keV, which is uncommon for Seyfert galaxies. This specific Kα-line therefore indicates emission from highly-ionized iron, dominated by hydrogen-like species.

Constructing a composite X-ray spectrum of eight Seyfert galaxies, Pounds et al. (1990) found that the iron emission line goes along with another spectral component forming a hump around 30 keV. This hump had been predicted early by theoretical work of Guilbert & Rees (1988) as well as

Lightman & White (1988). It is due to multiple Compton scattering successively decreasing photon energies. Modeling of X-ray reprocessing by a colder medium confirms the combined occurrence of the iron Kα-line and the reflection bump. Both effects are connected by the atomic physics of X-ray reprocessing. The unified scheme of quasars suggests several locations for the reprocessing media, such as the accretion disk, or the inner surfaces of the molecular and dusty torus. Hot clouds in the central region could also provide the high-ionization components seen in the iron lines (Karas et al., 2000).

For cold reprocessing, Magdziarz & Zdziarski (1995) found a parametrization for various shapes of the incident spectrum, the viewing angle, and the covering factor R measuring the strength of the reprocessed component. The value R is defined as the solid angle Ω subtended by the reprocessing material and the primary source: $R \equiv \Omega/2\pi$. Applying their method to a sample of Seyfert galaxies, Magdziarz & Zdziarski (1995) find a strong correlation between R and the photon index Γ of the power-law component. For increasing Γ, and thus for steeper X-ray spectra, the reprocessed component becomes stronger.

We already pointed out, that there is an observational correlation between the equivalent width of the Kα-line and Γ. Together with the X-ray Baldwin effect, a correlation between $EW(K_\alpha)$, Γ, R, and the soft X-ray luminosity is established.

3.2 X-ray variability of AGN

Spectral variability is a defining feature of AGN. During the era of the *EXOSAT*-satellite, rapid and large amplitude variability in the X-ray band was confirmed to be common in Seyfert galaxies (McHardy, 1988; Pounds & McHardy, 1988; McHardy, 1989). The variability is seen on time scales of weeks to months, and 40% of all Seyfert galaxies even vary significantly within one day (Grandi et al., 1992). Since no physical signal can proceed faster than light, such short variability time scales are connected to small light traveling distances of only $\sim 3 \times 10^{15}$ cm. Hence, the observed variability requires that the X-ray radiation of AGN is produced very close to the central engine. The overall X-ray variability is complex and only partly disentangled. In this section, we summarize the main observational results and their implications.

In Fig. 3.7, we show the X-ray light-curves of 3 Seyfert galaxies. The curves cover several years. The long-term behavior looks similar in all three objects, which is not evident in the first place, because they differ significantly in luminosity - for instance, NGC 5548 is a hundred times more luminous than NGC 4051. In contrast to the long-term similarities, the amplitudes of the short-term variations, on time-scales of ~ 1 day, are anti-correlated with the brightness (Barr & Mushotzky, 1986; Green et al., 1993; Nandra et al., 1997c). Brighter Seyfert galaxies thus vary less on short time scales.

With the launch of the *RXTE*-satellite it became possible to investigate X-ray variability in more detail. Extensive monitoring has been carried out for a few Seyfert galaxies (see e.g. Markowitz & Edelson, 2001; Markowitz et al., 2003) and for the radio-quiet quasar PG 0804+761 (Papadakis et al., 2003). Intensive observational campaigns allow construction of detailed *power density spectra* (PDS). The PDS is an efficient tool to analyze variability, as it quantifies the variability power exhibited for a given time-scale (section 3.2.1).

Meanwhile, strong X-ray variability can be traced down to time-scales of only hours or even minutes. Computing *rms-variability spectra* from long X-ray observations with *XMM-Newton* allows to investigate spectral changes around the iron Kα-line. As the line is the result of X-ray reprocessing,

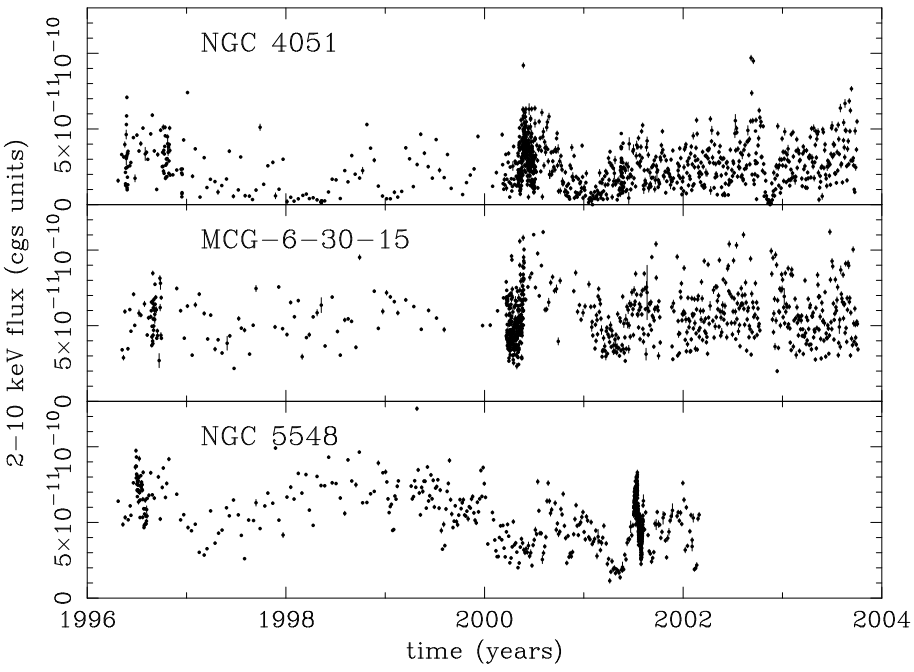

Figure 3.7: Long-term light curves for the Seyfert galaxies NGC 4051, MCG -6-30-15, and NGC 5548 (Uttley & Mhardy, 2004)

insights in the time evolution of the reprocessed component with respect to the primary radiation can be obtained (section 3.2.2).

3.2.1 Timing analysis using power density spectra

Lawrence & Papadakis (1993) and Green et al. (1993) analyzed *EXOSAT* data for AGN by constructing power density spectra $P(f)$. The PDS of a given light-curve is obtained by (discrete) Fourier-transformation. It hence gives a measure of the power contributed by periodic or quasi-periodic events with frequency f. Generally, PDS of AGN are monotonous functions with an overall negative slope. Such PDS are called "red noise", because they do not show any prominent features corresponding to characteristic time-scales. Therefore, the variability seemed to be the result of randomly distributed and uncorrelated events. A similar conclusion had been drawn by McHardy & Czerny (1987) doing a fractal analysis of a three-day light-curve for the Seyfert galaxy NGC 5506.

With the launch of the *RXTE*-satellite, the PDS of AGN became a lot better in quality. It was shown that they can be fitted by a *broken* power-law $P(f) \propto f^{-\alpha}$, with α changing significantly at specific break frequencies (see e.g. Edelson & Nandra, 1999, for the case of NGC 3516). The turnover frequencies typically correspond to time-scales of days and months (McHardy et al., 1998; Chiang et al., 2000; Markowitz et al., 2003). Combining extensive *RXTE* and *ASCA* observations of the Seyfert-1 galaxy MCG -6-30-15, Nowak & Chiang (2000) revealed a turning point of the PDS in the high frequency range between $f = 10^{-4}$ Hz and $f = 10^{-3}$ Hz (Fig. 3.8). The PDS of MCG -6-30-15 is very similar to the PDS of the galactic source Cygnus X-1 (e.g. Belloni & Hasinger, 1990), when scaled in frequency by a factor of $\sim 10^3$. A similar conclusion was drawn by McHardy et al. (2004) from combined *RXTE* and *XMM-Newton* data of NGC 4051.

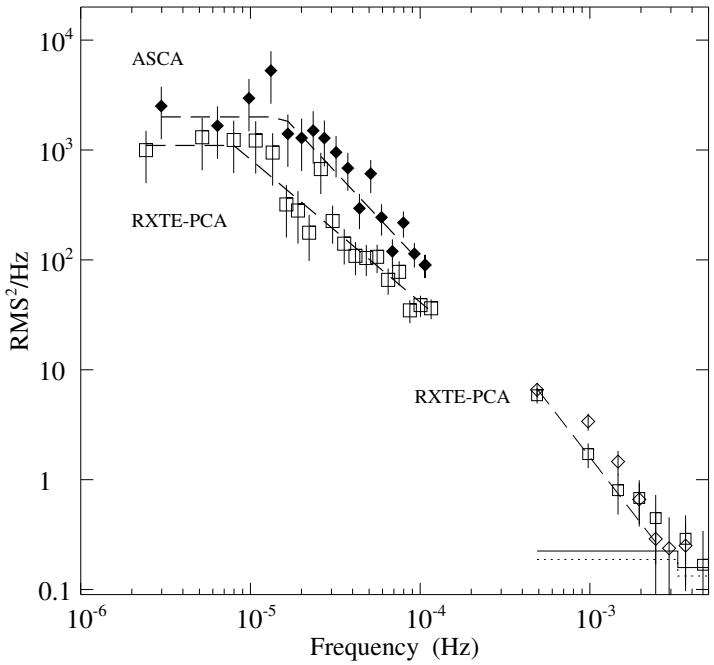

Figure 3.8: Power density spectrum of MGC -6-30-15 composed from observations taken with *ASCA* and *RXTE* (Nowak & Chiang, 2000).

For galactic black holes, the turnover frequency of the PDS points out the size of the emission regions. We assume that the variability of AGN is also connected to the accretion process. From the α-disk model (section 2.4.2), it follows that the local disk flux and therefore the luminosity of the object scale linearly with the black hole mass M. So does the Keplerian time scale as a characteristic time-scale for the accretion process at a given radius. Therefore, the correlation between short-term variability amplitude and luminosity is expected to constrain the black hole mass of AGN in the same way as for galactic black holes.

Green et al. (1993) pointed out that the PDS is correlated to the spectral shape. Objects showing a softer X-ray slope show more intense variability on short time-scales. In the analogy of galactic black holes this corresponds to a "high-state" with the inner edge of the accretion disk reaching closer in, and with a less developed inner hot flow (see section 3.1.1).

Furthermore, it has been known for a while that luminosity changes of many Seyfert galaxies are correlated to variations of the spectral slope. A general trend is that the X-ray spectrum over 2 keV —50 keV *softens when the luminosity increases* (see e.g. Halpern, 1985; Perola et al., 1986; Matsuoka et al., 1990; Maraschi et al., 1991; Grandi et al., 1992; Leighly et al., 1996; Markowitz et al., 2003). Such variations can be explained by recalling the spectroscopic decomposition of the X-ray spectrum into a primary power law component and reprocessed radiation (see section 3.1). The variability correlation between the spectral shape and the luminosity can then be reproduced by different relative normalizations of the two components. This model works well for NGC 5548 (Nandra et al., 1991) and MCG -6-30-15 (Nandra et al., 1990).

Analysis of PDS shows, that the variability behavior of NLS1 galaxies is different from that of regular Seyfert-1 galaxies. In comparison to regular Seyfert-1 galaxies of similar luminosity, the

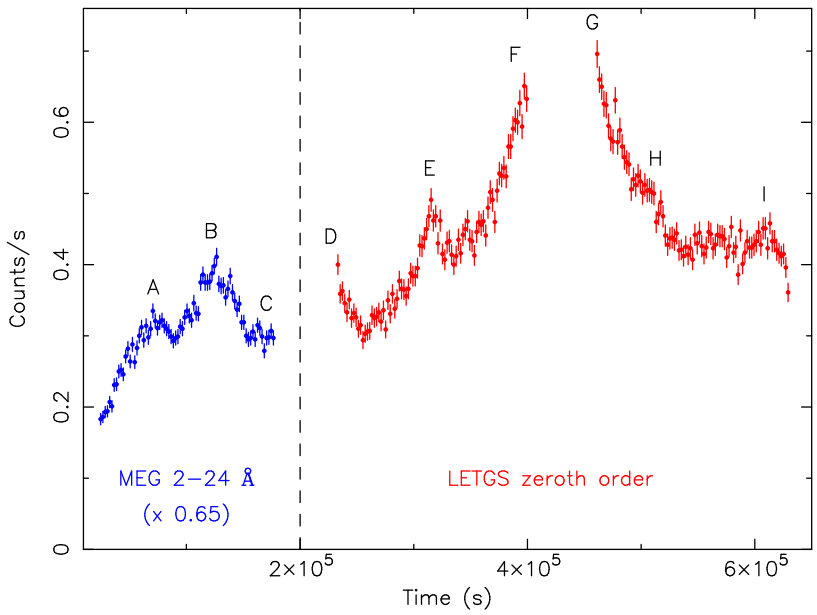

Figure 3.9: Chandra observation of the 1.2 keV —10 keV flux from the Seyfert-1 galaxy NGC 5548 (Kaastra et al., 2004). The capital letters denote several flaring events.

variability amplitude on time scales of days is significantly stronger. Hence, the connection between variability and accretion process must be different for NLS1 galaxies (Leighly, 1999; Turner et al., 1999). It is currently discussed, that NLS1-galaxies accrete at rates close to the Eddington rate, release a great fraction of the accretion power into a wind. It is possible that this wind contributes significantly to the observed variability, making the picture more complicated than for regular Seyfert galaxies or quasars.

Quasi-periodic variability is well-know for stellar mass black holes, with Cygnus X-1 being a famous prototype. For a stellar black hole, the emission region, the accretion disk, and the Keplerian time scales are smaller by several orders of magnitude compared to the case of AGN. Therefore, quasi-periodic oscillations (QPOs) of AGN are expected but very hard to observe today (Vaughan & Uttley, 2005). For a while it was claimed that QPOs had been found by *EXOSAT* observations of the Seyfert galaxy NGC 6814 (Mittaz & Branduardi-Raymont, 1989; Leighly et al., 1992) but, unfortunately, this had to be rejected when Madejski et al. (1993) reported a secondary, independent and periodic source appearing close to the center of NGC 6814.

3.2.2 X-ray flaring and the variability of the iron Kα-line

Recently, some AGN have been extensively observed, for $\sim 10^5$ s or more, using *XMM-Newton* and *Chandra*. Flux variability by factors of 1.5—3 within less than one hour was found - such *X-ray flares* have been reported for MCG -6-30-15 (Ponti et al., 2004), for NGC 5548 (Kaastra et al., 2004), and also for the bright quasar PDS 456 (Reeves et al., 2000). In Fig. 3.9 we show a light-curve of NGC 5548 taken with Chandra (Kaastra et al., 2004). Several flaring events are denoted by capital letters. Rising and fading of these eruptions are roughly symmetric in time. Judging by eye, one gets the impression that the X-ray variability on very short time scales is dominated by

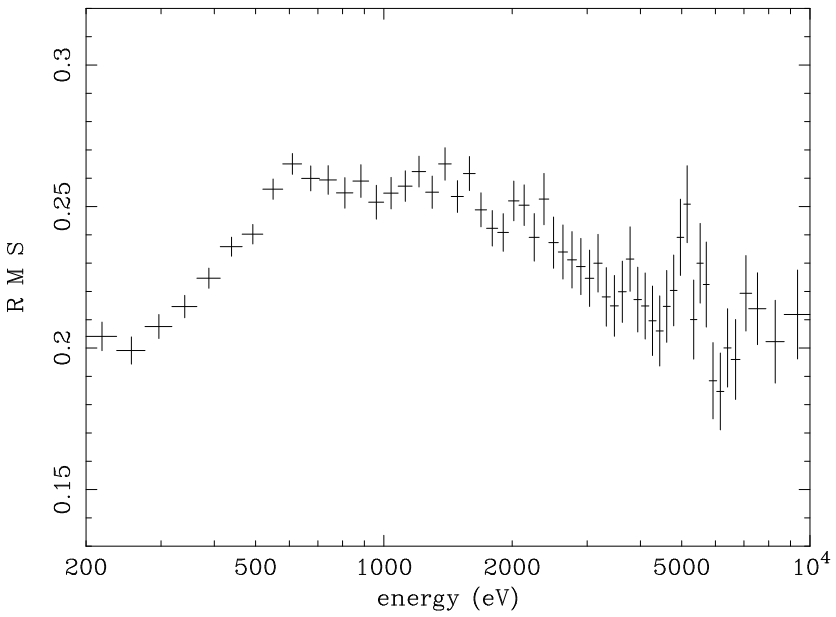

Figure 3.10: The rms-variability spectrum of a long *XMM-Newton* observation of MCG -6-30-15 as derived by Ponti et al. (2004).

flares. Supposedly, such short flares trace activity in very localized regions above the disk.

For the strong flare reported in MCG -6-30-15, Ponti et al. (2004) investigated spectral variations during the actual flare period, and during the whole observation of 95 ks conducted by Wilms et al. (2001). The series of single spectra taken during the relatively short flare period of $\sim$ 2000 s still suffers from a low signal-to-noise ratio. However, the spectral variability can be described with enough accuracy by computation of the *fractional variability spectrum* $F_{var}(E)$. This *rms-variability* gives a measure for the variability power exhibited at a given spectral energy. It can be defined as:

$$F_{var}(E) = \frac{\sqrt{\sum_{i=1}^{N} \frac{[x(E,\Delta t_i) - <x(E)>]^2}{N-1}}}{< x(E) >}, \tag{3.1}$$

where $x(E, \Delta t_i)$ is the source count rate in the energy band E during the time interval Δt_i, the value $< x(E) >$ is the mean source count rate at energy E during the whole observation, and N is the number of time bins. We show the resulting rms-spectrum in Fig. 3.10.

An interesting feature in this rms-spectrum is the relative lack of variability at the location of the iron Kα-line. Such a behavior has been confirmed for various Seyfert galaxies (Markowitz et al., 2003) and suggests a different variability pattern for the primary spectrum and for the reprocessed component.

In the case of MCG -6-30-15, the suggestion was made that the suppression of variability around 6.4 keV can be understood by strong relativistic effects in the vicinity of a rapidly spinning black hole (Miniutti & Fabian, 2005).

Chapter 4

Modeling of X-ray reprocessing in AGN

In the preceding chapter 3, we have given a description of the average X-ray spectrum of AGN, its main components and variability properties. It became clear that the X-ray appearance of AGN is complex and not yet entirely understood. However, more accurate data become available with current and next generation X-ray satellites. Equally important is the development of sophisticated theoretical models for the various physical processes contributing to the X-ray properties of AGN.

In this chapter, we present some recent modeling projects being related to our modeling purposes concerning the reprocessed spectral component of AGN. This description gives us a helpful basis for the modeling carried out in the remaining part of this thesis. In section 4.1 we briefly recall different scenarios for the origin of the incident hard X-ray radiation, while in section 4.2 we compare the reprocessed radiation computed under different assumptions for the density and ionization structure of the illuminated medium. In section 4.3 we discuss possible approaches to the modeling of the local spectra produced by magnetic flares illuminating small areas of the disk, and section 4.4 presents the application of relativistic corrections to the spectra coming from orbiting spots. In this context, we also describe Monte-Carlo simulations for random flare distributions across the disk in order to model X-ray variability.

4.1 Production of the primary component

A basic constituent of X-ray spectra from AGN is the primary component. It is believed that the primary radiation mostly forms due to Comptonization of soft photons within a hot optically thin plasma. The temperature of the plasma must be very high, in order to "up-scatter" the soft photons to hard X-ray energies. However, the accretion flow, at least in bright AGN, is assumed to proceed rather in the form of a cool, optically thick accretion disk. Thus, the origin of a hot Comptonizing plasma is not obvious (see e.g. Narayan et al., 1998; Collin et al., 2001; Czerny et al., 2003).

One way, to explain the formation of a hot-corona above the disk, is by invoking the concept of magnetic flares. This concept was established in analogy to solar flares. The main idea was outlined by Galeev et al. (1979) and developed in several subsequent papers for both AGN and galactic sources (see e.g. Haardt & Maraschi, 1991; Haardt et al., 1994; Poutanen & Fabian, 1999). As an accretion disk around the central black hole of an AGN is assumed, it is suggested that the differential rotation within the disk should create magnetic activity in the same way as it is generated in the sun. Driven by the rotation of the disk, the magnetic pressure in the disk rises, so that some flux tubes are pushed away form the disk by buoyancy and reconnect at a certain

height above the surface. Such reconnection events release large amounts of magnetic energy and form compact blobs of an optically thin and highly ionized medium producing the observed primary radiation. Such flares are local phenomena, the rise of the magnetic flux tubes may be triggered by the magneto-rotational instabilities inside the disk. Therefore, we expect flares to appear with a certain randomness in position on the disk. On a time average, X-ray flares therefore create an extended, patchy corona (Haardt et al., 1994). The plasma in the localized blobs contain free electrons at *high* temperatures. The primary spectrum resulting from inverse Compton scattering has a power-law shape (e.g. Rybicki & Lightman, 1979; Sunyaev & Titarchuk, 1980). However, this rather qualitative description still contains a number of uncertainties. For instance, the velocity distribution of the electrons in the hot magnetized plasma above the disk does not necessarily have to be thermal but also could have a non-thermal component (Coppi, 1999).

For the remainder of this chapter and this thesis we are going to assume a few simple properties of the primary component without considering the details of its production. The primary source of a flare event is supposed to emerge from a very compact region around the position of the reconnection and it should have a power-law shape. For the X-ray range it is mostly convenient to describe it by the photon index Γ for a photon number distribution $n(E) \propto E^{-\Gamma}$. The magnetic fields forming the newly connected flux loop are anchored in deeper layers of the accretion disk and therefore the compact source co-rotates with the disk. No specific assumptions about the angular distribution of the primary radiation are made, we simply assume the source emits an isotropic radiation field. In such a scenario, we expect half of the radiation to reach the disk where the reprocessed component emerges.

4.2 X-ray reprocessing by the accretion disk

The idea of X-ray radiation being reprocessed is known from other astrophysical contexts, such as the irradiation of the accretion disk by the compact X-ray source in a binary system (see e.g. Chiappetti et al., 1983). As explained in chapter 3, typical imprints of reprocessed spectra from irradiated media are the Compton hump at roughly 30 keV and atomic emission features, especially a fluorescent iron line around 6.4 keV.

Sunyaev & Titarchuk (1980) computed Comptonization effects and the time-development of incident photon spectra passing through ionized clouds. They conducted analytical modeling by solving the Kompaneets equations for Compton interaction in the energy range < 511 MeV, below pair production effects (Kompaneets, 1956). They investigated the effects of X-ray photons with photon energy E being scattered off a colder electron distribution with temperature T_e, so that $E > kT_E$. The bump feature observed in AGN spectra, but also Comptonization effects on the shape of an X-ray emission line were predicted for clouds with a Thomson scattering depth of a few.

While the bump feature can be represented by analytical solutions of the Kompaneets equation, atomic reprocessing features are not incorporated. In order to also consider atomic emission and absorption processes, detailed radiative transfer simulations have to be conducted. This has been done extensively (see e.g. Lightman & White, 1988; Ross & Fabian, 1993; Zycki & Czerny, 1994; Zycki et al., 1994; Nayakshin et al., 2000; Ballantyne et al., 2000, 2001; Matt et al., 1993a,b; Różańska et al., 2002). In the following, we present some projects for the modeling of the reprocessed component from an irradiated accretion disk.

4.2.1 Constant density models

As a first approach the reprocessed component can be modeled assuming a uniform density, plane-parallel slab for the medium. In most models both internal disk emission inside the slab and external X-ray radiation are defined. We present here some examples of models for the reprocessing.

Neutral medium with Comptonization

George & Fabian (1991) perform spectral modeling of Compton reflection and reprocessing by conducting Monte-Carlo simulations of photons irradiating a cold, neutral medium. The photons undergo Kα photo-absorption events with neutral iron or Compton scattering off bound electrons. The absorbed photons could then either be re-emitted as a fluorescent Kα- or Kβ-line photon and stay in the simulation or be lost by ejection of an Auger electron.

In their simulations George & Fabian (1991) investigate properties of the reprocessed medium for an incident radiation with a power-law shape. The photon index Γ of the power-law and the incident and viewing angles are changed systematically. It turns out that radiation being injected at grazing incident angles, has a higher probability to escape from the medium because these photons stay closer to the surface than those injected normally. For a given viewing angle the reprocessed radiation for low incident angles θ, measured from the normal to the surface, is hence lower than for higher θ. At the same time, photons escaping from the medium at directions close to the plane of the surface generally had to undergo several scattering events before. This is due to the Compton scattering phase function favoring forward and backward scattering. Therefore, the reprocessed flux for a given incident angle θ is a function of the viewing angle i, also measured from the disk normal, decreasing rapidly for grazing viewing directions.

Taking the approach a step further, George & Fabian (1991) perform simulations of Compton reflection and reprocessing by an accretion disk medium. The medium is either a semi-isotropically illuminated infinitely large slab, or a cylindrically-shaped disk irradiated by a source placed at a certain height above the disk surface on the disk-axis. The former model describes a model of X-ray irradiation, where the source of the primary continuum is embedded as a clumpy medium in the upper layers of the disk atmosphere, while the latter model assumes irradiation of the disk by a "lamppost". Both of these approaches reproduce reprocessed spectra, showing strong Kα and Kβ lines of iron and a Compton hump as we show in Fig. 4.1.

The figure presents the Compton reflection/reprocessed spectrum for an incident radiation with photon index of 1.7 having a semi-isotropic angular distribution. Such an angular dependence corresponds to an optically thin hot corona. For different metalicities the spectral level changes significantly. If the metalicity increases the soft X-ray absorption is stronger and most iron line fluorescent photons are destroyed by the Auger effect and do not escape from the medium any more. From the Monte-Carlo method the existence of the Compton hump can be understood by multiple Compton scatterings successively decreasing photon energies. Since the energy decrement per scattering increases with photon energy, while for lower photon energies only coherent Thomson scattering occurs, an accumulation of photons at intermediate energies around ~ 30 keV is expected.

Models for ionized material

Simulating Compton reflection and reprocessing by a cold, neutral medium is not a sufficient approach for accretion disks in AGN. The viscous heating of the disk together with the external hard X-ray irradiation assure that most elements are highly ionized. The reflected spectrum therefore

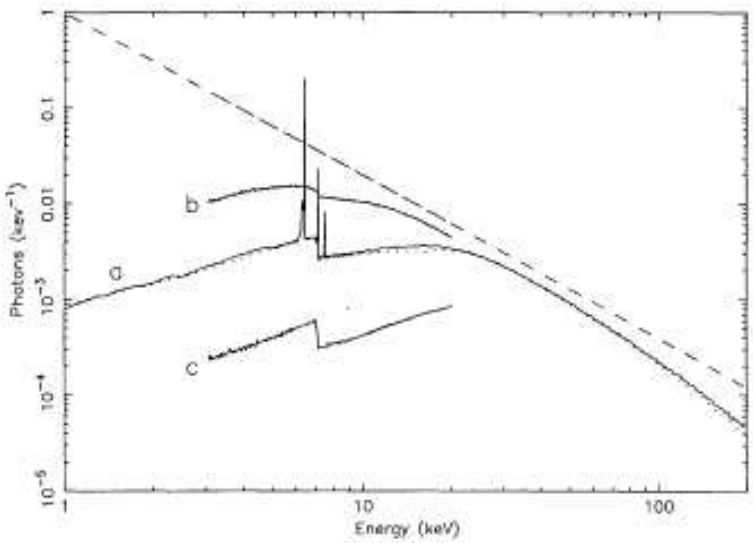

Figure 4.1: Modeling of the Compton reflection and iron line fluorescence performed by George & Fabian (1991). Here we show their results for an irradiated plane-parallel slab. The solid curve (a) denotes the reflected component including the Kα and Kβ lines. The other two solid curves denote the same for lower (b) and higher (c) metalicity of the slab. The dashed line corresponds to the incident spectrum

exhibits various atomic features in the optical and UV, but also in the soft X-ray range. In order to model correctly the X-ray spectra of AGN it is hence necessary to compute the ionization structure of the medium and to consider its impact on the reprocessing.

The ionization states at given point in the medium depend on the local temperature and on the radiation field. In the case of an accretion disk, these values can be obtained from the standard α-disk model given by Shakura & Sunyaev (1973) if the fundamental parameters, the black hole mass M, the accretion rate $\dot{m}$ expressed in units of the Eddington accretion rate, and the disk radius r are set. An important point in the modeling is that the α-disk model assumes a constant density of the medium. To add the external heating to the emission by the disk, a hard X-ray power-law spectrum is be added. The strength of the external X-ray heating is determined by the ionization parameter ξ defined as follows:

$$\xi = \frac{4\pi F_{inc}}{n_H}. \tag{4.1}$$

Herein, F_{inc} denotes the incident flux and n_H the surface number density of the medium.

This work was first conducted by Ross & Fabian (1993) who computed reprocessed spectra from an irradiated, plane-parallel element of an accretion disk at distance of 14 Rg. They chose the ionization parameter in such a way that the external X-ray flux equal the soft X-ray flux produced by the disk, and performed computations for two black hole masses, $10^7 M_\odot$ and $10^8 M_\odot$ and several accretion rates. It turned out that the overall spectral shape is governed by the ionization parameter ξ and that the black hole mass normalizes the overall spectral level. In Fig 4.2 we show the results of Ross & Fabian (1993). The various solid curves denote dimensionless accretion rates, normalized to the Eddington accretion rate, between 0.15 and 0.30 around a 10^7 solar mass black hole.

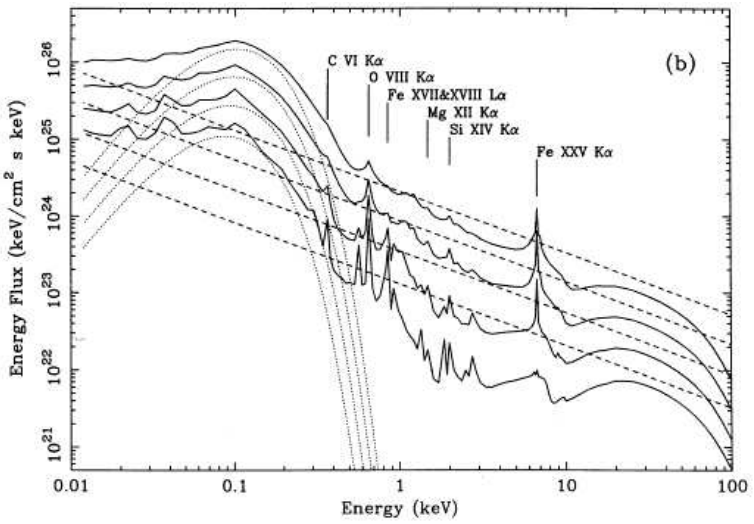

Figure 4.2: Modeling of the reprocessed spectra emitted by an ionized plane-parallel slab at constant density and illuminated by an external hard X-ray source (Ross & Fabian, 1993). The slab corresponds to an element at 14 Rg of the accretion disk around a 10^7 solar masses black hole. The ionization parameter ξ of the external X-rays is chosen so that the X-ray flux equals the viscous flux produced in the disk element. The solid curves denote the reprocessed radiation for various accretion rates (see text). The dashed lines show the incident power law, and the dotted line the viscous soft X-ray flux. The curves have different offsets to enable comparison. Several emission lines are indicated.

The ionization profile of the accretion disk leads to spectral emission lines as shown in the figure. The Kα-line complex occurs for all accretion rates, and therefore for all values of ξ. The strength of the other emission lines decreases for higher accretion rates, as the material becomes more and more ionized.

4.2.2 The hydrostatic equilibrium

Further sophistication can be added to the modeling of the reprocessed component by including the hydrostatic equilibrium of the accretion disk. Assuming that the disk atmosphere has a constant density, one neglects the influence of the gravitational field in the vicinity of the black hole, as well as the pressure exerted by the radiation field. To obtain a more physical model, the density structure of the medium should be computed self-consistently with the energy and ionization balance, radiative transfer, and hydrostatic pressure equilibrium equations. Such investigations have been carried out by Nayakshin et al. (2000); Nayakshin & Kallman (2001) or Ballantyne et al. (2001).

Here we refer to the study of Różańska et al. (2002). The code to compute the hydrostatic equilibrium of the disk is described in detail in chapter 5 and applied for our modeling presented in chapter 6. The hydrostatic equilibrium of the disk consists of a balance between the vertical component of the black hole's gravitational field and the gas and radiative pressure. Różańska et al. (2002) have conducted computations of the reprocessed spectra emitted by the accretion disk. The angular dependence of the incident radiation corresponds to the so-called lamp-post model, where the hard X-ray source is supposed to be located on the disk axis at a relatively large height above

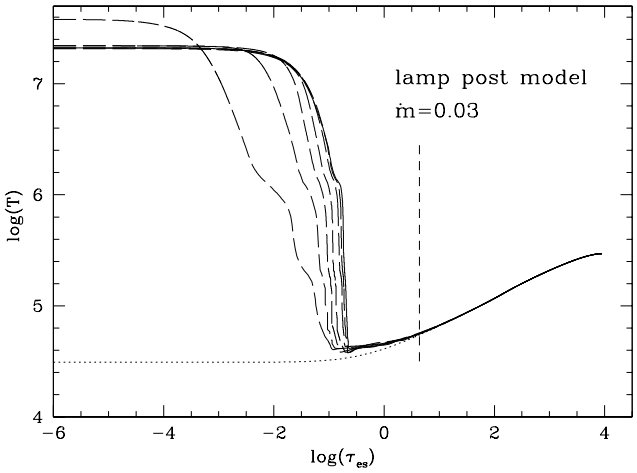

Figure 4.3: The vertical temperature profile of an irradiated accretion disk computed under the condition of hydrostatic equilibrium (solid line). The dashed lines mark the individual iterations between the computations for the structure and for the radiative transfer Różańska et al. (2002).

the black hole. This hard X-ray lamp irradiates the accretion disk from above along all disk radii. The simulations described here are valid for the disk radius of $20\,R_g$, with $R_g = GM/c^2$ being the gravitational radius for a black hole of the mass $M = 10^8 M_\odot$. The accretion rate in the disk is $\dot{m} = 0.03$ Eddington units. A thermal spectrum for the disk emission is added based on the total disk flux and the disk temperature resulting from the hydrostatic equilibrium.

The Compton reflection/reprocessed component is calculated using the radiative transfer codes *TITAN* and *NOAR* (Dumont et al., 2000). The code *TITAN* conducts radiative transfer inside optically thick media. It computes the spectrum in the UV and soft X-ray range and also determines the temperature and ionization structure of the medium. Compton effects modifying the X-ray spectrum and also the energy balance of the medium are taken into account by the Monte-Carlo code *NOAR*. The modeling results presented in chapter 6 were also obtained using *TITAN* and *NOAR*. Both codes are described in more detail in chapter 5.

The radiative transfer simulations are iteratively coupled with the computation of the hydrostatic equilibrium and self-consistently solved. The obtained spectra represent thus the spectrum coming from an accretion disk being in hydrostatic equilibrium with the local gravity field and the radiation produced in the disk and arriving from the X-ray lamp.

In Fig. 4.3 we plot the temperature profile obtained after convergence of the iterations between the calculations of the hydrostatic balance and the radiative transfer. The temperature marks a rapid transition from high temperatures $\sim 10^7$ K at the surface of the medium to more moderate values of $\sim 5 \times 10^4$ K at deeper in the plane-parallel slab. Such a rapid temperature drop has also been modeled by Nayakshin et al. (2000) and Ballantyne et al. (2001) who conducted similar investigations. In Fig. 4.4 the resulting reprocessed component together with the emerging total spectrum are shown. The total spectrum as seen by a distant observer is given by the sum of the reprocessing and the primary radiation, because both radiation sources are seen superimposed. The figure shows spectra for a detailed calculation of the vertical disk structure under the condition of hydrostatic equilibrium and also for a simpler model assuming a constant density in the disk.

The spectra for both models of the density structure in the disk exhibit a strong thermal component in the UV. The X-ray part of the spectra clearly shows that the medium is moderately ionized. In contrast to Fig. 4.1 the spectra are much softer due to less absorption occurring in the soft X-rays and the UV band. The spectral differences between the case of an accurately computed vertical disk structure and a constant density approach are significant, especially in the soft X-ray range.

Similar spectral behavior for the reprocessed radiation of accretion disks has been obtained by Nayakshin et al. (2000), despite the fact that in this work various parameters are different, as is the way in which the structure of the medium is computed.

4.3 Spectral modeling of flare spots

The concept of magnetic flares in accretion disks around black holes is inspired by the observation and investigation of solar flares where magnetic structures evolve due to the differential rotation of the sun. Galeev et al. (1979) suggested a model for growing magnetic field loops above the accretion disks. The development of the magnetic flux tubes is driven by convective forces and by the differential rotation within the disk and leads to magnetically charged blobs being driven away from the disk surface (Haardt et al., 1994). Due to reconnection of magnetic fields in the disk corona, compact sources of hard X-ray spectra are created. In the framework of this model several observed properties of quasar X-ray spectra can be explained. Aside from the hard X-ray component seen directly by a distant observer, a fraction of the primary is reprocessed by the underlying disk producing the observed reprocessed component seen in the observations (see section 3.1). The flares may also explain the existence of the hot, optically thin plasma Comptonizing the primary radiation.

Understanding of the exact mechanisms leading to magnetic reconnection events above the disk has only started recently, as powerful magneto-hydrodynamical models are developed allowing to model the evolution of the magnetic structures in accretion disk in three dimensions (see e.g. Hawley & Villiers, 2004). In any case, magnetic flares should give an attractive way to explain the heating of the corona above the accretion disk and the production of the reprocessed component. As the magnetic reconnection events above the disk supposedly happen with a certain randomness, the flare model offers a way to explains the short term variability of AGN (e.g. Done & Nayakshin, 2001).

Among several other research groups (e.g. Nayakshin & Kazanas, 2002; Ross et al., 1999; Poutanen & Fabian, 1999; Beloborodov, 1999; Merloni & Fabian, 2001a,b, and others), reprocessed spectra of magnetic flares were computed by Collin et al. (2003). In this work an emphasis was put on the time-evolution of a flare - the approach takes into account that the underlying medium changes due to the onset of the flare and its temperature and ionization structure changes. However, different properties of the medium change with different reaction-times. The most important of these reaction times are the following:

1. the radiation transfer time, t_{rt},
2. the time for readjustment of the ionization equilibrium, which is the longer of the ionization time, t_{ion}, and the recombination time, t_{rec},
3. the time for thermal equilibrium, t_{th},
4. the time for readjustment of the hydrostatic equilibrium t_{dyn}.

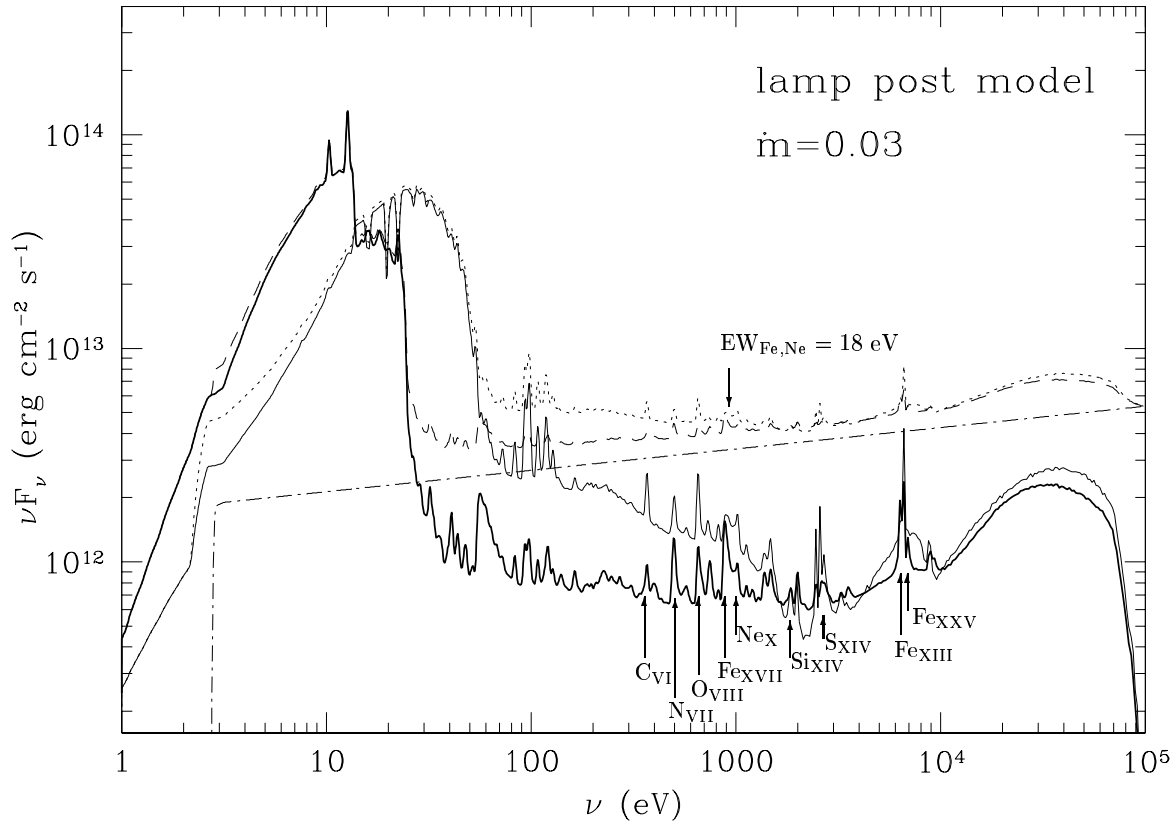

Figure 4.4: The reflected spectra of the irradiated disk for the lamp-post model computed under the condition of hydrostatic equilibrium (thick solid line) and for a constant density model (thin solid line). The total spectra, being the sum of the reprocessed component and the primary, are represented by dashed lines. The dashed-dotted line denotes the incident spectrum (Różańska et al., 2002).

In Collin et al. (2003) estimations for these time-scales are given to be compared to the characteristic time-scales of the flare. These are the following:

1. the "growing time" t_{grow} during which the flare builds up the compact flare source,
2. the time-scale t_{fl} for the *observed* increase of the X-ray continuum,
3. the intrinsic duration of the flare.

No reliable estimate can be given for the duration of the flare as there is no real indication yet. It could well be as large as 10^5 s as suggested by the highest time-scales derived from the analysis of power-density-spectra (Markowitz & Edelson, 2004). For the other time scales estimates can be found on physical grounds. Their comparison with the characteristic time-scales of the medium leads to:

$$t_{rt}, t_{ion}, t_{rec}, t_{th}, \ll t_{grow} \sim 10^3 \text{ s} \leq t_{fl} \ll t_{dyn} \sim 10^5 \text{ s}. \tag{4.2}$$

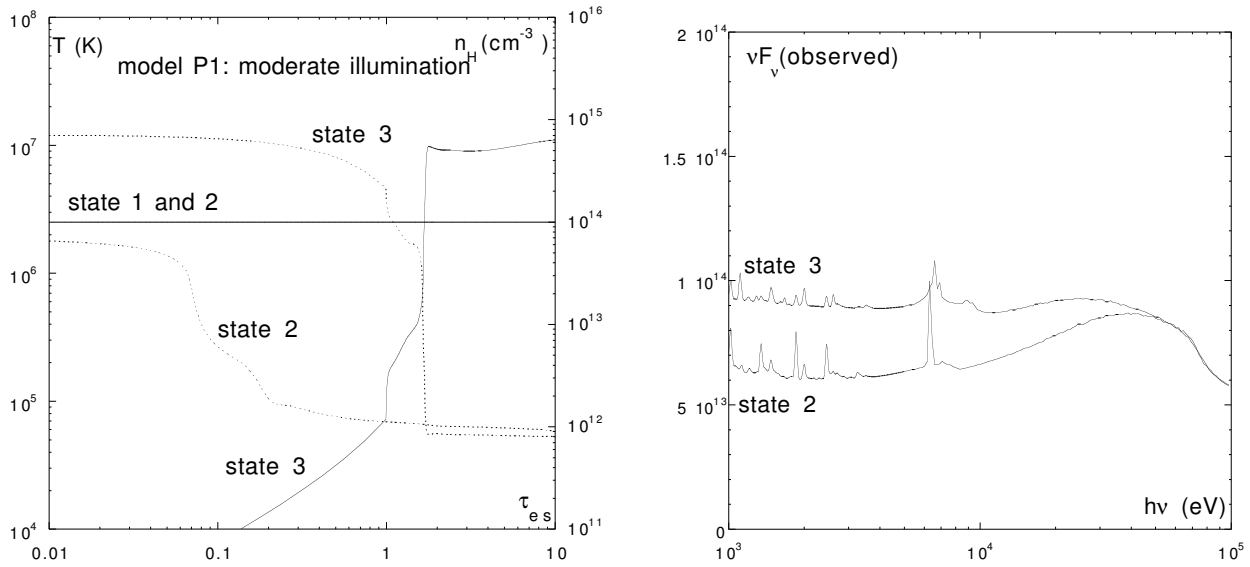

Figure 4.5: Results for the structure and radiative transfer computations at the three different states 1, 2, and 3. The left panel shows the vertical density (thick line) and temperature (thin line) structure in terms of optical depth (Thomson units), the right panel represents the spectral flux between 1 keV and 100 keV for state 2 and state 3 (Collin et al., 2003).

Compared to the sampling time of an observation, the onset of a flare could thus be observed. The temperature and the ionization equilibrium respond immediately to an increase of flux, but the density structure remains unchanged. The adjustment of the density structure to a new hydrostatic balance takes much longer, and might not be achieved before the flare emission ends. It therefore makes sense to consider the reprocessed spectra at several times during a whole flare period. Right after the onset of the flare, the reprocessed emission comes from a previously non-irradiated medium and only after a significant time the spectrum changes as the disk settles into a new hydrostatic equilibrium due to the flare irradiation.

In their work Collin et al. (2003) conduct modeling of the structure in the disk medium and of the emerging reprocessed spectra at three different states. In the first state (1) no illumination is assumed corresponding to the situation before the onset of the flare. The same code as mentioned in section 4.2.2 is used to compute the hydrostatic equilibrium of an accretion disk, but without being connected to any radiative transfer modeling with *TITAN* and *NOAR*. Then, for the state (2) the flare irradiation is switched on and the coupled computations between the disk structure and the radiative transfer are carried out. The illumination of the disk by the flare is supposed to be significantly stronger than the disk emission and the angular dependence of the incident radiation is assumed to be isotropic. The latter assumption does not entirely correspond to the flare geometry, as we are going to discuss in more detail in chapter 6. This fact is indeed an important starting point for the work described in this thesis. Finally, for the state (3) the hydrostatic equilibrium has changed and the medium has a different vertical density structure. Again, structure and radiative transfer are obtained self-consistently.

The results for the disk structure and the emerging spectral flux at all three states are compared in Fig. 4.5. During state 2 the spectrum displays the characteristics of a strongly illuminated, dense gas with very intense soft X-ray emission lines and a strong iron absorption edge. During state 3

the hot reflecting layer is thicker and thus the reflected continuum is more intense. The iron line indicates higher ionization states, it exhibits broadened Comptonized wings (Abrassart & Dumont, 2001), the soft X-ray spectra is much weaker than in state 2.

Comparing the observational properties with the prediction made in the context of this model, it is suggested that the observed luminosity is dominated by transient states having not reached hydrostatic equilibrium. An observed spectrum is likely to contain contributions from flares at different states. Therefore, model spectra derived for a state out of equilibrium, like the state 2, are useful to be compare with the data. We derive such spectra in chapter 6.

4.4 Relativistic effects and orbiting flares

An important idea about magnetic flares in accretion disks is the fact that they occur at random positions. This includes very close distances to the black hole, where we expect spectral deformations due to relativistic effects in the curved space-time near the black hole. Also Doppler shifts induced by the orbital motion become more important at smaller disk radii. In order to account for the spectral deformation of the reprocessing coming from the inner spots, the local spectra emitted at the disk surface have to be convolved with a relativistic transfer function calculated for a distant observer at a given viewing direction.

Application of relativistic ray-tracing in combination with the emission from orbiting flares becomes an important subject, since more frequently there are claims, that orbiting spots are actually seen in the data (see e.g. Kaastra et al., 2004, for NGC 5548). In the case of NGC 3516 (Iwasawa et al., 2004), the authors have applied a ray-tracing model including an orbiting spot. The emitted reprocessed spectrum contains iron line emission and the resulting time-resolved spectra of the iron fluorescent line compare very well to the data. The *XMM-Newton* observation of NGC 3516 seems to show a periodic event. However, the observation is not long enough to really confirm the periodicity, although the data looks quite promising (Miniutti & Fabian, 2005).

A rotating accretion disk with an asymmetric emissivity distribution induces strong variability already by its orbital motion. Flares, randomly distributed over the disk, hence produce a variable spectrum. As the signal-to-noise ratio for short time-dependent X-ray observations of a single flare is not yet available, variability considerations can give better access to model interpretations from X-ray data. Czerny et al. (2004) conducted Monte-Carlo simulations of many flare spots distributed across the accretion disk. The model includes relativistic effects and shows in particular that the observed variability level of Seyfert galaxies requires a larger number of flares if their intrinsic luminosity is not uniform across the disk but depends on the spot location. In general, the energy-dependent variability derived in Czerny et al. (2004) is not very high and never exceeds 2%. Such low variability levels are not sufficient to be compared to observational data. In chapter 8, we explain that this is related to some simplifying assumptions about the local spot emission. Using the same method, we are going to conduct similar simulations in chapter 8, where the method is described in more detail. It is based on the consecutive sampling of large flare distributions across the disk. For each consecutive time bin, relativistic ray-tracing between each flare spot and the distant observer at a given viewing direction is carried out with the help of the ray-tracing code *KY* (Dovčiak, Karas & Yaqoob, 2004; Dovčiak, 2004) described in chapter 5. From the resulting time series of spectra the rms-spectrum can be derived for various parameters, such as the black hole spin, the observer's inclination, or the average flare distribution across the disk.

Chapter 5

Applied radiative transfer methods

In this chapter we describe the radiative transfer methods we apply in our X-ray modeling codes. The first code we use computes the vertical structure of an accretion disk in hydrostatic balance. For the local radiative transfer we use the two iteratively coupled codes *TITAN* and *NOAR*. Effects due to the curved space-time in the vicinity of a black hole are computed by the code *KY*.

An algorithm to solve the differential equations describing the vertical profile of an accretion disk in hydrostatic equilibrium subsequently developed by Agata Różańska and described in Różańska & Czerny (1996), Różańska (1999), Różańska et al. (1999), and Różańska et al. (2002). The code uses an iterative method to find the density, temperature, and internal radiative flux along the vertical axis for a given radius of the accretion disk. The mass of the central black hole, and the accretion rate can be defined by the user. The code then includes viscous heating by applying the α-disk model of Shakura & Sunyaev (1973). It solves the radiative transfer of the total flux and also considers energy transport due to advection processes.

The code *TITAN*, developed by Anne-Marie Dumont and described in Dumont et al. (2000, 2003), computes the radiation field for the optical, UV, and soft X-ray range of a plane-parallel medium and calculates its thermal and ionization profile. In order to solve the radiative transfer equation, *TITAN* applies the *Accelerated Lambda Iteration* method (ALI). This method is frequently used in the modeling of stellar atmospheres. An arbitrary density stratification of the atmosphere can be adopted by *TITAN* or calculated self-consistently under the condition of constant gas or total (= gas + radiation) pressure. Incident and emitted spectra can be defined and evaluated at various angles with respect to the vertical axis of the plane-parallel atmosphere. The medium can be illuminated on both sides and the code calculates reflected and transmitted spectra at various angles. Compton interactions between the incident radiation and the ionized medium cause a net energy input and therefore contribute to the temperature profile of the medium. Also, Compton effects have an impact on the shape of spectral features in the X-ray range. Therefore *TITAN* is iteratively coupled to the Monte-Carlo radiative transfer code *NOAR* (Dumont et al., 2000, 2003).

The *NOAR* code was developed by Arnaud Abrassart and described in Dumont et al. (2000, 2003) computes reflected and transmitted spectra in the energy range of 0.8 keV —500 keV based on a vertical density, temperature, and ionization profile computed by *TITAN*. During the execution of *NOAR*, incident photons are sampled working their way through the medium. The photons undergo absorption, re-emission, and Compton scattering events, leading to a net Compton heating profile. All radiative processes are sampled using a random number generator in combination with given probability distributions of the atomic and radiative transfer processes. The photons escaping from the medium form the transmitted or reflected spectra. As for *TITAN*, all spectra can be defined

and evaluated at various angles. The *NOAR* code can be applied to a plane-parallel medium or to a stratified shell. During the following iteration between the two codes, the Compton heating profile obtained is read-in by *TITAN* and taken into account for the computation of the vertical temperature profile. The temperature and ionization profiles computed by *TITAN* are then re-injected into *NOAR*. This procedure continues until convergence between the two codes is achieved. Usually, this happens with the second or third iteration.

The codes *TITAN* and *NOAR* consider the ten most abundant chemical elements in the universe: H, He, C, N, O, Ne, Mg, Si, S, and Fe and all their ionic species. The atomic data used are identical for both programs and were recently updated.

For our modeling of X-ray emission in the closer vicinity of the black hole we have to include relativistic corrections in a curved space-time. This is done by the ray-tracing program *KY* (Dovčiak, Karas & Yaqoob, 2004; Dovčiak, 2004). This code integrates photon trajectories for a given emissivity distribution on a thin accretion disk located in the equatorial plane of a Schwarzschild or Kerr black hole. The disk is supposed to be in Keplerian motion at each disk radius. A time evolution of the disk emissivity can be included. The code computes time-dependent spectra for a distant observer at a defined viewing direction.

In the following we describe these four codes in more detail including the basic physical concepts behind them. Note that in our descriptions we frequently do not distinguish between the denotation of an angle θ and its cosine value $\mu = cos\theta$.

5.1 Determining the vertical disk structure

The vertical structure of an accretion disk is described by its density ρ, temperature T, flux F, and pressure P as a function of the vertical depth z inside the medium. In order to find these various profiles, they have to be connected by the differential equations in z that describe the physics of an accretion disk in hydrostatic equilibrium. In the following, we are going to list the relevant physical values and the corresponding equations. We briefly sketch out how they can be solved.

5.1.1 Description of the flux

We allow two kinds of radiation inside the medium: the viscous flux F_{disk} dissipated within the disk and X-ray flux F_X coming from above the disk, for instance from the optically thin and hot corona. Both fluxes are related to the accretion process powering the overall generation of emission. We define here a fraction f measuring the amount of radiation dissipated within the corona. It is therefore defined by:

$$(1-f)F_{disk} + fF_X = F_{gen}, \tag{5.1}$$

where F_{gen} is the total flux generated from the accretion process and dissipated in the disk and in the corona at a given position. Integrating F_{gen} over the whole disk surface, one obtains the bolometric luminosity L_{bol} of the object being connected to the accretion rate $\dot{M}$:

$$L_{bol} = 2 \times \int_{r_{in}}^{r_{out}} dr \int_{0}^{2\pi} d\phi F_{gen}(r, \phi, z = 0) = \eta \dot{M} c^2. \tag{5.2}$$

Herein, r_{in} and r_{out} denote the inner and the outer radius of the accretion disk. The disk surface is assumed to be circular, so that it can be described in cylindrical coordinates r and ϕ at the fixed

height $z = 0$. The efficiency of the energy transformation in the accretion process is measured by η, which is the fraction of accreted mass being radiated away on both sides of the accretion disk.

Assuming that the disk is axisymmetric, we drop the coordinate ϕ for the following and we only consider a given radius r. Then the only relevant dependence remains in the vertical direction given by the z-axis. At a given optical depth τ, the differentials of both components F_{disk} and F_X of the generated flux are given by:

$$dF_{disk} = \frac{3\Omega\alpha}{2} P dz, \tag{5.3}$$

$$dF_X = \rho\kappa_{tot} F_X(z)\, dz. \tag{5.4}$$

The disk flux is related to the viscous transformation of gravitational energy measured by the parameter α, as introduced by Shakura & Sunyaev (1973). The formula for dF_{disk} can be obtained from Shakura & Sunyaev (1976). The Keplerian angular velocity is denoted by Ω and κ is the total opacity coefficient. For the coronal X-ray flux a simple exponential decay due to absorption is assumed. For the total flux F at the depth z it follows:

$$\frac{dF}{dz} = \frac{dF_{disk}}{dz} + \frac{dF_X}{dz} = \frac{3}{2}\Omega\alpha P + \rho\kappa_{tot} F_X(z). \tag{5.5}$$

5.1.2 Description of the pressure

Equation 5.5 contains the pressure P of the medium at a given height. This pressure can be decomposed into gas pressure P_{gas} and radiation pressure P_{rad}:

$$P = P_{gas} + P_{rad} \tag{5.6}$$

The gas pressure is given by the condition of hydrostatic equilibrium in the gravitational field of the black hole. In the Newtonian limit, the vertical component g_z of the gravity field is given by:

$$g_z = -\Omega^2 (H - z), \tag{5.7}$$

where H denotes the height of the disk atmosphere measured from the equatorial plane. the gas pressure gradient dP_{gas} can be obtained from this equation by multiplication with the mass density ρ.

The radiation pressure P_{rad} can be obtained with the help of the total opacity coefficient κ_{tot}:

$$dP_{rad} = \frac{\rho\kappa_{tot} F}{c} dz. \tag{5.8}$$

Hence, for the total pressure gradient, we obtain the expression:

$$\frac{dP}{dz} = \frac{dP_{gas}}{dz} + \frac{dP_{rad}}{dz} = -\rho\Omega^2 (H - z) + \frac{\rho\kappa_{tot} F}{c}. \tag{5.9}$$

5.1.3 Description of the temperature

The expression 5.9 for the total pressure is related to the temperature by the thermal equation of state:

$$P = \frac{k}{\mu m_H} \rho T. \tag{5.10}$$

Herein, k is the Boltzmann constant and m_H denotes the hydrogen mass. For cosmic abundances we choose a molecular weight of $\mu = 0.5$.

The temperature profile of the medium is found by considering an energy balance between heating and cooling processes in each layer of the medium. Here we include viscous heating, Compton heating and atomic heating and cooling. This leads to the following balance equation:

$$\frac{3}{2}\Omega\alpha \frac{k}{\mu m_H} T + \kappa_{es} F_{tot} \frac{4k}{m_e c^2}(T_{IC} - T) - \rho\Lambda(\rho, T) + \rho\Gamma(\rho, T). \tag{5.11}$$

Herein, κ_{es} denotes the Thomson opacity, T_{IC} is the inverse Compton temperature, and Λ and Γ are the atomic cooling and heating functions, that can be obtained from numerical radiative transfer computations with the code *CLOUDY*. The inverse Compton temperature varies with the depth z in the medium but can be approximated by the function:

$$T_{IC}(z) = \frac{T_{IC}(0) F_X(z) + T_{disk}(z) F_{disk}(z)}{F_X(z) + F_{disk}(z)}, \tag{5.12}$$

where $T_{IC}(0)$ is the inverse Compton temperature determined by the incident spectrum $F_X(0)$ at the surface $z = 0$ of the medium and T_{disk} denotes the black-body temperature $T_{disk}(z) = \left[\sigma^{-1} F_{disk}(z)\right]^{\frac{1}{4}}$ of the disk.

5.1.4 Determining the structure of the medium

The overall structure of the medium is obtained by solving the equations 5.5, 5.9, and 5.11 for all layers. This can be done by the iteration scheme described in Pojmanski (1986). A unique solution of these coupled differential equations requires boundary conditions at the top and bottom borders of the slab. These can be established by assuming given values of certain parameters. In order to compute the vertical profile of an accretion disk for instance, the surface density is assumed in advance and set to a considerably low value. Otherwise, the atmosphere would be infinitely high. At the equatorial plane of the disk, which is the bottom limit of the model slab, a total flux equal to zero is assumed due to the plane symmetry of the disk.

5.2 The photoionization code *TITAN*

The radiative transfer code *TITAN* computes the radiation field and the physical state of a given plane-parallel medium. It considers the temperature, ionic abundances, and the level populations of all ionic species throughout the atmosphere by assuming a stationary state. This condition ensures a local balance between all ionizing and recombining processes as well as between excitations and relaxations. Furthermore, conservation of energy is maintained locally and over the whole medium.

The *TITAN* code connects two iteration schemes, one regarding the solution of the radiative transfer equation (section 5.2.1) and another one to calculate the physical properties of the gas (section 5.2.2). We describe both iteration procedures and their interaction (section 5.2.3).

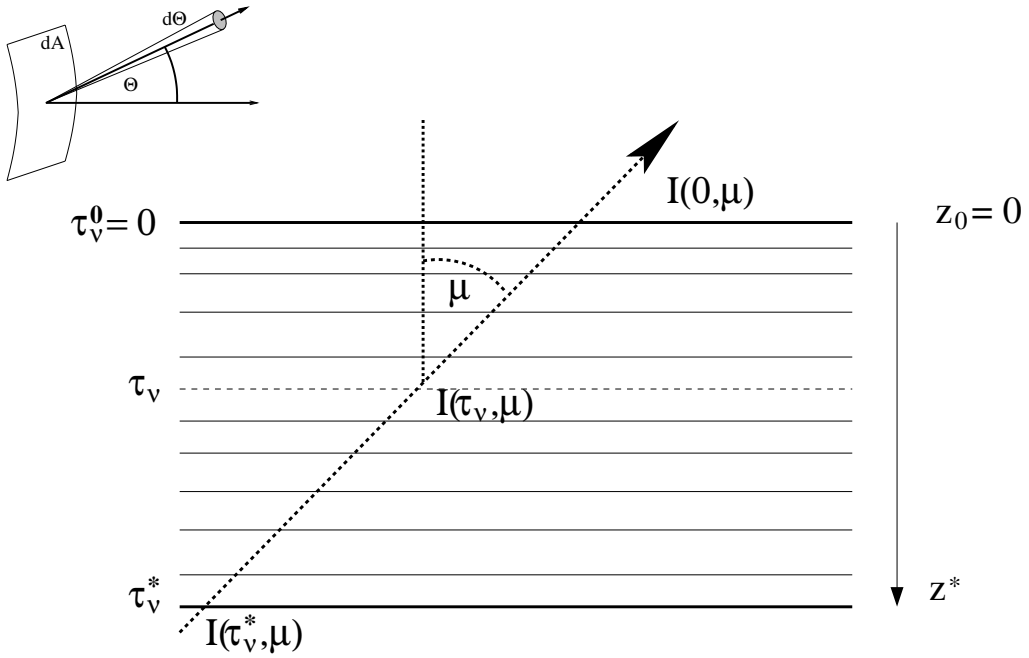

Figure 5.1: Definition of the specific intensity in the general case (upper-left) and for a plane-parallel atmosphere as assumed in *TITAN*

5.2.1 Solving the radiative transfer problem

A radiation field at frequency ν is defined by its *specific intensity* I_ν at every point of the region considered. Using the denotations shown in Fig. 5.1 (upper-left), I_ν measures the energy dE_ν of bandpass $d\nu$, that during a time period dt progresses through a surface dA and into the solid angle $d\Omega$:

$$dE_\nu = I_\nu \, dA \, \cos\theta \, d\Omega \, dt \, d\nu. \tag{5.13}$$

Using this definition, the "zeroth" moment of I_ν in $\mu = \cos\theta$ is called the *mean intensity* J_ν giving a measure for the energy density of the radiation field:

$$J_\nu = \frac{1}{2} \int_{-1}^{1} d\mu \, \mu^0 \, I_\nu = \frac{1}{2} \int_{-1}^{1} d\mu \, I_\nu. \tag{5.14}$$

The first and second moments of I_ν in $\cos\theta$ determine the *energy flux* F_ν and the radiative pressure P_ν^{rad}:

$$F_\nu = \frac{1}{2} \int_{-1}^{1} d\mu \, \mu I_\nu, \tag{5.15}$$

$$P_\nu^{rad} = \frac{2\pi}{c} \int_{-1}^{1} d\mu \, \mu^2 I_\nu. \tag{5.16}$$

For the modeling of spectra emitted by an astrophysical medium we want to compute the flux leaving the medium at its boundaries. These fluxes are connected to the field of I_ν throughout the whole medium. In order to determine this field, interactions between radiation and matter by emission and absorption have to be considered at every point. To quantify these processes we recall the coefficients for emission η_ν, absorption κ_ν, and scattering σ_ν. They measure the energy added to or removed from the specific intensity at a given location and for a given frequency. The astrophysical problems we consider in our work, are treated in plane-parallel geometry as shown in Fig. 5.1 (right). The vertical depth inside the medium is denoted by the coordinate z and μ measures the angle of the light ray with respect to the negative z-direction. With these denotations the transfer equation for I_ν reads:

$$\begin{aligned} \mu \frac{dI_\nu(z,\mu)}{dz} &= [\kappa_\nu(z,\mu) + \sigma_\nu(z,\mu)]\, I_\nu(z,\mu) + \\ &\quad -\frac{\sigma_\nu(z,\mu)}{2} \int_{-1}^{+1} d\mu' I_\nu(z,\mu') + \\ &\quad -\eta_\nu(z,\mu). \end{aligned} \tag{5.17}$$

The first term on the right hand-side of this equation denotes extinction by the medium being directly proportional to the specific intensity. Both, radiation removed from the beam by pure absorption and by scattering is considered. The second term describes the radiation scattered back into the beam scaling with the local mean intensity of the radiation field. Finally, the third term quantifies the radiation added to the beam by emission.

The above equation is an integro-differential equation of first order, that can be rewritten in a more compact form:

$$\mu \frac{dI_\nu(\tau_\nu,\mu)}{d\tau_\nu} = I_\nu(\tau_\nu,\mu) - S_\nu(\tau_\nu), \tag{5.18}$$

where we switched to the *elementary optical depth*, which is given by $d\tau_\nu = [\sigma_\nu(z) + \kappa_\nu(z)]\, dz$. Thereby, we assume that the coefficients η_ν, κ_ν, and σ_ν are independent of μ, and we define the so-called *source function*

$$S_\nu(\tau_\nu) = \frac{\sigma_\nu(\tau_\nu) J_\nu(\tau_\nu) + \eta_\nu(\tau_\nu)}{\sigma_\nu(\tau_\nu) + \kappa_\nu(\tau_\nu)}. \tag{5.19}$$

Solving equation 5.18 generally is a difficult task. Its solution depends on the values of the coefficients κ_ν, σ_ν, and η_ν that may vary significantly with the radiation field. Unless very simplifying assumptions about the emission and absorption properties of the medium are made, the solution has to be found by iterative processes that consider the radiation and the properties of the matter self-consistently.

In the following, we will present a formal solution of the radiative transfer equation in I_ν for both continuum radiation and absorption/emission lines. We consider the case of a plane-parallel atmosphere with finite height z^* corresponding to the total elementary optical depth τ^*. In *TITAN* the transfer for the continuum and for the lines is treated separately by the ALI method. For the lines, the statistical equilibrium of the level population has to be connected to the radiative transfer equation.

Computing the continuum radiation

The formal solution of equation 5.18 for the specific intensity at the optical depth τ_ν is given by:

$$I_\nu(\tau_\nu,\mu) = I_\nu(0,\mu)e^{\frac{\tau_\nu}{\mu}} - \frac{1}{\mu}\int_0^{\tau_\nu} d\tau'_\nu\, S_\nu(\tau'_\nu)e^{-\frac{\tau'_\nu-\tau_\nu}{\mu}},\ \text{for } \mu>0, \tag{5.20}$$

$$I_\nu(\tau_\nu,\mu) = I_\nu(\tau^*_\nu,\mu)e^{-\frac{\tau^*-\tau_\nu}{\mu}} + \frac{1}{\mu}\int_{\tau_\nu}^{\tau^*_\nu} d\tau'_\nu\, S_\nu(\tau'_\nu)e^{-\frac{\tau'_\nu-\tau_\nu}{\mu}},\ \text{for } \mu<0. \tag{5.21}$$

Herein I_ν denotes the specific intensity for $\mu > 0$ going toward the top surface and for $\mu < 0$ going toward the bottom surface of the slab. For the special case of $\mu = 0$ the formal solution is simply $I_\nu(\tau_\nu) = S_\nu(\tau_\nu)$. Calculating the first moment in μ of the above formal solution, we obtain the mean intensity as a function of S_ν:

$$J_\nu(\tau_\nu) = J^{BC}_\nu(\tau_\nu) + \frac{1}{2}\int_0^{\tau^*_\nu} d\tau'\, S_\nu(\tau')E_1(|\tau'-\tau_\nu|), \tag{5.22}$$

where J^{BC}_ν sums up the contributions by the intensities $I_\nu(0,\mu)$ and $I_\nu(\tau^*,\mu)$ at the boundaries of the slab and $E_1(x)$ is the first order exponential integral defined by:

$$E_n(x) \equiv \int_1^\infty dt\,\frac{e^{-xt}}{t^n}. \tag{5.23}$$

By convenience, we will drop any dependencies on τ_ν for all symbols to follow. The mean intensity can be synoptically expressed with the help of the so-called Λ-operator:

$$J_\nu = J^{BC}_\nu + \Lambda\left[S_\nu\right], \tag{5.24}$$

Herein, Λ is defined by the expression:

$$\Lambda[S_\nu] = \frac{1}{2}\int_0^{\tau^*_\nu} d\tau'\, E_1(|\tau'-\tau_\nu|)S_\nu(\tau'), \tag{5.25}$$

Both, the mean intensity J_ν and the source function S_ν are continuous functions defined along the vertical axis of the medium. However, for computational purposes, it is necessary to discretize them and the integral contained in the definition 5.25 of the Λ-operator becomes a quadrature sum:

$$J^d_\nu = J^{BC}_\nu + \sum_{d'}\Lambda^{dd'}_\nu S_{d'}. \tag{5.26}$$

Herein, d and d' denote indexes for the discretized optical depth. The above equation shows that the Λ-operator can be represented by a square matrix. The entries of the Λ-matrix depend on the source function S_ν that again is a function of the mean intensity J_ν to calculate. Therefore the Λ-operator must be obtained by an iterative method between S_ν and J_ν. In order to develop an iterative scheme for S_ν, we split up equation 5.19 into a sum of a J_ν-dependent and an independent part and combine it with equation 5.24:

$$S_\nu = (1-\epsilon_\nu)\Lambda_\nu\left[S_\nu\right] + (1-\epsilon_\nu)J_\nu^{BC} + \epsilon_\nu B_\nu^*. \tag{5.27}$$

Herein, we have defined the values $\epsilon_\nu = \frac{\kappa_\nu}{\kappa_\nu+\sigma_\nu}$ and $B_\nu^* = \frac{\eta_\nu}{\kappa_\nu}$. The above expression is a self-consistent equation for S_ν that, however, is very inconvenient to solve. It represents a set of differential equations to be solved simultaneously for all optical depths τ_ν and all directions μ considered, which quickly leads to unrealistic calculation times. Therefore, equation 5.27 is solved by the Λ-*iteration method*, which is classical in numerical analysis. It starts from the following representation of the Λ-operator (Cannon, 1973):

$$\Lambda_{\tau_\nu} = \tilde{\Lambda}_{\tau_\nu} + (\Lambda_{\tau_\nu} - \tilde{\Lambda}_{\tau_\nu}). \tag{5.28}$$

We denote by $\tilde{\Lambda}_\nu$ an approximate Λ_ν-operator that is easy to invert. The source function and the mean intensity of the current iteration is given by the symbol S_ν^n. Based on equations 5.27 and 5.28 we construct a value S_ν^{n+1} of the following iteration:

$$S_\nu^{n+1} = \left[1-(1-\epsilon_\nu)\tilde{\Lambda}_\nu\right]^{-1}\left[(1-\epsilon_\nu)(\Lambda-\tilde{\Lambda})\left[S_\nu^n\right] + (1-\epsilon_\nu)J_\nu^{BC} + \epsilon_\nu B_\nu^*\right], \tag{5.29}$$

where the expression $[...]^{-1}$ denotes operator inversion. In the code *TITAN* the operator $\tilde{\Lambda}_\nu$ is chosen as a diagonal matrix taking the elements on the diagonal of Λ_ν. This is justified by the fact that the kernel of the exponential integral $E_1(|\tau'-\tau|)$ peaks in a narrow range around τ. The computations are accelerated by the implementation of an algorithm extrapolating the source function of every fourth iteration based on the three preceding points (Ng, 1974).

Computing the line transfer

The basic difference between continuum and line transfer lies in the source function depending on the emission and absorption coefficients. The *TITAN* code solves the radiative transfer for the continuum as well as for $\sim$ 1000 lines in emission and absorption. The application of the ALI method for the lines is very similar to the calculations conducted for the continuum, with the exception that the emission and absorption coefficients η_ν and κ_ν are defined in a different way. In the spectral region of a line, the emission and absorption part of the source function contains both a continuum part S_ν^c and a line contribution S_ν^l. The whole source function reads as follows:

$$S_\nu = \frac{S_\nu^l\kappa_\nu^l\phi_\nu + S_\nu^c(\kappa_\nu^c+\sigma_\nu) + J_\nu^l\sigma_\nu}{\kappa_\nu^l\phi_\nu + \kappa_\nu^c + \sigma_\nu}. \tag{5.30}$$

Herein, all expressions with index c denote the continuum values, while the index l stands for the line. The line is described by a line profile ϕ_ν defined around the centroid. In *TITAN*, ϕ_ν is given by a Voigt-profile. The source function S_l contains the Einstein coefficients and the populations for the specific ion and transitions considered. Photo-absorption processes are considered as well as induced and spontaneous emission. Further details can be found in Coupé (2002).

The iterative scheme of the ALI method is then constructed analogously as for the continuum, as the source function in equation 5.30 can again be separated in a J_ν-dependent part and a part independent of it.

5.2.2 Physical state of the medium

Equation 5.29 depends on the emission, absorption and scattering properties of the medium. The coefficients η_ν, κ_ν, and σ_ν generally are a function of the level populations depending on the radiation field, hence on J_ν as computed from equation 5.24. Therefore, the coefficients have to be computed self-consistently with the radiation field using an iterative method. The ALI-algorithm is thus embedded into a global loop to calculate the properties of the medium. The code *TITAN* considers the following emission and absorption processes:

free-free-emission and absorption

free-bound-processes: radiative ionizations and recombinations, dielectronic recombinations, collisional ionizations and recombinations, charge transfer by H- and He-atoms, Auger effects

bound-bound processes: collisional excitation and relaxation, photo-excitation and relaxation, two-photon-processes

Thomson-scattering

Most of these interactions lead to an exchange of energy between radiation and matter, that can be summarized in net heating terms depending on the temperature T. For the free-free processes, the heating term $G_{ff}(T)$ and cooling term $P_{ff}(T)$ read:

$$G_{ff}(T) = 4.64 \times 10^{9} \sum_i \frac{N(X^i)i^2}{N_{tot}} \int_\nu J_\nu \frac{1 - e^{-\frac{h\nu}{kT}}}{\nu^3\sqrt{T}} g_{ff} d\nu, \tag{5.31}$$

$$P_{ff}(T) = -6.84 \times 10^{-38} \sum_i \frac{N(X^i)i^2}{N_{tot}} \int_\nu \frac{e^{-\frac{h\nu}{kT}}}{\sqrt{T}} g_{ff} d\nu, \tag{5.32}$$

where g_{ff} is the integrated Gaunt factor calculated by Karzas & Latter (1961), i denotes the charge of the ion X^i, and N stands for the density of the species indicated. For the free-bound processes the analogous formulae are:

$$G_{bf}(T) = \frac{4\pi}{N_e N_H} \int_\nu \kappa_{tot}(\nu) d\nu, \tag{5.33}$$

$$P_{bf}(T) = -\frac{4\pi}{N_e N_H} \int_\nu \eta_{tot}(\nu) d\nu, \tag{5.34}$$

with $\kappa_{tot}(\nu)$ and $\eta_{tot}(\nu)$ being the total absorption and emission coefficients at a given frequency. These values are computed from photoionization cross-sections and recombination coefficients, from the electron density, and from the density of all ions. Finally, the bound-bound processes have the following net energy balance:

$$P_{bb}^{net} = \sum_{lines} \left[N_2 A_{21} - (N_1 B_{12} - N_2 B_{21}) J_{12} \right] \frac{h\nu}{N_e N_H}, \tag{5.35}$$

which is a sum over all line transitions. The populations of the two levels for each transition are given by N_1 and N_2, J_{12} is the mean energy for the line, and A_{12}, B_{12}, and A_{21} denote the Einstein coefficients. The populations of the levels are calculated from balance equations, again assuming a stationary state between processes increasing and those decreasing the population. These equations consider the changes of the populations by the radiation-matter-interactions listed above.

For a stationary state, the sum of all heating processes, including the net Compton heating computed by *NOAR* (see section 5.3), is compensated by the sum of the cooling processes. Hence, the local temperature of the gas can be derived by summing up equations 5.31 —5.35 and setting this sum equal to zero.

5.2.3 Computational scheme of *TITAN*

Before launching the program, *TITAN* requires the definition of several input parameters, in particular the shape of the incident spectrum on both sides of the plane-parallel slab, the total incident flux F_{inc}, the number of angles μ to consider, and a Compton heating profile.

Assuming an initial value of the mean intensity J_ν and some boundary conditions, the iteration scheme starts with the computation of the temperature T in every layer of the medium, as outlined in section 5.2.2. This calculation can be performed under the condition of constant pressure throughout the medium. It is possible to put the condition of constant gas pressure only, or of constant total pressure, i.e. gas plus radiation pressure. If this option is not used, the code adopts a given density stratification defined by the user.

From the temperature, the depending coefficients η_ν, κ_ν, σ_ν, and the optical depth τ_ν are derived for all frequencies ν. Once these values are obtained throughout the medium, the radiative transfer is computed, according to what is presented in section 5.2.1, and a new value of J_ν is obtained. From here, the iteration scheme starts over until the initially chosen total number of iterations has been completed.

At the end, *TITAN* saves the final spectra obtained on both sides of the slab, the density and the ionization profile of the medium, and its temperature structure. The physical profiles of the medium can then be injected into *NOAR* to obtain a more accurate Compton heating profile for the next iteration between the two codes.

5.3 The Monte-Carlo code *NOAR*

The code *NOAR* is a Monte-Carlo radiative transfer code modeling X-ray spectra for energies between 0.8 keV and 500 keV. The code takes specific care of Compton scattering events. It follows individual photons through a medium in plane-parallel or shell geometry. The incident photons enter the medium at one side either at a given angle μ to the normal of the surface or in a semi-isotropic angular distribution. During their passage through the medium they generally undergo electron/Compton scattering, absorption, and re-emission events (see Fig. 5.2). The occurrence of particle interactions, scattering directions, and photon path-lengths, are ruled by Monte-Carlo routines.

The incident spectrum can be defined by a power-law $I(E) \propto E^{-\alpha}$ or it may have an arbitrary shape read from a file. Outgoing photons are captured on both sides of the medium forming a

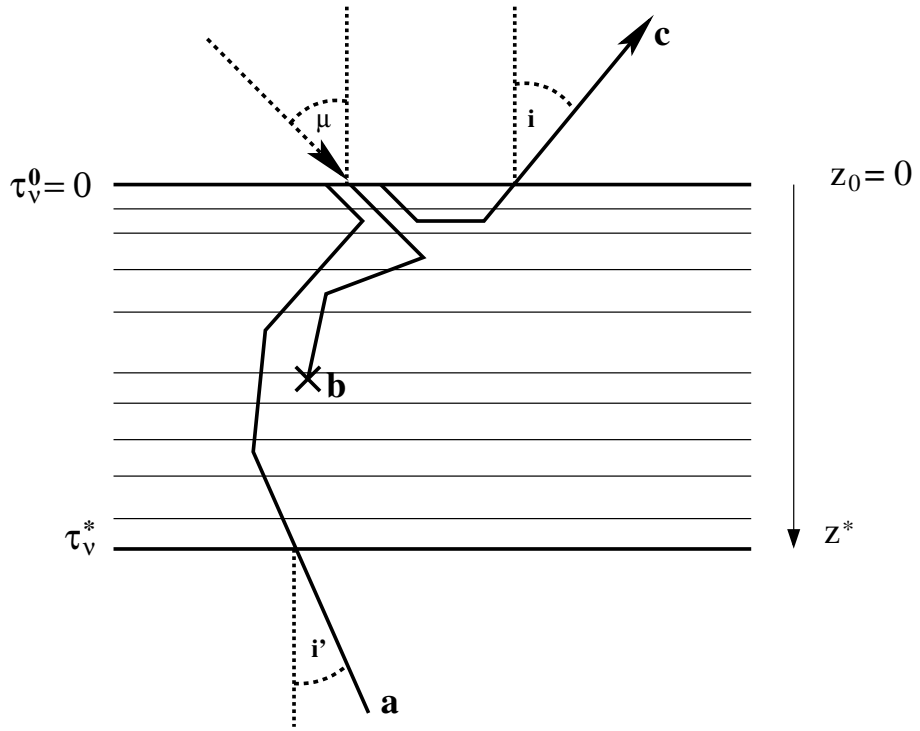

Figure 5.2: Illustration of three different photon trajectories during a run of the Monte-Carlo code *NOAR*. The photons are injected into the medium at a defined angle μ. Some of them are transmitted through the medium (a) after several scattering events, others are absorbed (b). A certain fraction of photons is "reflected" leaving the medium on the same side (c).

reflected/reprocessed spectrum and a transmitted component. The *NOAR* code requires definition of the vertical stratification in temperature, density, and ionization fraction for each species. These data are obtained by the *TITAN* code (see section 5.2).

The code traces the reflected and transmitted spectrum and calculates the vertical profile of the net energy transferred to the medium by Compton scattering events. The Compton heating structure is an important result to be used by the *TITAN* code.

In the following, we briefly recall the principle of the Monte-Carlo method (section 5.3.1) and its application to the physical processes considered in *NOAR* (section 5.3.2). Then, we briefly describe the necessary input data and the output produced by the code (section 5.3.3).

5.3.1 The Monte-Carlo method

Radiative transfer problems can be solved using the Monte-Carlo method, which works by sampling individual photons and following their path through a given model space. In order to determine the photon trajectory, path-lengths and scattering angles are sampled by "throwing the dice", hence using a random number generator on the given probability distribution $P(x)$ of a physical value x having a probability density $p(x)$:

$$r = P(x) = \int_0^x p(x')dx'. \tag{5.36}$$

Herein, r denotes a random number between 0 and 1 corresponding to the possible span of the physical value x. The monotonous probability distribution function $P(x)$ can be inverted to obtain a single value x:

$$x = P^{-1}(r). \tag{5.37}$$

In the following, we give an overview of the physical processes of *NOAR* that are based on the Monte-Carlo method and we present the sampling equations derived from equations 5.36 and 5.37. Random numbers are denoted by r_i.

5.3.2 Physical processes and photon transfer

The Monte-Carlo code *NOAR* follows single photons from their creation until they are absorbed or escape from the medium. While conducting a random walk through the model atmosphere, it is affected by the following physical processes and transfer methods.

Injection of a new photon

A newly created photon starts out at the surface of the medium and enters at a certain direction, defined by two angles θ and ϕ with respect to a regular Cartesian coordinate system. The initial position of the photon is at the center of this system.

In the spherical case, the initial direction is normal, because it is assumed, that the shell is irradiated by a compact source at the center. In the plane parallel case, the angle ϕ can be set arbitrarily for symmetry reasons:

$$\phi = 2\pi r_1. \tag{5.38}$$

If the incident radiation is defined at a specified angle θ_0, it directly follows $\theta = \theta_0$. Hence, the illumination of the slab happens by an infinitely thin cone with a fixed half-opening angle θ_0. However, it is also possible to define the incident radiation with a semi-isotropic distribution, which corresponds to a constant specific intensity at all incident directions. In this case the angle θ is sampled by:

$$\theta = \arccos(1 - 2r_2). \tag{5.39}$$

Sampling photon path lengths

If we ignore scattering back into the beam, the intensity of a photon beam traversing a slab of scattering material with particle number density n and extinction cross-section σ will drop by a factor $e^{n\sigma l}$, with l being the distance traveled inside the scattering region. The same factor therefore determines the probability density of a photon-particle interaction at the distance l. This leads to the sampling function:

$$l = \frac{1}{n\sigma} \ln(1 - r_3). \tag{5.40}$$

The factor $\frac{1}{n\sigma}$ denotes the mean free path length, calculated for each layer from the density and ionization profile given by *TITAN*. The extinction cross-section represents the sum of all absorption and scattering cross-sections involved. Aside from photoionization and Compton scattering, this includes a cross-section for free-free absorption.

After the photon was shifted by a path length and before conducting the next scattering event, it is necessary to check if the photon is still inside the scattering cloud. The geometry of the scattering region, either a plane-parallel slab or a spherical shell, is described by simple mathematical inequalities that are compared to the current photon position.

Sampling scattering angles

In *NOAR*, a photon can undergo two sorts of scattering events, "atomic scattering", which actually means absorption and re-emission of the photon, and Compton scattering. In the former case, the "scattering" is assumed to be isotropic and the new flight direction of the photon is derived by the sampling equations:

$$\theta = \arccos(1 - 2r_4), \tag{5.41}$$

$$\phi = 2\pi r_5. \tag{5.42}$$

In the case of Compton scattering, the scattering phase function is more complicated to compute. We assume a photon of energy $h\nu$ proceeding along an initial direction Ω_i. Then, the probability $p(h\nu, v, \Omega_i, \Omega_s)$ for this photon to be scattered off an electron of velocity v and to end up in the direction Ω_s is given by the following expression:

$$p(h\nu, v, \Omega_i, \Omega_s) = \frac{N(v)(1 - v\frac{\Omega_i}{c})\frac{d\sigma}{d\Omega_s}}{\int\int N(v)(1 - v\frac{\Omega_i}{c})\frac{d\sigma}{d\Omega'}d^3\Omega' d^3v}, \tag{5.43}$$

where $\frac{d\sigma}{d\Omega}$ denotes the differential cross-section for Compton scattering. The above formula assumes an isotropic velocity distribution $N(v)$ of the electrons. It can be integrated and inverted in order to deliver sampling equations for the scattering angles (Gorecki & Wilczewski, 1984). In *NOAR* a Maxwellian velocity distribution of the electrons, according to the local temperature of the medium is used.

The outgoing photon undergoes a shift in energy. The new energy $h\nu'$ is given by the usual Compton formula:

$$h\nu' = \frac{h\nu(1 - v\frac{\Omega_i}{c})}{1 - v\frac{\Omega_s}{c} + \frac{h\nu}{m_e c^2}\gamma(1 - \Omega_i\Omega_s)}, \tag{5.44}$$

with the electron mass m_e and the Lorentz-factor γ associated with the velocity v of the electron. The difference in energy $h\nu - h\nu'$ is added to the net Compton heating profile at the local position of the medium.

Absorption and emission by ions

The photon path length is sampled according to the total cross-section at a given location of the material. Following, from the populations and cross-sections for each ion considered, the random number generator decides which kind of interaction between photon and matter is to be considered.

In the case of Compton scattering, the photon is scattered and shifted in energy. If the photon is absorbed by an ion, there are several options:

Photo-ionization of the outer electron shell: In this case the photon is lost. However, for all hydrogen-like or helium-like ions, the Monte-Carlo cycle starts over by creating a new photon at the same position. This photon is assumed to be the result of a recombination event - the method corresponds to the on-the-spot-approximation stating, that at each location, a photoionization event is counter-balanced by an electron recombination. The recombining electron arrives at some energy level of the ion and then falls down the levels in a relaxation cascade. From this cascade, only the last transition to the fundamental level is considered for the re-emission of a new photon.

Photo-ionization of the inner electron shell: In the case of photo-ionization of a K-shell electron, the ion is brought into an unstable excited state. This state can relax by the Auger effect leading to a secondary ionization of the ion, or by fluorescent emission of a Kα-line photon.

$$X^i + h\nu \rightleftharpoons X^{i+1*} + e^- \rightleftharpoons \begin{cases} X^{i+2} + e^- + e^-, \\ X^{i+1} + e^- + h\nu_{K\alpha}. \end{cases} \tag{5.45}$$

Herein, X^i denotes an ion with charge i, the star stands for the excited unstable state. The initial photon energy $h\nu$ has to be large enough to exceed the ionization threshold of the strongly bound Kα photons. In the case of fluorescent emission by iron, also the Kβ-line lies in the X-ray range. Thus, in this case, *NOAR* also takes into account a third option:

$$Fe^i + h\nu \rightleftharpoons Fe^{i+1*} + e^- \rightleftharpoons Fe^{i+1} + e^- + h\nu_{K\beta}. \tag{5.46}$$

Recalling the specific fluorescence yields, the random number generator of *NOAR* decides, if the relaxation leads to the emission of a Kα- or Feβ-photon, which then is created at the same position. In the case of the Auger effect, the photon is lost and a complete new cycle starts.

Free-free processes

In *NOAR* a free-free contribution is considered for the calculation of the total extinction cross-section σ. For the spectra, free-free emission is neglected, because in the modeling cases we are interested in here, the bremsstrahlung spectrum already cuts off below 0.8 keV.

5.3.3 Input and output of *NOAR*

To launch *NOAR*, it is necessary to define basic model parameters, such as the shape of the incident spectrum, the angular distribution of the incident photons, and the total number of photons to be sampled. The density, temperature and ionization profiles of the medium are obtained from the preceding run of *TITAN*.

The code then samples a user-defined number of photons, injecting them into the medium. Photons escaping from the model region are "detected" on both sides of the slab. They are counted in different channels depending on their flight direction, so that the medium can be observed at several inclinations. The viewing angles are divided in equal steps of $\mu = \cos\theta$. Constant count rates in all angular channels, neglecting the usual Monte-Carlo fluctuations, hence correspond to semi-isotropically transmitted or reflected radiation.

5.4 Relativistic ray-tracing with *KY*

The ray-tracing code *KY* (Dovčiak, Karas & Yaqoob, 2004; Dovčiak, 2004) allows to compute relativistic effects induced by the curved space-time around a Schwarzschild or Kerr black hole. It requires the definition of the local emissivity across an accretion disk located in the equatorial plane of the black hole. The disk is supposed to be optically thick, geometrically thin, and in Keplerian motion. The *KY* code includes time-evolution effects, as the local emissivity can be defined as a time-dependent function. It then produces a series of spectra over a defined "observational" period. In the following, we briefly describe the physical concept of ray-tracing and its application in *KY*.

5.4.1 The transfer functions

Radiation coming from an accretion disk and traveling in the vicinity of a black hole is affected by several effects. Already the Keplerian motion of the disk induces a Doppler shift of photon energy; at the same time all photons are gravitationally redshifted. Light beams passing very close to the black hole undergo a significant lensing effect. Imagining the radiation as bundles of light rays, the lensing deforms the cross-section of such bundles, which changes the flux they represent. Furthermore, there is an aberration effect, since the photon trajectories are bent and hence the local emission angle generally differs from the viewing angle. Finally, the photon trajectories linking different regions of the accretion disk with a distant observer often differ in length. Furthermore, regions with different gravity have separate time scales. This causes a relativistic time-delay between events that in Euclidean space would coincide.

In order to account for these effects, individual transfer functions can be found. They rely on the analytical description of the photon trajectory that is obtained by integrating the 4-momentum vector p_e^α of the photon, starting in the equatorial plane and ending in infinity, where we assume the distant observer to be. The description of the photon momentum p_e^α in Kerr metric was given by Carter (1968). Integration of p_e^α over the coordinate time leads to the transfer functions we are going to present here. For further details we refer to Dovčiak (2004) and the extensive textbook of Misner et al. (1973).

For the following formulae, we adopt the convenient convention of $GM = c = 1$, where G is the gravitational constant, M is the black hole mass, and c is the speed of light. As usually done in relativistic calculations, summation signs are omitted and expressed by equal co-variant and contra-variant indexes (Einstein sum convention).

Photon energy shift: the g-factor

The so-called g-factor, combining the gravitational and Doppler shifts, is simply defined as the ratio between the photon energy $h\nu_e$ in the co-rotating frame of the disk element and the relativistically corrected energy $h\nu_o$ observed at infinity. It can be computed from:

$$g = \frac{h\nu_o}{h\nu_e} = \frac{p_{o\,0}}{p_{e\,\alpha} U^\alpha} = -\frac{1}{p_{e\,\alpha} U^\alpha}, \tag{5.47}$$

where U^α denotes the 4-velocity of the disk element considered, and $p_{o\,0}$ is the time-coordinate of the photon vector at infinity, which is equal to unity. Far away from the black hole, g approaches unity.

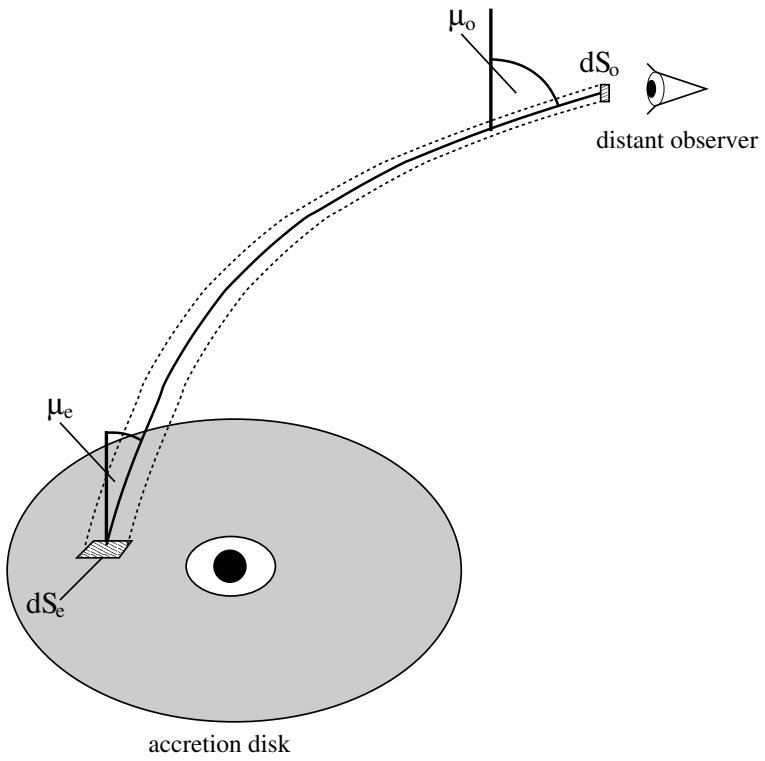

Figure 5.3: Illustration of the geometry assumed in *KY*. Photon trajectories connect a small region of the accretion disk with a distant observer. The local emission angle μ_e and the emitting region dS_e are transformed due to relativistic effects and result in μ_o and dS_o.

Aberration of the emission angle

The local emission angle μ_e, defined in the local co-rotating frame of the disk, measures the cosine of the angle between the outgoing direction of the photon trajectory and the normal of the disk surface. Following the bended trajectory, this angle is generally different from the distant viewing angle μ_o (see Fig. 5.3). For a given μ_o it is possible to trace back the original μ_e by the equation:

$$\mu_e = -\frac{p_{e\,\alpha} n^\alpha}{p_{e\,\alpha} U^\alpha} \tag{5.48}$$

Herein, n^α denotes the 4-vector of the disk normal that depends on the viewing angle μ_O. The aberration effect is strongest for light rays passing very closely to the black hole, and, in the case of a Kerr black hole, for large inclinations (edge-on view).

Gravitational lensing

Understanding the gravitational lensing becomes more clear, when we consider a small surface area dS oriented perpendicular to a given bundle of light-rays. Let dS_e, as defined at the emission point in the co-rotation frame of the disk, be a parallelogram subtended by the two 4-vectors dY_{e1} and dY_{e2}. Then the area of dS_e is given by the expression $\|dY_{e1}\|^2\|dY_{e2}\|^2 - < dY_{e1}, dY_{e2} >^2$. Herein, the magnitude of a 4-vector is denoted by $\|...\|$ and the scalar product of two 4-vectors by

$< ..., ... >$. Following the light-rays from their origin in the disk to the distant observer at infinity, dS_e is assumed to be deformed to the area of unity. The vectors dY_{e1} and dY_{e2} are transported along geodesics by the equation of geodesic deviation (see Fig. 5.3). For the ratio l of the surface elements dS_e and dS_o this leads to:

$$l = \frac{dS_o}{dS_e} = \frac{1}{\sqrt{\|dY_{e1}\|^2 \|dY_{e2}\|^2 - < dY_{e1}, dY_{e2} >^2}}, \tag{5.49}$$

and since the measured flux is proportional to dS_o the value l directly gives the change in flux due to gravitational lensing. Lensing becomes particularly important for emissivities located "behind" the black hole with respect to the observer. In such a situation the light-rays are focused toward the observer.

Relativistic time-delays

In order to compute time-delays between different emission regions of the accretion disk, we have to know the time Δt elapsing in the rest-frame of a distant observer, while radiation proceeds along a geodesic from its initial position in the disk to the observer at infinity. This delay is obtained by numerically integrating the time component of the photon 4-vector p_e^α.

The overall transfer function

We are interested in the time-dependent photon flux $\Delta N_o^\Omega(E, \Delta E, t)$, observed between energy E and $E + \Delta E$, and at the time t, coming from the entire accretion disk. Therefore, the individual transfer functions have to be evaluated across the disk and for all times t, with respect to the radiation ending up in the observer's direction. If we denote the viewing direction with Ω_o, we obtain the following relation for the observed flux:

$$\Delta N_o^{\Omega_o}(E, \Delta E, t) = \int_{r_{in}}^{r_{out}} dr \int_{\phi}^{\phi+\Delta\phi} d\phi \int_{E/g}^{(E+\Delta E)/g} dE_l N_l(E_l, r, \phi, \mu_e, t - \Delta t) g^2 l \mu_e r, \tag{5.50}$$

where $N_l(E_l, r, \phi, \mu_e, t - \Delta t)$ is the local photon flux, defined in the co-rotating frame of the disk at the position (r, ϕ) being usual 2D-polar coordinates. The expression $g^2 l \mu_e$ is usually called the *overall transfer function*. The values, r_{in} and r_{out} denote the inner and outer radius of the disk region to consider.

5.4.2 Computational scheme of *KY*

For practical reasons, the individual transfer functions are pre-calculated and stored in data tables. In order to launch *KY*, it is necessary to give a measure for the local emissivity over the whole disk. This can be done by calculating reprocessed spectra using *TITAN* and *NOAR* and implementing them into *KY*. Furthermore, a viewing direction has to be chosen in polar and azimuthal directions. If the emissivity of the disk is not isotropic, the azimuthal position has an impact on the "observed" spectra. Finally, the code needs a definition of the time period T_{obs} to consider. The main routine of *KY* integrates all photon trajectories connecting the disk with the user-defined viewing direction according to equation 5.50. This results in a time-series of spectra covering the period T_{obs}.

Chapter 6

Spectral modeling of X-ray flares

In this chapter, we perform detailed spectral modeling of the radiation we expect from a magnetic flare event occurring above the accretion disk of an AGN. Our particular interest is laid on the reprocessed component re-emitted by the accretion disk atmosphere. The flare is supposed to last shorter than the dynamical time-scale of the disk, so that the hydrostatic equilibrium of the disk atmosphere remains constant and only its thermal and radiative properties change (see chapter 4).

In a first step, we describe the method of our modeling starting out with the computation of the disk's density profile under the condition of hydrostatic balance (section 6.1). In this context, we present vertical density, temperature, and flux profiles of accretion disks at different radii and for several model configurations of AGN. These results for the structure of the disk atmosphere *before* the illumination by the flare serve as a basis for the following radiative transfer modeling of the reprocessed spectra.

We analyze the local spectrum as seen by a co-moving observer at the hot spot underneath the flare source (section 6.2). The spot is structured because the properties of the irradiating hard X-ray emission change with the distance from the spot-center. This structure leads to spectral differences for the reprocessed radiation coming from different positions inside the spot. We therefore conduct detailed radiative transfer simulations varying the input parameters with respect to the flare geometry across the spot. We show reprocessed spectra of hot spots for an accretion disk around a Schwarzschild black hole with a mass $M = 10^8 M_\odot$ and a disk accretion rate of $\dot{m}_{disk} = 0.001$, where $\dot{m}$ is expressed in units of the Eddington accretion rate (called Eddington units in the following). In this case, the irradiating flux of the flare largely dominates the local emission by the disk. We consider spectra coming from two disk radii, at $7\,R_g$ and at $18\,R_g$. The spectra are evaluated by measuring spectral flux ratios and by analyzing the equivalent width of the iron Kα-line. Integration over the hot spot leads to the total locally emitted spectrum, at different inclination angles.

For hot spots orbiting on the accretion disk at radii close to the black hole, relativistic effects and Doppler shifts due to the Keplerian motion of the spot become important. We take them into account in order to construct the spectrum seen by a distant observer (section 6.3). We investigate the effects on the reprocessed spectra with the help of a relativistic ray-tracing technique. Spectra are then evaluated for various phases of an orbiting spot. We then construct time-dependent spectral simulations for short-term flares assuming that a magnetic reconnection event creates a short-lasting hard X-ray source above the disk. The distance between the source and different positions of the underlying hot spot induces time-delay effects that can be taken into account by our ray-tracing technique. We construct light-curves and integrated spectra of such short-term flares.

Finally, we summarize and discuss our modeling results in section 6.4.

6.1 The vertical profile of the accretion disk

In a first step, we compute the vertical structure at a given radius R of a *non-irradiated* accretion disk. Compared to the expansion of the whole disk, we only consider a small, locally illuminated region. Therefore, we can approximate the disk atmosphere R by an infinitely wide, plane-parallel, vertically stratified slab. For such a slab, we compute the vertical structure in hydrostatic equilibrium using a modified version of the code described in Różańska & Czerny (1996) and Różańska (1999). Since for the radiative transfer we are going to include relativistic corrections, we also implement such corrections into the computation of the density structure. We describe these modifications in section 6.1.1. Then, we apply the code to several examples of accretion disks and compare the obtained vertical profiles (section 6.1.2). Thereby, we also make comparisons between calculations of the hydrostatic equilibrium with and without including the relativistic corrections.

6.1.1 Implementation of the relativistic corrections

For the disk radius at the center of the hot spot we compute the vertical density, temperature, and radiation flux profile within the accretion disk. The calculations using the code described in Różańska & Czerny (1996) and Różańska (1999) consider thermal emission inside an α-disk around a central black hole of mass M, dimensionless spin parameter a, and accretion rate $\dot{m}$. The radiative transfer in the medium is computed in the diffusion approximation and vertical energy transport by advection is also included. The hydrostatic balance of the medium is determined by the equilibrium between radiative and gas pressure on the one hand-side and the vertical component of the gravitational field in the vicinity of the black hole on the other (see chapter 5). In its most recent version, relativistic corrections based on the work of Novikov & Thorne (1973) and Page & Thorne (1974) have been added to the code. It was shown that the influence of general relativistic effects on the dynamics of a time-stable, axis-symmetric accretion disk around a Kerr black hole can be summarized in three correction functions depending on the disk radius. Following the notation of Krolik (1999), we call these functions $R_R(x)$, $R_T(x)$, and $R_Z(x)$, with $x = R/R_g$. For the equation describing the viscous heat produced at a given disk radius we then obtain:

$$F(r) = \frac{3G\dot{M}M}{8\pi r^3} R_R(x), \tag{6.1}$$

hence the factor $1 - \sqrt{x^{-1}}$ for the classical boundary condition at the inner edge of the disk is replaced by $R_R(x)$ (see equation 2.1). The second correction factor $R_T(x)$ enters in the equation for the conservation of the disk momentum:

$$\int dz T_{r\phi}(z) = -\frac{\dot{M}\Omega_K(r)}{2\pi} R_T(x). \tag{6.2}$$

Herein, the left side denotes the vertically integrated element $T_{r\phi}$ of the stress-tensor, $\dot{M}$ is the mass accretion rate, and Ω_K denotes the non-relativistic Keplerian orbital frequency. Finally, the last correction factor affects the equation for the vertical component of the black hole's gravity field:

$$g_z = -\frac{GMz}{r^3} R_z(x). \tag{6.3}$$

In Fig. 6.1, we plot the three correction factors as a function of the normalized disk radius x for the Schwarzschild metric and for the case of a Kerr black hole with maximum spin.

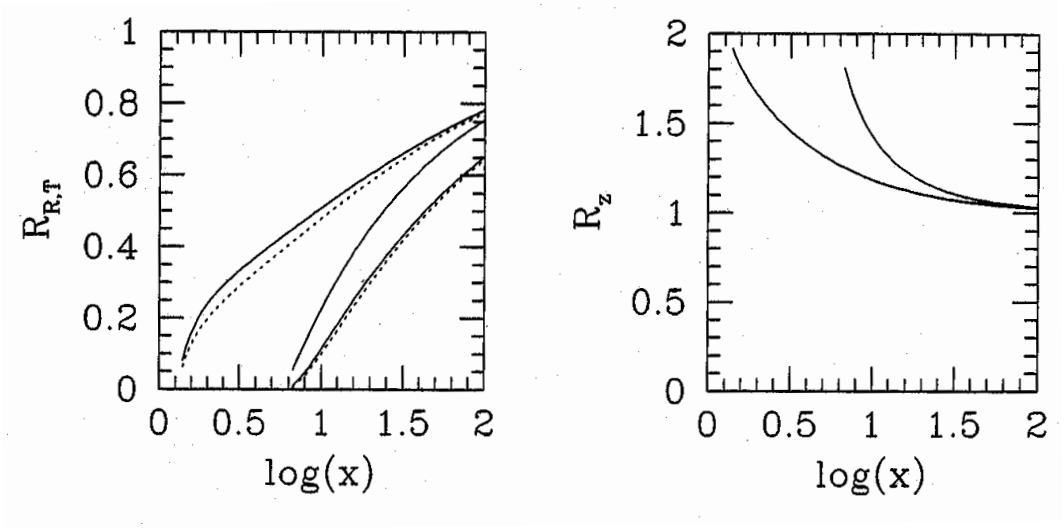

Figure 6.1: The three general relativistic correction factors as a function of the normalized radius x. The left panel shows the factors $R_r(x)$ (solid curves) and $R_T(x)$ (dotted curves). The solid curve in the middle shows the Keplerian value $R_K(x) = 1 - \sqrt{x^{-1}}$ with the marginally stable orbit at $x_{ms} = 6$. The curves extending to $x = 1.24$ are for a black hole with $a = 0.998$, those stopping at $x = 6$ are for Schwarzschild black holes. The right panel shows $R_z(x)$ again for a Schwarzschild and for a Kerr black hole (Krolik, 1999).

6.1.2 Results for the vertical disk profile

We present results for the vertical profile of an accretion disk in hydrostatic equilibrium *before* the illumination of the flare. The computations are carried out with a value of $\alpha = 0.1$ for the viscosity parameter. The opacity $\kappa = 0.343$ cm^2/g represents the Thomson opacity for a completely ionized medium with solar abundances, and the transformation efficiency is set to $\eta = 1/12$ as widely used in the literature. In Fig. 6.2 we show the density, temperature, and flux distributions at several distances of an accretion disk with $\dot{m} = 0.02$ around a black hole with $M = 10^8 M_\odot$. We consider a Schwarzschild metric with the relativistic corrections for the hydrostatic balance turned off (a), the same black hole with the relativistic effects turned on (b), and the relativistic results for a Kerr black hole with the maximum spin parameter $a = 0.998$ (c).

For all cases, the density profiles rise toward higher depths within the medium. Partly, this can be explained by the barometric effect, which is also known from the earth's atmosphere. The deeper the layer of the medium considered, the heavier the column of material above, which leads to a higher density. However, the analogy is more complex for the accretion disk around a black hole, as the vertical gravitational force decreases toward the equatorial plane. Besides, at small disk radii viscous heating and radiative pressure effects have an important impact on the hydrostatic equilibrium of the medium.

The density profiles change almost regularly with the distance from the black hole. The smaller the radius considered, the higher the density values. Only at higher depths of the medium the behavior of the density profile seems to be slightly more complex. For a given case (a), (b), or (c) of Fig. 6.2, the overall shape of the density profile is similar at different disk radii. From the limiting z-values of the density curves one can tell that the total height of the atmosphere depends on the

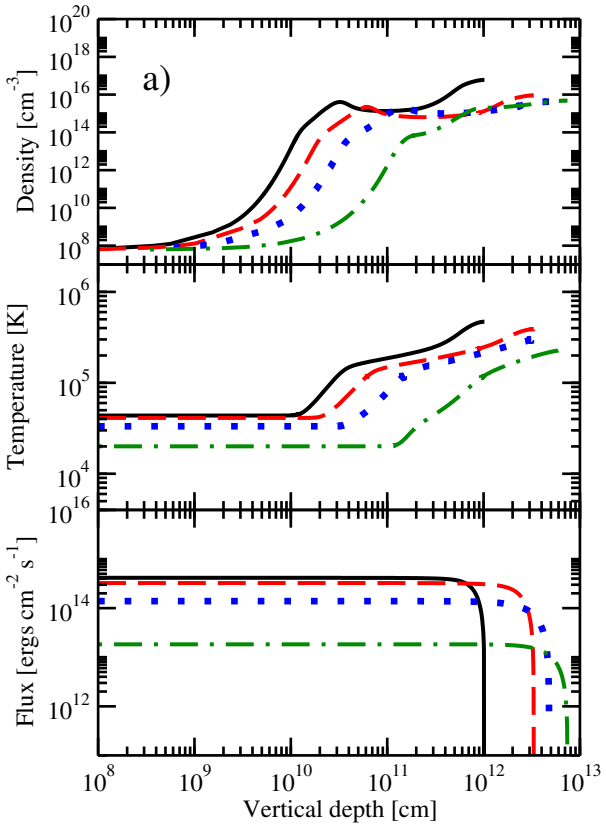

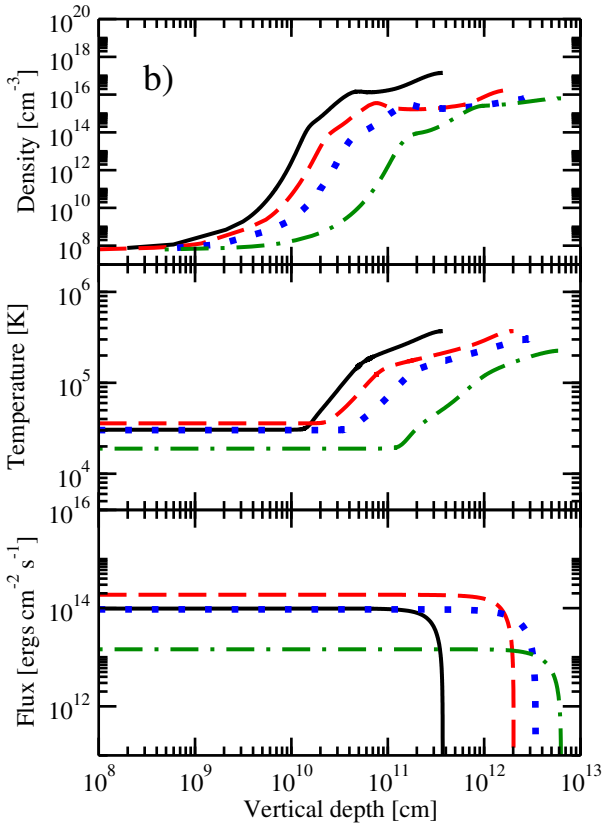

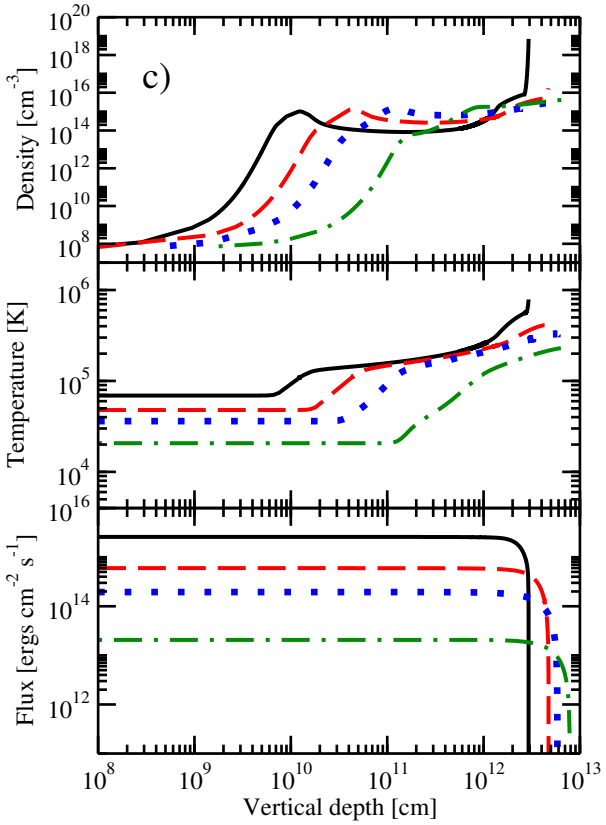

Figure 6.2: The vertical density, temperature, and flux profiles of an accretion disk around a black hole with a mass of $10^8 M_\odot$. The two top figures represent results for an accretion rate of $\dot{m}_{disk} = 0.02$ Eddington units and a spin parameter $a = 0$ with the relativistic effects turned off (a) and on (b). The bottom figure shows results for the same setup but with $a = 0.998$ (c). The various curves denote different disk radii: $7\,R_g$ (black, solid), $12\,R_g$ (red, dashes), $18\,R_g$ (blue, dots), and $40\,R_g$ (green, dashes/dots).

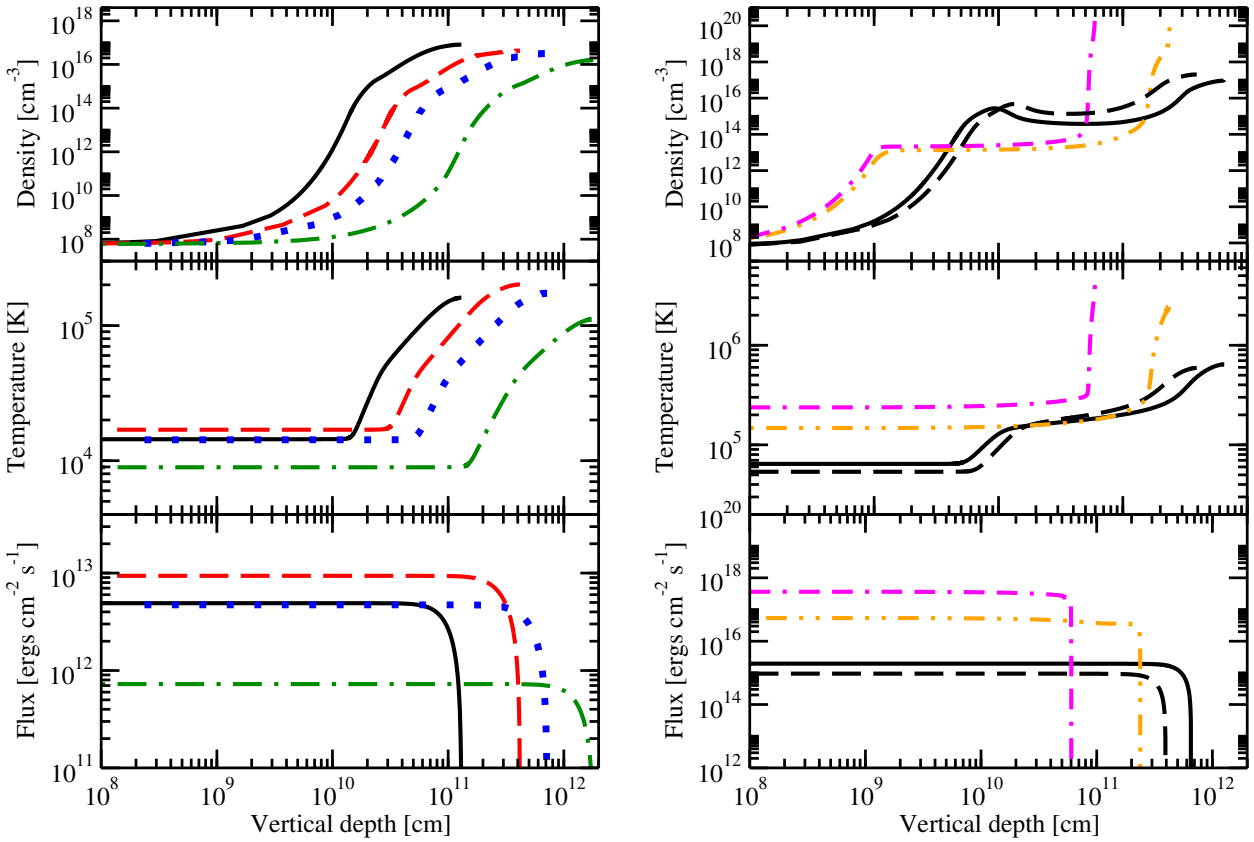

Figure 6.3: Left graph: plots of the vertical density, temperature, and flux profile of an accretion disk around a non-rotating black hole with a mass of $10^8 M_\odot$ and an accretion rate of $\dot{m} = 0.001$ Eddington units. The various curves denote different disk radii: $7\,R_g$ (black, solid), $12\,R_g$ (red, dashes), $18\,R_g$ (blue, dots), and $40\,R_g$ (green dashes/dots). Right graph: Similar curves for a maximally rotating black hole with $a = 0.998$, $M = 10^7 M_\odot$, and an accretion rate of $\dot{m} = 0.02$. Here the different curves represent the disk radii of $18\,R_g$ (black, solid), $6\,R_g$ (orange, dashes/double-dots), and $3\,R_g$ (magenta, dots/double-dashes). In addition to that, the non-relativistic profiles are plotted for comparison (black, dashes).

disk radius considered. The height rises from inner to outer disk radii, hence, under the condition of no external illumination, the disk has a "flared" shape.

The temperature profiles remain flat in the upper part of the disk atmosphere. They rapidly rise toward the equatorial plane, after reaching a turning-point, which varies regularly with R. The flux profiles remain constant along the whole vertical depth and only drop sharply close to the equatorial plane, where the boundary condition of a zero net flux is imposed. The regular dependence of the density profiles with the disk radius is generally not the same for the temperature and flux curves. The zero-torque boundary condition at the marginally stable orbit induces a drop of the viscous heating at small radii, which reduces the net flux and the temperature. The position of this drop varies with the relativistic corrections. In our examples it can be seen in the case (b) of a Schwarzschild black hole, that flux and temperature values at $7Rg$ are smaller than those at $12R_g$, while for the Kerr black hole of case (c) these distances are still too far away from the marginal

stable orbit to show the drop of the viscous heating.

In Fig. 6.3 (left), we present the density, temperature, and flux profiles for the case of a Schwarzschild black hole with $M = 10^8 M_\odot$ and an Eddington accretion rate of $\dot{m}_{disk} = 0.001$. Comparing Fig. 6.3 (left) with the equivalent case of a higher accretion rate shown in Fig. 6.2 (right) reveals a similar behavior of all profiles. The main difference between the two cases is given by the total thickness of the disk, which increases with the accretion rate.

In Fig. 6.3 (right) we show the vertical profiles for a Kerr black hole of maximum spin with $M = 10^7 M_\odot$ and $\dot{m}_{disk} = 0.02$. We also plot the profiles for a Schwarzschild black hole at $18\,R_g$ for comparison. One can tell that at $18\,R_g$ the influence of the black hole spin is of a minor importance. However, for a Kerr black hole with maximum spin, the profiles change significantly as one considers smaller radii. At $3\,R_g$ the emerging flux at the disk surface is more than 100 times higher than at $18\,R_g$ while the total thickness of the disk is by a factor of 10 lower.

6.2 The local properties of the reprocessed spectra

We want to explore local tendencies for the spectral shape and its changes during the appearance of a flare event. In our approach, we focus on the reprocessed component coming from the α-disk after the flare source has been switched on. The hydrostatic equilibrium of the disk is computed for the spot center as shown in the previous section 6.1. We do not expect it to vary significantly across the spot, since we choose a flare height of only $h = 0.5\,R_g$, which leads to a relatively small spot radius as shown in section 6.2.1.

The reprocessed spectra of the consecutive concentric spot-rings depend on the incident X-ray flux F_{inc} coming from the flare source and on the flux F_{disk} emerging from the underlying disk. We choose a normalizing value F_0 at the spot center in such a way so that the integrated incident flux over the whole spot F_{inc}^{tot} gives a fixed ratio to the disk flux F_{disk}. We set $F_{inc}^{tot}/F_{disk} = 144$. This ratio assures that the incident radiation by the flare is much stronger than the disk emission. The incident flux from the source arriving at a given spot-ring decreases with the third power of $\cos\theta$ as shown in section 6.2.1. Herein, θ denotes the incident angle of the X-rays with respect to the disk's normal.

We consider a Schwarzschild black hole, with the mass $M = 10^8 M_\odot$ accreting with an accretion rate of $\dot{m} = 0.001$ Eddington units. The surrounding α-disk is considered at two radii, $7\,R_g$ and $18\,R_g$. Following the argument of Collin et al. (2003) mentioned in chapter 4, we assume that the dynamical time-scale of the atmosphere is significantly longer than its thermal time-scale, so that the onset of the flare radiation does not immediately change the density structure of the disk. Thus, an initial solution for the hydrostatic equilibrium, calculated for a *non-irradiated* accretion disk atmosphere at radius R (see section 6.1) remains valid for the whole flare period. The assumed vertical density profiles of the accretion disk for our modeling cases are shown in Fig. 6.3 (left).

6.2.1 Geometrical aspects of magnetic flares

We imagine a magnetic reconnection event above the accretion disk producing a compact blob of hot plasma, which emits hard X-ray radiation. Let this flare source be located at a height h above the accretion disk and illuminate the disk surface (see Fig. 6.4). Since we assume isotropic emission, half of the primary radiation coming from the source will reach the disk surface. However, the main fraction of the flux is reprocessed directly underneath the flare source because radiation emitted further sideways reaches the disk far away and thus becomes geometrically diluted. Hence, the hot

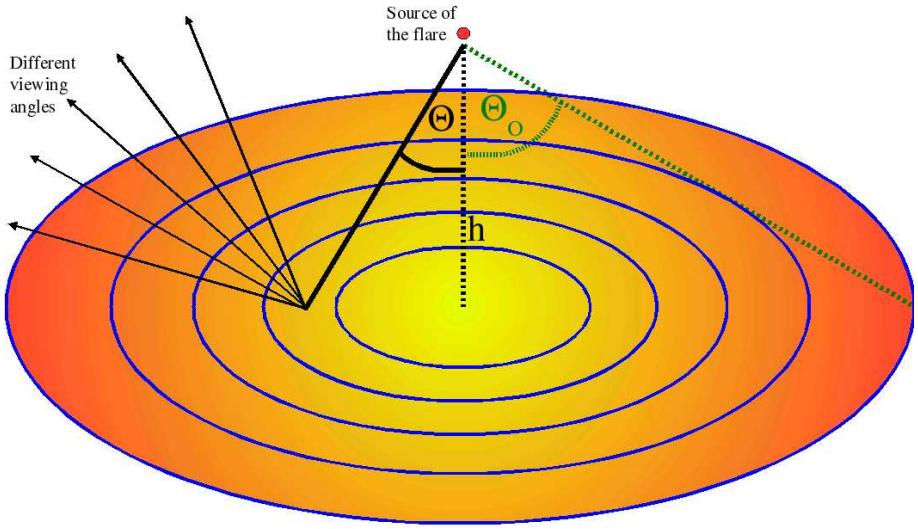

Figure 6.4: Illustration of the hot spot at the disk surface underlying the flare. The illuminated region is divided into concentric rings of equally intercepted fractions of the flare luminosity. Each spot ring corresponds to a different incident angle θ of the hard X-ray radiation. For the outer rings the flare source is farther away and hence the illuminating flux is lower than for the inner rings. The spot is limited by the flare half-opening angle $\theta_0 = 60°$. The reprocessed spectra can be evaluated at various emission angles ψ.

spot is defined with a finite radius and centered on the point directly underneath the flare source. The hot spot and the point-like flare source define a limiting cone of half-opening angle θ_0. In the following, we assume that all the radiation is reprocessed inside this cone and we neglect the disk irradiation outside the hot spot. The distance R of the flare from the central black hole is measured for the spot center. The density and temperature profiles we calculate for the hydrostatic balance are valid only for this specific distance from the center of the disk. In order to have a sufficiently good approximation for the radiative transfer, we therefore limit the half-opening angle of the flare cone to $\theta_0 = 60°$ and the height h of the source above the disk to $h = 0.5R_g$. We thus obtain a small spot radius of $h \tan\theta_0 \sim 0.866\, R_g$, hence the vertical disk structure across the spot should not change significantly and can be approximated by the solution obtained for the spot center.

In the previous flare modeling carried out by Collin et al. (2003) and described in chapter 4 the spot irradiation was assumed to have a semi-isotropic angular dependence. Here, we add some sophistication to the model by taking into account that the hot spot is structured due to the flare geometry. From Fig. 6.4 it becomes clear that the properties of the incident radiation change with the position inside the hot spot. As one moves away from the spot center, the incident angle of the radiation reaching the disk becomes larger, while the irradiating flux becomes lower due to the larger distance from the source and by projection onto the inclined surface. We divide the spot into five concentric rings (see Fig. 6.4). Within each ring, the incident angle of the hard X-ray illumination and the irradiating flux are approximately constant. It is convenient to parametrize the rings not with their radial distance from the projected position of the flare but with the cosine $\mu = \cos\theta$ of the incident angle θ of irradiating flux.

It is not necessary to perform radiative transfer computations for the whole vertical disk structure

because the principal spectral features are produced within a few Thomson depths of the disk surface. We hence limit our radiative transfer calculations to the disk surface layer, defined down to a Thomson optical depth of 7, and we assume that this layer is heated from underneath by the black body radiation of an underlying disk that we define by its black body temperature T_{disk} and the emerging total flux F_{disk}. These values are read from the temperature and flux profiles computed as described in section 6.1.2.

The primary radiation is modeled as a power-law spectrum with the photon index $\Gamma = 1.9$, extending from 0.001 keV to 100 keV. The external illumination of each spot ring is then determined by the incident angles, parametrized by their cosine values μ_i, and by the ionization parameters ξ_i. These values are connected to the X-ray luminosity L_{flare} of the flare by the relation:

$$\xi = \frac{L_{flare}\,\mu_i^3}{nh^2}, \tag{6.4}$$

as derived from the geometry shown in Fig. 6.4. In the above equation n denotes the surface number density of the disk that can be obtained from the density profiles computed before. The reflected spectrum of each ring is computed accurately by solving the radiative transfer locally. The computations are performed with the coupled use of the codes *TITAN* and *NOAR* (Dumont et al., 2000, 2003) as described in chapter 5. The resulting spectra can be evaluated separately at different emission angles ψ, i.e. local viewing angles, varying in constant steps of $\cos\psi$.

The total spectrum of one spot, as it would be seen by a local observer, is obtained by integration over the rings. Due to their adopted parametrization, the integration actually reduces to a simple summation of the contributions from all rings.

6.2.2 Temperature structure of the medium

In Fig. 6.5 (top graph) we show the vertical temperature structure underneath the five concentric rings forming a hot spot at $7\,R_g$ (left) and $18\,R_g$ (right) *after* the onset of the flare. The profiles are plotted as a function of the optical depth τ increasing toward the equatorial plane of the disk. The overall response of the irradiated material to the incident flux confirms results that were shown before (see chapter 4). A hot layer forms at the top of the disk atmosphere followed by a rapid transition to a colder, less ionized medium. However, considering also the horizontal structure of the irradiation, the individual temperature profile at each ring shows the dependence on the varying ionization parameter. At the spot center the temperatures are higher and the less ionized layers lie deeper in the medium.

For a given spot-ring, the temperature profiles at $7\,R_g$ and at $18\,R_g$ are about at the same level. This can be understood from the corresponding vertical disk structure presented in section 6.1 and from the fact that the ratio of F_{inc} to F_{disk} is defined equally at both distances. For a Schwarzschild black hole, the density, temperature, and flux profiles at $7\,R_g$ and $18\,R_g$ *before* illumination already are roughly at the same level (see Fig. 6.3, left). Thus, the incident radiation F_{inc} is of the same order at both distances and also the temperature profiles *after* the onset of the flare have a similar normalization.

6.2.3 The reprocessed emission across the hot spot

In the following, we analyze the obtained reprocessed spectra and their dependencies on the position in the spot and on the emission angles in more detail. In Fig. 6.5 (bottom graph) we show local reprocessed spectra emitted from concentric rings covering the spot surface for a distance to the

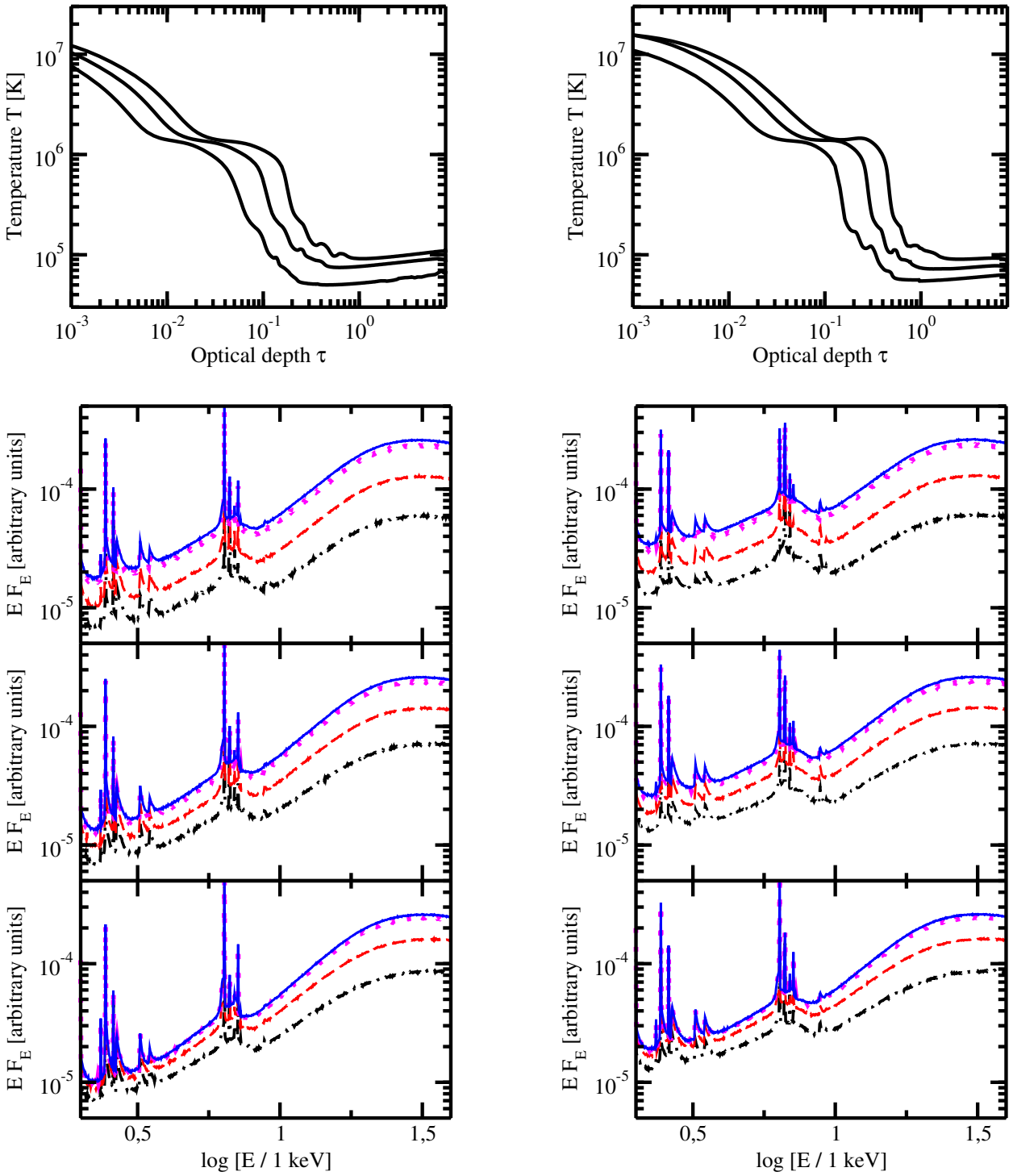

Figure 6.5: The top graph shows the vertical temperature profiles for three concentric rings of the hot spot. They correspond to incident angles of $\theta = 18°$ (top curves), $\theta = 41°$ (middle curves), and $\theta = 57°$ (bottom curves). In the same order, the three panels of the bottom graph show the corresponding local reprocessed spectra at four different emission angles: $\psi = 10°$ (blue, solid), $\psi = 30°$ (magenta, dots), $\psi = 60°$ (red, dashes), and $\psi = 80°$ (black, dashes/dots). The angles θ_0 and ψ are measured to the disk normal. Results for a spot at the distance $R = 7\,R_g$ (left) and $R = 18\,R_g$ (right) are presented.

black hole of $7\,R_g$ (left) and $18\,R_g$ (right) respectively. The three panels refer to different radial positions inside the spot, presenting results for the inner, for an intermediate, and for the outer ring. The four flux spectra of each panel correspond to different emission angles ψ. For a local observer, they represent a range from a nearly face-on view at $\psi = 10°$ to a nearly edge-on view at $\psi = 80°$. Between different emission angles, the spectra reveal different slopes and proportions. At both distances from the black hole, the Compton hump over 10 keV —60 keV is similar for all rings at the two lower emission angles at $\psi = 10°$ and $\psi = 30°$, which correspond to a type-1 view of an AGN. The bump splits up to different levels and the spectral slope becomes flatter as one goes toward edge-on viewing directions. The overall normalization of the spectra in Fig. 6.5 (bottom graph) levels down as ψ rises.

The continuum

The dependencies on the local viewing angles are analogous for both distances from the black hole. We investigate them in more detail by considering the spectral intensity in narrow energy bands at 4 keV and 28 keV and by computing the intensity ratio for each of the five spot rings at both distances from the black hole. The spectral intensity can be obtained from the flux spectra simply by dividing them by $\cos\psi$. The results are plotted as a function of the local inclination angle in Fig. 6.6.

From the spectral intensities one can derive a *limb-brightening effect*. Practically all spectra have a rising tendency toward larger local viewing angles. Only for the spot center at $18\,R_g$ the intensity at 28 keV goes slightly down toward higher emission angles. This effect can be understood from the vertical temperature structure of the plane-parallel medium (see Fig. 6.5, top graph) observed at different inclinations ψ. We illustrate the situation in Fig. 6.7. The upper layers of the disk surface are very hot, therefore highly ionized, and optically thin. A local observer looking at the medium at a normal direction $\psi \sim 0°$ can see down to the deeper, less ionized layers, because along his line-of-sight the temperature drops significantly within $\tau = 1$. However, a local observer looking at the same medium from a higher inclination $\psi \sim 60°$ rather sees the highly ionized surface layers dominated by electron scattering and exhibiting less absorption. Along his line-of-sight the extinction within $\tau = 1$ is dominated by scattering and thus more intensity is preserved than for the observer at low inclinations.

For the intensities at 28 keV, absorption is less important because the photon energies largely exceed the ionization thresholds. Therefore, at low emission angles, the intensity curves in the middle panels of Fig. 6.5 are very similar. However, they diverge at higher inclinations with the intensities from the outer rings being higher than for the spot center. This effect can be understood from the Compton scattering phase function. As the top layers of the atmosphere are highly ionized, the incident photons are likely to undergo Compton interactions largely favoring forward scattering of the radiation. Hence, an electron entering the medium at the spot center ($\theta = 0°$) is likely to proceed in the same direction until reaching the deeper, colder layers where it can become absorbed. Photons entering the medium at higher angles θ are likely to remain closer to the surface and thus they have a higher probability to escape.

The intensity ratios show that the *spectra become harder at lower inclinations*, i.e. when the emission direction is close to the normal of the spot surface. This behavior varies quantitatively with the location in the spot considered. In the spot-center, for $\cos\theta = 0.95$, the irradiating flux is strongest and the softest spectra appear. This is true for all possible emission angles. The matter can be understood by the relatively thicker high-temperature layer at the disk surface (see Fig.6.5,

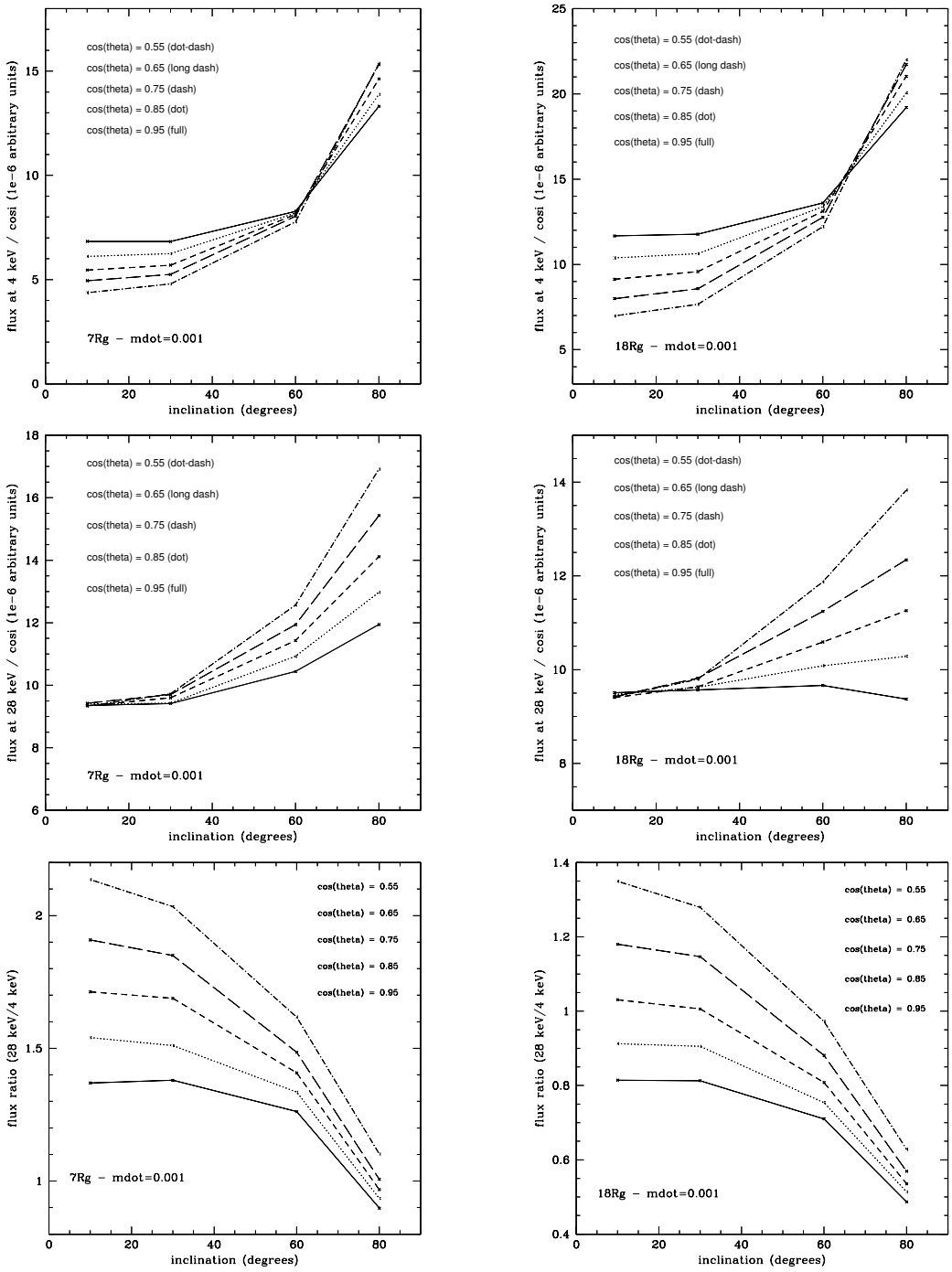

Figure 6.6: Spectral intensities at 4 keV (top) and 28 keV (middle) and their ratio (bottom) as a function of the local viewing angle ψ (inclination) for a hot spot at $7R_g$ (left) and at $18\,R_g$ (right). The five curves denote the consecutive concentric rings forming the hot spot. They are parametrized by the cosine of the incident angle θ of the illuminating primary radiation. The angles θ and ψ are measured to the disk normal.

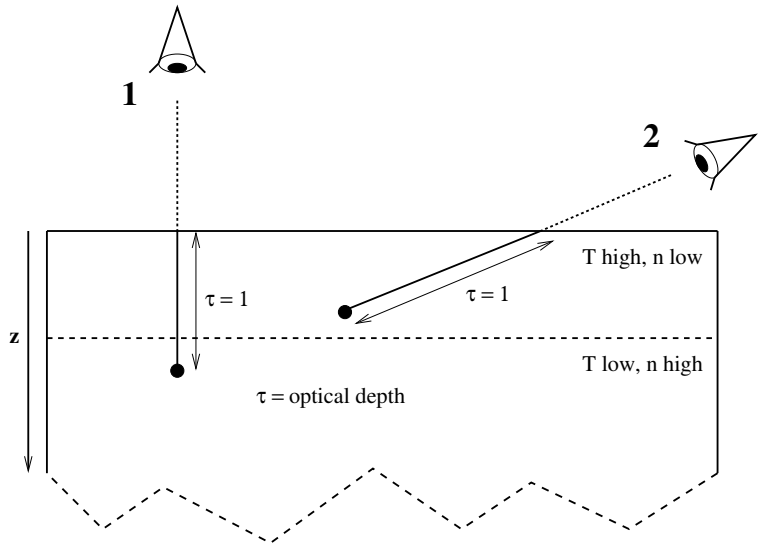

Figure 6.7: Stratified plane-parallel slab seen at two different local viewing angles. The medium is separated into a hot, dilute surface layer and an underlying colder, denser layer. Observer 1 can see the low-temperature medium and the extinction on his line-of-sight contains a significant absorption component. Observer 2 rather sees the high-temperature surface layer; along his line-of-sight, scattering is dominating.

top graph). At the spot center, less photons reach the deeper, colder medium to be absorbed. Thus the probability of escaping from the atmosphere after a few electron scattering events is higher and so the soft X-ray part is less absorbed as it is the case at the rim of the spot. This is confirmed by the behavior of the intensities at 4 keV (see Fig.6.6). At the spot rim the irradiating flux is weaker, the medium therefore cooler and more efficient for absorption.

The iron fluorescence complex

Effects due to the emission angle and the position in the spot can also be derived from the spectral appearance of the iron Kα-line complex that we investigate in Fig. 6.8. This figure presents a zoom of Fig. 6.5 (bottom graph) onto the region between 1 keV and 12 keV. For clarity, the spectra of different inclinations contain a vertical offset. Several components of the line complex are visible for all rings and inclinations shown: the component at 6.4 keV of weaker ionization states of iron, the helium-like iron Kα-line at 6.7 keV, and sometimes even the hydrogen-like iron Kα-line at 6.9 keV. A Kβ-line at 7.1 keV of weakly ionized iron is also visible if the Kα line at 6.4 keV is strong.

The different components of the iron-line complex vary strongly with the inclination. For a given spot-ring the lines seen at high inclinations denote more strongly ionized iron than those seen toward a face-on view. Again, the effect is analogous for both distances from the black hole and can be understood from the temperature and ionization structure of the medium and from the geometry (see Fig. 6.7). Since the temperature drops with increasing vertical depth, the highest ionization states of iron are found closer to the surface.

In order to quantify the behavior of the iron emission line complex as a function of the position in the spot and of the inclination, we investigate the equivalent width (EW) of the line. Therefore we

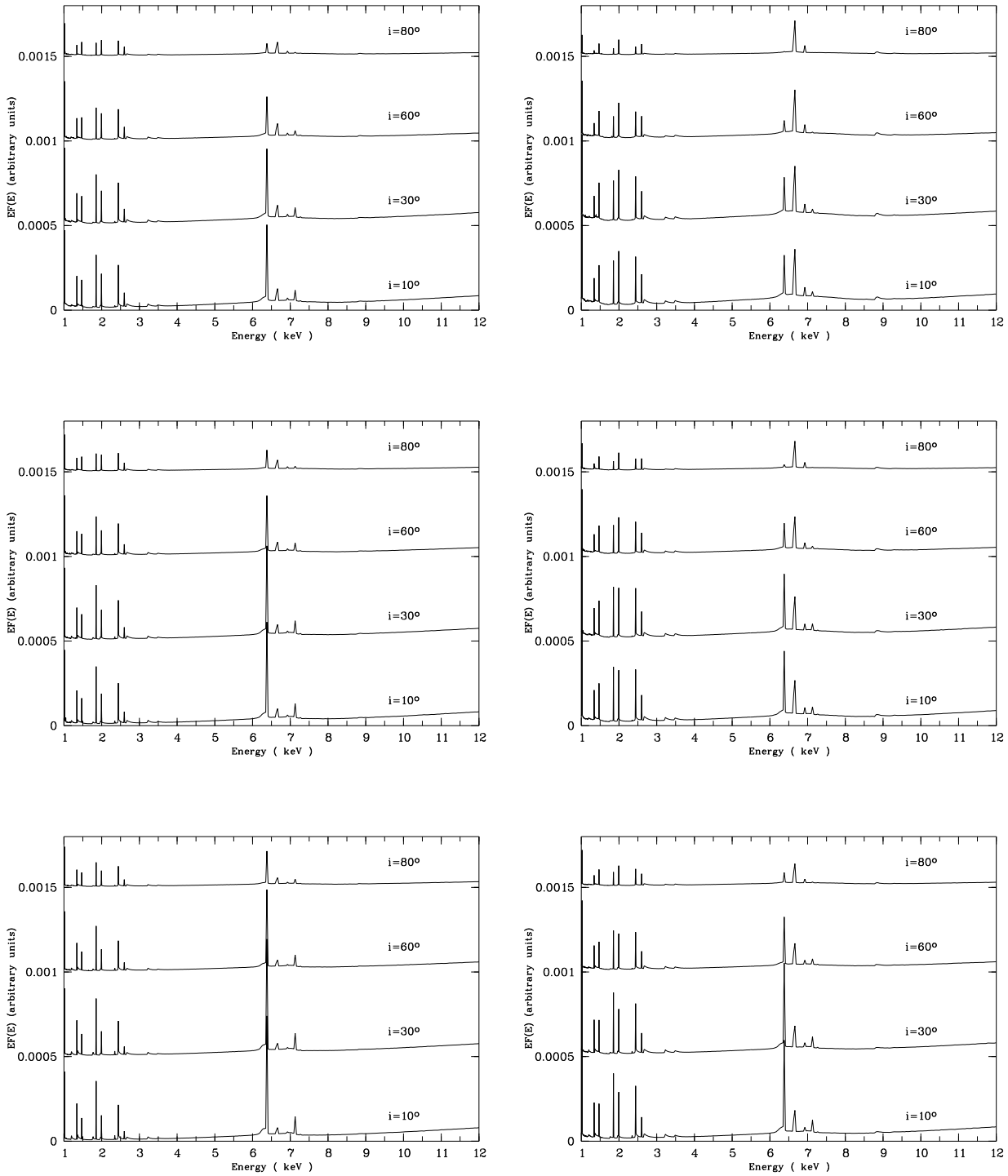

Figure 6.8: Zoom of the spectra shown in Fig. 6.5 (bottom graph) on the region of the iron Kα-line. From top to bottom the panels correspond to incident angles of $\theta = 18°$ (top), $\theta = 41°$ (middle), and $\theta = 57°$ (bottom). Each panel shows curves at four different viewing directions ψ as indicated (inclination). The angles θ and ψ are measured to the disk normal. Results for a spot at the distance $r = 7\,R_g$ (left) and $r = 18\,R_g$ (right) are shown. For clarity the spectra of different inclinations contain a vertical offset.

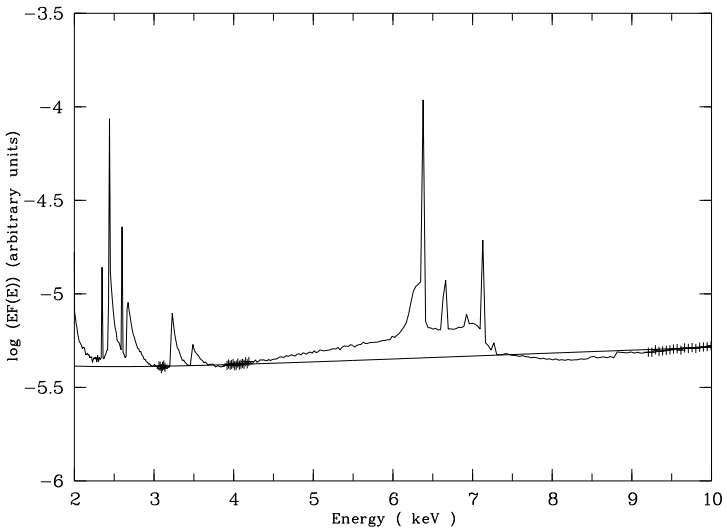

Figure 6.9: Illustration of our measurements for the equivalent width of the Kα-line. The underlying continuum is fixed at three featureless bands and approximated by a parabolic function.

define a continuum at three different locations between 3 keV and 10 keV avoiding other emission and absorption features. The continuum is then approximated by a parabolic function, as we illustrate in Fig. 6.9, and the EWs are computed assuming that the line flux is the whole flux above the continuum in this region. In Fig. 6.10 we show the resulting EWs for each spot ring as a function of the inclination angle for both distances of $7\,R_g$ and $18\,R_g$ from the black hole. The dependence of the EWs on the inclination varies systematically with the spot-ring considered. For the spot center the EW of the Kα-line rises toward higher (edge-on) inclinations, while at the spot rim the tendency is reversed. At intermediate positions inside the spot, the relation between the EW and the inclination depends on the distance of the spot from the central black hole.

All values of the EW measured are higher than 1 keV - which is significantly higher than the usually observed values. One reason for this is given by the fact that we only consider the pure reprocessed radiation and we leave aside any dilution by the primary component. Furthermore, we expect strong lines with respect to the continuum, because in our model relatively cold disk matter of roughly 10^5 K is irradiated by hard X-rays corresponding to a temperature of 10^7 K —10^8 K. Since we consider the medium only for a short instance assuming that the flare duration is significantly shorter than the dynamical time-scale, the density structure does not change. For longer flare durations, the medium must expand, as we show in Czerny & Goosmann (2004), and obtain a lower density leading to weaker line emission (Collin et al., 2003).

6.2.4 Integrated spectra of a whole spot

For magnetic flares close to the black hole, it is important to take the structure of the hot spot into consideration. as the modifications due to general relativistic effects affect different parts of the spot in a different way. However, if the spot is located farther away from the disk center, the relativistic modifications generally play a minor role and the observed spectrum can be constructed as a simple integration of the individual ring-spectra.

Due to the parametrization of the rings chosen, the integration is equivalent to a simple sum-

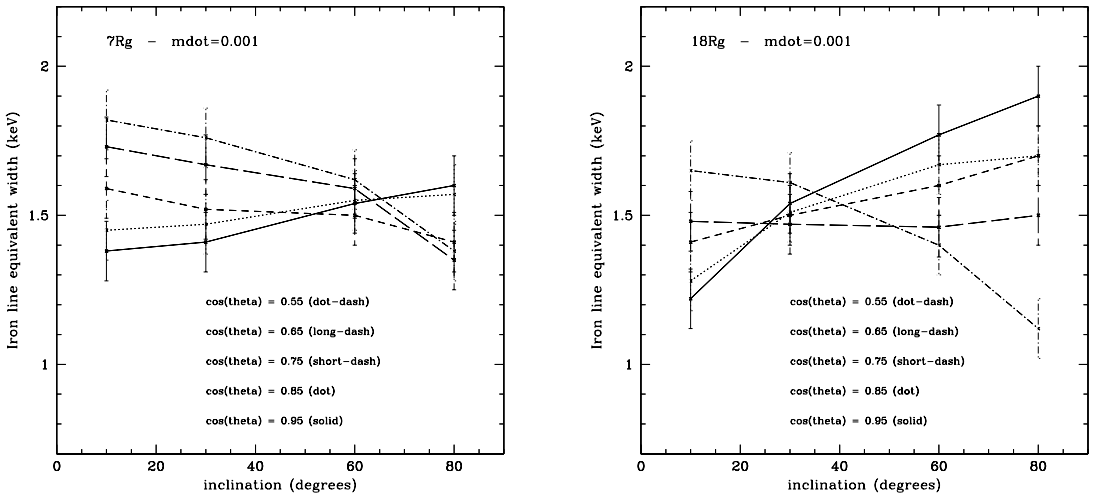

Figure 6.10: Equivalent widths of the iron Kα-line as a function of the local viewing angle ψ for a hot spot at $7\,R_g$ (left) and $18\,R_g$ (right). The five curves denote the consecutive concentric rings forming the hot spot. They are parametrized by the cosine of the incident angle θ of the illuminating primary radiation as indicated. The angles θ and ψ are measured with respect to the disk normal.

mation of the emitted flux at each viewing direction. We show the spectra of the entire spot, i.e. for incident angles between 0° and 60°, at $7\,R_g$ and at $18\,R_g$ in Fig. 6.11 (top graph). The reprocessed spectra are shown for a continuum of inclination angles ψ varying in 20 constant steps of $\cos\psi$ between $\cos\psi = 0.975$ (face-on) and $\cos\psi = 0.025$ (edge-on). We plot flux (top panel) and intensity spectra (bottom panel).

The limb-brightening effect toward higher emission angles is again clearly visible in the intensity spectra. The effect is more important in the soft X-ray region. The properties of the integrated spectra can be understood from the analogous properties of the single-ring spectra. In Fig. 6.12 (bottom) we plot the two flux ratios characterizing the overall spectral slope and the equivalent width of the Kα-line as a function of the inclination. As expected from the analysis of the single-rings in the previous section, the integrated spectrum softens as one changes from a face-on toward an edge-on viewing direction. The flux ratios computed between 28 keV and 4 keV and as well between 5.5 keV and 4 keV both decrease toward higher emission angles. The behavior of the equivalent widths has a slightly different tendency for the two distances from the black hole.

6.3 Computation of the spectra seen by a distant observer

We now investigate the effects of general relativity in the vicinity of the black hole on the observed reprocessed spectra. We therefore apply the ray-tracing code *KY* using the local single-ring spectra described in section 6.2.3 to define the emissivity of the disk. In a first step, we only consider time-stable spots orbiting around the black hole with the Keplerian velocity of a given distance R to the disk center (section 6.3.2). Then, time-dependent effects induced by the distance to the flare source that varies with the position in the spot are investigated.

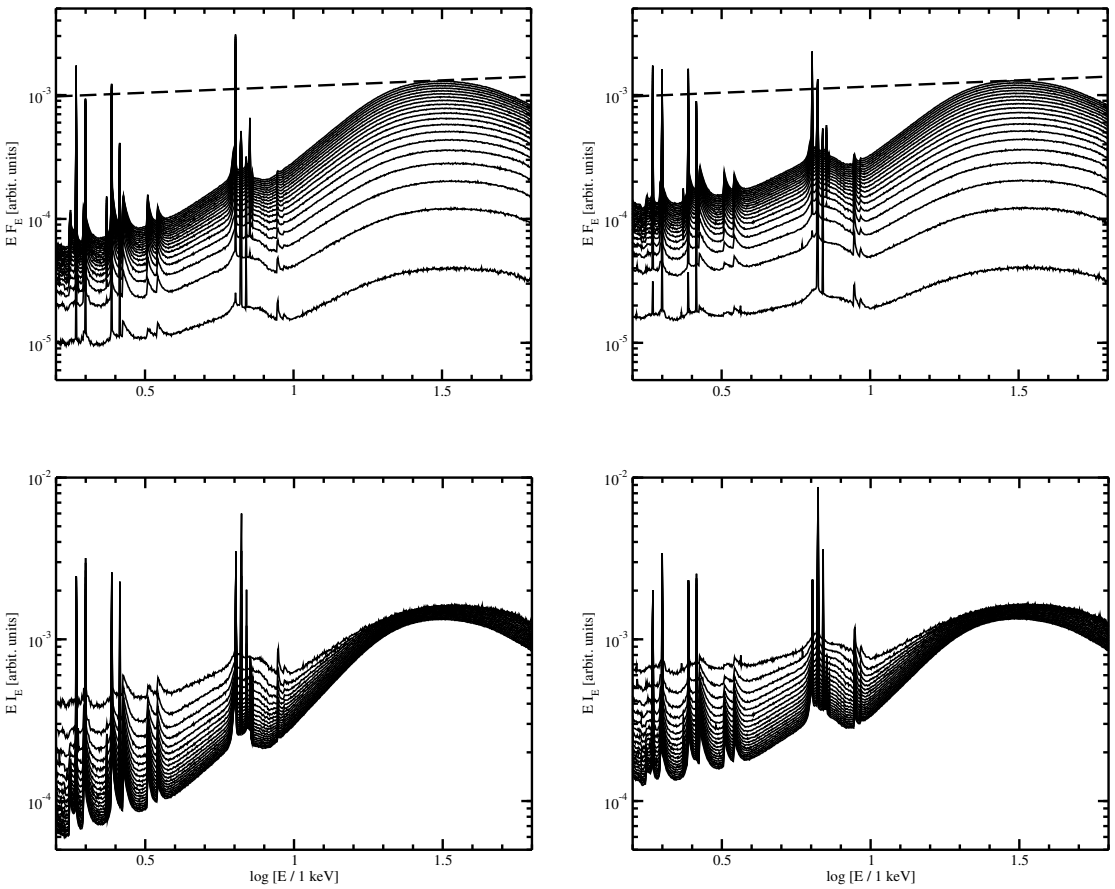

Figure 6.11: Integrated spectra from the entire hot spot seen at different local viewing angles ψ. The top panel shows *spectral fluxes*. From top to bottom, the inclination ψ corresponding to the curves *decreases* in 20 constant steps of $\cos\psi$ between $\cos\psi = 0.975$ (face-on) and $\cos\psi = 0.025$ (edge-on). The middle panels shows the same data but plotted as *spectral intensities*. Here, the inclination for the curves *increases* from top (edge-on) to bottom (face-on). The distance of the hot spot from the disk center is 7 Rg (left) and 18 Rg (right).

6.3.1 Keplerian motion and relativistic effects

The propagation of radiation through the curved space time around the black hole is computed by using the code *KY* (Dovčiak, Karas & Yaqoob, 2004; Dovčiak, 2004) described in chapter 5. The program integrates the photon geodesics between a position withing the flare spot and a distant observer. The integration method takes into account the energy shift of the photon along the geodesics, arrival time-lags, and the lensing-effect. Spectra can be computed for various viewing directions of a distant observer based on a given emissivity distribution of the disk. We define this emissivity for a local hot spot corresponding to a compact source at the height $h = 0.5R_g$. From the half-opening angle $\theta_0 = 60°$ of the flare-cone, a spot radius of $r_0 = \sqrt{3}h = 0.866\,R_g$ follows.

The flare above the disk surface is assumed to be in a Keplerian motion. This is rather a natural assumption if flares form as magnetic field lines expelled from the disk interior due to buoyancy. The spot center directly underlying the flare follows the same Keplerian orbit. The overall shape of

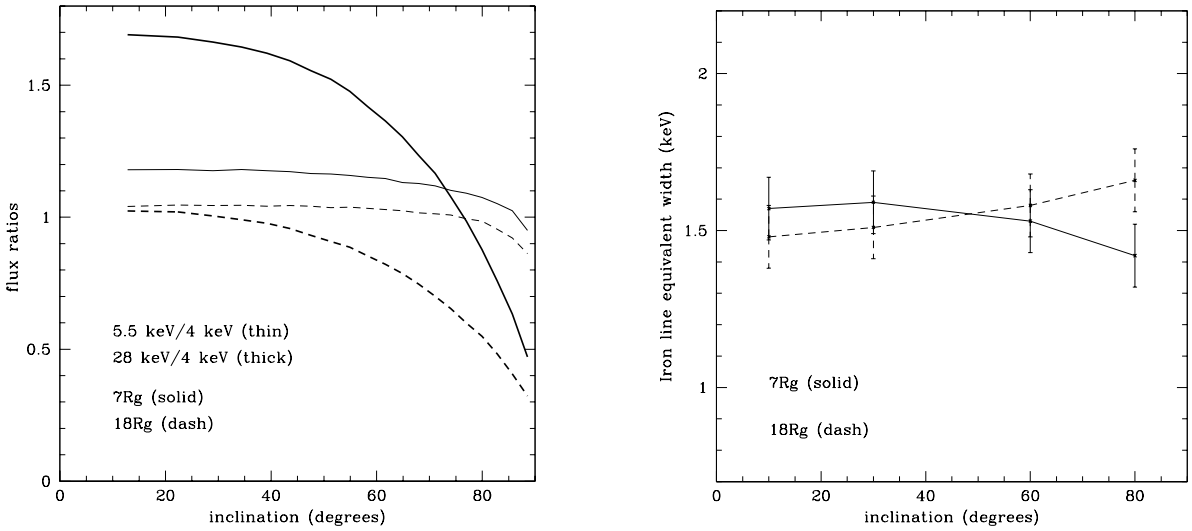

Figure 6.12: Flux ratios of 28 keV / 4 keV and 5.5 keV / 4 keV (left) and the equivalent width of the Kα-line complex (right) for the integrated spectrum of a hot spot at a distances of $7\,R_g$ and $18\,R_g$ from the black hole.

the spot stays circular. However, the kinematics of the spot is affected by the differential rotation of the disk: spot regions located closer to the black hole have a larger angular velocity than spot regions farther away. This means that there is a relative drift of the material through the spot, with some material leaving the spot region and cooling off while new material enters and is heated. We assume that at each part of the spot the motion is Keplerian. However, for simplicity, we neglect the effect of the drift of the material, hence, we assume that the heating and cooling of the drifting material is instantaneous. This is a good approximation since the heating and cooling timescales are short compared to the dynamical time-scale (see chapter 4). From the Keplerian motion of the spot it follows that the observed spectrum depends not only on the disk inclination i but also on the azimuthal starting position ϕ_0 of the spot within the disk.

We mention here that we consider the relativistic corrections only for the radiation coming from the hot spot *after* reprocessing. Modeling also the relativistic effects for the incident radiation on the way between the flare source and the disk is not included. However, this can be justified by several explicit ray-tracing computations we performed for photons traveling along the limiting flare-cone as defined by $\theta_0 = 60°$. In a flat space, these photons define a circle in the surface plane of the disk. We perform ray-tracing computations of photons along the limiting flare cone for a Schwarzschild black hole. The result is shown in Fig. 6.13 (left) where we plot the trace of the limiting cone on the disk surface with and without relativistic corrections.

The spot-center is located at $7\,R_g$ from the black hole. One can tell immediately, that the relativistic trace does not differ significantly from the circle obtained in flat space. Treating the incident radiation as traveling through flat space is hence a good approximation.

Repeating the same simulations for a Kerr black hole with maximum spin parameter $a = 0.998$ and for several distances from the disk center, we evaluate the limit of our simplifying assumption for the incident radiation. In Fig 6.13 (right) we show the trace of the limiting flare-cone on the surface of the disk. Again the inner circle denotes the results in a flat space, while the deformed lines

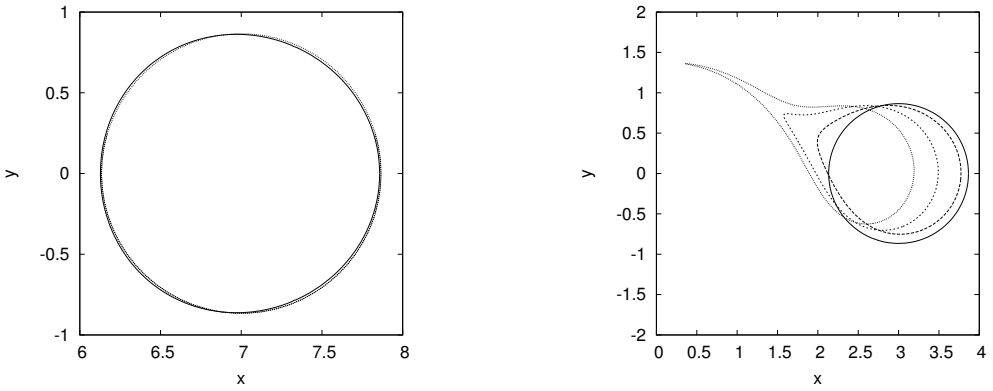

Figure 6.13: Traces on the disk surface of the trajectories for photons emitted by the compact flare source along the limiting flare-cone with $\theta_0 = 60°$. The disk surface is seen from above and parametrized by plane-coordinates x and y given in units of R_g. In flat space, the limiting cone leaves the trace of a circle, which is included in the figures for orientation. The projected position of the flare source at the height $h = 0.5R_g$ is above the center of the circle. The left figure shows the transformation of the circle as one switches to the metric at a distance of $7\,R_g$ of a Schwarzschild black hole. The differences to the case of a flat space are very small. In the right figure, the same transformation to a Kerr metric for several distances to the black hole is shown. With increasing deformation the trace-lines denote distances at $3\,R_g, 2.75\,R_g$ and $2.5\,R_g$. At a disk radius of $3\,R_g$ the trace-line still reminds of a circle.

represent the case of a Kerr black hole with maximum spin. The stronger the lines are deformed in comparison to the circle, the closer is the disk radius considered. From the figure we derive that a limiting disk radius for the modeling of the hot spot as a circle lies around $3\,R_g$.

6.3.2 Spots at different phases of the orbit

In the KY-code, the disk surface is parametrized by plane radial coordinates R and ϕ. The spot radius is determined by the height $h = 0.5R_g$ of the flare source and by the maximum half-opening angle $\theta_0 = 60°$ to $r_0 = h \tan\theta_0$. In order to define the spot with the spot center at (R_0, ϕ_0), we derive the following formula for the local emissivity $\epsilon(E, R, \phi, \psi)$ at the photon energy E, disk position (R, ϕ), and emission angle ψ:

$$\epsilon(E, R, \phi, \psi) = \begin{cases} F(E, r, \psi), & r < r_0), \\ 0, & \text{otherwise.} \end{cases} \tag{6.5}$$

Herein, F denotes the local flux and $r = \sqrt{R^2 + R_0^2 - 2RR_0\cos(\phi - \phi_0)}$ the distance between the spot center and the point (R, ϕ) considered. We are interested in the spectral effects induced by general relativity and by the orbital motion of the spot at various phases of the orbit. Therefore, we conduct the ray-tracing for a whole orbital period ignoring the fact that the hydrostatic equilibrium should change over the dynamical time-scale. The spectra produced here, can, however, provide helpful insights into the spectral behavior along the orbit.

In Fig. 6.14 we show color coded plots of the spectral flux received by a distant observer at four different inclinations for a theoretical hot spot completing a full orbit. On the horizontal axis the

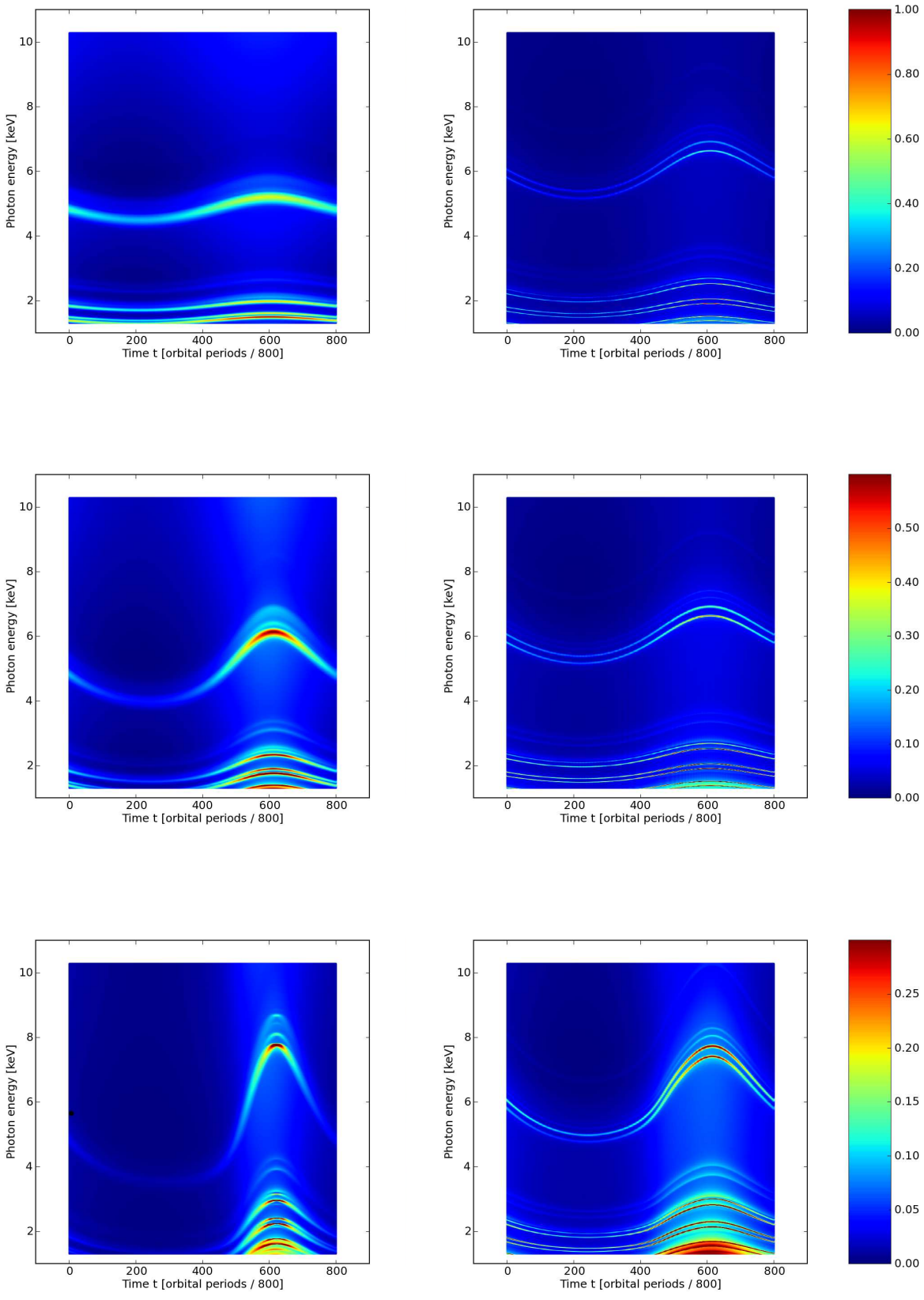

(figure caption on next page)

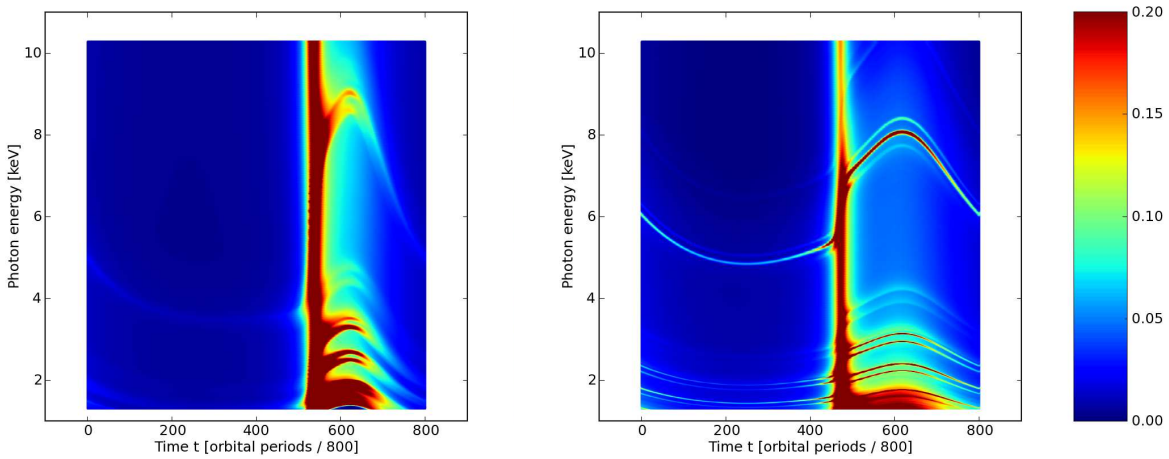

Figure 6.14: Color-coded maps of the spectral flux coming from a theoretical hot spot completing an entire Keplerian orbit. The horizontal axis denotes the orbital phase divided into 800 units; the vertical axis marks the photon energy between 1.3 keV and 10.3 keV. The color codes follow the rainbow-colors with blue representing the lowest flux. The maps are normalized to the maximum flux of all energies and orbital phases in each case. The color-codes are not extended up to unity, in order to allow clearer distinction of the fainter features. The panels consecutively represent different viewing angles i of a distant observer as measured with respect to the disk normal: $i = 10°$, $i = 30°$, $i = 60°$, and $i = 85°$. The distance of the hot spot to the black hole is $7\,R_g$ for the left panels and $18\,R_g$ for the right ones. The orbit starts at the closest approach to the observer.

orbital period is given, the vertical axis denotes the photon energy. Prominent features, especially strong emission lines, appear in red. The combined Doppler and gravitational energy shift is clearly visible by the position and S-like shape of the line traces. For lower inclinations corresponding to a face-on view, the Doppler effect causing the wavy shape of the line is weaker but the trace remains gravitationally redshifted with respect to the laboratory minimum energy 6.4 keV of the line complex. This gravitational redshift is stronger for the shorter distance to the black hole as expected.

When the spot passes behind the black hole with respect to the observers direction, a strong lensing-effect can be observed especially for high inclinations corresponding to an edge-on view. At this orbital period, marked at $\sim$ 450 units on the horizontal axis of Fig. 6.14, the flux rises particularly strongly for inclinations i becoming larger than 60°. At the quasi-alignment, of the spot, the black hole, and the distance observer, the black hole acts like a lense collecting the radiation of the spot emitted in various directions to focus it along the line of sight. The spectra at all other periods are relatively low.

In order to better understand the spectral behavior we divide the orbit into eight phases and provide the integrated spectrum for each phase at four different local viewing angles $i = 10°$, $i = 30°$, $i = 60°$, and $i = 85°$. The result is shown in Fig. 6.15 and Fig. 6.16. For the two distances of the spot to the black hole considered, we illustrate the spectra over 2 keV and 50 keV (left panels) and for a zoom on the range between 1 keV and 10 keV (right panels) at different phases of the accretion

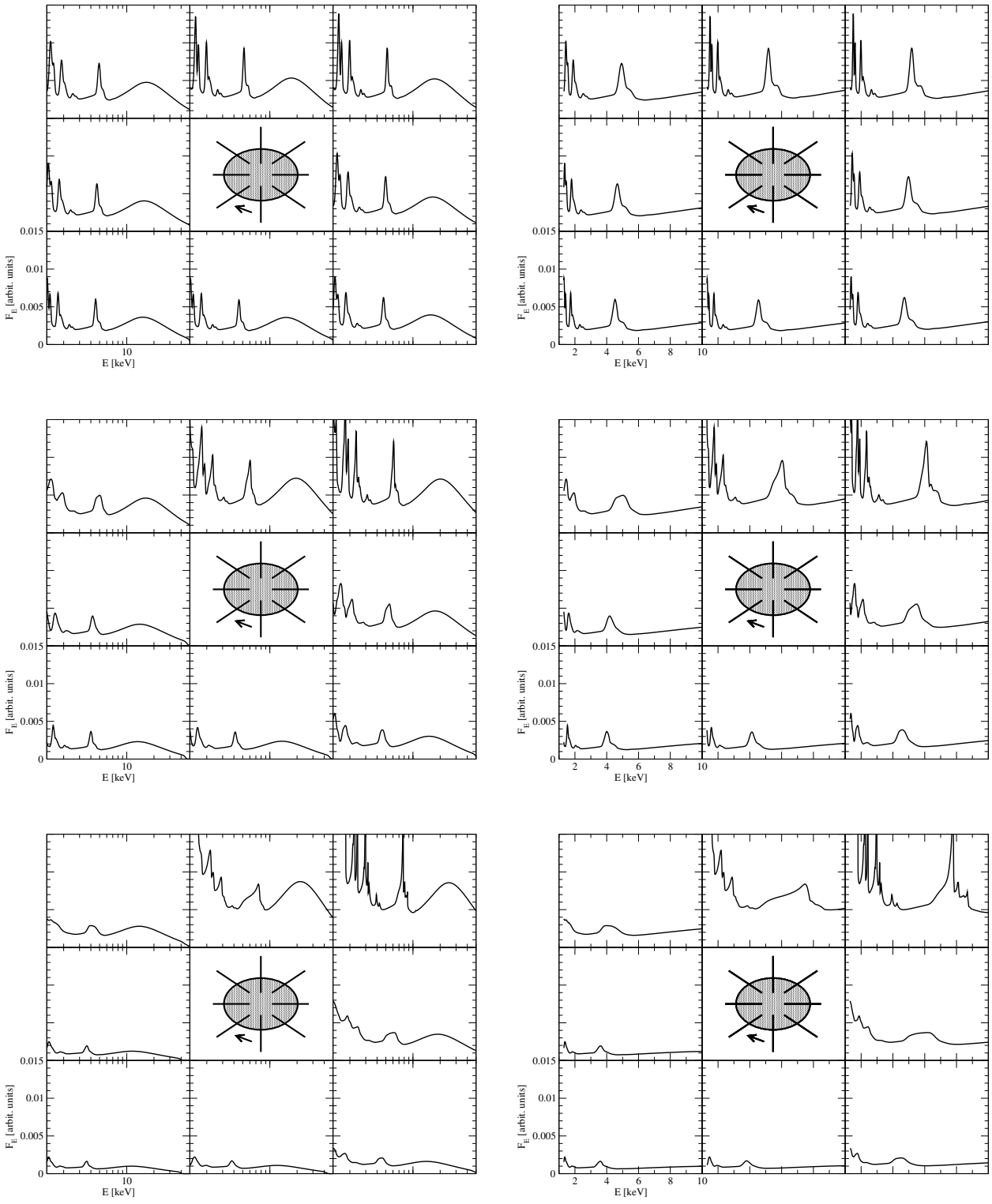

(figure caption on next page)

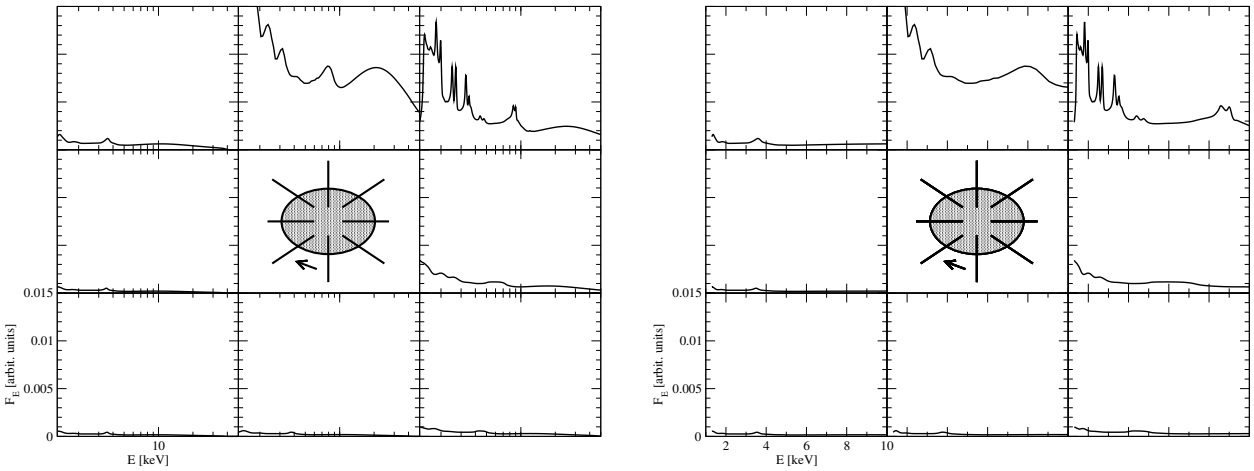

Figure 6.15: Spectra coming from a theoretical hot spot at 8 different phases of an entire orbit. In each panel the bottom/middle spectrum denotes the closest approach of the hot spot to the observer. The disk is supposed to rotate clock-wise. The spot is located at a distance of $7\,R_g$ from the black hole. The panels consecutively represent different viewing angles i of a distant observer as measured with respect to the disk normal: $i = 10°$, $i = 30°$, $i = 60°$, and $i = 85°$. The panels on the left show the whole spectra modeled over 2 keV to 50 keV, while the panels on the right present a zoom on the region of the Kα line between 1 keV and 10keV.

disk. The effects due to general relativity and Doppler shifts, induced by the Keplerian motion of the spot, become more important for higher inclinations. They affect the normalization of the reprocessed spectra as well as the shape of specific spectral features.

The effects are relevant even at the relatively large distance of 18 R_g from the black hole. The spectra are significantly deformed at some orbital phases and already at low inclinations. This can be seen especially from the zoom onto the Kα-line region shown in Fig. 6.16. For $i = 10°$ the line complex shows a slight gravitational red-shift and phase-dependent deformations of the Kα-line complex. At higher inclinations these deformations become stronger due to the larger velocity component of the spot along the line-of-sight, which smears out the lines. When the spot passes behind the black hole, from the point of view of a distant observer, the lensing-effect becomes important especially at high inclinations.

As expected, the deformations are much stronger at $7\,R_g$ than at $18\,R_g$. At $7\,R_g$ basically all orbital periods and for all inclinations the Kα-line complex cannot be decomposed into single components any more. An exception is given at the inclination of $i = 60°$, where shortly "after" the passage behind the black hole some structure of the line appears. However, the spectral deformations due to the lensing-effect remain very strong. The stronger deformations of the spectra in comparison to the larger distance at $18\,R_g$ are explained by a higher gravitational redshift of the photons but also by the higher Keplerian velocity of the spot.

The decomposition into eight orbital phases also shows that for inclinations smaller than 60° the flux enhancement during the passage behind the black hole takes its maximum at a slightly "later" orbital phase, i.e. when the spot already accelerates again toward the observer. One can see that in Fig. 6.15 and Fig. 6.16, high normalizations of the spectra do not only appear in the upper-middle panel but also in the upper-right one. Physically, this can be explained by the interplay of two

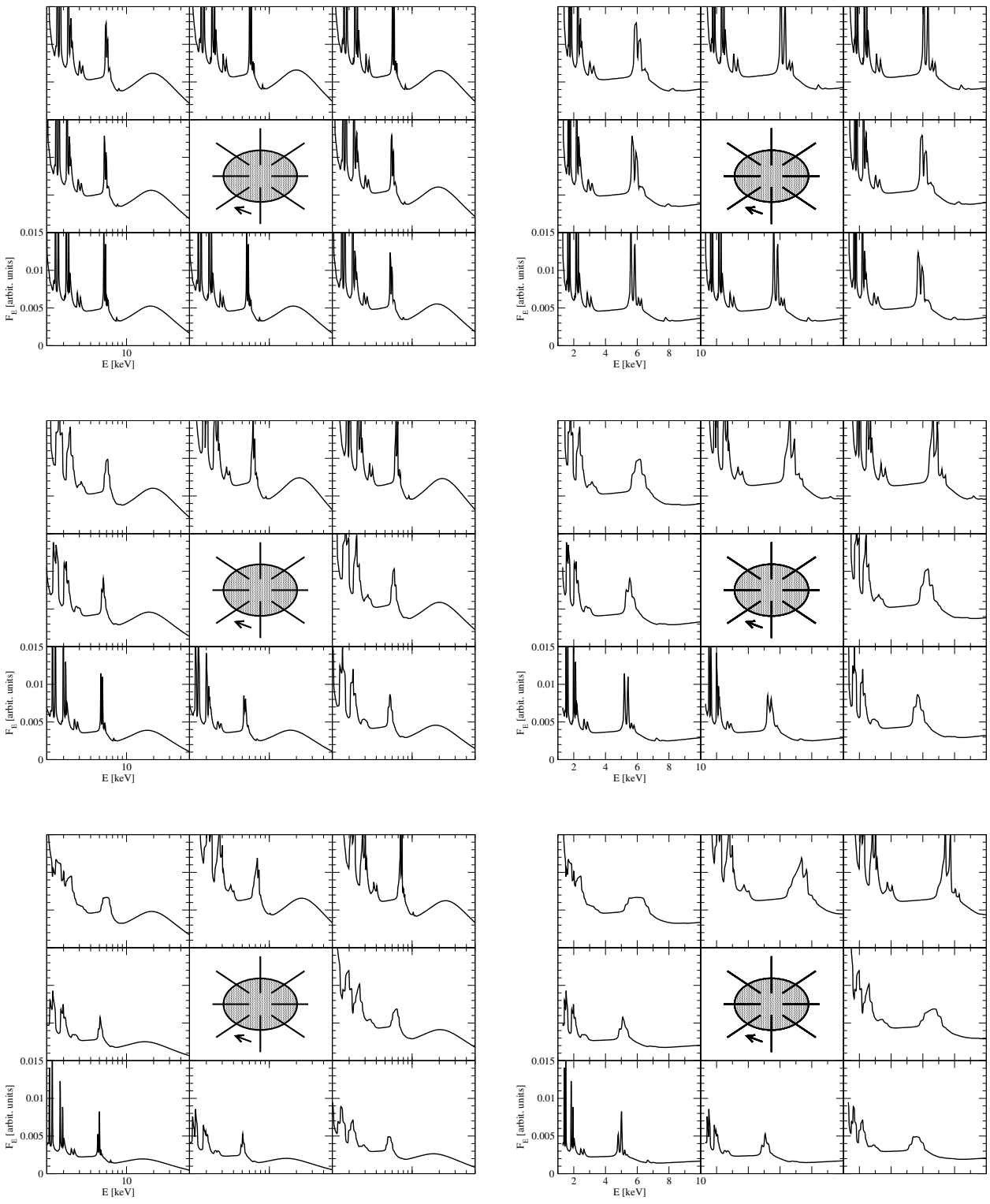

(figure caption on next page)

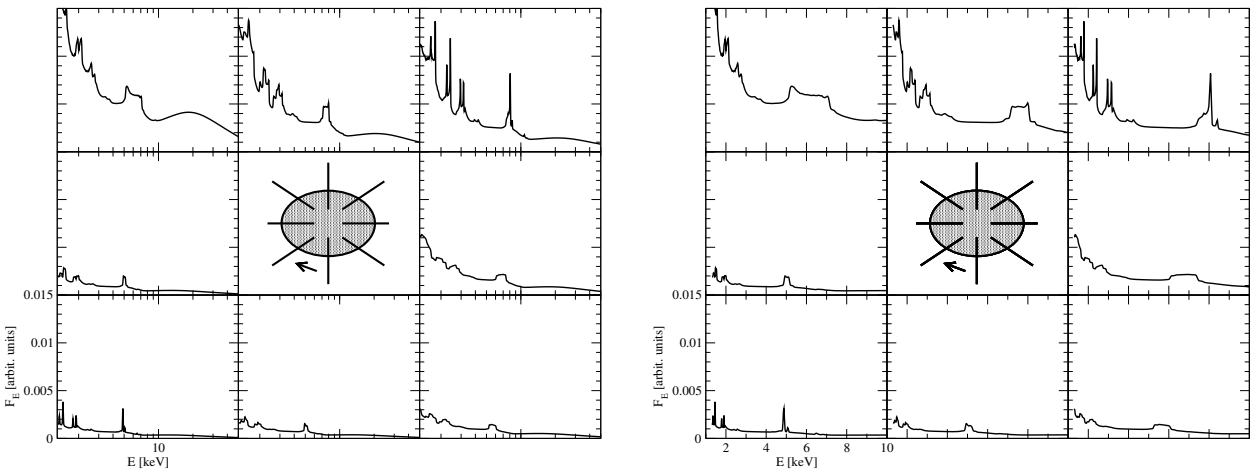

Figure 6.16: Spectra coming from a theoretical hot spot at 8 different phases of an entire orbit. In each panel the bottom/middle spectrum denotes the closest approach of the hot spot to the observer. The disk is supposed to rotate clock-wise. The spot is located at a distance of $18\,R_g$ from the black hole. The panels consecutively represent different viewing angles i of a distant observer as measured with respect to the disk normal: $i = 10°$, $i = 30°$, $i = 60°$, and $i = 85°$. The panels on the left show the whole spectra modeled over 2 keV to 50 keV, while the panels on the right present a zoom on the region of the Kα line between 1 keV and 10keV.

effects: the lensing which indeed produces a maximum flux enhancement for a spot-position *exactly behind* the black hole, and the energy blueshift rising along the approaching phase. Both effects combine and create the maximum flux enhancement at the slightly "later" orbital phase. For the extreme inclination of $i = 85°$ the gravitational lensing is so strong that the effect of energy blue shift can not compete and the maximum flux enhancement appears again during the passage of the spot directly behind the black hole. The combination of lensing-effect and photon energy shift also explains why the traces of the emission lines in the color-coded plots of Fig. 6.14 do not look entirely sinusoidal: the concave phases of the traces are always longer than the convex ones and this trend becomes stronger with increasing inclination.

The plots of the reprocessed spectra at various orbital phases clearly show modifications of the spectral slope and of the emission lines depending on the azimuthal position of the hot spot. These deformations are stronger for a closer distance to the black hole and therefore we are going to analyze them in more detail for our case of a hot spot at the disk radius of $7\,R_g$.

6.3.3 Short-term spots at different orbital phases

The previous investigation of a theoretical hot spot completing a whole orbit illustrates the consequences of the relativistic effects and the Keplerian motion on the reprocessed spectra. However, the results are not entirely consistent as we assume that the spot emission is persistent over the whole Keplerian time-scale of the disk. During this time, the illuminated disk would settle into a new hydrostatic equilibrium and the properties of the locally emitted spectra would change.

In the following investigation, we therefore consider only short-term flares completing a small fraction of the orbit. The model configuration is identical to the one described in section 6.3.2,

only the flare duration is much shorter. The flare is assumed to occur at a defined orbital phase and the radiation of the flare source is switched on instantaneously. It lasts for a time period T corresponding to the light-crossing time of the hot spot and then the source is instantaneously switched off again. The geometry illustrated in Fig. 6.4 shows that the time-dependent emissivity pattern across the spot depends on the distance to the flare source and on the duration of the primary emission. During the onset and fading of the flare the hot spot will evolve from the center, where the first primary photons arrive, to the rim. For a long-living flare observed at an even longer integration time, the irradiation can be considered as a stationary process, as it was done in section 6.3.2. Therefore, the results obtained for hot spots completing a whole Keplerian orbit can serve as a guideline to the interpretation of the spectra we obtain for the short-flares. However, if the duration of the primary emission and of the observation are short, the evolution of the hot spot emissivity induces new time-dependent effects on the spectrum.

The intrinsic evolution of the emissivity across the hot spot starts at a certain time t_0 at the spot center and ends there at $t_0 + T$. If $r = \sqrt{R^2 + R_0^2 - 2RR_0\cos(\phi - \phi_0)}$ denotes the distance of a given position (R, ϕ) on the disk and the spot center (R_0, ϕ_0), the time-dependent local emissivity ε_i at the time t is given by:

$$\varepsilon(E, R, \phi, \psi, t) = \begin{cases} \epsilon(E, R, \phi, \psi), & t_0 < t - \frac{r^2}{\sqrt{h^2+r^2}} < t_0 + T, \\ 0, & \text{otherwise.} \end{cases} \tag{6.6}$$

Herein E is the photon energy, ψ denotes the local emission angle, and h the height of the flare source above the disk. Implicitly, we assume in the above formula that the reprocessing happens instantaneously.

As before, we consider hot spots at the two different distances of $R = 7\,R_g$ and $R = 18\,R_g$ from a Schwarzschild black hole with the mass $M = 10^8 M_\odot$ and the accretion rate 0.001 Eddington units. The radiative transfer solutions for the local reprocessed spectra are the same as in section 6.3. We compute sets of time-dependent spectra at four viewing angles $i = 10°$, $i = 30°$, $i = 60°$, and $i = 85°$ of a distant observer. The viewing angle is measured with respect to the disk symmetry axis. For the initial azimuthal position ϕ_0 of the flare we consider the four values $\phi_0 = 0°$, $\phi_0 = 90°$, $\phi_0 = 180°$, and $\phi_0 = 270°$. The origin of the azimuthal scale at $\phi = 0°$ is at the closest approach of the hot spot to the (inclined) observer, for $\phi = 180°$ the spot is farthest away and behind the black hole for very high inclinations around $i \sim 90°$.

In Fig. 6.17 and Fig. 6.18 we present the obtained integrated spectra for the whole observed flare periods and corresponding lightcurves. The four panels of each figure denote the different azimuthal positions.

The spectral appearance

The figures show that the line broadening is important also for short-term flares. However, in this case the contribution of the Doppler energy shift due to the Keplerian motion to the line broadening should be weak. During the flare period the spot only proceed for $\sim 3°$ on the orbit, which is almost negligible. From the short flare spectra we can therefore conclude that the line broadening is caused to a large extent by general relativity. Due to the expansion of the spot, the photons arriving at the distant observer originate at different distances from the central black hole. Hence, their gravitational redshift, which only depends on the distance of the emission point from the black hole, covers a whole range and the line appears to be broadened. At $18\,R_g$ the gravitational line broadening and the orbital motion are weaker and the iron Kα line appears resolved into its

sub-components at all orbital phases. Comparing them at different inclinations for a flare at a given orbital phase, the effect of the vertical ionization and temperature profiles become visible as explained for the local emission spectra of the single concentric rings (see Fig. 6.8).

Some aspects of the spectral shape are consistent with the results obtained in section 6.3.2 for hot spots over the whole orbit. The Doppler shift of the emission line, for instance, corresponds to the orbital phase of the flare and increases with higher inclination due to a larger velocity component along the line-of-sight. For a flare occurring "behind" the black hole, i.e. for $\phi_0 = 180°$ the lensing effect strongly modifies the spectrum and increases the overall flux. At this phase and for high inclinations the iron Kα-line is entirely smeared out.

The lightcurves

The new time-dependent element in this model is given by the consideration of the different light-travel times between the elevated source and the different positions of the hot spot. This effect can be seen in the shape of the lightcurves that were integrated over the whole spectra between 2 keV and 50 keV. The observed flare period is not the same for all inclinations and orbital phases. Physically, it depends on the difference in length between the longest and the shortest photon trajectories connecting the spot with the distant observer. These trajectories are a function of the defined geometry and of the time-dependent emission across the spot. In the figures, the origin of the time axis is set when the photons coming from the spot-center arrive at the distant observer.

At low inclinations the lightcurves have a characteristic and regular shape showing consecutively the rising and fading period of the flare emission. The shape of the lightcurve is not at all box-like as assumed for the incident radiation illuminating the disk. The geometrical expansion of the spot induces different time-delays for the reprocessed radiation and so the onset and fading of the spot emission are smoothed out.

Going toward higher inclinations the shape of the light curve changes and generally becomes more symmetric - with an exception for the phase $\phi = 180°$, which corresponds again to the passage of the spot "behind" the black hole. Quite complete symmetry is reached for inclinations of $\sim 60°$. However, for even larger angles the flux decreases rapidly and the lightcurves become much flatter.

In the diagrams, the time axis is given in units of one orbital time-scale. At the two distances from the black hole, with $M = 10^8 M_\odot$, considered, the Keplerian time-scales are 5.5×10^4 s at $7\,R_g$ and 2×10^5 s at $18\,R_g$. Hence, the observed flare durations are of the order of a few hundreds or thousands of seconds.

6.4 Summary and discussion

In this chapter we analyzed in a detailed way the reprocessed emission from an irradiated hot spot orbiting on the accretion disk around the black hole. Such spots are expected to develop during magnetic flares producing compact X-ray lamps above the disk. Before the onset of the flare we assume the disk to be in hydrostatic equilibrium.

We modeled the vertical disk profile including relativistic corrections. Our simulations for the density, flux, and temperature reveal correlations with the distance of the flare from the central black hole. For closer distances, the disk is geometrically thinner while the densities are higher. Also the flux and temperature distributions increase toward the disk center, but when approaching the marginally stable orbit, they level down due to the imposed boundary conditions. Such a behavior is similar for the temperature and flux at the disk surface computed from the standard

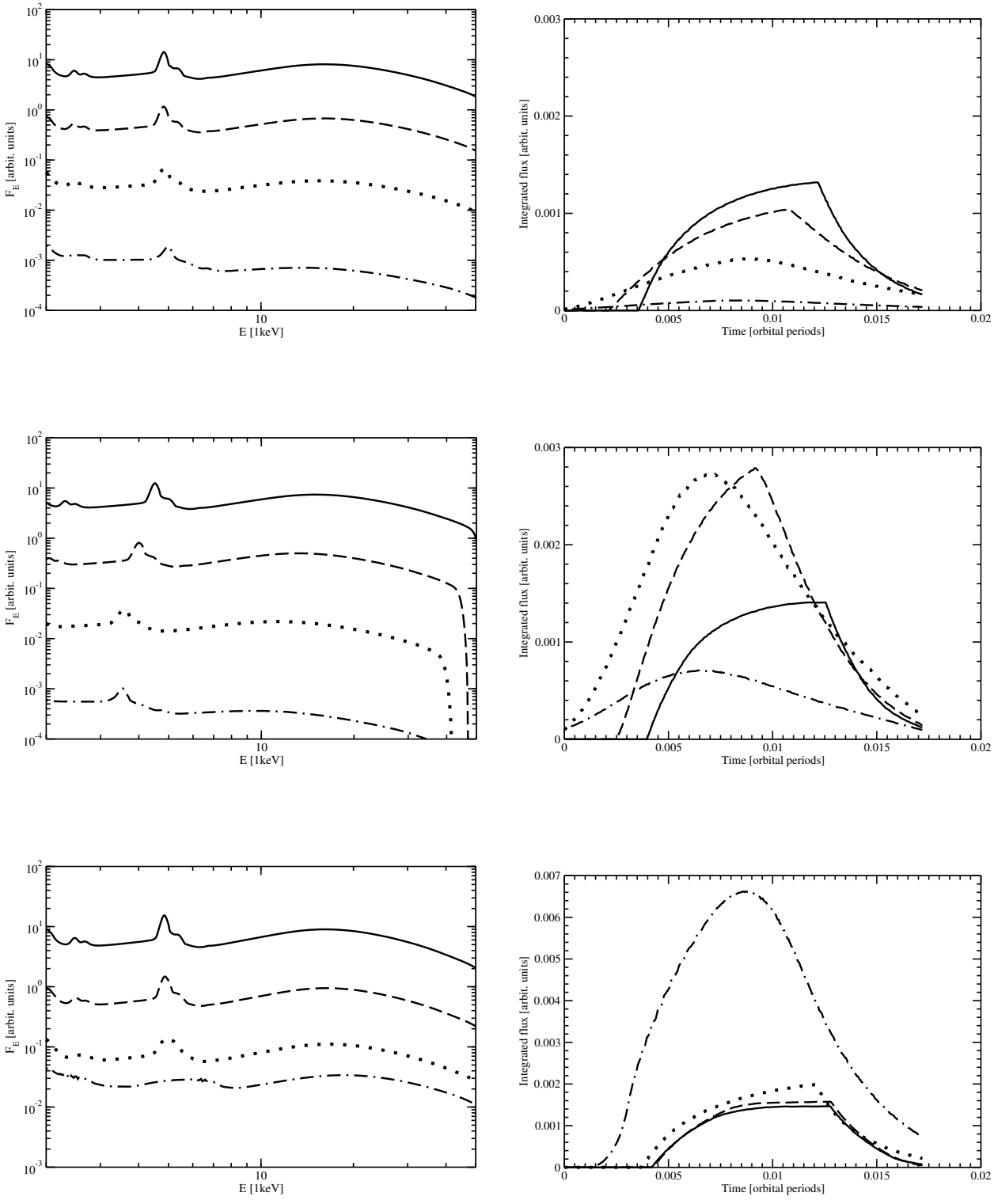

(figure caption on next page)

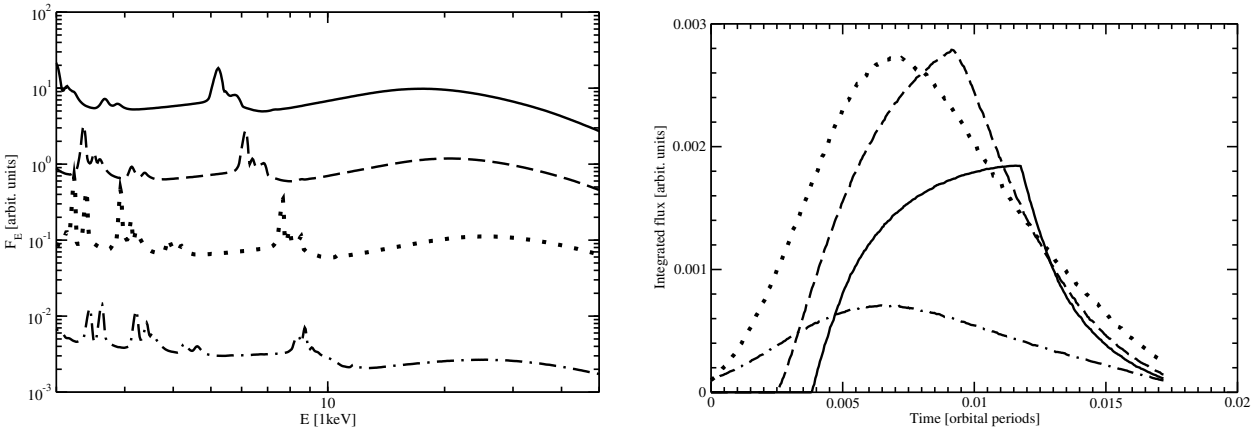

Figure 6.17: Flux spectra and lightcurves for short-term flares at four different initial azimuthal positions of the spot: $\phi_0 = 0°$ (top panels, left), $\phi_0 = 90°$ (middle panels, left), $\phi_0 = 180°$ (bottom panels, left), and $\phi_0 = 270°$ (above panels). The left panels show broad spectra between 2 keV and 50 keV, they were integrated over the whole observed flare period. From top to bottom the spectra denote the disk inclinations $i = 10°$, $i = 30°$, $i = 60°$, and $i = 85°$. The spectra contain a systematic offset of a factor of 10 between each other for clarity. The right panels show the corresponding lightcurves integrated over the whole spectra. The distance of the spot to the black hole is $R = 7\,R_g$

formulae of Shakura & Sunyaev (1973). The surface values for the flux and for the temperature we obtain are close to the standard values calculated by equation 6.1 and by other standard formulae of the α-disk model. However, in our modeling we also obtain the vertical disk structure, which differs significantly from the assumption of constant density as assumed by Shakura & Sunyaev (1973). Including the relativistic effects into the computation of the vertical disk profiles, induces changes particularly when the spot is close to the black hole because the cut-off function at the inner boundary is different.

Using the vertical disk profiles at a given distance from the black hole, we investigated the Compton reflection/reprocessed component coming from an irradiated hot spot on the disk surface. The local spectra show dependencies on the position in the spot due to the changing incident flux coming from the flare source. In the soft X-ray range and for local inclinations $\psi < 60°$, the strongest intensity appears at the spot-center. It levels down toward the spot rim. This is due to higher ionization and less absorption in the more strongly irradiated medium at the spot center. In the hard X-ray range the emission intensity rises and the spectra hardens at all inclinations as one goes from the center toward the rim. At the same time, the hot spot exhibits a limb-brightening effect, as the emission rises toward larger local viewing angles. The different components of the Kα-line complex indicate the temperature and ionization state of the medium seen at a given inclination.

Adding relativistic ray-tracing to the model of orbiting hot spots leads to strong dependencies of the spectra on the orbital phase. For long-term flares completing a significant fraction of the Keplerian orbit, relativistic and Doppler effects induce time-variability for the lines and for the continuum. The orbital variations of the Kα-line position and intensity are enhanced for small

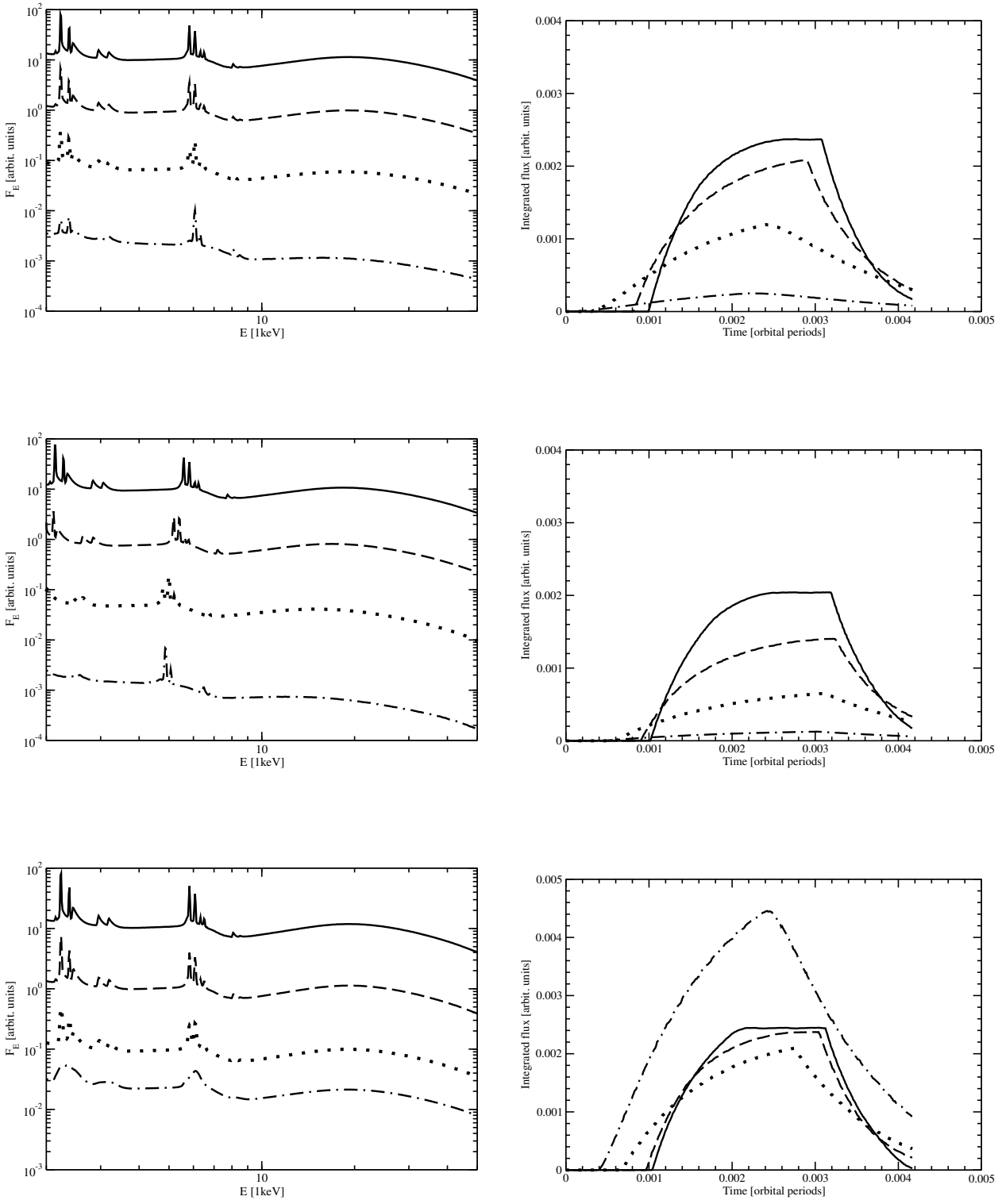

(figure caption on next page)

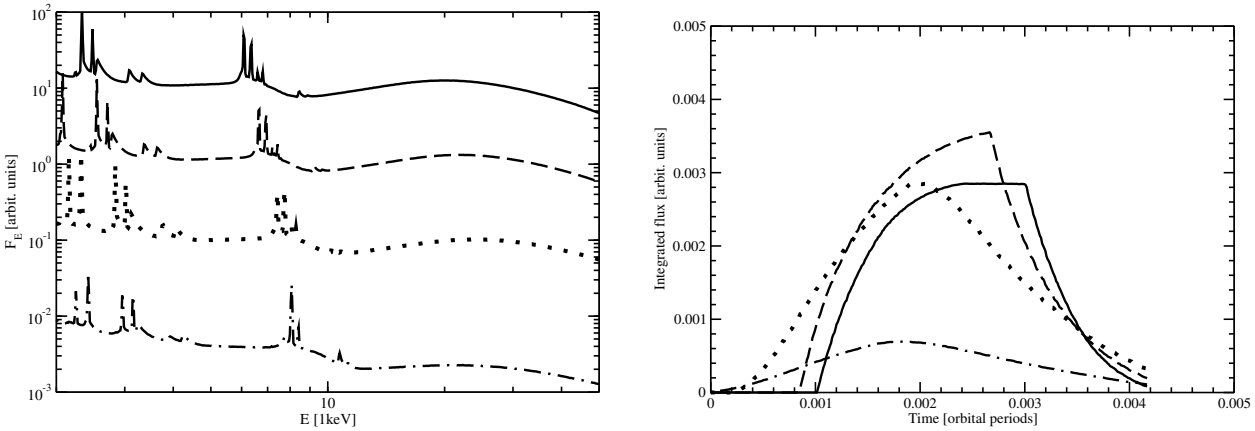

Figure 6.18: Flux spectra and lightcurves for short-term flares at four different initial azimuthal positions of the spot: $\phi_0 = 0°$ (top panels, left), $\phi_0 = 90°$ (middle panels, left), $\phi_0 = 180°$ (bottom panels, left), and $\phi_0 = 270°$ (above panels). The left panels show broad spectra between 2 keV and 50 keV, they were integrated over the whole observed flare period. From top to bottom the spectra denote the disk inclinations $i = 10°$, $i = 30°$, $i = 60°$, and $i = 85°$. The spectra contain a systematic offset of a factor of 10 between each other for clarity. The right panels show the corresponding lightcurves integrated over the whole spectra. The distance of the spot to the black hole is $R = 18\,R_g$

distances from the central black hole and at high inclinations of the disk. Such results have been presented by several authors (see e.g. Ruszkowski, 2000; Dovčiak, Karas & Yaqoob, 2004) and these results can now be confronted to the recent discovery of a quasi-periodic pattern in the iron line profile of the Seyfert-1 galaxy NGC 3516 (Iwasawa et al., 2004; Fabian & Miniutti, 2005), as mentioned in chapter 4.

For short-term flares, additional time-variability is caused by the light-traveling paths of the incident radiation to different positions within the hot spot. However, the modeling of single short-term flares requires the declaration of many free parameters: distance R to the black hole, mass M, spin parameter a, and accretion rate $\dot{m}$ of the black hole, disk inclination i, initial azimuthal angle ψ_0 of the spot, flare duration T, height h of the flare above the disk. In the preceding investigation, we did not yet vary the spectral slope of the incident spectrum and neither the height of the flare. Nevertheless, it would be useful to expand the grid of models as already in current X-ray data, the lightcurves of AGN show features corresponding to short-term flares. In the following chapter, such a flare event reported for MCG -6-30-15 is investigated in terms of its time variability. The lightcurve is shown in Fig. 7.1 (left). The flare part has a rather symmetric shape that, however, we cannot yet explain with our short-term flare model. Our results for the short-flares show symmetric shapes of the lightcurve only if the inclination of the object is at higher inclinations of $\sim 60°$ or more (see Fig. 6.17 and Fig. 6.18), which is not the case for this object. Furthermore, in MCG -6-30-15, the low mass black hole is supposedly rapidly spinning (Young et al., 2005), a case that we have not considered yet in our modeling. Especially at small disk radii there are important consequences on the disk structure, the local radiative transfer, and on the relativistic effects.

More precise tests of our flare-modeling are expected from the X-ray data obtained by future

satellite missions such as *Constellation-X* and *XEUS*. The time-resolved spectra obtained with these observatories will be of much higher quality than the ones obtained at the present day. For the flare event in MCG -6-30-15, mentioned in the preceding paragraph, Ponti et al. (2004) have provided a series of time resolved spectra during the flare period from the *XMM-Newton* data. However, the signal-to-noise ratio of these spectra is far from being comparable to the model. With the next generation of X-ray satellites the data should be of much higher quality and it will be useful to analyze theoretically magnetic flare emission at different time periods of their existence. However, the present data can still be powerful in testing the statistical variability properties predicted by time-resolved simulations of large numbers of flares. In chapter 8, we therefore conduct Monte-Carlo simulations for large number distributions of flares across the disk and characterize the expected variability behavior of such a configuration.

Chapter 7

Modeling time-lags of X-ray flares

Time-lags between soft and hard X-ray spectra of accreting sources can be modeled as a result of multiple scattering within the hot, optically thin plasma producing the power law component. Such an interpretation was also suggested for a flare event in MCG -6-30-15 as described by Ponti et al. (2004). In this chapter we discuss an alternative possibility. We assume that the source of the primary power law emission is given by magnetic reconnection above the disk, and the delay in various energy bands is due to a delay of the radiation traveling between the source and the reprocessing disk. This leads to a time-dependent behavior of the observed spectral shape. We construct a simple toy model to show general trends of the observed time-lags between various energy bands.

In section 7.1 we present the modeling setup and the mathematical functions describing the time-evolution of the primary component and of the reprocessed radiation. We then compute a grid of models varying systematically the height of the flare source above the disk and the properties of the primary and the reprocessed radiation. General results of this modeling are presented in section 7.2, as well as an application to the flare event seen in MCG -6-30-15. We discuss implications of our results in section 7.3. Further details of the modeling we present here can be found in Goosmann & Czerny (in preparation).

7.1 Description of the model

The investigation we conduct is analogous to the data analysis done by Ponti et al. (2004) for the Seyfert-1 galaxy MCG -6-30-15. The object was observed for 95 ks with *XMM-Newton* (Wilms et al., 2001) and showed a bright flare lasting for $\sim$ 2000 s. We show the light-curve over the flare-period in Fig. 7.1 (top). From their data, Ponti et al. (2004) computed X-ray time-lags using cross-correlation functions between the light-curves of separate X-ray bands. These computations reveal the reaction time of the spectrum as a function of energy, shown in Fig. 7.1 (bottom).

For our model, we assume that the flare is created by a magnetic reconnection event at a height h above the surface of the accretion disk. The reconnection creates a compact source of hard X-ray radiation. This primary component I_p partly shines up and is detected by a distant observer, partly it irradiates the disk and creates a hot spot. The hot spot gives rise to a Compton reflection/reprocessed component I_r providing an iron Kα-line around 6.4 keV and a Compton hump centered at $\sim$ 30 keV. In Fig. 7.2 we illustrate the geometrical setup between the flare source, the reprocessing disk, and the viewing direction of a distant observer. From the figure it becomes clear

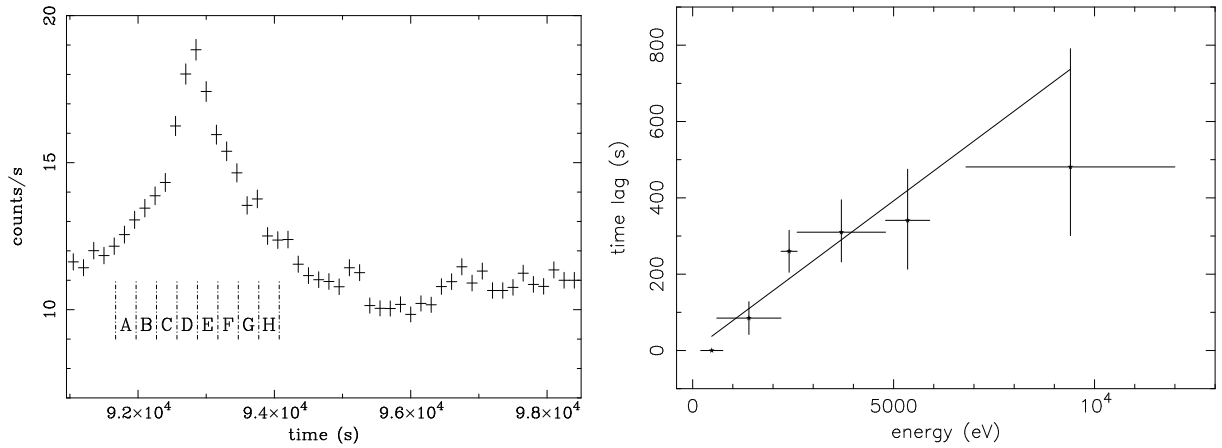

Figure 7.1: The light-curve (left) between 0.2 keV —10 keV for a strong flare in MCG -6-30-15 and the energy-dependent reaction-time (right) of the flare spectrum. (Ponti et al., 2004).

that the response of I_r to spectral variations of I_p is delayed by the light-travel time to the disk surface and back. This time-lag depends on the location inside the hot spot and on the viewing direction.

We define mathematical descriptions of the intensities I_p and I_r depending on energy E and time t. They read as follows:

$$I_p(E,t) = \mathcal{L}_p(t,t_0,\Omega)E^{-\alpha_p}, \tag{7.1}$$
$$I_r(E,t) = N\mathcal{L}_r(t,t_0,\delta,\Omega,b)E^{-\alpha_r}. \tag{7.2}$$

Herein, the two functions $\mathcal{L}_p$ and $\mathcal{L}_r$ are given by the expressions:

$$\mathcal{L}_p(t,t_0,\Omega) = \frac{\Omega^2}{(t-t_0)^2+\Omega^2}, \tag{7.3}$$
$$\mathcal{L}_r(t,t_0,\delta,\Omega,b) = \frac{b^2\Omega^2}{[t-(t_0-\delta)]^2+b^2\Omega^2}. \tag{7.4}$$

For both I_p and I_r we assume a power-law shape in energy with different indexes α_p and α_r. In the case of the reprocessed component, this description neglects particular features like the emission lines, we will thus only examine the time-dependent effects relying on the spectral slope of I_r. Although some spectroscopy during the flare in MCG -6-30-15 is given in Ponti et al. (2004), its signal-to-noise ratio is not sufficiently high to enable an observational constraint for α_r. We therefore adopt a value taken from modeling of the reprocessed component emitted by a hot spot as presented in chapter 6. It follows from this work that the X-ray spectrum between 1 keV and 30 keV for a hot spot orbiting a $10^7 M_\odot$ black hole at 7 gravitational radii can be roughly approximated by a power-law with $\alpha_r = -0.1$. Regarding the primary emission we explore two different values for α_p, the average value of large samples of radio-quiet AGN, $\alpha_p = 0.9$ (Nandra et al., 1997b; Piconcelli et al., 2005; George et al., 2000), and a limiting case derived from time analysis of a long observation of MCG -6-30-15 conducted by Vaughan & Edelson (2001). In their work, the observed spectral

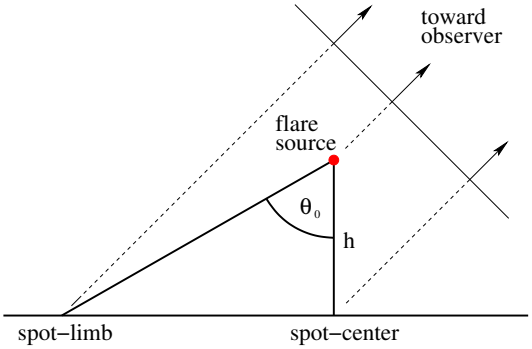

Figure 7.2: Geometry of a flare. A compact hard X-ray source above a reprocessing accretion disk. The hot spot underneath the flare source and the flare source define a cone of the half-opening angle θ_0.

shape can be fitted by a power-law component with a spectral index varying around 1.2 . Assuming, that the primary radiation is still slightly steeper to account for the reprocessed component in the observed spectrum, we choose $\alpha_p = 1.3$.

The time-development of both functions is modeled by Lorentzians, $\mathcal{L}_p$ and $\mathcal{L}_r$, taking a point in time t_0 for the maximum of the primary emission to appear and a half-width Ω. These functions are chosen according to the shape of the light-curve for the observed flare in MCG -6-30-15 (see Fig. 7.1, top), which can be approximated by a Lorentzian. We imagine the time modulation of I_p and I_r as consecutive pulses. The primary leads the reprocessed spectrum by a delay $\delta = h/c$ giving a measure of the light travel-time between the source of the flare and the accretion disk. From the reported flare in MCG -6-30-15 we adopt $t_0 = 2200$s and $\Omega = 500$s. For the reflected component, the width of the Lorentzian can be broadened by a parameter b. This is expected from the geometrical setup as the time-lag between I_p and I_r depends on the path between the source and the flare-spot (see Fig. 7.2). There are path lengths possible between h, for the center of the spot, and $h/\cos\theta_0$ for the spot's rim. Note that it is also influenced by the inclination at which the flare-spot is seen. Exact quantification of the broadening is not necessary for our purposes. Generally, we assume b to be in the range of 1.5 to 4.5.

An overall factor N is included in I_r to normalize the reflected component against the primary. We define N with respect to the ratio K of the total energy release of I_p to I_r over the range between $E_{min} = 0.2$ keV and $E_{max} = 12$ keV as used for the analysis by Ponti et al. (2004). To obtain the total values, the intensities are integrated over time and energy:

$$K = \frac{N \int_{-\infty}^{+\infty} dt \mathcal{L}_r(t_0, \delta, \Omega, b) \int_{E_{min}}^{E_{max}} dE\, E^{-\alpha_r}}{\int_{-\infty}^{+\infty} dt \mathcal{L}_p(t_0, \Omega) \int_{E_{min}}^{E_{max}} dE\, E^{-\alpha_p}} \tag{7.5}$$

$$= \frac{Nb(1-\alpha_p)}{1-\alpha_r} \frac{E_{max}^{1-\alpha_r} - E_{min}^{1-\alpha_r}}{E_{max}^{1-\alpha_p} - E_{min}^{1-\alpha_p}}. \tag{7.6}$$

Hence, for a given value of K, the normalization N is a function of the energy limits, the broadening, and the spectral indexes. If we again consider the modeling conducted in chapter 6, we

Table 7.1: Defined energy bands and other model constants

Energy bands		Model constants	
ΔE_1	0.2 keV — 0.57 keV	E_{min}	0.2 keV
ΔE_2	0.6 keV — 2.2 keV	E_{max}	12 keV
ΔE_3	2.2 keV — 2.6 keV	α_p	0.9, 1.3
ΔE_4	2.6 keV — 4.8 keV	α_r	-0.1
ΔE_5	4.8 keV — 6.8 keV	t_0	2200 s
ΔE_6	6.8 keV — 12.0 keV	Ω	500 s

find values of $K \sim 0.15$. This leads to a normalization of $N \sim 0.022$, for a broadening of $b = 2$ and the spectral slopes assumed here.

The distant observer is supposed to detect the sum I_{tot} of I_p and I_r, thereby we make the assumption that all the primary radiation going toward the disk is reprocessed inside the spot.

$$I_{obs}(E,t) = I_p(E,t) + I_r(E,t). \tag{7.7}$$

We now compute cross-correlation functions for $I_{obs}(E,t)$ taken for the energy bands ΔE_i as defined in Ponti et al. (2004). These energy bands are summarized in Table 7.1, together with all other model constants.

On the basis of the energy bands ΔE_i, we construct light-curves L_i:

$$L_i(t) = \int\limits_{\Delta E_i} I_{obs}(E,t)dE. \tag{7.8}$$

To investigate the time-lag between the spectral response of the energy band ΔE_i and ΔE_j we compute (normalized) cross correlation functions $F^{ij}_{CCF}(\tau)$:

$$F^{ij}_{CCF}(\tau) = \frac{\int\limits_{-\tau_{max}}^{+\tau_{max}} L_i(t)L_j(t-\tau)d\tau}{\sqrt{\int\limits_{-\tau_{max}}^{+\tau_{max}} L_i^2(t')dt'} \times \sqrt{\int\limits_{-\tau_{max}}^{+\tau_{max}} L_j^2(t'')dt''}}, \tag{7.9}$$

where τ_{max} has to be sufficiently big, to lead to a converged shape of $F^{ij}_{CCF}(\tau)$. The global maximum of the cross-correlation function appears at the observed time-lag of the spectral variations between the two energy bands.

In Ponti et al. (2004), the spectral and cross-correlation analysis reveal a time-lag of ~ 600 s between the hard (ΔE_6) and soft (ΔE_1) X-ray variations. We compute a set of models in order to compare our results to the flare found by Ponti et al. (2004). Exploring parameter space will deliver some instructive insights on how the time-lags are influenced by the spectral shape of the intrinsic radiation or the emission geometry.

7.2 Modeling results

In a first step, we calculate several sets of models for the two given slopes $\alpha_p = 0.9$ and $\alpha_p = 1.3$ of I_p. We vary the intrinsic delay δ, and the normalization N of I_r. Physically, this is equivalent

to assuming different heights of the flare and different reflectivities of the hot spot. We plot the time-lag as a function of the energy bands ΔE_i. Then, we investigate the behavior of the time-lags depending on the broadening parameter b. Finally, we compare our results to the time-lags observed in MCG -6-30-15.

7.2.1 Dependencies on the intrinsic delay and on the relative normalization

We vary the intrinsic delay δ between the two pulses, δ being 500 s, 700 s, 1000 s and 1700 s. Different values of the normalization N between 0.01 and 0.9 are set. The results for the case of $\alpha_p = 0.9$ and a broadening parameter of $b = 2$ are shown in Fig. 7.3. From the cross-correlation functions F_{CCF}^{ij} we obtain the time-lags of the spectral response for each energy band ΔE_i, with $i > 1$, compared to the lowest energy band E_1 defining the origin of the scale.

It is obvious, that for the very low normalization value of $N = 0.023$, taken from radiative transfer modeling of hot spot emission, *no significant time-lags appear*. Reasonable time-lag curves, which can be compared to actual observations, only appear for values of N being higher by at least one order of magnitude. Hence, measurable time-lags in the range of minutes between the energy bands require a higher amount of reflection, than is expected for an isotropically emitting flare source. In addition to that, the following trends can be derived from the graphs:

1) As expected, the overall normalization for the time-lag curves increases with the intrinsic delay δ.

2) All time-lag curves have a positive slope, the spectra therefore evolve from softer to harder X-ray energies.

3) The level of the time-lag curves increases with the relative normalization N. However, for higher values of N, the curves start to become concave and saturate at a level, which scales with δ if δ does not become too big.

4) For very high intrinsic delays δ, the concave shape of the curves disappears again.

The first statement can be understood by the fact that δ gives a measure for the height of the flare source above the disk. For higher values of δ the reflected component appears later and the time-lags must become larger.

In order to understand the shape of the time-lag curves in more detail, we plot in Fig 7.4 model curves for I_p and I_r and their sum I_{tot}^{obs} across the defined energy bands ΔE_i. Assuming a normalization $N = 0.7$, the solid pink curve describes I_{tot}^{obs} at $t = 0$, before the two pulses, when I_p and I_r are still very low. We now imagine, that I_p increases by a certain factor, here we choose 10, while I_r remains still constant. This transforms the solid curve into the dashed one. The figure shows that I_{tot}^{obs} increases by a larger factor at the low energy bands than at higher ones. During the rise of I_p, the main changes thus happen in the soft X-ray bands, therefore their time-lags are shorter. Then the rise of the reflection component I_p follows, and the dashed curve changes into the dotted one. From the diagram it becomes clear, that now the main changes happen in the hard X-ray range, thus showing longer lags. This qualitative reasoning helps to understand the positive slope of the time-lag curves in Fig. 7.3 scaling with the relative normalization N. The concave

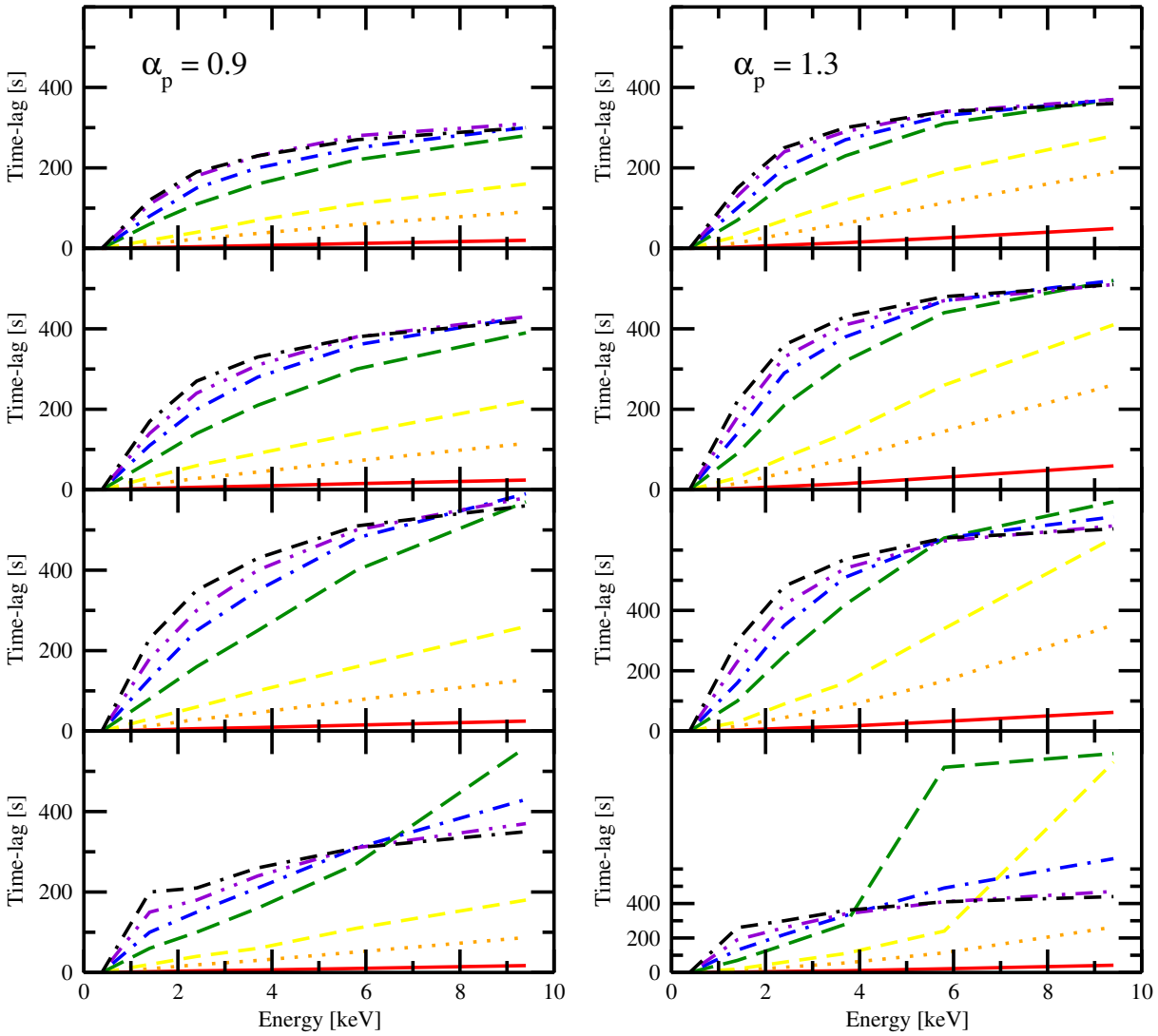

Figure 7.3: Time-lags calculated as a function of energy. The left column shows the results for the case of $\alpha_p = 0.9$, the right column for $\alpha_p = 1.3$. From top to bottom the panels were obtained for intrinsic delays $\delta = 500$ s, 700 s, 1000 s and 1700 s. The various curves denote the following values for N: 0.01 (red, solid), 0.05 (orange, dots), 0.1 (yellow, short dashes), 0.3 (green, long dashes), 0.5 (blue, dashes/dots), 0.7 (pink, dashes/double-dots), and 0.9 (black, double-dashes/dots). Note, the change in the vertical scale for the last two panels of the right column.

shape of the time-lag curve is due to the fact that the rising phases of I_p and I_r partly overlap. The variations in the hard X-ray band are thus partly caused already by I_p, which diminishes the time-lags that would be induced by I_r alone.

For low values of N, this effect is less relevant and the time-lag curves are straight lines. If the time variations of I_p and I_r do not overlap enough because δ is too high, the concave shape of the time-lag curves vanishes.

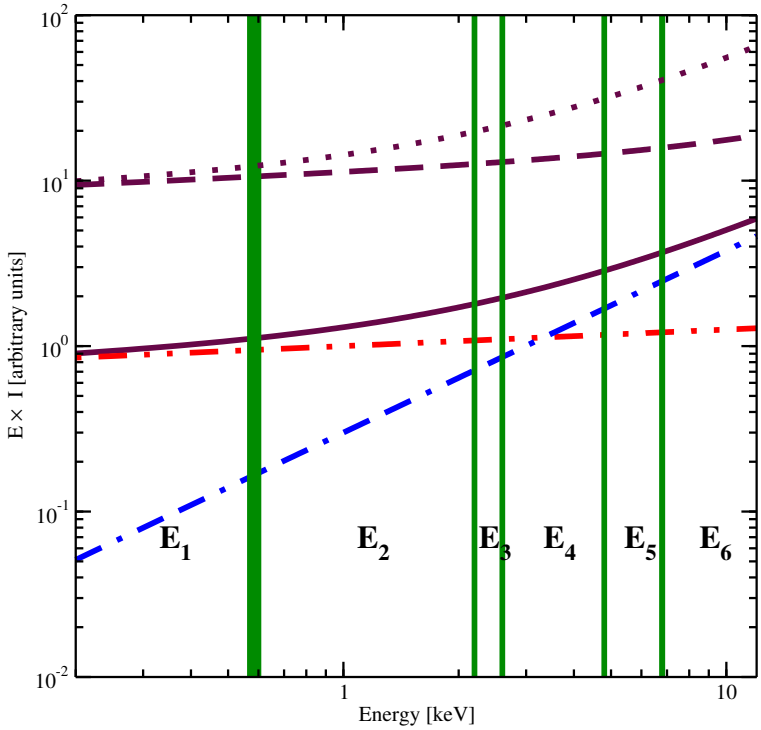

Figure 7.4: Illustration to qualitatively explain the shape of the time-lag curves obtained. The diagram shows the primary component I_p (red, dashes/double-dots), the reflection I_r (blue, double-dashes/dots), and their sum I_{tot}^{obs} (brown) before the two pulses (solid), after the rise of I_p (dashed), and after the rise of I_p and I_r (dotted). The curves are plotted on logarithmic scales and in terms of $E \times I$.

We repeat the same modeling for a steeper primary spectrum choosing $\alpha_p = 1.3$. The results are shown in Fig. 7.3 (right) and contain the same general features and tendencies than for the flatter slope investigated before. However, the overall normalization of the time-lag curves is higher and the curves are generally slightly steeper in the soft X-ray range. It is interesting to note that the overall shape of the time-lag curves and their scaling with N and δ are quite robust against changes of α_p and α_r. By obtaining sets of models for various values of these parameters, we continue to find the same qualitative shape of the time-lag curves, which have only different normalizations.

7.2.2 Influence of the broadening

We now examine the behavior of the time-lags as a function of the broadening b of the light-curve for I_r in comparison to I_p. One can imagine, that the radiation is beamed toward the accretion disk and released within a cone of a certain half-opening angle θ_0 (see Fig. 7.2). This half-opening angle determines the size of the hot spot for a given height h of the flare. In the geometry of our reprocessing model, a larger half-opening angle leads to a wider range of light-travel times between the flare source and the disk, and hence the broadening of the pulse for I_r changes. Therefore, by varying b we change the physical picture assuming a different angle θ_0, i.e. a different angular release of the primary radiation.

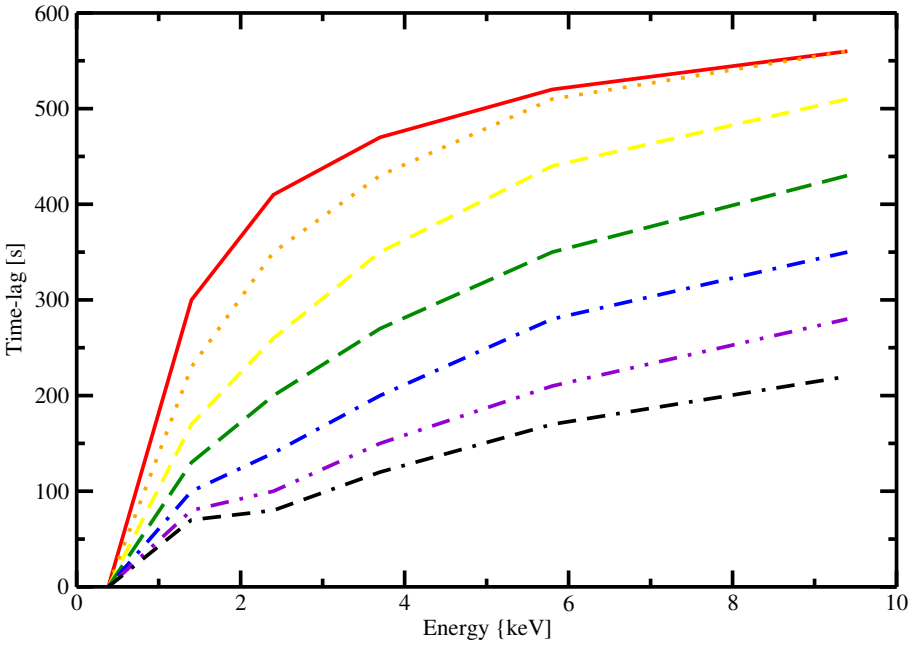

Figure 7.5: Time-lag curves derived for various values of the broadening b. The normalization Nb of the total energy released is kept constant at $Nb = 1.8$. The upper curve (solid) represents the value $b = 1.5$. From top to bottom, the value increases in steps of 0.5 for each curve and ends up at $b = 5$ for the lowest curve (dots/double-dashes).

To investigate the influence of θ_0 on the time-lags, we conduct another series of models varying the broadening parameter b. However, we would like to keep the time-integrated luminosity for the reprocessed component. Hence, for each value of b we have to find the corresponding value of N, otherwise, we would vary the half-opening angle of the flare cone and the strength of the reflection at the same time. Equation 7.6 shows, that for a constant ratio between the total primary and the reprocessed luminosity, b and N are connected by inverse proportionality. Therefore, we choose a grid of seven values for b and N with $bN = 1.8$. The resulting time-lag curves for an intrinsic delay $\delta = 1000$ s are shown in Fig. 7.5.

It can be seen, that for a given luminosity of the reprocessed component a whole range of curves for the time-lags can be obtained. Therefore, the half-opening angle θ_0 or, equivalently, the spot-size have an important impact. For larger values of b, the time-lags remain smaller. This can be explained qualitatively by the lower normalization N required to keep the same value of $bN = 1.8$. As was shown in section 7.2.1, the time-lag curves level down for lower values of N. However, the larger value of b has an impact too, due to the fact that the variations of I_r start early in time and hence, the time evolution of I_p is less ahead.

In this example, the choices of $bN = 1.8$ and $\delta = 1000$ s are more or less arbitrary. Conducting the same investigation for other values of bN delivers similar results. The overall normalization of the time-lag curves is again given by the choice of δ, as one would expect from the geometrical setup.

7.2.3 Modeling measured time-lags of MCG -6-30-15

Having described some general dependencies on the modeling parameters, we now attempt to find a model fit to the time-lags for the flare of MCG -6-30-15, as shown in Fig. 7.1 (bottom). In the preceding sections we have shown that three physical parameters have to be considered:

1) The height h of the flare source above the disk described by the model parameter δ

2) The reflectivity of the hot spot giving the normalization N of I_r with respect to I_p.

3) The half-opening angle θ_0 approximately described by the broadening factor b.

Conducting the modeling attempt of the time-lag data for the flare in MCG -6-30-15, it turns out that several combinations of values of δ, N, and b could reproduce the data with sufficient accuracy. Partly, this is due to the large error bars attached to the data points in Fig. 7.1 (bottom). But another problem is intrinsic to the toy model. We have seen in the preceding sections, that for a given δ, similar time-lag curves can be produced for quite different parameter values of N and b. This becomes clear for the case of $\delta = 1000$ s when comparing Fig. 7.3 (third panel on the left) with Fig. 7.5. Given the error bars in the data of MCG -6-30-15, obtaining an accurate fit leading to some physical constraints becomes difficult.

For higher accuracy of this modeling, an absolute normalization K of the reprocessed power with respect to the primary is required. In this case the value bN can be computed from equation 7.6, and N and b are no longer independent.

In order to obtain the value K for the specific case of the observed flare in MCG -6-30-15, it would be necessary to conduct a more detailed spectral analysis. A spectral decomposition in primary component and reprocessing with the help of a radiative transfer model would be necessary, such as explained in chapter 6. However, the flare period only lasted ~ 2000 s and the obtained spectra are not of a sufficient accuracy to allow such an investigation. Therefore, we present here, our best possible representations of the time-lag curve for the data of MCG -6-30-15, relying on individual sets of parameters. The curves are shown in Fig. 7.6 together with the time-lag data provided by Ponti et al. (2004).

The representations shown indicate that an intrinsic time delay of at least 900 s is required. This corresponds to a flare height $h \geq 2.7 \times 10^{13}$ cm. Lower values of δ did not deliver any satisfying fits.

The lower limit of the normalization N is at 0.6, hence the reprocessing has to be much stronger than expected from the modeling we conducted in chapter 6.

The broadening values range around 3 or 4, which implies that the hot spot underneath the flare should have a significant expansion.

7.3 Summary and discussion

The simple toy model we present in this chapter is capable to reproduce qualitatively the observed time-lag curve for the flare in MCG -6-30-15, as reported by Ponti et al. (2004). It turns out that the overall *shape* of the curves is rather robust against changes of the parameters. However, the *normalization* of the graphs is rather sensitive to the parameters considered here. This makes it difficult to find an appropriate fit to the observational data of MCG -6-30-15.

The intrinsic delay δ defined here can only give an upper limit of the real intrinsic delay between I_p and I_r, as this model does not include the delay induced by the reprocessing in the medium itself. The medium of the accretion disk atmosphere is optically thick and therefore the reprocessed

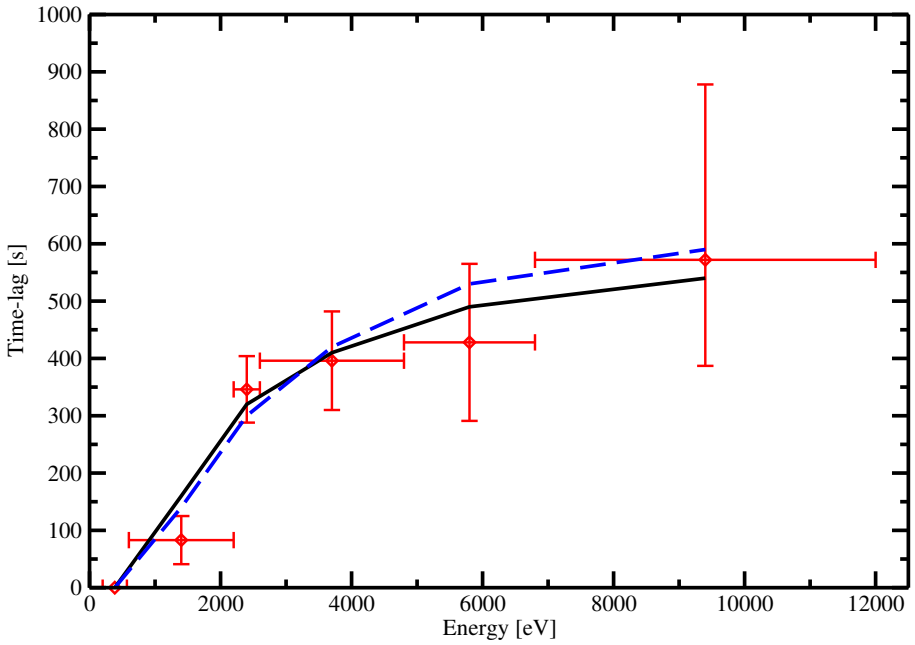

Figure 7.6: Best representation of the measured time-lags (red diamonds with error bars) for the flare of MCG -6-30-15 for our toy-model. The two curves rely on the following parametrization: $\delta = 1000$ s, $N = 0.9$, and $b = 4$ (blue dashed line); $\delta = 900$ s, $N = 0.6$, and $b = 3$ (black solid line).

photons undergo random walks and multiple scattering events. This represents another delay that would have to be added to δ if one wants to estimate the flare height h.

In chapter 6, we have shown that the shape of the local reprocessed spectrum depends on several parameters like the distance from the black hole, and the strength of the incident X-ray emission. The reprocessed spectra, shown on a logarithmic flux scale, have a convex curvature over the energy range of 0.2 keV to 12 keV. However, for this toy model, we represent them by straight lines, hence by simple power-laws with a spectral index α_r. This is a major simplification and has to be kept in mind for the interpretation of our results. The values we obtain for the fit of the flare in MCG -6-30-15 can only give a rough estimation. To obtain more accurate results, it would be necessary, to repeat a similar investigation using representations for I_r that are computed by a radiative transfer model.

Another approximation we make, is the description of the spot expansion by a simple broadening of the pulse for the reprocessed radiation. The time evolution of the reprocessing could be connected more accurately to the one of I_p on the basis of the given illumination geometry and by including also the viewing angle and the relativistic distorsions of the light rays.

However, despite these simplifications, the qualitative results we obtain are encouraging to continue this line of research and to perform more sophisticated modeling of time-lags.

Chapter 8

Modeling variability by X-ray flares

The variability of the X-ray emission is one of the basic characteristics of Active Galactic Nuclei (AGN) and expected to be an important tool in the study of the accretion process. Variability observations in the X-rays on time-scales from minutes to years have enabled the computations of power-density-spectra (PDS) for a number of AGN. In chapter 4 we have presented examples for PDS-analysis giving a hint to significant time-scales of the central engine. Nevertheless, the physical processes behind the observed variability are not established because several models can account for the average radiation spectra. The primary radiation and the reprocessed component may emerge locally from a distribution of flare spots such as investigated in chapter 6. However, we also mentioned the possibility of an extended corona, or a hot inner flow as possible sources of the primary radiation (see chapter 4).

Apparently, it is impossible to uniquely determine the accretion flow geometry on the basis of power spectra alone or just from the analysis of the mean spectral shape, as too many free parameters remain. Therefore, here we try a two-dimensional approach combining time and energy dependence. We are going to evaluate expected variability properties of an accretion disk carrying a time-dependent random distribution of individual magnetic flares. We perform Monte-Carlo simulations of such flare distribution and we compute the expected energy-dependent fractional variability spectrum F_{var}. Such spectra have started to be observed for a few AGN in so-called "long-look" observations using *XMM-Newton* or *Chandra*.

The procedure of modeling the fractional variability spectrum from Monte-Carlo distributions of flares has been applied before as described in chapter 4. The method was outlined in detail in Czerny et al. (2004). We extend the previous work by including the detailed description of the Compton reflection/reprocessed component coming from the hot spot underneath the flare source. So far, the spot irradiation was assumed to be uniform. However, in chapter 6 we have obtained new results for the local spectra including the radial spot structure. Furthermore, we include the anisotropic emission of the hot spot, while in Czerny et al. (2004) the same average spectrum was considered for all local viewing angles. We attempt to model an observed F_{var} rms-spectrum of the Seyfert-1 galaxy MCG -6-30-15.

The modeling method is described in section 8.1. We conduct a series of models to explore the dependencies of the rms-spectrum on the parameters and then attempt to reproduce the observed fractional variability of the Seyfert-1 galaxy MCG -6-30-15 (section 8.2). We sum up and discuss our results in section 8.3.

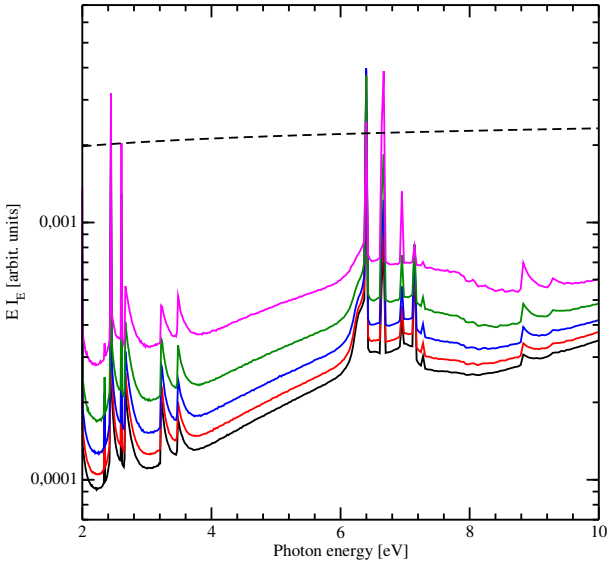

Figure 8.1: The spot spectra, plotted as intensity, integrated over the rings for five values of the local emission angle ψ: $\cos\psi$ =0.1, 0.3, 0.5, 0.7 and 0.9. From top to bottom the spectra change from an edge-on to a face-on view. The dashed line denotes the primary spectrum.

8.1 Description of the model

The computation of the fractional variability is based on several model components: the spectrum emitted by a single hot spot, the global properties of the flare distribution across the disk, and the relativistic effects due to the curved space-time in the vicinity of the black hole. In the following, we give an overview of these different model components and how they are parametrized.

8.1.1 The applied local spot spectra

In order to compute the fractional variability spectrum from a flare distribution across the disk, we first have to define the properties of a single hot spot. In chapter 6 we have presented the influence of the spot structure induced by the irradiation from a compact source. However, for the computation of a large number of spots, taking the individual spot structure into consideration is too consuming in computation time. We therefore use reprocessed spectra that are integrated over the whole spot. Such spectra are shown in Fig. 6.11. We use the integrated spectra for a spot located at $18\,R_g$ from a Schwarzschild black hole with the mass $M = 10^8 M_\odot$ and an accretion rate of $\dot{m} = 0.001$ Eddington units. As usual, R_g defines the gravitational radius $R_g = GM/c^2$ of the black hole. The incident spectrum has a power-law shape defined over 0.001 keV to 100 keV with a spectral index of $\alpha = 0.9$. The ratio of incident flux F_{inc} to disk flux F_{disk} is set equal to 144.

This parametrization corresponds to one of the cases presented in chapter 6, where the single-ring spectra are shown and analyzed. Here, we integrate the spectra over the whole spot and define it at five different local emission angles ψ, which are measured with respect to the disk normal. The angles are given in constant steps of $\cos\psi$ between 0.1 and 0.9. The locally emitted spectra we apply here are shown in Fig. 8.1.

The figure shows again the limb-brightening effect discussed in chapter 6. In the modeling

carried out by Czerny et al. (2004), this effect was not yet included and we expect changes of the variability results when taking the intrinsic anisotropy of the local emission into consideration. The inclination-dependent spot spectra of Fig. 8.1 are further adopted as representative for computations of a whole accretion disk covered with many hot spots.

8.1.2 Flare distribution

In our modeling, we assume for any given point in time a distribution of flares above the disk. The mean number of flares assumed is n_{mean}, while the actual number fluctuates around this value according to a Poisson probability distribution. We sample such spot distribution using a Monte-Carlo method. Parametrizing the disk surface by plane polar coordinates (R, ϕ), we obtain the following probability density for the appearance of a flare at a given position (R_i, ϕ_i):

$$p(R_i, \phi_i) \equiv p(R_i)\, p(\phi_i) = \frac{(\gamma_{rad}+2) R_i^{\gamma_{rad}+1}}{R_{out}^{\gamma_{rad}+2} - R_{in}^{\gamma_{\rm rad}+2}} \times \frac{1}{2\pi}. \tag{8.1}$$

Herein, R_{in} and R_{out} denote the inner and the outer disk radius. The inner radius is identical with the marginally stable orbit of the black hole. The factor γ_{rad} provides the scaling of the radial flare distribution. For $\gamma_{rad} = 0$ the distribution of flares across the disk is uniform, while for positive (negative) γ_{rad} the number of flares in the outer (inner) disk increases.

The luminosity of an individual flare and consequently the local spot radiation flux generally scales with the flare position, R_i:

$$F_{spot} = F_0 \left(\frac{R_i}{R_{in}} \right)^{-\beta_{rad}}, \tag{8.2}$$

where F_0 is a normalization constant measuring the incident flux at R_{in}. The dissipation within the Keplerian disk varies as r^{-3} so the typical value of $\beta_{\rm rad}$ is expected to be of that order. The duration of the flare may also depend on the flare location, so we describe it as:

$$t_{life} = t_{life_0} \left(\frac{R_i}{R_i n} \right)^{\delta_{rad}}. \tag{8.3}$$

Here $\delta_{rad} = 0$ means that the flare lifetime is independent from the flare location while for $\delta_{rad} = 1.5$ the flare lifetime scales with the local Keplerian timescale. The observational appearance additionally depends on the duration of the observation (i.e. integration time) and the inclination angle of an observer with respect to the disk symmetry axis. The black hole mass M also enters as a parameter because all distances and timescales scale with M.

The flare distribution is fully described by the model parameters: M, n_{mean}, R_{in}, R_{out}, r_{spot}, F_0, β_{rad}, γ_{rad}, δ_{rad}, and t_{life_0}. The spot radius r_{spot} can be expressed, if convenient, in terms of the mean X-ray luminosity of the source, L_X because

$$L_X = \sum_i \left[\pi r_{spot}^2 \sum_j F_{spot}(R_i, \psi_j) \right], \tag{8.4}$$

for a given flare distribution. Herein, the angle-dependent local flux F_{spot} is summed over the five local emission angles ψ_j of one hot spot that we obtain from the model spectra presented in chapter 6.

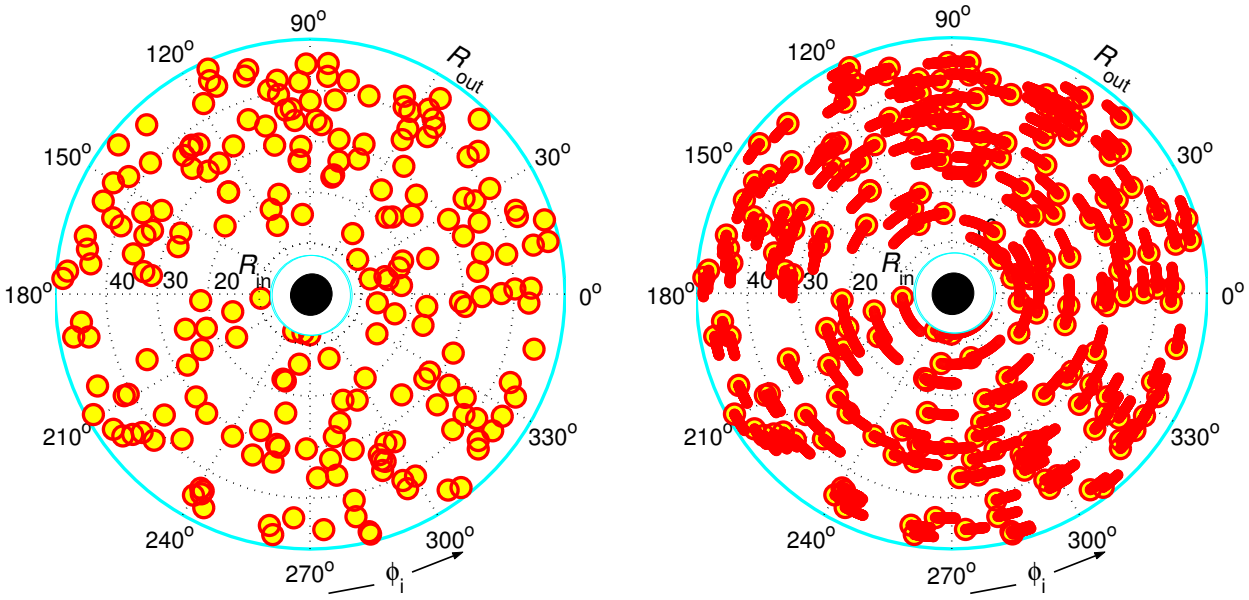

Figure 8.2: Illustration of a flare distribution at a given point in time (left) and smeared out over a certain time period (right). The individual spots describe arches determined by the corresponding flare life time and by the local Keplerian velocity (Czerny et al., 2004).

8.1.3 Ray-tracing and time integration

The observed spectra from a spot distribution are expected to be significantly modified due to effects of general relativity and photon energy shifts induced by the orbital motion. The influence of such effects has been discussed in chapter 6. For the calculation of the fractional variability spectrum we would have to construct time resolved sequences of spectra for each hot spot of the distribution. However, such an integration over the disk surface is very time-consuming - hence we look for a more efficient way to compute the rms-spectrum.

In fact, in order to model observational data, it is not needed to have a perfectly resolved light-curve for every spot, because X-ray observatories collect the data over integration times ΔT of the order of a few thousands of seconds. Therefore, within each time bin we consider the onset, orbital motion, and fading of each spot by smearing it out along a belt on the disk as illustrated in Fig. 8.2. The spots are in Keplerian motion during their lifetime t_{life} and therefore they circumscribe an arch of the length $\Delta\phi(R) = \Omega_K(R)t_{life}$. Herein, Ω_K denotes the Keplerian velocity at disk radius R. From the integrated local spectra presented in section 8.1.1 we can then compute the total flux F_{belt} of one belt according to:

$$F_{belt}(\psi) = \frac{\pi r_{spot}^2}{2 r_{spot} R_i \Delta\phi(R_i)} F_{spot}(\psi), \tag{8.5}$$

where the fraction measures the ratio between the surface of an individual spot and of the belt. Note, that the above equation is depending on the local emission angle ψ.

The total "observation time" for our model is now divided into integration intervals ΔT_k. For each of such time bins, the emissivity distribution of the accretion disk is given by the ensemble

of belts falling into the time interval ΔT_k. The code *KY* (see chapter 5) conducts the relativistic ray-tracing based on the modeled ensemble of belts and thus produces a time sequence of "observed" spectra $S_k(E)$. We calculate N of such sequences. Each sequence is based on a flare distribution sampled by our Monte-Carlo routines. Usually, we adopt $N = 50$ since this corresponds to the best long lightcurves of the total duration of a few hundred thousand seconds. From such time-sequences of spectra the rms-spectrum can be derived. We calculate the fractional variability spectrum F_{var} as applied by Ponti et al. (2004) for the analysis of a 95 ks *XMM-Newton*-observation of the Seyfert-1 galaxy MCG -6-30-15. This definition of the rms-spectrum emphasizes the character of the long-term variability timescale. It is calculated by:

$$F_{var}^2(E) = \sum_{k=1}^{N} \frac{(S_k(E) - < S(E) >)^2}{(N-1) < S(E) >^2}, \tag{8.6}$$

where N is the number of time bins and $S_k(E)$ is the spectrum belonging to the time bin ΔT_k.

In the previous modeling of Czerny et al. (2004), the sampling of belts for one time bin happened independently of the time bins before or after. Each ΔT_k therefore corresponded to an entirely new distribution of flares. This is a correct approach, when compared to observations for which the data of each time bin are not collected within one long observation. Also, for the case that the flare life-times are significantly shorter than one time bin the approach is valid. However, some spots may live longer than a given ΔT_k. In the current version of the model, the belts are therefore cross-checked with the limits of each time bin and, if necessary, they "survive" for two or even more time intervals.

8.2 Modeling results

In a first step, we compare the rms-variability using the single-spot spectra obtained in chapter 6 with the previous models of Czerny et al. (2004) based on semi-isotropically irradiated, uniform spots. Then, we investigate the resulting rms-spectra for various parameter configurations of the model and compare our results to actual observations of MCG -6-30-15.

8.2.1 Effect of the spot structure and non-isotropic emission

We compute two fractional variability spectra for the same model configuration differing only in the emissivity structure of the spot. In one model, the spots are uniform and the locally emitted spectra have no angular dependence (as applied in Czerny et al. (2004), see their Fig. 2). In the second model the integrated spectra from a structured spot defined at several local emission angles (see section 8.1.1) are adopted. The results are plotted in Fig. 8.3, where the upper panel shows rms-spectra for a Schwarzschild black hole with $M = 10^8 M_\odot$, while the lower panel represents an extreme Kerr black hole of the same mass but with $a = 0.998$. The flare distribution is characterized by the following parameters: the inner radius R_{in} of the distribution is set equal to the marginally stable orbit, the outer radius to $R_{out} = 50\, R_g$, where the impact of the relativistic effects is supposed to be much lower. The radial distribution parameter is $\gamma_{rad} = 0$, hence the distribution of the flares is uniform across the disk. The flux scales with the Keplerian velocity of the disk as $\beta_{rad} = 3$ and the life time of the flares is set to $t_{life_0} = 10^5$s with $\delta_{rad} = 0$. We assume a total X-ray luminosity of all flares of $L_X = 10^{44}$ erg s^{-1} and a mean number $n_{mean} = 30$ for the Schwarzschild black hole and $n_{mean} = 100$ for the Kerr case. The number of time bins is $N = 300$, each of them having a width

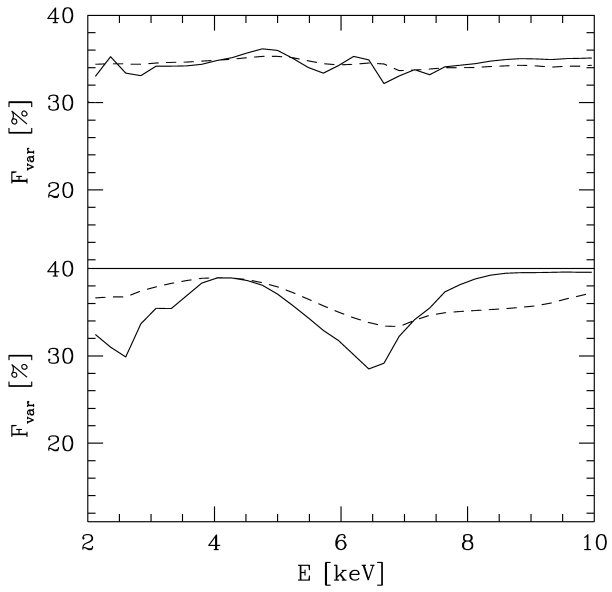

Figure 8.3: Fractional variability amplitude for a Schwarzschild black hole (upper panel) with a mean flare number $n_{\rm mean} = 30$ and for a maximally rotating Kerr black hole with $n_{\rm mean} = 100$ (lower panel). The dashed lines represent computations for uniform, isotropically radiating spots, while the continuous lines present the model of structured, non-isotropic spots. The other model parameters are given in the text.

of $\Delta T_k = 10^5$ s. The disk inclination with respect to a distant observer is $i = 30°$. Only the pure reprocessed emission from the spot is used to compute the rms-spectrum, no primary contribution is assumed.

The difference between the Schwarzschild and the Kerr black hole lies mainly in the normalization. However, a profound change is introduced when switching in between the two sorts of local spectra. For the structured spots with isotropic emission, a stronger energy dependence of the rms-spectrum appears. This is promising from the point of view of modeling the data. The model of Czerny et al. (2004) predicted a far too shallow dependence on energy in comparison with observations of MCG -6-30-15. This can be explained by the much stronger reprocessing features in the spectra used in the new version of the model. As described in chapter 6, the strong emission lines result from the fact that the medium is now assumed not to be irradiated *before* the onset of the flare. In the previous version of the model, the local spectra were computed from a disk-structure in hydrostatic equilibrium *with* the irradiation. The medium was less dense and hence the resulting emission lines were weaker.

The increase of the fractional variability with the strength of the emission lines can be understood from the relativistic line broadening in combination with the orbital motion of the hot spots. We have seen in chapter 6 that the line broadening is particularly strong for hot spots close to the black

hole. For these spots, also the Doppler energy shift of the line centroid is important. The resulting emission lines are strongly broadened, their central part do not have a prominent maximum but rather present a flat plateau - the energy shift due to the orbital motion therefore does not change the spectrum significantly at the line core. However, the situation is different in the line wings, where the spectra are much steeper. Then, the energy shift produces stronger variability when the spot emission is integrated over a significantly long belt.

Furthermore, the included angular dependence of the reprocessed emission from the spot together with the effects of relativistic light-bending plays a role, especially for spots completing a larger fraction the entire orbit. In these cases, the radiation detected for a given inclination can sum up from trajectories that correspond to several local emission directions.

We also calculated $F_{var}(E)$ taking into account the contribution of the primary emission from the flare. However, for computational convenience, the primary source is not elevated above the accretion disk but added to the central part of the spot. Since here we do not include the time-lag effects due to the distance between the flare source and the hot spot, and since this distance is supposed to be small compared to the disk region considered, we still obtain a good approximation for the rms-spectrum. The relative level of the additional primary component is chosen assuming isotropic flare emission. Hence, no beaming of the primary component is involved. For the dilution with the primary component, the rms-spectra turn out to be weaker as the reprocessed spectrum contributes less to the total spectrum than the primary does. This is due to partial absorption in the disk. Hence, in the fractional variability the smoothly shaped primary component dominates, which produces less energy-dependent variability and hence F_{var} decreases.

8.2.2 Dependencies on the model parameters

The position of the features in F_{var} and their shape strongly depend on the relativistic effects. Hence, the observed features should give constraints on both the inclination angle i of the disk and on the black hole spin a. A larger inclination tends to move the features towards higher energies while a faster black hole rotation produces slightly broader and much deeper features.

A strong suppression of F_{var} at $\sim$ 6.5 keV, in the range of the iron Kα-line, appears if the radiation is strongly concentrated toward the disk center. For a constant flare life time with $\delta_{rad} = 0$, the dip $\sim$ 6.5 keV becomes stronger, when the spot brightness radially decreases like the standard disk dissipation rate, which means $\beta_{rad} = 3$, and the flares are distributed uniformly across the disk surface, meaning $\gamma_{rad} = 0$. In Fig. 8.3 we show an example of this behavior by the continuous line. If β_{rad} is considerably larger, e. g. $\beta_{rad} \sim 4.5$, the same pattern is seen even for flare life times scaling with the local Keplerian value given by $\delta_{rad} = 1.5$. The parameters γ_{rad} and δ_{rad} act predominantly in the same way because having more flares at larger distances is roughly equivalent to longer flare life times at large radii. However, the effect of the two parameters is not strictly identical. The situation is similar with β_{rad} and γ_{rad}: a decrease in β_{rad} is roughly equivalent to a decrease in γ_{rad}.

Summarizing, the most important property of the given parameter set is the sum of the parameters, $2 + \gamma_{rad} + \delta_{rad} - \beta_{rad}$. It represents the index of an effective radial distribution of energy generation, as the total energy produced per unit is proportional to the product of the right hand-sides in equations 8.2, 8.3, and 8.4. If this value is negative, the model is likely to show a suppression of the variability around 6 keV. If this value is positive, the model is likely to show complex behavior around 6.5 keV in F_{var}, as seen in Fig. 8.3. However, the specific values of all other model parameters are also important to some extent.

The mean number of flares affects mostly the overall normalization of F_{var}. The normalization of the flare life time distribution, t_{life_0}, also has an impact on the overall normalization of the variability: larger values of t_{life_0} require larger values of n_{mean} to achieve the same overall variability level. However, the timescale also influences the energy dependence of F_{var}. If the timescales are too short the energy dependence in the variability is smeared.

As one can tell from the preceding description, the overall interplay of the model parameter is complex, however, we were able to find a few major guidelines being of assistance for comparison of our model to actual data.

8.2.3 Intrinsic randomness in the model

Exploring the rich parameter space of this model revealed an important property of our simulations: they contain a considerable *intrinsic randomness* in the results for some model parameters and they are *relatively stable* for others. The effect is shown in Fig. 8.4, where we illustrate the results for two sets of parameters. In the first set, shown in the upper panel, the spot brightness decreases with the radius as $\beta_{rad} = 3$, in the second set, plotted in the lower panel, with $\beta_{rad} = 2$. We adjusted the mean number of clouds in each model to have roughly the same level of variability. We had to assume $n_{mean} = 125$ for the first model and $n_{mean} = 30$ for the second one, while all other model parameters were the same in both cases: $M = 10^7 M_\odot$, $a = 0.95$, $L_X = 8 \times 10^{43}$ erg s^{-1}, $i = 30°$, $R_{out} = 50\, R_g$, $\gamma_{rad} = 0$, $\delta_{rad} = 1.5$, $t_{life_0} = 2 \times 10^4$ s, $T_{obs} = 6146$ s, $N = 50$.

For both parameter sets we sampled five 300 ks long time sequences and calculated F_{var} for each of the sequences independently. The expected statistical one sigma errors were marked for one of the curves only, for clarity. These errors are determined for a *single* simulated lightcurve. In our simulations we use a fine energy grid of 800 points over the energy range between 2 keV and 10 keV. The dimensionless value of $F_{var}(E)$ is determined at each energy point. When we compare the model result to observational data, we bin the results using broader energy bins. If n original energy points contribute to the new energy bin centered around E_k we introduce:

$$\delta F_{var}(E_k) = \sqrt{\frac{\sum_{i=1}^{n} F_{var}(E_i)^2 - n F_{var}(E_k)^2}{n^2} + \frac{(F_{var}(E_k)^2 + 1) F_{var}(E_k)^2}{n(N-1)}} \tag{8.7}$$

This error does not take into account the errors due to limited length of a single sequence which are modeled by comparing many different statistical realizations of the lightcurve.

In Fig. 8.4, we can see that the curves in the upper panel are roughly similar, and they do not differ more than expected from the simple error analysis. However, the curves in the lower panel differ rather widely. It means that for such a set of model parameters we cannot use a single lightcurve, with standard error description, in order to estimate whether the model well represents any specific data. This effect is still stronger for the observed rms-spectrum of MCG -6-30-15 data covering only 95 ks instead of 300 ks, as adopted in these simulations.

The intrinsic randomness is due to the different total mean numbers of flares required for the two data sets. Since the flare duration distribution was the same in both models, the total, time-integrated number of flares in the lightcurve is 726 for the first set of parameters and only 174 for the second one. The standard determination of the statistical error δF_{var} of course does not include this effect. This result supports the conclusion given by Vaughan et al. (2003) who also did Monte-Carlo simulations of lightcurves and found out that the overall normalization of the variance is rather unreliable. However, our energy-dependent calculations indicate that although the *overall*

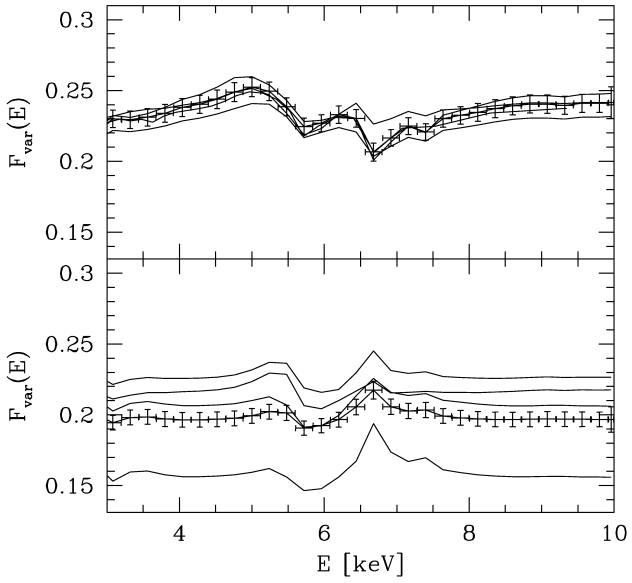

Figure 8.4: Fractional variability calculated from different sets of lightcurves obtained separately for the same model configuration. The formal errors are given for one of the curves. Upper panel: $n_{mean} = 125$, $\beta_{rad} = 3$, lower panel: $n_{mean} = 30$, $\beta_{rad} = 2$. The other model parameters are set to: $M = 10^7 M_\odot$, $a = 0.95$, $L_X = 8 \times 10^{43}$ erg s^{-1}, $i = 30°$, $R_{out} = 50\, R_g$, $\gamma_{rad} = 0$, $\delta_{rad} = 1.5$, $t_{life_0} = 2 \times 10^4$ s, $T_{obs} = 6146$ s, $N = 50$.

level of the F_{var} changes strongly for some sets of parameters, the *shape* of F_{var} varies less from sequence to sequence. The energy pattern is roughly preserved and can be used to estimate the source properties.

Since our conclusion is based on a specific flare model we want to compare the trend to the sampling effects in real data. In Fig. 8.5 we show three $F_{var}(E)$ plots obtained by division of a single 325 ks long lightcurve of MCG -6-30-15 into three equal parts. This observations was taken by *XMM-Newton* and reported by Fabian et al. (2002). The fractional variability spectrum $F_{var}(E)$ was calculated for each of the three parts independently. The overall change in the variability level of the three sub-sequences compared to the full time-sequence is about 50%. However, most of the variability is in overall $F_{var}(E)$ normalization, the shape actually varies much less, although some changes in energy dependence are also seen. The variability is always suppressed just above 6 keV but one of the sets does not show the complex structure in the band between 4 keV and 6 keV.

This analysis shows that also the observational errors are actually much larger than indicated by simple statistical analysis of a given single curve. However, the errors in the shape are not as large as the overall change of fractional variability amplitude from one to another time sequence due to the long timescales present in the system. Of course, an increase of the duration of observation

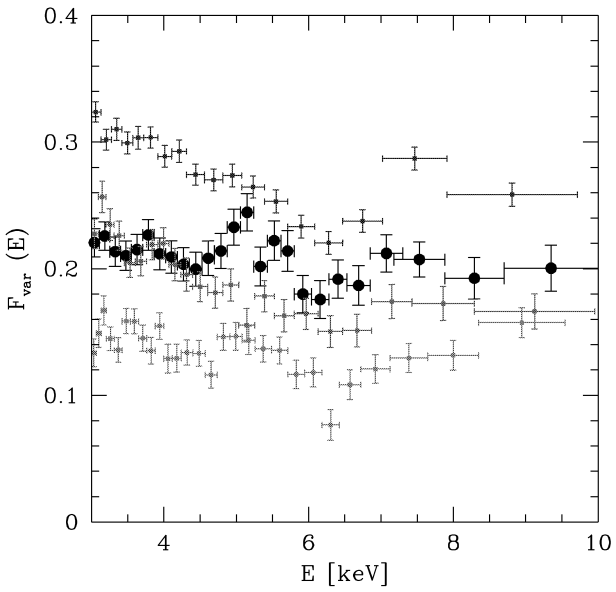

Figure 8.5: Fractional variability calculated independently for three separate parts of the 325 ks lightcurve of MCG -6-30-15 reported by Fabian et al. (2002) (thin points). The set with filled circles represents the result obtained from the 95 ks lightcurve obtained by Wilms et al. (2001). The time bins are 6146 s wide.

would give less scatter. But this requirement may be difficult to meet. The model from the lower panel of Fig. 8.4 gives results for F_{var} almost within the statistical errors of a single lightcurve if the number of time bins is increased to $N = 300$, corresponding to a real-time observation of roughly 20 days.

8.2.4 The rms-spectrum of MCG -6-30-15

We apply our Monte-Carlo flare model to an observed rms-spectrum of the Seyfert-1 galaxy MCG -6-30-15. A long X-ray exposure lasting 95 ks was obtained with *XMM-Newton* for this source and reported by Wilms et al. (2001). Its time variability was analyzed in detail by Ponti et al. (2004) who also computed the rms-spectrum (see Fig. 3.10).

In our simulations, we adopt $N = 16$ time bins having a width of $\Delta T_k = 6146$s. These values have also been used in the computations of F_{var} done by Ponti et al. (2004). We set the black hole mass to $10^7 M_\odot$, and the X-ray luminosity of the source to $L_X = 8 \times 10^{43}$ ergs s^{-1}. We assume an inclination of $i = 30°$ and a high black hole spin of $a = 0.95$. All these parameters correspond to the current picture of MCG -6-30-15 as discussed in the literature. We suppose a uniform density of spots across the disk by setting $\gamma_{rad} = 0$. The outer disk radius is fixed to a relatively large distance of $R_{out} = 50\, R_g$, where we expect the relativistic effects to play a minor role.

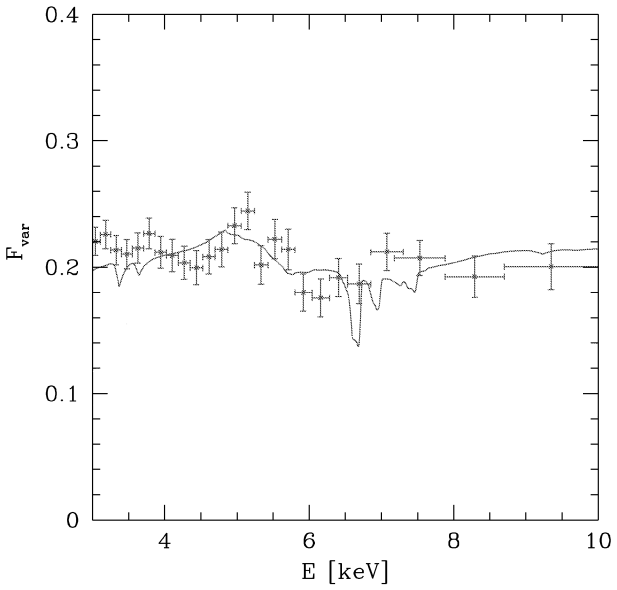

Figure 8.6: Best model of F_{var} (continuous line) compared to the corresponding data (dots with error bars) given by Ponti et al. (2004). We obtained the following model parameters: $\beta_{rad} = 3$, $\gamma_{rad} = 0$, $\delta_{rad} = 1.5$, $t_{life_0} = 2 \times 10^5$ s, $n_{mean} = 100$. The other parameters are at their standard values as given in the text. The model is shown unbinned for clarity.

In Fig. 8.6 we show the best representation of the standard $F_{var}(E)$ of MCG -6-30-15 we found among a very large set of sampled models. It roughly reproduces the observed "wiggles" of the F_{var} obtained from the whole lightcurve. The model parameters reveal the interesting facts that the flare life time scales with the Keplerian time scale, the flux of the individual flares scales with the energy dissipation in the disk, and the spot distribution over the disk is uniform. However, due to the intrinsic randomness of our modeling discussed in the previous section 8.2.3, we do not obtain an accurate fit but rather a semi-quantitative analysis of the rms-spectrum.

8.3 Summary and discussion

In this chapter, we study the time-dependent spectra from a multi-flare model using the energy-dependent fractional variability amplitude F_{var} as a diagnostic tool. We show that the model can explain a decrease in the variability level at $\sim$ 6.5 keV derived from the rms-spectra of Seyfert galaxies, such as MCG-6-30-15 (Inoue & Matsumoto, 2001; Vaughan & Fabian, 2004; Ponti et al., 2004). A similar behavior was observed in Mrk 766 (Pounds et al., 2003) and several other objects listed in Markowitz et al. (2003).

The overall variability level predicted by the multi-flare model expressed in terms of F_{var} depends

strongly on the adopted number of flare-spots. By adjusting this number, the model is capable to reproduce the overall normalization of observed rms-spectra as we demonstrated for the case of MCG -6-30-15. However, the form of the energy dependence of F_{var} is more difficult to adjust and provides a strong diagnostic tool either for proof or for falsification of our model.

The prediction of the multi-flare model for the shape of F_{var} depends predominantly on the radial profile of the energy dissipation characterizing a given set of parameters (see section 8.2.2). If the energy dissipation in the form of flares weighted within the emission area decreases with the radius the model shows a suppression of the variability at 6.5 keV. This can be qualitatively understood considering the hot spots at the innermost parts of the disk.

The present data predict the rms-spectrum F_{var} with a significant error, mostly due to the importance of timescales much longer than a typical lightcurve (Vaughan et al., 2003). The errors in the shape of the energy dependence seem to be lower but still rather difficult to determine observationally.

There are still certain inconsistencies present in our model. The local computations were performed for a black hole mass $10^8 M_\odot$ although for MCG a smaller mass is more appropriate. In our computations we assumed $10^7 M_\odot$ for the mass of the central black hole, and McHardy et al. (2005) suggested even a smaller value, $\sim (3-6)\times 10^6 M_\odot$). However, we do not expect strong direct dependence of the local spectrum on the black hole mass. The computations were performed at a single radius of $18R_g$ but from the results in chapter 6 we derive that the local spectra calculated at $7R_g$ do not differ strongly when computed for the same ratio between flare flux and disk flux at the hot spot center. Therefore, for models calculated with this ratio preserved, i.e. models with $\beta_{rad} = 3$, we do not introduce a large error. However, for models with different values of β_{rad} the local spectrum may be different, so a range of local models should be actually calculated to incorporate this effect.

We have found that our multi-flare model with a time-independent shape of the energy spectrum of the flare emission provides an interesting interpretation of the drop in the variability around 6.5 keV. But there are also other models under discussion. The energy-dependent form of the variability was also modeled as a variable primary emission with constant reflection (e.g. Taylor et al., 2003; Shih et al., 2002). However, in this class of models it is difficult to explain why the reflection component should be constant since either it forms close to the black hole, i.e. close to the source of the primary emission, and should respond to changes of the primary, or it forms far away, but then it is difficult to explain why it is relativistically broadened. An attractive way out of this paradox was proposed by Martocchia et al. (2001), Miniutti & Fabian (2004), and Miniutti & Fabian (2005), who describe a model where the change in the primary intensity is predominantly due to the minor changes in the position of the source of the primary radiation on the disk rotation axis, which gives effects strongly enhanced due to general relativity.

Chapter 9

Modeling the warm absorber

In this last chapter presenting the modeling results we obtained during the preparation of this thesis, we switch focus and take into consideration the warm absorber. We pointed out in chapter 3.1.3 that the warm absorber in several Seyfert-1 galaxies has been successfully modeled assuming two or three absorbing, constant density clouds on the line-of-sight. This was the case for NGC 4051 (Collinge et al., 2001), for NGC 5548 (Kaastra et al., 2002), and for NGC 3783 (Kaspi et al., 2002; Krongold et al., 2003). In NGC 3783, the two phases of the warm absorber differ significantly in temperature and ionization state. However, it was shown that they appear to be in pressure equilibrium (Netzer et al., 2003; Krongold et al., 2003).

The actual properties and particularly the dynamics of the warm absorber continue to be a matter of debate. The blueshifted absorption lines observed emphasize the fact, that the material is outflowing. Several suggestions for the origin of such outflows have been made, for instance evaporation of "bloated stars" (Netzer, 1996), or winds blowing of the inner edge of the torus (Krolik & Kriss, 1995, 2001). Such outflows are very likely to create turbulences, hence they would become inhomogeneous. The modeling approach assuming a constant density therefore should not be valid throughout the whole medium, which is observationally confirmed by the fact, that the above-mentioned models always need several thermal phases.

In summary, it is thus possible to think of the warm absorber as a continuous medium of constant total pressure, with position-dependent density and temperature. Therefore, for the modeling presented in this chapter, we assume the warm absorber to be in *total pressure equilibrium*. Total pressure P_{tot} means here the sum of gas pressure P_{gas} and radiation pressure P_{rad}. This condition imposes a physical equilibrium on the absorbing gas that still allows a wide range of densities and temperatures to coexist along the same line-of-sight.

The chapter is organized as follows: in section 9.1 we present the setup of our model and describe the parameters we vary. It turns out that a brief discussion about the impact of thermal instabilities is important for modeling of a warm absorber at constant pressure (section 9.2). We then give results for the structure of the absorbing material (section 9.3). We present spectral results in section 9.4 and discuss our modeling in section 9.5. Further details about the modeling we present here can be found in Różańska et al. (2005).

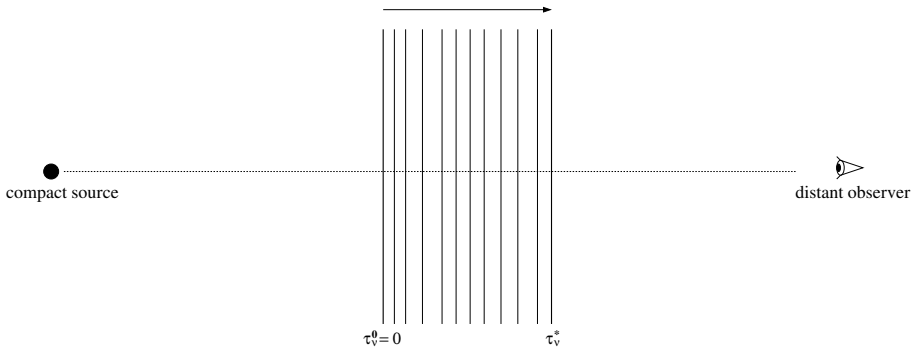

Figure 9.1: Setup for our warm absorber modeling. The absorbing medium is represented by a plane-parallel atmosphere seen in transmission and irradiated from the back-side by a compact source. The medium is stratified along its optical depth τ.

9.1 Description of the model

We use the radiative transfer codes *TITAN* and *NOAR* (see chapter 5) to conduct our modeling. The warm absorber is located relatively far from the black hole - lower limits of a few light days were given for its distance to the central engine (Krolik, 2002). Hence, we do not have to consider relativistic corrections at all. The condition of constant total pressure is considered in *TITAN* computing the density-, temperature-, and ionization-profile of the medium.

Geometrically, we assume that the warm absorber is given as a plane-parallel slab illuminated from the back-side as shown in Fig. 9.1. Although, *TITAN* and *NOAR* can be applied to multi-angle radiative transfer, we only consider the component seen in transmission. This also justifies the geometrical approximation of the medium as a plane-parallel slab. In reality, the geometrical shape of the warm absorber surely is more complex, but would only have to be taken into account if we considered emission from parts of the medium that are not on the line of sight.

In a first approach to investigate the warm absorber using the condition of constant total pressure, we compute a grid of models for three different parameters:

the index α of the incident power-law spectrum $I(\nu) \propto \nu^{-\alpha}$,

the total column density N_H of the absorbing medium,

the ionization parameter ξ.

Here we recall the definition of the ionization parameter including the total incident flux F_{inc}, integrated over all frequencies, and the number density n_H of the medium at the irradiated surface:

$$\xi = \frac{4\pi F_{tot}}{n_H} = \frac{L}{r^2\, n_H}. \tag{9.1}$$

In the alternative formulation, L denotes the luminosity of the central illuminating object and r its distance to the medium. For our modeling, we assume a low surface density of $n_H = 10^{11}\mathrm{cm}^{-3}$ to define the "inner border" of the slab. As the density structure is computed self-consistently during the run of *TITAN*, we tested that varying n_H does not have a significant impact on determining the thermal profile of the medium. It turned out that this is the case for low values around $n_H = 10^{11}\mathrm{cm}^{-3}$.

In the choice of the parameter space to explore, we take into account existing observational constraints. We attempt to calculate a grid of models with the following parameters:

For the spectral index we consider the three values $\alpha = 0.5$, 1.5, and, 1.5.

For the total column density, we compute models for the range of $\sim 10^{21}\mathrm{cm}^{-2}$ —$10^{24}\mathrm{cm}^{-2}$.

For the logarithmic value of the ionization parameter ξ we adopt the values 3, 4, and 5.

It turns out, that the occurrence of thermal instabilities restricts the possible range for N_H. We are going to discuss this problem in the following section 9.2.

The incident spectrum is defined between 10 eV and 10000 eV. Observationally, the hard X-ray part does not reveal any spectral features of the warm absorber, but it is included because it contributes to the Compton heating profile and therefore to the thermal and ionization structure of the medium. We assume solar abundances of all elements.

9.2 The difficulty of thermal instabilities

The first result of our modeling is that we confirm some principle restrictions that are due to thermal instabilities. It has been known for a while that such instabilities may occur, when hard X-ray radiation penetrates through a medium with a significant metalicity being comparable to solar values. Imposing a constant density throughout the medium suppresses such instabilities - hence, they are no problem in constant density models. However, in the case of constant pressure we have to take them into consideration.

The development of thermal instabilities has been discussed in Field (1965) and Krolik et al. (1981). It can be understood from the so-called *instability curve* shown in Fig.9.2. The S-shaped graph represents equilibrium states for a range of temperatures and ionization parameters Ξ. Note that the definition of the ionization parameters differs from ours given above. Following Krolik et al. (1981), Ξ is defined by:

$$\Xi = \frac{F_{tot}}{ckn_H T} = \frac{P_{rad}}{P_{gas}}, \tag{9.2}$$

with k being the Boltzmann constant. The values P_{rad} and P_{gas} denote the pressure exerted by the radiation and by the gas at the surface of the medium. The above relation of the pressure components to the ionization parameter Ξ only holds if the radiation is confined to a small solid angle and is normally incident upon the medium (Krolik et al., 1981). The expression Ξ of the ionization parameter relates to our previous definition of ξ by:

$$\Xi = \frac{\xi}{4\pi ckT}. \tag{9.3}$$

Again, Ξ and ξ are the surface values. The instability curve or *S-curve* can be constructed by taking into account heating and cooling processes due to the incident spectrum F_{tot} while imposing P_{tot} =const. This leads to a correlation between T and Ξ that, for a certain parameter range, delivers several possible solutions of T. The fact, that the Ξ-T is partly not uniquely defined is due to the complex behavior of the heating and cooling processes.

Let us consider some distinguished parts of the instability curve: for maximum values of T and Ξ the medium is *hot*, highly ionized, and the cooling processes are dominated by free-free emission

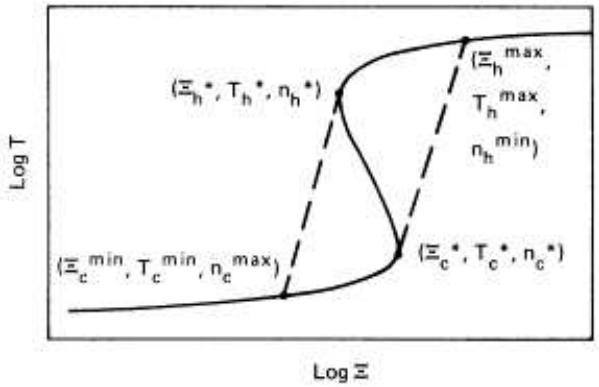

Figure 9.2: The instability curve, or S-curve, given by Krolik et al. (1981) showing the correlation between temperature T and ionization parameter Ξ. A functional relation $T(\Xi)$ is not well-defined in the regime between the two dashed lines. Only for very hot states of the medium (index h) and for cool states (index c) the relation between T and Ξ is exact.

and inverse Compton scattering giving an exact functional relation $T(\Xi)$ that builds the upper-right part of the curve. The density is at its minimum value in this regime. A similar situation is given for very low values of T and Ξ, when the medium is *cold*, close to being neutral, and the balance between heating and cooling is predominantly due to atomic processes. This parameter range defines again an exact functional relation $T(\Xi)$ for the lower-left part of the S-curve and produces a state of maximum density.

The situation becomes more complex for intermediate values of T and Ξ, as then the heating and cooling processes go through a critical regime and allow several solutions of the temperature for a given ionization parameter. This critical range is denoted by the strip between the dashed lines in Fig. 9.2. Critical high values (T_h^*, Ξ_h^*, n_h^*), and low values (T_c^*, Ξ_c^*, n_c^*) denote the limits of the instability range, and a physical medium with parameters in between these limits allows regions of strong thermal difference to coexist.

While offering a "real" physical option for a warm absorber in pressure equilibrium, the thermal instabilities present a major computational difficulty... Radiative transfer codes are based on exact solutions of self-consistent differential equations, which cannot be found when the medium is thermally unstable. The only solution for our modeling lies in a restriction of the parameter values in order to avoid entering the instability range. We therefore investigated for which combinations of α, N_H, and $\xi \propto \Xi T$ the medium became unstable and excluded these cases from our grid.

Computationally, the appearance of thermal instabilities reveals itself by the fact that the transfer code *TITAN* does not manage to converge. The temperature profile for a specific range of the medium does not approach an asymptotic value but oscillates between possible solutions for T. These solutions correspond to the "S-part" of the instability curve where the relation between Ξ and T is not exact.

However, it also turned out that the occurrence of thermal oscillations is correlated to the total column density N_H, and therefore the total optical depth of the medium. For two given values of ξ and α, it is possible to find a maximum column density N_H^{max}, so that *TITAN* converges for all N_H with $N_H < N_H^{max}$. The values of N_H^{max} for all combinations of ξ and α are summarized in Table 9.1.

Luckily, the thermal instabilities can be avoided for a significant range of N_H. Therefore it

Table 9.1: Maximum column densities N_H^{max} below which no thermal instabilities occurred for the modeling of a warm absorber in pressure equilibrium.

α	$\log \lvert\xi\rvert$	$\log \lvert N_H^{max}\rvert$
0.5	3	22.6
1.0	4	22.5
1.5	5	23.8
0.5	3	23.2
1.0	4	23.4
1.5	5	23.5
0.5	3	23.5
1.0	4	23.6
1.5	5	24.0

makes sense to conduct the investigation, even though the parameter range is more restricted than originally intended.

9.3 The structure of the warm absorber

In this section we are going to present our modeling results for the structure of the warm absorber medium. In Fig. 9.3 we show the temperature profile for all nine parameter combinations of ξ and α. The curves represent increasing values of N_H for $N_H < N_H^{max}$. In the horizontal direction, from left to right, the figure shows the temperature profiles for the three parameter values of $\log|\xi| = 5$, 4, and 3. In the vertical direction, from top to bottom, the spectral indexes $\alpha = 0.5$, 1.0, and 1.5 are represented.

At the illuminated back-side of the medium, the density $n_H = 10^{11}\mathrm{cm}^{-3}$ is low and the irradiating flux is high for all parameter values of ξ we consider. Therefore, at this part of the medium, the thermal balance is located on the upper-right part of the instability curve in Fig. 9.2 and the medium is highly-ionized. The initial temperature at the back-surface of the medium increases with both parameters ξ and α.

From Fig. 9.3 we learn that if the total optical depth of the medium is too small, the temperature profile stays nearly at a constant level. Only for higher optical depths we observe a temperature drop, which is due to the fact that at higher optical depths more radiation becomes absorbed by heavy elements and the radiation flux decreases. Hence, the heating is less efficient and the temperature declines. The temperature drop by at least one order of magnitude is rather sharp and generally located at about the same optical depth for all values of N_H. We therefore conclude that back-scattered radiation from deeper layers of the atmosphere does not play an important role in determining the temperature of the upper layers, because the medium is too optically thin.

The situation is different for the special case of $\log|\xi| = 4$ and $\alpha = 0.5$. Here, the optical depth for the temperature drop is a linear function of the total column density chosen. It turns out that, for this specific parameter combination, the medium becomes optically thick in several absorption lines of iron. In this case, heating by back-scattering of line radiation becomes important and therefore the temperature drop of the medium is very close to the total optical depth, where the outgoing radiation is released into free space and cannot be back-scattered.

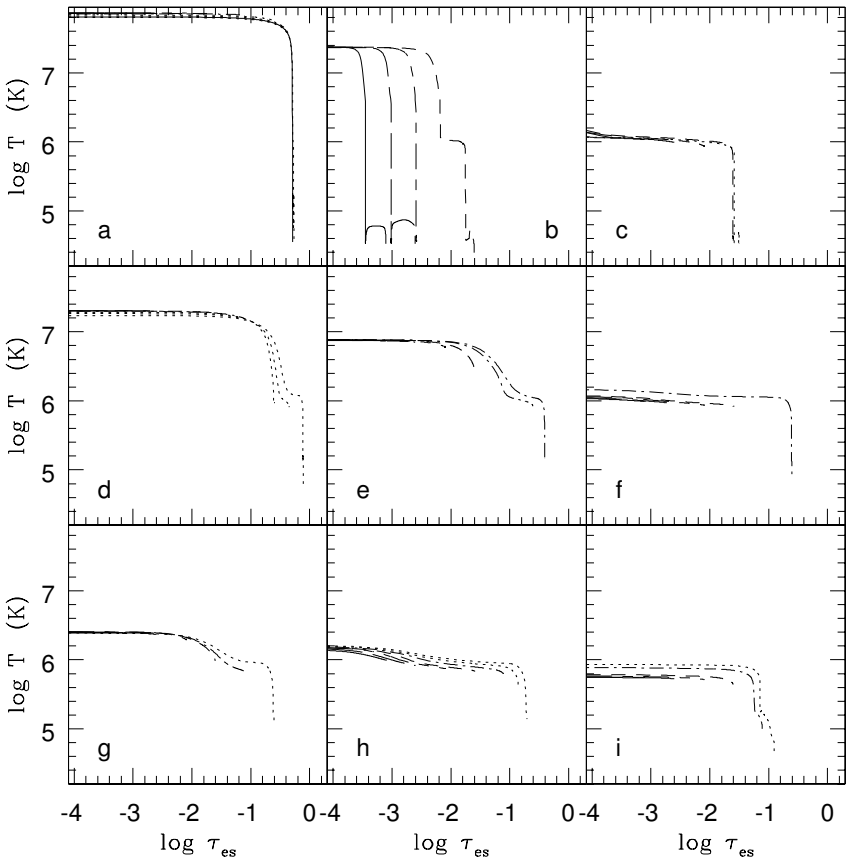

Figure 9.3: Temperature profiles along the optical depth of the warm absorber cloud for the nine combinations of values of $\log|\xi|$ and α. The panels a, b, and c, denote the results for $\log|\xi| = 5$, 4, 3 with $\alpha = 0.5$. The panels d, e, and f, show analogous results but for $\alpha = 1.0$. Finally, panels g, h, and i represent the cases for $\alpha = 1.5$. The various curves represent different column densities starting with $\log|N_H| = 21$ and increasing in steps ΔN_H of 0.5 until reaching the maximum value N_H^{max}, which corresponds to the curve ending at the highest optical depth. Close to N_H the step ΔN_H decreases to 0.1 to better reveal the asymptotic behavior.

9.4 Spectral imprints of the warm absorber

We now discuss the spectra relying on the properties of the warm absorber medium as presented in the previous section 9.3. In Fig. 9.4, we show transmitted spectra for several combinations of ξ, α, and N_H. For all panels the curves denote, from the top to the bottom, values of $\log|\xi| = 5$, 4, and 3. The column density is kept constant in each panel.

For all spectra shown, the number and strength of the absorption features increases with decreasing values of the ionization parameter. This is due to the fact that the medium becomes less ionized and hence more ionization states contribute to the absorption. However, the overall slope given by the incident spectrum is preserved, only above 0.8 keV a slight curvature of the spectrum is induced by several absorption edges.

An exception is again given by the case of $\log|\xi| = 4$ and $\alpha = 0.5$, where the additional line

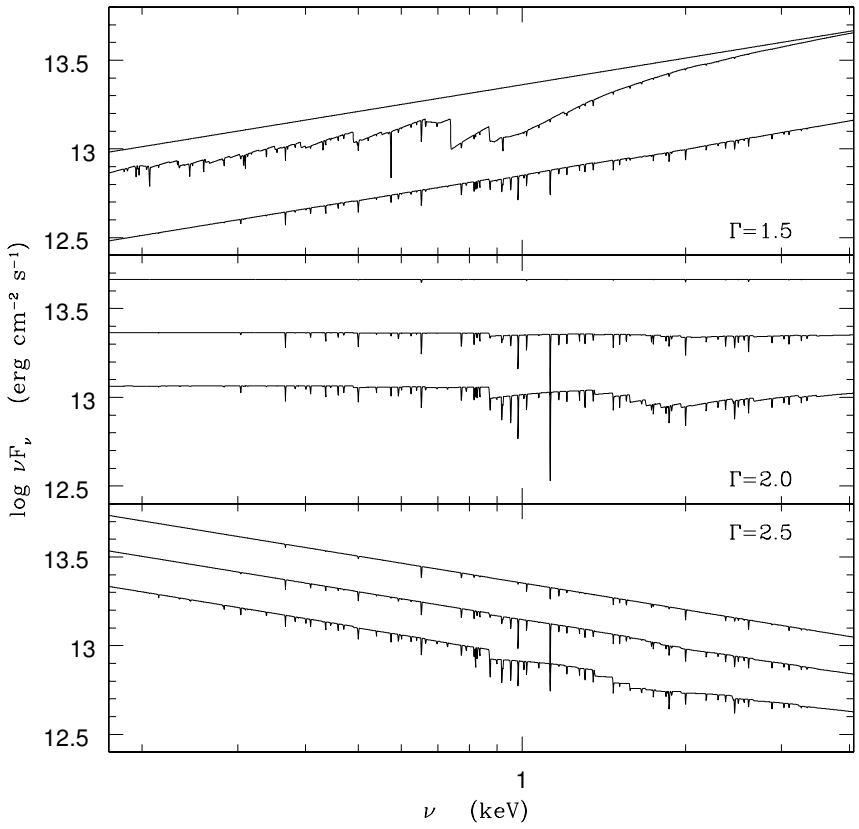

Figure 9.4: Transmitted spectra of a warm absorber for the nine combinations of values of $\log|\xi|$ and α. The top panel denotes $\alpha = 0.5$ and $N_H = 10^{22}\mathrm{cm}^{-2}$, the middle panel $\alpha = 1.0$ and $N_H = 10^{23}\mathrm{cm}^{-2}$, and finally the bottom panel represents $\alpha = 1.5$ and $N_H = 3.16 \times 10^{22}\mathrm{cm}^{-2}$. In all panels the curves from top to bottom represent values of $\log|\xi| = 5$, 4, 3 successively. Note that in the figure the spectral index $\alpha = 0.5$ is described in terms of the photon index $\Gamma = \alpha + 1$.

cooling mentioned in section 9.3 provides an effective suppression of the temperature and hence the absorption features are relatively stronger.

Analyzing a zoom of the obtained spectra, it is possible to measure equivalent widths of the absorption lines. We find out that, generally, these equivalent widths range below 1 eV and are therefore lower than those derived from X-ray observations. This might be explained by a combination of several effects, such as observational blending of the lines or turbulent velocities of the medium that are not considered in our modeling. Turbulences in the absorbing medium may cause a significant increase of the measured equivalent widths (Różańska et al., 2004).

An important simplification of our modeling is given by the fact that we assume a power-law shape for the incident spectrum. However, it has been known for a while that the reprocessing of primary X-ray radiation by the accretion disk produces emission features and, in particular, a strong Kα-line complex around 6.4 keV. The emission features should be partly suppressed by the warm absorber and modify the spectral shape around their line centroid.

In order to investigate the possible effects of the warm absorber on the iron Kα-line we convolve a hard X-ray spectrum, produced by the multi-flare modeling presented in chapter 8, with one

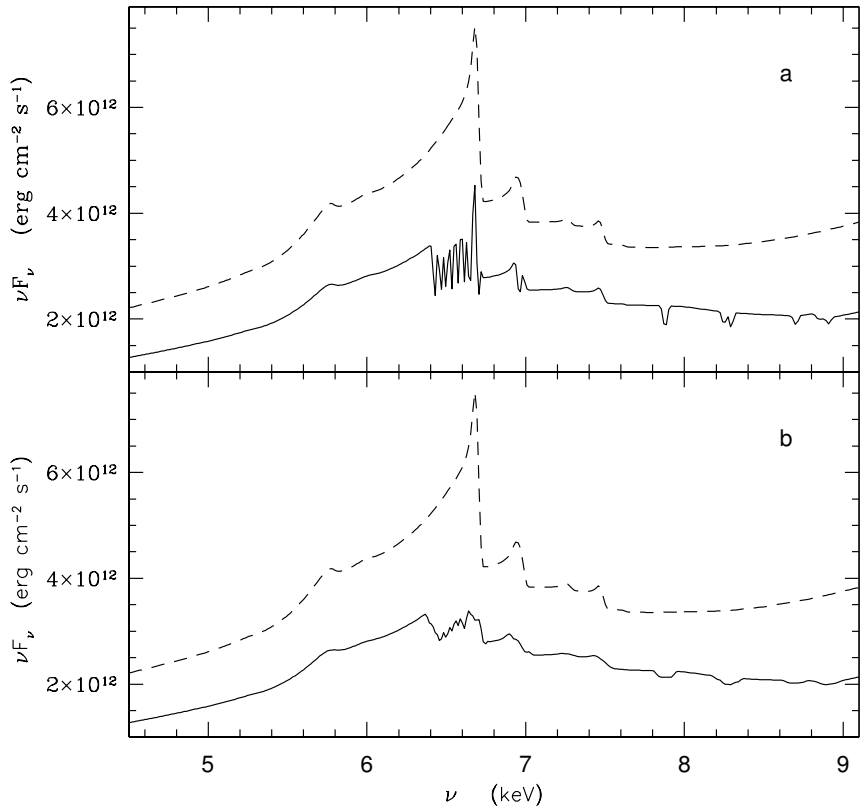

Figure 9.5: The effect of the warm absorber on a relativistically iron Kα-line produced by the reprocessing of multi-flare emission. We show the unabsorbed line (dashes) and a convolution with a warm absorber model (solid). The top panel has a higher resolution of 390 points, while the bottom panel represents the resolution of the *Chandra High-Energy-Grating* around 6 keV with 200 points.

of our warm absorber spectra. The intrinsic disk spectrum was obtained assuming an accretion disk around a Kerr black hole covered with X-ray flares at random positions. The disk is seen at an inclination of $i = 30°$. The parameters of the intrinsic spectrum were chosen consistently with the warm absorber model. In Fig. 9.5 we show the unabsorbed Kα-line as dashed lines and the convolved spectra as solid lines. The two panels represent different resolutions, the top panel contains 390 bins, the bottom one 200. The latter case is comparable to the resolution of the *Chandra High-Energy-Grating* around 6 keV.

The effect of the warm absorber on the iron line is impressive. In the higher resolution, single narrow absorption lines associated with different ionization states of iron significantly modify the red wing of the line and diminish the component at 6.4 keV. Plotted at a lower resolution the Kα-line is practically gone.

9.5 Implications of a warm absorber in pressure equilibrium

Modeling the warm absorber under the condition of constant total pressure is motivated by recent X-ray observations of AGN. We have shown, that radiative transfer computations for such a medium present a challenge to the numerical solution of the transfer equation, because of thermal instabilities that occur for certain combinations of parameters. However, it is possible to compute the structure of the medium and the spectra seen in transmission when restricting the total column density N_H of the medium to limiting values N_H^{max} depending on the individual modeling case. As one can tell from Table 9.1, the maximum values of N_H are comparable to the values of $10^{21}\mathrm{cm}^{-2}$ —$10^{23}\mathrm{cm}^{-2}$ derived observationally. Our results are thus comparable to actual X-ray data. Such comparisons were done for *Chandra* observations of the NLS1-galaxy Ton S180 (Różańska et al., 2004). The soft X-ray spectrum of Ton S180 compared well to a constant pressure model and delivered constraints on the total column density of the warm absorber.

The physical picture behind a warm absorber in pressure balance puts previous observational results into a larger context. It has been pointed out that the warm absorber in several objects can be modeled by a multi-component medium with each component having a constant density. Relating these components by the condition of constant pressure may give the key to a common dynamical origin, such as a multi-temperature outflow.

A difficulty of the constant pressure hypothesis lies in the spatial extension of the warm absorber. Slow variability of the absorption lines tells us, that the light traveling times between the illumination source and the warm absorber are in the range of light-days or light-weeks at least. Together with the fact that warm absorbers are seen in many type-1 objects, we must conclude that the medium is extended over a large region in the polar regions of the AGN. Maintaining an equilibrium between gas and radiation pressure over such big a distance is difficult, as the variable continuum source induces pressure fluctuations at the inner surface of the medium that progress to the outer parts on dynamical time-scales.

The nature of the warm absorber could be further constrained, if radiative transfer modeling is connected to detailed modeling of its dynamics. This requires hydrodynamical simulations of the gas that are self-consistently linked to radiative transfer calculations.

Chapter 10

Conclusions and Perspectives

This thesis presents new results for the modeling of the ultraviolet and X-ray spectra of AGN. Most of this work is about the reprocessed component expected from magnetic flares above the accretion disk. Results for the spectrum and for the X-ray variability properties due to such flares are derived. An interesting aspect of the modeling is that it provides some powerful tools to put constraints on the mass and the spin of the central black hole of a given AGN by observing its X-ray variability and spectral shape.

The importance in the basic black hole parameters lies in their connection to the accretion process and the fueling of the black hole by an accretion disk transporting material from the environment to the center. From the models of stellar mass black holes, for which the spectral state of an object is connected to the geometry and dynamics of the inner accretion flow, conclusions can be drawn for AGN by scaling up the mass of the black hole. In order to see the reprocessed component of magnetic flares in the AGN spectrum, the magnetic reconnections have to happen *above* the disk in order to present a relatively colder reflecting/reprocessing mirror. In this manner, the flare activity should allow to constrain the inner radius of the accretion disk and to investigate on the existence of a hot inner flow. If there is a high flare activity, a larger fraction of the disk should reach into the closer environment of the black hole, where the energy release due to accretion is high enough to power the development of reconnecting magnetic flux tubes. If there is less flare activity, the disk is likely to be truncated and replaced by a hot inner flow laking the reprocessing mirror.

Magnetic flares are also connected to the global energy budget of AGN picking up a fraction of the accretion rate to dissipate hard X-ray radiation in the corona and, in case of long-term flares, heating the underlying disk and causing its thermal expansion. To estimate the total accretion flow of the AGN it is necessary to know how much energy goes into the production of the flares and their emission. In this case it is important to understand not only the details of reprocessing, which we treat in this thesis, but also to connect the intrinsic emission to the flare evolution. The formation of the magnetic loops, their reconnection, and the production of the primary component have to be understood in the same context. Such models could describe the energy partition between different aspects of the flare, with the goal to estimate the total energy taken out of the accretion flow by the flare activity.

It follows, that there is a strong interest to identify contributions to the spectrum and to the variability from magnetic flares, distinguishing them from other processes that are relevant for the X-ray spectrum of AGN. We therefore attempt to model the emission expected from flares as accurately as possible. In the following, we briefly summarize possibilities to connect our modeling

to X-ray observations (section 10.1) and we mention constraints on global AGN properties that can be obtained from the model. We also discuss its current limitations and how we intend to further improve our method (section 10.2).

10.1 Connection of the flare model to the observations

The modeling of the local Compton reflection/reprocessed component presented in this work brings detailed results for the dependence of the spectrum upon several parameters. The various spectra we have computed clearly show differences depending on the local emission angle ψ and on the position inside the hot spot. However, the local spectrum cannot be seen in actual observations, we therefore have to trace it back taking into account the physical assumptions about its production and modifications on the way to the earth. An important modification of the flare spectra is due to the curved space-time in the vicinity of the black hole and due to the orbital motion. We present the spectra seen by a distant observer that include relativistic corrections based on the local radiative transfer simulations. Hence, if magnetic flares exist and if they "work" approximately as we have assumed, we deliver consistent spectra for the observed reprocessed component.

However, constraints on the underlying flare, would require time-resolved spectral data with very high signal-to-noise quality even for very narrow time-bins having a width below 50 s or so. In chapter 6 we have already mentioned that with current X-ray satellites this is not possible. Only future missions like the *Constellation-X* observatory should provide much higher precision of the X-ray observations for AGN. They could deliver data that would enable us to construct a detailed time-resolved picture of the spectral behavior during a flare period. In the data obtained to the present day, there are already clear hints in short-term X-ray light curves (bin width = 10^2s —10^3s) on individual flare-like events.

Another possibility to constrain the physical parameters for our flare modeling is by connecting it to AGN variability as it was done in chapter 8. The modeling of rms-variability we present delivers quite promising results and a rather direct link to fundamental parameters like the mass M and the spin a of the black hole. For instance, the modeling confirmed that a high spin-parameter of the central black hole in the Seyfert-1 galaxy MCG -6-30-15 is necessary to reproduce the features of the rms-spectrum. As we mentioned in chapter 8, there are still some inconsistencies in our method due to the limited number of local spectra calculated so far. Although, it is a practical challenge to compute a large grid of flare spectra for various parameter configurations, this could enable more accuracy for the local spot spectra used in the modeling of the rms-variability.

A more conceptual question lies in the assumption about the nature of the flares. For the variability investigation the mean number of coexisting flares is large. But observationally we see occasional large "single" flares in the lightcurves. Such resolved single flares are seen in the present data. We have taken a closer look at the flare analyzed by Ponti et al. (2004) for MCG -6-30-15. Porquet et al. (2004) considered a localized flare as a plausible explanation of the ESO 113-G010 spectrum. The events can dominate the X-ray luminosity for a short while, which indicates that the physical process behind such "single" flares is very powerful. Hence, from a phenomenological point of view, we currently have to divide flares into two categories:

1) Weaker flares that appear more frequently creating small-scale X-ray variability. These flares assure a substantial level of X-ray radiation.

2) Strong flares with luminosities comparable to the disk luminosity. These flares are

much less frequent, but when they appear, they dominate the X-ray spectra for a short time period.

In order to check if this assumption is reasonably consistent within the physical model, further investigation is necessary on the formation of the flare source and the energetic processes involved. This could also give better constraints on the shape of the incident spectrum. Here we model it using a power-law, which, however stands on some physical grounds by the theory of Compton up-scattering of soft disk photons in the hot gas of the flare source. But the actual mechanism to produce the primary spectrum could be more complicated, including for instance a synchrotron emission component.

The toy-model for the time-lag analysis presented in chapter 7 refers to the analysis of "single" strong flares. The model could be improved significantly by repeating the computations we conducted using more realistic spectra. Instead of defining the reprocessed spectrum as a power-law which only differs from the primary by the spectra index, the disk emission can be defined by the consistently computed spectra presented in chapter 6. The results could give better constraints on the height h of the flare source above the disk from observed time-lags between different X-ray bands.

The study about the warm absorber modeling presented in this thesis is connected to the flare modeling because for many type-1 objects the warm absorber introduces an additional modification of the soft X-ray spectrum. Detailed modeling of flares close to the central engine thus includes a careful subtraction of the warm absorber effects. We present results for the modeling of the warm absorber in a state of pressure equilibrium that has poorly been investigated so far. Currently, the incident spectrum for this modeling was a simple power-law. An important improvement of our modeling in terms of consistency would be to combine the results of the flare modeling, which give an additional contribution to the primary power-law radiation, with the modeling of the warm absorber. One would expect detailed results on the interplay between the central disk/corona and the warm absorber.

10.2 Further improvements of our modeling technique

From the discussion in the previous section it becomes clear that more detailed studies of the model predictions and comparison with the data are needed. In order to constrain the true nature of the X-ray properties in AGN, the models should consider several aspects of the observations at the same time. We describe here some developments we intend to implement into our method in the future.

The azimuthal dependence of the locally emitted spectra. The re-processed spectra computed by *TITAN* and *NOAR* that we implement into *KY* do not consider spectral variations in the azimuthal direction yet. However, due to the fact that the incident photons hit the disk surface at an angle that differs from the normal direction, the reflected component is not expected to be axis-symmetric with respect to this normal. From some test results with *NOAR* we found variations in the azimuthal direction up to 40%. These variations can become important for flares located closer to the central black hole where the relativistic effects are strong. The current version of *KY* does not process local emissivities with an azimuthal dependence. We hence intend to modify *KY* and compute new observed spectra including the azimuthal dependence for the reprocessed radiation.

The time-scale of the flare duration. The short-term flares presented in chapter 6 are fully consistent with the local spectra only for relatively short flare durations. On the other hand there is no physical constraint observed that would justify such an assumption. Flares are likely to exist

longer than one orbit or even more. This requires consistent modeling also for later states after the onset of the flare. The most realistic approach is to treat the flare emission after the disk has settled into a new hydrostatic equilibrium between viscous heating, gravitational force, *and* the external emission. On the other hand, Czerny & Goosmann (2004) have shown, that flares existing for longer time-periods change the geometry of the underlying reprocessing medium. In some cases, depending on the global parameters, the underlying disk material expands and enshrouds the flare source by material of a significant optical thickness. This, of course, changes the spectrum and hence the required modeling configuration. However, for the local spectrum these changes in geometry can be met to a good extent because both *TITAN* and *NOAR* can solve the radiative transfer at various angular distributions of the incident radiation. In case of *NOAR* it is even possible to switch to a different geometry of the model region. In the future, we therefore intend to also model specific configurations for flares in the hydrostatic balance adjusted to the external emission.

Spectral polarimetry in the X-ray range. The next generation of satellites is supposed to enable X-ray polarimetry as a new tool to investigate the X-ray properties of astrophysical objects. Namely, the *XEUS*-satellite is planned to carry an X-ray polarimeter. In other wavebands, polarimetry has shown to be an effective tool to constrain geometrical aspects. In the investigation of magnetic flares presented in this thesis, geometrical aspects play an important role, and it would give us a further constraint on the multi-parameter problem that the current modeling represents. On the modeling side, our technique already is partly equipped to include polarization, as the *KY*-code computes the transfer functions of the Stokes parameters. The important step to take is for the local radiative transfer, namely the Monte-Carlo code *NOAR*. It could be modified to consider the Stokes parameters of the sampled photons and thus to also produce the Stokes-spectra across the hot spot. The results would provide modeling results that can be compared to polarimetric *XEUS*-observations of AGN.

Bibliography

Abrassart, A., & Dumont, A. M. 2001, AIP Conf. Proc. 599: X-ray Astronomy: Stellar Endpoints, AGN, and the Diffuse X-ray Background, 599, 489

Antonucci, R. 1993, ARA&A, 31, 473

Antonucci, R. R. J., & Miller, J. S. 1985, ApJ, 297, 621

Antonucci, R. R. J., & Cohen, R. D. 1983, ApJ, 271, 564

Awaki, H., Koyama, K., Inoue, H., & Halpern, J. P. 1991, PASJ, 43, 195

Baldwin, J. A. 1977, ApJ, 214, 679

Baldwin, J. A., Wampler, E. J., & Gaskell, C. M. 1989, ApJ, 338, 630

Balestra, I., Bianchi, S., & Matt, G. 2004, A&A, 415, 437

Ballantyne, D. R., Ross, R. R., & Fabian, A. C. 2001, MNRAS, 327, 10

Ballantyne, D. R., Ross, R. R., & Fabian, A. C. 2000, Bulletin of the American Astronomical Society, 32, 1185

Barr, P., & Mushotzky, R. F. 1986, Nature, 320, 421

Beckmann, V., Gehrels, N., Favre, P., Walter, R., Courvoisier, T. J.-L., Petrucci, P.-O., & Malzac, J. 2004, ApJ, 614, 641

Behar, E., Rasmussen, A. P., Blustin, A. J., Sako, M., Kahn, S. M., Kaastra, J. S., Branduardi-Raymont, G., & Steenbrugge, K. C. 2003, ApJ, 598, 232

Behar, E., Sako, M., & Kahn, S. M. 2001, ApJ, 563, 497

Belloni, T., & Hasinger, G. 1990, A&A, 227, L33

Beloborodov, A. M. 1999, ApJL, 510, L123

Bianchi, S., Balestra, I., Matt, G., Guainazzi, M., & Perola, G. C. 2003, A&A, 402, 141

Blandford, R. D., & Rees, M. J. 1974, MNRAS, 169, 395

Bowyer, C. S., Lampton, M., Mack, J., & de Mendonca, F. 1970, ApJL, 161, L1

Brandt, W. N., Fabian, A. C., & Pounds, K. A. 1996, MNRAS, 278, 326

Cannon, C. J. 1973, J. Quant. Spectrosc. Radiat. Transfer., 13, 627

Carter, B. 1968, Physical Review , 174, 1559

Chandrasekhar, S. 1960, New York: Dover, 1960,

Chevallier, L., Collin, S., Dumont, A.-M., Czerny, B., Mouchet, M., Gonçalves, A., & Goosmann, R. 2005, A&A(in press)

Chiang, J., Reynolds, C. S., Blaes, O. M., Nowak, M. A., Murray, N., Madejski, G., Marshall, H. L., & Magdziarz, P. 2000, ApJ, 528, 292

Chiappetti, L., Maraschi, L., Treves, A., & Tanzi, E. G. 1983, ApJ, 265, 354

Collinge, M. J., et al. 2001, ApJ, 557, 2

Collin, S., Coupé, S., Dumont, A.-M., Petrucci, P.-O., & Różańska, A. 2003, A&A, 400, 437

Collin, S., Abrassart, A., Czerny, B., Dumont, A.-M., & Mouchet, M. 2001, EAS Publications Series, 1, 35

Collin, S. 2001, Advanced Lectures on the Starburst-AGN, 167

Collin-Souffrin, S., & Lasota, J.-P. 1988, PASP, 100, 1041

Collin-Souffrin, S. 1987, A&A, 179, 60

Coppi, P. S. 1999, ASP Conf. Ser. 161: High Energy Processes in Accreting Black Holes, 161, 375

Coupé, S., M̈odélisation des régions émissives autour des trous noirs dans les noyaux actifs de galaxies; PhD-thesis (2002)

Crenshaw, D. M., Kraemer, S. B., Boggess, A., Maran, S. P., Mushotzky, R. F., & Wu, C.-C. 1999, ApJ, 516, 750

Crenshaw, D. M., et al. 1996, ApJ, 470, 322

Czerny, B., Nikołajuk, M., Różańska, A., Dumont, A.-M., Loska, Z., & Zycki, P. T. 2003, A&A, 412, 317

Czerny, B., Li, J., Loska, Z., & Szczerba, R. 2004, MNRAS, 348, L54

Czerny, B., Różańska, A., Dovčiak, M., Karas, V., & Dumont, A.-M. 2004, A&A, 420, 1

Czerny, B., & Goosmann, R. 2004, A&A, 428, 353

de Rosa, A., Piro, L., Matt, G., & Perola, G. C. 2004, A&A, 413, 895

de Gouveia dal Pino, E. M. 2005, Advances in Space Research, 35, 908

Done, C., & Gierliński, M. 2004, Progress of Theoretical Physics Supplement, 155, 9

Done, C., & Nayakshin, S. 2001, MNRAS, 328, 616

Dovčiak, M., Karas, V., & Yaqoob, T. 2004, ApJS, 153, 205

Dovčiak, M., "Radiation of accretion disks in strong gravity", PhD-thesis (2004)

Dumont, A.-M., Collin, S., Paletou, F., Coupé, S., Godet, O., & Pelat, D. 2003, A&A, 407, 13

Dumont, A.-M., Abrassart, A., & Collin, S. 2000, A&A, 357, 823

Edelson, R., et al. 2000, ApJ, 534, 180

Edelson, R., & Nandra, K. 1999, ApJ, 514, 682

Edelson, R. A., et al. 1996, ApJ, 470, 364

Elvis, M. 2000, ApJ, 545, 63

Elvis, M., et al. 1994, ApJS, 95, 1

Elvis, M., Maccacaro, T., Wilson, A. S., Ward, M. J., Penston, M. V., Fosbury, R. A. E., & Perola, G. C. 1978, MNRAS, 183, 129

Fabian, A. C., & Miniutti, G., to appear in "Kerr Spacetime: Rotating Black Holes in General Relativity", D.L. Wiltshire, M. Visser, S.M. Scott (eds), Cambridge Univ. Press, astro-ph/0507409

Fabian, A. C., et al. 2002, MNRAS, 335, L1

Fabian, A. C. 1979, Royal Society of London Proceedings Series A, 366, 449

Fanaroff, B. L., & Riley, J. M. 1974, MNRAS, 167, 31P

Field, G. B. 1965, ApJ, 142, 531

Francis, P. J., Hewett, P. C., Foltz, C. B., Chaffee, F. H., Weymann, R. J., & Morris, S. L. 1991, ApJ, 373, 465

Friedman, H., & Byram, E. T. 1967, Science, 158, 257

Galeev, A. A., Rosner, R., & Vaiana, G. S. 1979, ApJ, 229, 318

Gaskell, C. M., Goosmann, R. W., Antonucci, R. R. J., & Whysong, D. H. 2004, ApJ, 616, 147

George, I. M., Turner, T. J., Yaqoob, T., Netzer, H., Laor, A., Mushotzky, R. F., Nandra, K., & Takahashi, T. 2000, ApJ, 531, 52

George, I. M., Turner, T. J., Netzer, H., Nandra, K., Mushotzky, R. F., & Yaqoob, T. 1998, ApJS, 114, 73

George, I. M., & Fabian, A. C. 1991, MNRAS, 249, 352

Giannuzzo, E., Rieke, G. H., & Rieke, M. J. 1995, ApJL, 446, L5

Gierliński, M., & Done, C. 2004, MNRAS, 349, L7

Glass, I. S. 2004, MNRAS, 350, 1049

Gondek, D., Zdziarski, A. A., Johnson, W. N., George, I. M., McNaron-Brown, K., Magdziarz, P., Smith, D., & Gruber, D. E. 1996, MNRAS, 282, 646

Goosmann, R. W., & Gaskell, C. M. submitted to A&A, astro-ph/0507072

Gorecki, A., & Wilczewski, W. 1984, Acta Astronomica, 34, 141

Grandi, P., Tagliaferri, G., Giommi, P., Barr, P., & Palumbo, G. G. C. 1992, ApJS, 82, 93

Green, A. R., McHardy, I. M., & Lehto, H. J. 1993, MNRAS, 265, 664

Guilbert, P. W., & Rees, M. J. 1988, MNRAS, 233, 475

Haardt, F., Maraschi, L., & Ghisellini, G. 1994, ApJL, 432, L95

Haardt, F., & Maraschi, L. 1991, ApJL, 380, L51

Halpern, J. P. 1985, ApJ, 290, 130

Halpern, J. P. 1984, ApJ, 281, 90

Hao, L., et al. 2005, ApJL, 625, L75

Hawley, J. F., & Villiers, J. D. 2004, Progress of Theoretical Physics Supplement, 155, 132

Hughes, P. A., Aller, H. D., & Aller, M. F. 1989a, ApJ, 341, 54

Hughes, P. A., Aller, H. D., & Aller, M. F. 1989b, ApJ, 341, 68

Hunt, L. K., Zhekov, S., Salvati, M., Mannucci, F., & Stanga, R. M. 1994, A&A, 292, 67

Inoue, H., & Matsumoto, C. 2001, Advances in Space Research, 28, 445

Iwasawa, K., Miniutti, G., & Fabian, A. C. 2004, MNRAS, 355, 1073

Iwasawa, K., Lee, J. C., Young, A. J., Reynolds, C. S., & Fabian, A. C. 2004, MNRAS, 347, 411

Iwasawa, K., et al. 1996, MNRAS, 282, 1038

Iwasawa, K., Fabian, A. C., Mushotzky, R. F., Brandt, W. N., Awaki, H., & Kunieda, H. 1996, MNRAS, 279, 837

Jaffe, W., et al. 2004, Nature, 429, 47

Janiuk, A., Czerny, B., & Madejski, G. M. 2001, ApJ, 557, 408

Jiménez-Bailón, E., Piconcelli, E., Guainazzi, M., Schartel, N., Rodríguez-Pascual, P. M., & Santos-Lleó, M. 2005, A&A, 435, 449

Kaastra, J. S., et al. 2004, A&A, 422, 97

Kaastra, J. S., Steenbrugge, K. C., Raassen, A. J. J., van der Meer, R. L. J., Brinkman, A. C., Liedahl, D. A., Behar, E., & de Rosa, A. 2002, A&A, 386, 427

Kaastra, J. S., Mewe, R., Liedahl, D. A., Komossa, S., & Brinkman, A. C. 2000, A&A, 354, L83

Karas, V., Czerny, B., Abrassart, A., & Abramowicz, M. A. 2000, MNRAS, 318, 547

Karzas, W. J., & Latter, R. 1961, ApJS, 6, 167

Khare, P., et al. 2004, Proceedings of the IAU Colloquium #199 "Probing Galaxies through Quasar Absorption Lines", astro-ph/0504532

Kaspi, S., et al. 2002, ApJ, 574, 643

Kellermann, K. I., Sramek, R., Schmidt, M., Shaffer, D. B., & Green, R. 1989, AJ, 98, 1195

Kinkhabwala, A., et al. 2002, ApJ, 575, 732

Komossa, S. 1999, ISAS Report, p. 149-160, T. Takahashi, H. Inoue (eds), 149

Komossa, S., & Bade, N. 1998, A&A, 331, L49

Komossa, S., & Fink, H. 1997, A&A, 327, 483

Kompaneets, A. S. 1956, Soviet Phys., JETP 31, 876

Konigl, A., & Kartje, J. F. 1994, ApJ, 434, 446

Krolik, J. H. 2002, X-ray Spectroscopy of AGN with Chandra and XMM-Newton, 131

Krolik, J. H., & Kriss, G. A. 2001, ApJ, 561, 684

Krolik, J. H. 1999, Active galactic nuclei : from the central black hole to the galactic environment /Julian H. Krolik. Princeton, N. J. : Princeton University Press, c1999.,

Krolik, J. H. 2002, X-ray Spectroscopy of AGN with Chandra and XMM-Newton, 131

Krolik, J. H., & Kriss, G. A. 1995, ApJ, 447, 512

Krolik, J. H., Horne, K., Kallman, T. R., Malkan, M. A., Edelson, R. A., & Kriss, G. A. 1991, ApJ, 371, 541

Krolik, J. H., McKee, C. F., & Tarter, C. B. 1981, ApJ, 249, 422

Krongold, Y., Nicastro, F., Brickhouse, N. S., Elvis, M., Liedahl, D. A., & Mathur, S. 2003, ApJ, 597, 832

Kukula, M. J., Dunlop, J. S., Hughes, D. H., & Rawlings, S. 1998, MNRAS, 297, 366

Laor, A., Fiore, F., Elvis, M., Wilkes, B. J., & McDowell, J. C. 1997, ApJ, 477, 93

Lawrence, A., & Papadakis, I. 1993, ApJL, 414, L85

Lee, J. C., Ogle, P. M., Canizares, C. R., Marshall, H. L., Schulz, N. S., Morales, R., Fabian, A. C., & Iwasawa, K. 2001, ApJL, 554, L13

Leighly, K. M. 1999, ApJS, 125, 297

Leighly, K., Kunieda, H., Awaki, H., & Tsuruta, S. 1996, ApJ, 463, 158

Leighly, K., Kunieda, H., & Tsuruta, S. 1992, American Institute of Physics Conference Series, 254, 93

Lightman, A. P., & White, T. R. 1988, ApJ, 335, 57

Lovelace, R. V. E., Romanova, M. M., & Biermann, P. L. 1998, A&A, 338, 856

Lynden-Bell, D. 1969, Nature, 223, 690

Madejski, G. M., Done, C., Turner, T. J., Mushotzky, R. F., Serlemitsos, P., Fiore, F., Sikora, M., & Begelman, M. C. 1993, Nature, 365, 626

Magdziarz, P., Blaes, O. M., Zdziarski, A. A., Johnson, W. N., & Smith, D. A. 1998, MNRAS, 301, 179

Magdziarz, P., & Zdziarski, A. A. 1995, MNRAS, 273, 837

Maiolino, R., Marconi, A., Salvati, M., Risaliti, G., Severgnini, P., Oliva, E., La Franca, F., & Vanzi, L. 2001, A&A, 365, 28

Malkan, M. A. & Sargent, W. L. W. 1982, ApJ, 254, 22

Maraschi, L., Chiappetti, L., Falomo, R., Garilli, B., Malkan, M., Tagliaferri, G., Tanzi, E. G., & Treves, A. 1991, ApJ, 368, 138

Markowitz, A., & Edelson, R. 2004, ApJ, 617, 939

Markowitz, A., Edelson, R., & Vaughan, S. 2003, ApJ, 598, 935

Markowitz, A., et al. 2003, ApJ, 593, 96

Markowitz, A., & Edelson, R. 2001, ApJ, 547, 684

Martocchia, A., Matt, G., & Karas, V. 2001, AIP Conf. Proc. 599: X-ray Astronomy: Stellar Endpoints, AGN, and the Diffuse X-ray Background, 599, 746

Mathur, S., Wilkes, B., & Elvis, M. 1998, ApJL, 503, L23

Marshall, H. L., et al. 1997, ApJ, 479, 222

Mathur, S., Wilkes, B., Elvis, M., & Fiore, F. 1994, ApJ, 434, 493

Matsuoka, M., Piro, L., Yamauchi, M., & Murakami, T. 1990, ApJ, 361, 440

Matsuoka, M., Ikegami, T., Inoue, H., & Koyama, K. 1986, PASJ, 38, 285

Matt, G., Bianchi, S., D'Ammando, F., & Martocchia, A. 2004, A&A, 421, 473

Matt, G. 2004, Nuclear Physics B Proceedings Supplements, 132, 97

Matt, G., Fabian, A. C., & Ross, R. R. 1993, MNRAS, 264, 839

Matt, G., Fabian, A. C., & Ross, R. R. 1993, MNRAS, 262, 179

McHardy, I. M., Gunn, K. F., Uttley, P., & Goad, M. R. 2005, MNRAS, 359, 1469

McHardy, I. M., Papadakis, I. E., Uttley, P., Page, M. J., & Mason, K. O. 2004, MNRAS, 348, 783

McHardy, I. M., Papadakis, I. E., & Uttley, P. 1998, The Active X-ray Sky: Results from BeppoSAX and RXTE, 509

McHardy, I. M. 1989, ESA SP-296: Two Topics in X-Ray Astronomy, Volume 1: X Ray Binaries. Volume 2: AGN and the X Ray Background, 1111

McHardy, I. 1988, Memorie della Societa Astronomica Italiana, 59, 239

McHardy, I., & Czerny, B. 1987, Nature, 325, 696

Merloni, A., & Fabian, A. C. 2001, MNRAS, 328, 958

Merloni, A., & Fabian, A. C. 2001, MNRAS, 321, 549

Miller, K. A., & Stone, J. M. 2000, ApJ, 534, 398

Miniutti, G., & Fabian, A. C. in "Kerr Spacetime: Rotating Black Holes in General Relativity" eds. D.L. Wiltshire, M. Visser and S.M. Scott, (Cambridge Univ. Press), astro-ph/0507409

Miniutti, G., & Fabian, A. C. 2004, MNRAS, 349, 1435

Mittaz, J. P. D., & Branduardi-Raymont, G. 1989, IAU Symp. 134: Active Galactic Nuclei, 134, 179

Misner, C. W., Thorne, K. S., & Wheeler, J. A. 1973, San Francisco: W.H. Freeman and Co., 1973

Monier, E. M., Mathur, S., Wilkes, B., & Elvis, M. 2001, ApJ, 559, 675

Murray, N., & Chiang, J. 1995, ApJL, 454, L105

Mushotzky, R. F., Done, C., & Pounds, K. A. 1993, ARA&A, 31, 717

Nandra, K., George, I. M., Mushotzky, R. F., Turner, T. J., & Yaqoob, T. 1999, ApJL, 523, L17

Nandra, K., George, I. M., Mushotzky, R. F., Turner, T. J., & Yaqoob, T. 1997, ApJL, 488, L91

Nandra, K., George, I. M., Mushotzky, R. F., Turner, T. J., & Yaqoob, T. 1997, ApJ, 477, 602

Nandra, K., George, I. M., Mushotzky, R. F., Turner, T. J., & Yaqoob, T. 1997, ApJ, 476, 70

Nandra, K., & Pounds, K. A. 1994, MNRAS, 268, 405

Nandra, K., & Pounds, K. A. 1992, Nature, 359, 215

Nandra, K., Pounds, K. A., Stewart, G. C., George, I. M., Hayashida, K., Makino, F., & Ohashi, T. 1991, MNRAS, 248, 760

Nandra, K., Pounds, K. A., & Stewart, G. C. 1990, MNRAS, 242, 660

Narayan, R., Mahadevan, R., & Quataert, E. 1998, Theory of Black Hole Accretion Disks, 148

Nayakshin, S., & Kazanas, D. 2002, ApJ, 567, 85

Nayakshin, S., & Kallman, T. R. 2001, ApJ, 546, 406

Nayakshin, S., Kazanas, D., & Kallman, T. R. 2000, ApJ, 537, 833

Netzer, H., et al. 2003, ApJ, 599, 933

Netzer, H. 1996, ApJ, 473, 781

Netzer, H. 1993, ApJ, 411, 594

Neugebauer, G., Soifer, B. T., Matthews, K., & Elias, J. H. 1989, AJ, 97, 957

Ng, K.-C. 1974, Journal of Chemical Physics, 61, 2680

Nowak, M. A., & Chiang, J. 2000, ApJL, 531, L13

Novikov I. D. & Thorne, K. S. 1973, in "Black Holes", eds. C. DeWitt and B. DeWitt, New York: Gordon & Breach

Osterbrock, D. E., & Shaw, R. A. 1988, ApJ, 327, 89

Page, K. L., Schartel, N., Turner, M. J. L., & O'Brien, P. T. 2004, MNRAS, 352, 523

Page, D. N., & Thorne, K. S. 1974, ApJ, 191, 499

Perola, G. C., et al. 1986, ApJ, 306, 508

Papadakis, I. E., Reig, P., & Nandra, K. 2003, MNRAS, 344, 993

Peterson, B. M. 1998, Advances in Space Research, 21, 57

Peterson, B. M. 1997, An introduction to active galactic nuclei, Publisher: Cambridge, New York Cambridge University Press, 1997 Physical description xvi, 238 p. ISBN 0521473489,

Perola, G. C., et al. 2000, A&A, 358, 117

Pfefferkorn, F., Boller, T., & Rafanelli, P. 2001, A&A, 368, 797

Piconcelli, E., Jimenez-Bailón, E., Guainazzi, M., Schartel, N., Rodríguez-Pascual, P. M., & Santos-Lleó, M. 2005, A&A, 432, 15

Pier, E. A., & Krolik, J. H. 1992, ApJL, 399, L23

Pringle, J. E., Rees, M. J., & Pacholczyk, A. G. 1973, A&A, 29, 179

Pojmanski, G. 1986, Acta Astronomica, 36, 69

Ponti, G., Cappi, M., Dadina, M., & Malaguti, G. 2004, A&A, 417, 451

Porquet D., Reeves J.N., Uttley P., Turner T.J., 2004, A&A, 427, 101

Pounds, K. A., Reeves, J. N., Page, K. L., Wynn, G. A., & O'Brien, P. T. 2003, MNRAS, 342, 1147

Pounds, K., Reeves, J. 2002 in " Proceedings of the Symposium on 'New Visions of the X-ray Universe in the XMM-Newton and Chandra Era', 26-30 November 2001, ESTEC, The Netherlands", astro-ph/0201436

Pounds, K. A., Nandra, K., Stewart, G. C., George, I. M., & Fabian, A. C. 1990, Nature, 344, 132

Pounds, K. A., Nandra, K., Stewart, G. C., & Leighly, K. 1989, MNRAS, 240, 769

Pounds, K. A., & McHardy, I. M. 1988, Physics of Neutron Stars and Black Holes, 285

Poutanen, J., & Fabian, A. C. 1999, MNRAS, 306, L31

Poutanen, J. 1998, Theory of Black Hole Accretion Disks, 100

Raymond, J. C. 1993, ApJ, 412, 267

Rees, M. J. 1984, ARA&A, 22, 471

Reeves, J. N., Nandra, K., George, I. M., Pounds, K. A., Turner, T. J., & Yaqoob, T. 2004, ApJ, 602, 648

Reeves, J. 2003, ASP Conf. Ser. 290: Active Galactic Nuclei: From Central Engine to Host Galaxy, 290, 35

Reeves, J. N., & Turner, M. J. L. 2000, MNRAS, 316, 234

Reeves, J. N., O'Brien, P. T., Vaughan, S., Law-Green, D., Ward, M., Simpson, C., Pounds, K. A., & Edelson, R. 2000, MNRAS, 312, L17

Reynolds, C. S. 1997, MNRAS, 286, 513

Ross, R. R., Fabian, A. C., & Young, A. J. 1999, MNRAS, 306, 461

Ross, R. R., & Fabian, A. C. 1993, MNRAS, 261, 74

Różańska, A., Goosmann, R. W., Dumont, A.-M., Czerny, B. submitted to A&A

Różańska, A., Czerny, B., Siemiginowska, A., Dumont, A.-M., & Kawaguchi, T. 2004, ApJ, 600, 96

Różańska, A., Dumont, A.-M., Czerny, B., & Collin, S. 2002, MNRAS, 332, 799

Różańska, A. 1999, MNRAS, 308, 751

Różańska, A., Czerny, B., Życki, P. T., & Pojmański, G. 1999, MNRAS, 305, 481

Rozanska, A., & Czerny, B. 1996, Acta Astronomica, 46, 233

Rush, B., Malkan, M. A., Fink, H. H., & Voges, W. 1996, ApJ, 471, 190

Ruszkowski, M. 2000, MNRAS, 315, 1

Rybicki, G. B. & Lightman, A. P. 1979, New York, Wiley-Interscience, 1979. 393 p.,

Sako, M., et al. 2001, A&A, 365, L168

Salpeter, E. E. 1964, ApJ, 140, 796

Sanders, D. B., Phinney, E. S., Neugebauer, G., Soifer, B. T., & Matthews, K. 1989, ApJ, 347, 29

Schmidt, M. 1963, Nature, 197, 1040

Schmitt, H. R., Ulvestad, J. S., Antonucci, R. R. J., & Kinney, A. L. 2001, ApJS, 132, 199

Seyfert, C. K. 1943, ApJ, 97, 28

Shakura, N. I., & Sunyaev, R. A. 1976, MNRAS, 175, 613

Shakura, N. I., & Sunyaev, R. A. 1973, A&A, 24, 337

Shields, J. C., Ferland, G. J., & Peterson, B. M. 1995, ApJ, 441, 507

Shields, G. A. 1978, Nature, 272, 706

Shih, D. C., Iwasawa, K., & Fabian, A. C. 2002, MNRAS, 333, 687

Siebenmorgen, R., Krügel, E., & Spoon, H. W. W. 2004, A&A, 414, 123

Sobolewska, M., & Done, C. 2005, AIP Conf. Proc. 774: X-ray Diagnostics of Astrophysical Plasmas: Theory, Experiment, and Observation, 774, 317

Stocke, J. T., Morris, S. L., Weymann, R. J., & Foltz, C. B. 1992, ApJ, 396, 487

Sunyaev, R. A., & Titarchuk, L. G. 1980, A&A, 86, 121

Svensson, R. 1996, A&AS, 120, 475

Tanaka, Y., et al. 1995, Nature, 375, 659

Taylor, R. D., Uttley, P., & McHardy, I. M. 2003, MNRAS, 342, L31

Torricelli-Ciamponi, G., Pietrini, P., & Orr, A. 2005, A&A, 438, 55

Tovmassian, H. M. 2001, Astronomische Nachrichten, 322, 87

Turner, N. J., Blaes, O. M., Socrates, A., Begelman, M. C., & Davis, S. W. 2005, ApJ, 624, 267

Turner, T. J., George, I. M., Nandra, K., & Turcan, D. 1999, ApJ, 524, 667

Ulrich, M., Maraschi, L., & Urry, C. M. 1997, ARA&A, 35, 445

Ulrich, M.-H., & Horne, K. 1996, MNRAS, 283, 748

Ulrich, M. H., et al. 1984, MNRAS, 206, 221

Uttley, P., & Mhardy, I. M. 2004, Progress of Theoretical Physics Supplement, 155, 170

Vaughan, S., & Uttley, P. 2005, MNRAS, 362, 235

Vaughan, S., & Fabian, A. C. 2004, MNRAS, 348, 1415

Vaughan, S., Edelson, R., Warwick, R. S., & Uttley, P. 2003, MNRAS, 345, 1271

Vaughan, S., & Edelson, R. 2001, ApJ, 548, 694

Walter, R. & Fink, H. H. 1993, A&A, 274, 105

Ward, M., Elvis, M., Fabbiano, G., Carleton, N. P., Willner, S. P., & Lawrence, A. 1987, ApJ, 315, 74

Weedman, D. W., et al. 2005, accepted by ApJ, astro-ph/0507423

Weymann, R. J., Morris, S. L., Foltz, C. B., & Hewett, P. C. 1991, ApJ, 373, 23

Wilkes, B. J., & Elvis, M. 1987, ApJ, 323, 243

Wills, B. J., Netzer, H., & Wills, D. 1985, ApJ, 288, 94

Wilms, J., Reynolds, C. S., Begelman, M. C., Reeves, J., Molendi, S., Staubert, R., & Kendziorra, E. 2001, MNRAS, 328, L27

Wozniak, P. R., Zdziarski, A. A., Smith, D., Madejski, G. M., & Johnson, W. N. 1998, MNRAS, 299, 449

Young, A. J., Lee, J. C., Fabian, A. C., Reynolds, C. S., Gibson, R. R., & Canizares, C. R. 2005, ApJ, 631, 733

Zheng, W., Kriss, G. A., Telfer, R. C., Grimes, J. P., & Davidsen, A. F. 1997, ApJ, 475, 469

Zhou, X.-L., & Wang, J.-M. 2005, ApJL, 618, L83

Zdziarski, A. A., & Gierliński, M. 2004, Progress of Theoretical Physics Supplement, 155, 99

Zdziarski, A. A., Johnson, W. N., Poutanen, J., Magdziarz, P., & Gierlinski, M. 1997, ESA SP-382: The Transparent Universe, 373

Zdziarski, A. A., Johnson, W. N., Done, C., Smith, D., & McNaron-Brown, K. 1995, ApJL, 438, L63

Zycki, P. T., & Czerny, B. 1994, MNRAS, 266, 653

Zycki, P. T., Krolik, J. H., Zdziarski, A. A., & Kallman, T. R. 1994, ApJ, 437, 597